

# **Digital Profiling of Circulating Extracellular Vesicles at Single-Upconversion Nanoparticle Sensitivity and Resolution**

by Guan HUANG

Thesis submitted in fulfilment of the requirements for the degree of

**Doctor of Philosophy**

under the supervision of Prof. Dayong Jin,  
Dr. Gungun Lin, Dr. Ying Zhu

University of Technology Sydney  
Faculty of Science

01/07/2022

# **CERTIFICATE OF ORIGINAL AUTHORSHIP**

I, Guan Huang declare that this thesis is submitted to fulfilment of the requirements for the award of Doctor of Philosophy, in the School of Mathematical and Physical Sciences, Faculty of Science, at the University of Technology Sydney.

I certify that the work in this thesis has not previously been submitted for a degree nor has it been submitted as part of requirements for a degree.

I also certify that the thesis has been written by me. Any help that I have received in my research work and the preparation of the thesis itself has been acknowledged. In addition, I certify that all information sources and literature used are indicated in the thesis.

This research is supported by an Australian Government Research Training Program, Guangzhou Elite Program Scholarship and Translation Cancer Research Network PhD Scholarship Top-up Award.

Signature of Student:

Production Note:

Signature removed prior to publication.

Date: 01 July 2022

## Acknowledgements

First and foremost, I would like to thank my principle supervisor Distinguished Professor Dayong Jin for his supervision throughout the PhD project. You helped me look at research in a way that optimized my time at the bench and by understanding what was required to tackle a problem effectively and efficiently. At the same time, I am very grateful to your insightful comments, expertise and guidance in driving my research in the right direction.

I am thankful for having had the opportunity to work with such passionate and hardworking fellow researchers, Dr. Yinghui Chen, Dr. Gungun Lin and Dr. Ying Zhu. Thank you for your always supportive and willing to meet if I have questions or concerns. I would like to acknowledge my colleagues and collaborators who contributed to my research. Thanks to our IBMD colleagues, Dr. Yongtao Liu for optical knowledge sharing and optical system setup, Dr. Shihui Wen for UCNPs knowledge sharing and providing me with UCNPs at a high constant quality, Dr. Qian Peter Su for TIRF setup, Dejiang Wang for cell transfection, Mahnaz Maddahfar for providing polymers, Dr. Yuan Liu for microfluidic fabrications, and everyone in IBMD group. Thank you, Haoqi Mei for spending a lot of time in Western blotting and Dr. Yan Liao for providing materials to plasmid amplification. And this acknowledgement could never be complete without the collaborators from Garvan Institute of Medical Research. My thanks to A/Professor David Gallego-Ortega for his input in the project and for his support on preclinical models. I am grateful to Laura Rodriguez de la Fuente for enumerable amount of time and effort to helping me extract blood from mouse models. Thanks all, everything from experimental design to scientific writing has been invaluable over the years I've been here.

“In a PhD student's life, research is a 24x7 thing, if we aren't physically doing experiments, we most likely are mentally preparing for one.” I could not have done this without the love and support from my parents. I also want to thank my loving and warm boyfriend Peng Nie who listened with enthusiasm and curiosity to the minutiae of the project itself, and with great sympathy and understanding whenever I was feeling overwhelmed, anxious and hopeless. And I want to thank all my friends for helping me have a life outside my research. I am blessed to have you all in my life.

Finally, I would like to acknowledge the support provided by Australian Government Research Training Program, Guangzhou Elite Program Scholarship and Translation Cancer Research Network PhD Scholarship Top-up Award through which most of the work in this dissertation was funded. I sincerely apologize if I have forgotten to acknowledge anyone.

## List of publications

1. **G. Huang**, Y. Zhu, S. Wen, H. Mei, Y. Liu, D. Wang, M. Maddahfar, Q. P. Su, G. Lin, Y. Chen and D. Jin. Single Small Extracellular Vesicle (sEV) Quantification by Upconversion Nanoparticles. *Nano Letters*. 22, 3761–3769 (2022).
2. **Guan Huang**, Yongtao Liu, Dejiang Wang, Ying Zhu, Shihui Wen, Dayong Jin\*. Upconversion Nanoparticles for Super-resolution Imaging of Single Small Extracellular Vesicles (in preparation)
3. **Guan Huang**, Laura Laura Rodriguez de la Fuente, David Gallego-Ortega, Ying Zhu, Yongtao Liu, Dayong Jin\*. Preclinical detection of circulating EVs (in preparation)
4. **Huang, G.**; Lin, G.; Zhu, Y.; Duan, W.; Jin, D. Emerging Technologies for Profiling Extracellular Vesicle Heterogeneity. *Lab on a Chip* **20**, 2423–2437 (2020) (highlighted on front cover)
5. Chen, Y, Shimoni, O, **Huang, G**, Wen, S, Liao, J, Duong, HTT, et al. Upconversion nanoparticle-assisted single-molecule assay for detecting circulating antigens of aggressive prostate cancer. *Cytometry Part A*. 2021; 1– 11.
6. Liu, Y., Lin, G., Bao, G., Guan, M., Yang, L., Liu, Y., Wang, D., Zhang, X., Liao, J., Fang, G., Di, X., **Huang, G.**, Zhou, J., Cheng, Y., and Jin, D. Stratified Disk Microrobots with Dynamic Maneuverability and Proton-Activatable Luminescence for in Vivo Imaging. *ACS Nano* 2021 15 (12), 19924-19937
7. Lin, G., Liu, Y., **Huang, G.**, Chen, Y., Makarov, D., Lin, J., Quan, Z. and Jin, D. 3D Rotation-Trackable and Differentiable Micromachines with Dimer-Type Structures for Dynamic Bioanalysis. 2021. *Adv. Intell. Syst.*, 3: 2000205.  
([1,2,3,4,5] are closely related to my PhD program)

## Conferences

1. Background-free single luminescent nanoparticle assay for detecting tumor-derived extracellular vesicles, Oral Poster, Thomas Ashworth CTC & Liquid Biopsy Symposium 2021, Sydney, Australia
2. Profiling Single Extracellular Vesicles from Single Cells, Oral Presentation, Australasian Extracellular Vesicles Conference 2021, Auckland, New Zealand

## Award

1. Vice-Chancellor's Postgraduate Research Conference Fund 2021, UTS, Australia.

2. TCRN PhD Scholarship Top-up Awards 2020, Translational Cancer Research Network, Australia
3. Australasian Extracellular Vesicles Conference Outstanding student presentation award 2020, ANZSEV, Australia and New Zealand

## Structure of Thesis

This thesis has five chapters. Chapter 1 is on the basic knowledge and literature review. Chapter 2-4 are the three core result chapters reporting the experiments, the research results and discussions of developing nanoparticles and imaging tools to detect and qualify the surface biomarkers of single extracellular vesicles (EVs). In chapter 2, the types and numbers of EV surface markers have been quantified and profiled at single nanoparticle sensitivity. In chapter 3, super-resolution imaging techniques have been used to digitize the number of nanoparticles on single EVs. In chapter 4, the developed technology platform has been applied to prognose the cancer metastasis on two mouse models, both relevant breast cancer cohort. Chapter 5 is the conclusion of this thesis and discussions for future works. I organize the five chapters following the flowchart below:

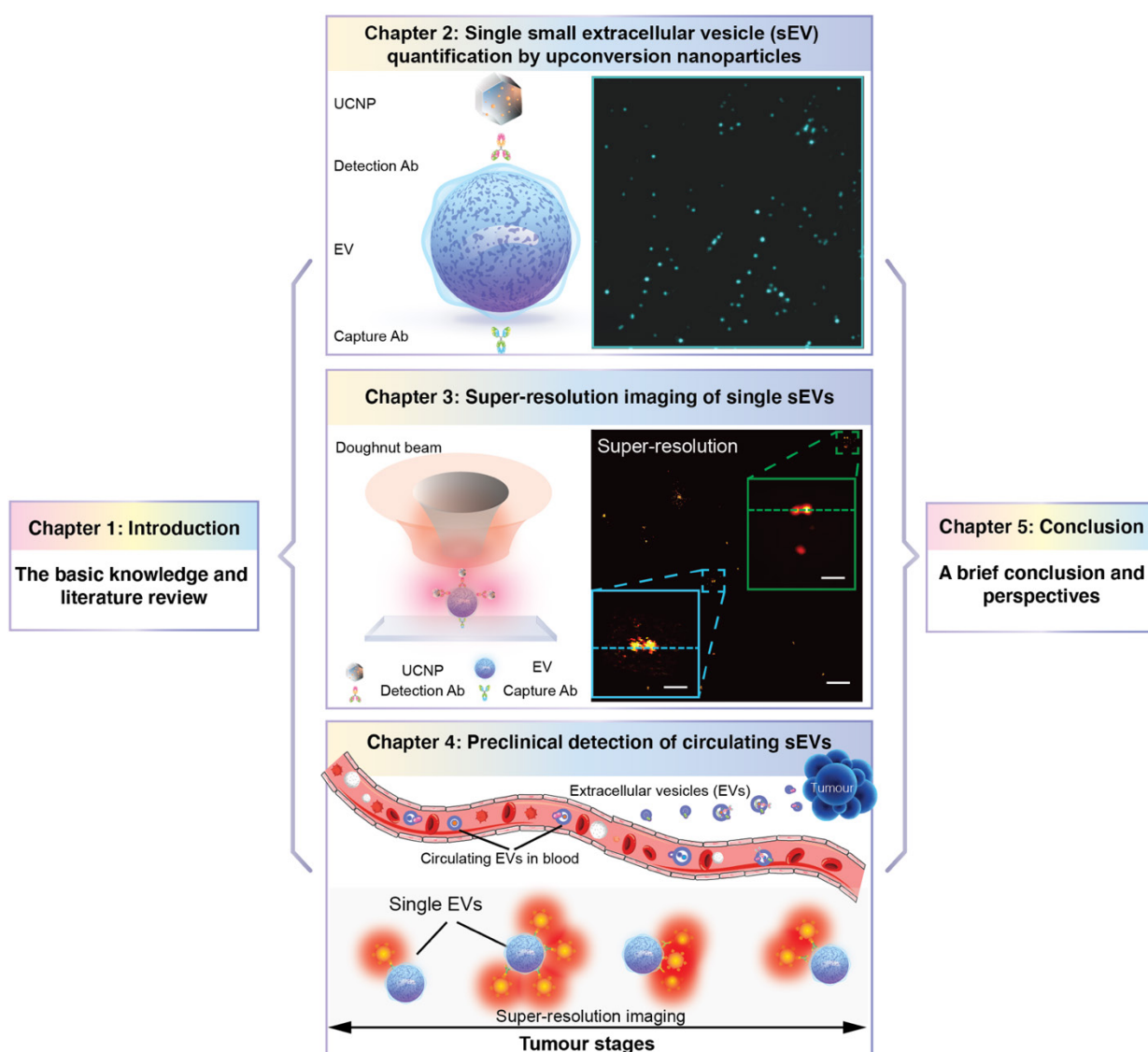


# Table of Contents

<b>Acknowledgements</b> .....	<b>i</b>
<b>List of publications</b> .....	<b>ii</b>
<b>Structure of Thesis</b> .....	<b>iv</b>
<b>Table of Contents</b> .....	<b>v</b>
<b>Abstract</b> .....	<b>1</b>
<b>Statement of Contribution of Authors for chapter 1</b> .....	<b>2</b>
<b>Chapter 1 Introduction</b> .....	<b>3</b>
1.1 Liquid biopsy in cancer diagnostics and management .....	3
1.2 Liquid biopsy biomarkers.....	4
1.2.1 Circulating tumour cells (CTC) .....	4
1.2.2 Circulating tumour DNA (ctDNA) .....	5
1.2.3 Circulating RNA .....	5
1.2.4 Circulating Proteins .....	5
1.2.5 Circulating extracellular vesicles .....	6
1.3 Role of EVs in liquid biopsy .....	7
1.4 EV separation and concentration techniques.....	8
1.5 EV characterisation techniques .....	9
1.6 Strengths of circulating EVs in liquid biopsy.....	10
1.7 Limitations of circulating EVs in liquid biopsy .....	11
1.7.1 Heterogeneity - A hidden world beneath population averages .....	12
1.7.2 Current Approaches for EV Heterogeneity Analysis .....	13
1.8 Nanomaterials for EV detection .....	22
1.8.1 Magnetic nanoparticles (MNPs) .....	23
1.8.2 Graphene oxide (GO).....	23
1.8.3 Gold nanoparticles (AuNPs) .....	23
1.8.4 Quantum dots (QDs) .....	24
1.8.5 Semiconducting polymer dots (Pdots).....	24
1.8.6 Carbon nanotubes (CNT) .....	26
1.8.7 Upconversion nanoparticles (UCNPs).....	27
1.9 UCNPs in bio-applications .....	27
1.9.1 Mechanism of UCNPs.....	27
1.9.2 Synthesis of UCNPs .....	29
1.9.3 Surface modification of hydrophobic UCNPs .....	29
1.9.4 UCNPs in biosensing .....	32

1.10 EVs and super-resolution microscopy.....	36
1.10.1 Single EV imaging technique .....	37
1.10.2 UCNPs in super-resolution techniques .....	39
1.10.3 Diffraction limit in microscopy.....	39
1.10.4 UCNP-based STED-like super-resolution nanoscopy .....	40
1.10.5 Photon transition system in UCNPs.....	40
1.10.6 Saturation effect with doughnut-shaped beam.....	41
1.11 Aim.....	43
<b>Statement of Contribution of Authors for Chapter 2.....</b>	<b>45</b>
<b>Chapter 2 Single small extracellular vesicle (sEV) quantification by upconversion nanoparticles</b> .....	<b>46</b>
Abstract.....	46
2.1 Introduction .....	46
2.2 Methods .....	48
2.2.1 Cell culture.....	48
2.2.2 EVs isolation from Cell culture medium.....	48
2.2.3 Cryogenic Electron Microscopy.....	49
2.2.4 Nanoparticle tracking analysis.....	49
2.2.5 Western blotting.....	49
2.2.6 Flow cytometry .....	50
2.2.7 Synthesis of NaYF <sub>4</sub> :20%Yb <sup>3+</sup> ,2%Er <sup>3+</sup> .....	51
2.2.8 Transmission electron microscopy.....	51
2.2.9 Synthesis of PEOGMEA <sub>13</sub> -b-PMAEP <sub>7</sub> .....	51
2.2.10 Surface modification of UCNPs.....	52
2.2.11 Characterization of functionalised UCNPs.....	52
2.2.12 TIRF setup and imaging.....	52
2.2.13 LENS assay.....	53
2.2.14 Image and data processing .....	53
2.3 Results .....	54
2.3.1 Production and isolation of cancer cell-derived EVs.....	54
2.3.2 Characterization of Cancer cell-derived EVs.....	55
2.3.3 Preparation and characterisation of LENS.....	57
2.3.4 Quantification of EpCAM <sup>+</sup> EVs from cell line model.....	63
2.4 Conclusion and discussion .....	67
<b>Statement of Contribution of Authors for Chapter 3.....</b>	<b>69</b>
<b>Chapter 3 Super-resolution imaging of single sEVs.....</b>	<b>70</b>
Abstract.....	70
3.1 Introduction .....	70
3.2 Methods .....	72
3.2.1 Cell transformation.....	72
3.2.2 EV isolation.....	73



3.2.3 Synthesis of NaYF <sub>4</sub> :40%Yb <sup>3+</sup> ,4%Tm <sup>3+</sup> nanocrystals. ....	73
3.2.4 Fabrication of LENS. ....	73
3.2.5 GFP-LENS colocalization procedure.....	73
3.2.6 Dual-LENS assay procedures. ....	73
3.2.7 Deconvolution methods for wide-field imaging .....	74
3.2.8 Super-resolution setup. ....	74
3.3 Results .....	75
3.3.1 Optical performance evaluation of LENS doped with different kinds of emitters .....	75
3.3.2 Co-localization and comparison of EpCAM-mGFP EV with LENS.....	79
3.3.3 Single EV imaging by super-resolution microscope.....	82
3.3.4 Future direction of the technique - Size related steric hindrance.....	85
3.4 Conclusion and discussion .....	88
<b>Statement of Contribution of Authors for Chapter 4.....</b>	<b>89</b>
<b>Chapter 4 Preclinical detection of circulating EVs.....</b>	<b>90</b>
Abstract.....	90
4.1 Introduction .....	90
4.1.1 Limitations in breast cancer clinical management.....	90
4.1.2 Role of EVs in tumour metastases .....	91
4.1.3 Role of EVs in indexing the stage of metastatic tumour progression .....	92
4.1.4 Murine preclinical cancer modelling .....	93
4.2 Methods .....	99
4.2.1 Experimental Animal Models .....	99
4.2.2 Intraductal mammary carcinoma implantation. ....	99
4.2.3 Blood and lungs collection.....	100
4.2.4 Plasma isolation from fresh blood.....	100
4.2.5 EVs isolation from Plasma.....	100
4.3 Results .....	101
4.3.1 Preclinical prognosis of Syngeneic Models.....	102
4.3.2 Preclinical prognosis of GEMMs.....	107
4.4 Conclusion and discussion .....	113
<b>Chapter 5 Conclusion and Perspectives.....</b>	<b>115</b>
5.1 Conclusion .....	115
5.2 Technical limitations .....	116
5.3 Clinical translation limitations .....	117
5.4 Perspectives .....	118
<b>Reference .....</b>	<b>122</b>

## Abstract

Circulating extracellular vesicles (EVs) carry significant information about the progression stages of tumour sites. Quantification of low-abundant EVs and statistical profiling of the heterogeneity of single EVs, particularly from liquid biopsy sampling, will guide clinical decisions on the stages of tumour progression. However, the nanoscopic sizes (typically 40-200 nm) and the extremely small quantity of cargo materials demand the high detection sensitivity, stability, resolution and throughput to be simultaneously achieved.

Nanotechnology has been broadly used in the field of liquid biopsy. This thesis explores a new strategy for ultra-sensitive, photo-stable, and super-resolution immunoassay of single EVs, which is based on the development, bio-conjugation and application of upconversion nanoparticles (UCNPs). In chapter 2, we apply UCNPs for direct enumeration of single CD9 and EpCAM positive EVs ( $CD9^{+}EpCAM^{+}EVs$ ). The achieved single-molecule sensitivity results in a femtomolar detection limit ( $1.8 \times 10^6$  EVs mL<sup>-1</sup>), which was nearly 3 orders of magnitude lower than the standard enzyme-linked immunosorbent assay (ELISA). Compared with previous luminescence resonance energy transfer (LRET) method using UCNPs for detection of EVs, our technique achieves single tumour-derived sEV quantification. In chapter 3, we report super-resolution imaging technique for single  $CD9^{+}EpCAM^{+}EV$  analysis. The upconversion luminescence of single UCNPs can nonlinearly response to a donut-shaped scanning beam, so that a resolution better than 40 nm can be achieved beyond the diffraction limit. In chapter 4, with the ultra-sensitivity and photo stability achieved by UCNPs as well as super resolution offered by a donut-shaped scanning, the preclinical translation capability of the integrated technology platform has been examined by two types of breast cancer mouse models. Our results suggest that the population of cancer-derived circulating EVs, detected and classified by the number of UCNPs, can be used to monitor the metastatic tumour progression, including non-metastasis/high-metastasis and low-metastasis/high-metastasis mouse models. Furthermore, we find that the number of UCNPs on single EVs can be used to index the stage of metastatic tumour progression. In chapter 5, we discuss the challenges and opportunities of this thesis towards clinical translation, which suggests a new scope of research by integrating nanotechnology, microscopy imaging and lab-on-a-chip devices for EV research and applications. This thesis presents a viable approach of using the EVs-based liquid biopsy for tumour diagnosis and prognosis.

**Key words:** extracellular vesicles, upconversion nanoparticles, super-resolution, cancer metastases, liquid biopsy

## Statement of Contribution of Authors for chapter 1

(Section 1.7.1, 1.7.2 and 1.10.1)

[1] Huang, G.; Lin, G.; Zhu, Y.; Duan, W.; Jin, D. Emerging Technologies for Profiling Extracellular Vesicle Heterogeneity. *Lab Chip* **20**, 2423–2437 (2020)

	G. H	G.L	Y.Z	D.W	D.J
Experiment Design					
Sample preparation					
Data collection					
Analysis	▪	▪	▪	▪	
Manuscript	▪	▪	▪		▪

The review paper (section 1.7.1, 1.7.2 and 1.10.1) was written under supervisors of Dr. Gungun Lin, Dr. Ying Zhu, and Prof. Dayong Jin.

---

# Chapter 1 Introduction

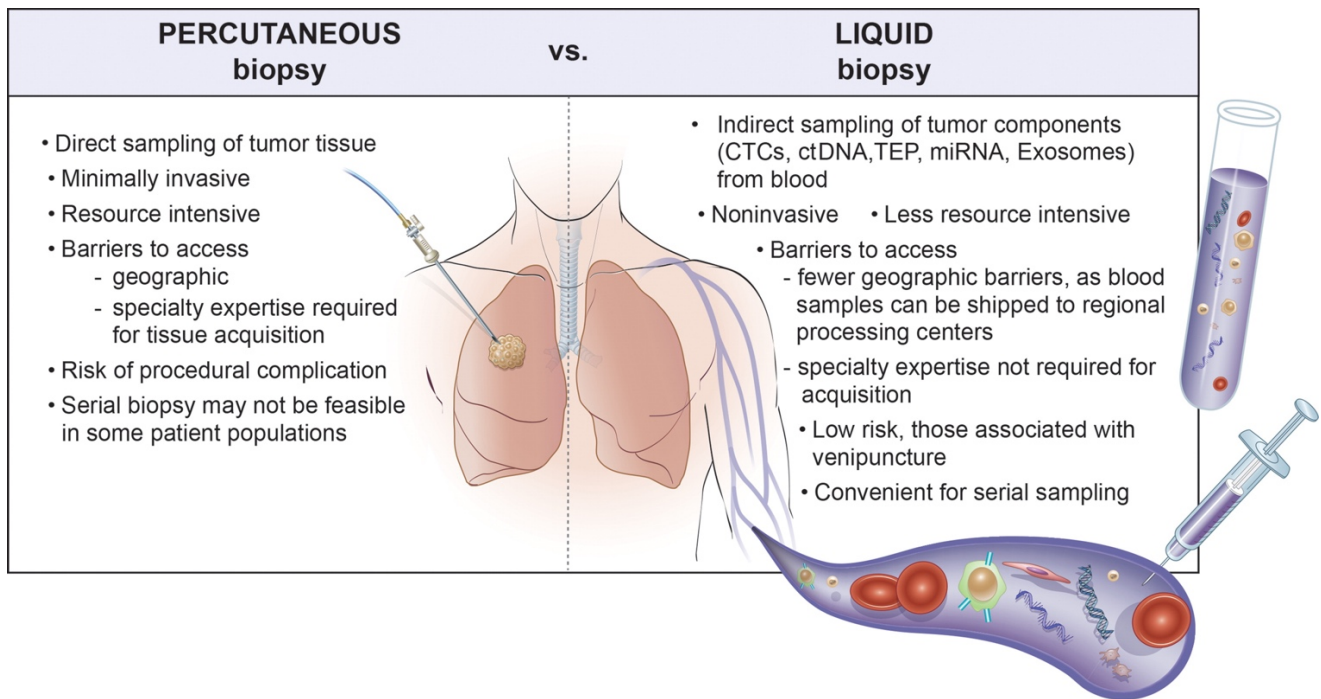
---

This PhD thesis focuses on applying upconversion nanoparticles (UCNP) and single-molecule imaging techniques to classify and digitalize both the types and amounts of surface biomarkers on single extracellular vesicles (EVs). The set of heterogeneity characteristics has been further found highly correlative to the stage of cancer metastasis. This introduction chapter provides the background knowledge related to this research program and introduces the motivations to develop new technologies for EV heterogeneity study. We firstly emphasized on the significance of liquid biopsy in early diagnosis of cancers and longitudinal monitoring of cancer progression, followed by a review of currently discovered biomarkers used in liquid biopsy. We then summarized the current understandings of cancer-derived and tumour microenvironment-derived EVs, their roles in tumour progression and their use as cancer biomarkers for diagnosis. Moreover, we discussed the current limitations in EV-based liquid biopsy and introduced the concept of studying heterogeneity of the EV populations. The majority of the literature review in this chapter relating techniques for EV heterogeneity studies, including sections 1.7.1, 1.7.2 and 1.10.1, has led to a published review paper. Finally, we highlighted the luminescent properties of UCNPs and their utilisation in super-resolution imaging, single molecule assay, and biomedical applications.

## **1.1 Liquid biopsy in cancer diagnostics and management**

Tumour tissue biopsy is considered the gold standard for detecting and routinely monitoring of the cancer progression. However, tissue biopsy has limitations in capturing spatial and temporal tumour heterogeneity as its information is limited to a single location and time point besides being an invasive method. Liquid biopsy has revolutionized the oncology field as it enables comprehensive, serial and non-invasive molecular profiling of any tumour-derived material shedded into the blood or other bodily fluids, and thereby allows longitudinal monitoring of cancer progression<sup>1</sup>. Liquid biopsies extract biomarkers from bodily fluids such as blood, urine, saliva, or cerebrospinal fluid for detecting, diagnosing, or monitoring disease. They are minimally invasive and more accurately convey the heterogeneous nature of cancer as well as allowing for more frequent sampling over a longer period when compared to traditional tissue biopsy or imaging modalities (**Fig. 1-1**). Therefore, clinical oncology research has

focused on investigating the capability of liquid biopsies to provide equivalent or new information to clinicians than is currently received from solid tissue analysis or new imaging.



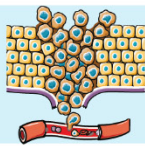
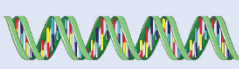
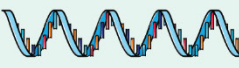


**Figure 1-1 | Illustration compares percutaneous biopsy versus liquid biopsy characteristics.**  
Reprinted from Reference<sup>2</sup>.

## 1.2 Liquid biopsy biomarkers

Different types of liquid biopsy biomarkers have been investigated and evaluated extensively in the past years. The strengths and limitations of circulating biomarkers in cancer are summarised in **Figure 1-2**<sup>3</sup>.

### 1.2.1 Circulating tumour cells (CTC)

CTCs are released from primary tumours and metastases into the blood. Extensive research on CTC for clinical uses helped FDA approve the CellSearch System<sup>TM</sup> as a prognostic tool for metastatic breast cancer. At present, CTC detection remains a challenging diagnostic approach as a result of numerous technical limitations current facing. This is especially problematic during the early stages of the disease due to the small number of CTCs released into the blood of cancer patients. Clinical guidelines do not suggest isolating CTCs<sup>4</sup> in clinical practice due to the lack of actionable information provided from quantification alone<sup>5</sup>. For example, a phase III clinical trial found enumeration of CTCs by the CellSearch System<sup>TM</sup> to provide no benefit for high-risk patients when changing therapy based on the CTC results<sup>6</sup>.

	Biomarker types	Biomarkers	Strengths	Limitations
	Circulating tumour cells	Particular surface markers	Direct derived from tumour sites	Low counts in circulation, technical challenge
	Circulating DNA	Mutant ctDNA, e.g., EGFR mutation, KRAS mutation	Easy examination with technical advances	Not suitable for tumour without mutations
	Circulating RNA	miRNAs, mRNA, lncRNA, etc	Enriched in the circulation and convenient detection	Unstable, easy degraded by RNase
	Circulating proteins	Primarily cancer-specific proteins, e.g. CA19-9, CEA	Enriched in the circulation and convenient detection	Low-specificity, present in patient without cancer
	Circulating EVs	DNA, RNA, proteins, etc	Protected by lipid bilayer membrane structure, direct derived from tumour sites	Technical challenges for isolation, purification and quantification

**Figure 1-2 | The strengths and limitations of circulating biomarkers in cancer.**

### 1.2.2 Circulating tumour DNA (ctDNA)

Tumour-derived cfDNA (ctDNA) is released mainly through apoptosis or necrosis of tumour cells and normal cells but active secretion may play an additional role. ctDNA can be detected by sensitive molecular assays targeting mutations or structural genomic aberrations. However, ctDNA is present in very low concentrations depending on the tumour type and stage and not suitable for tumours without mutations.

### 1.2.3 Circulating RNA

microRNAs (miRNAs) and other RNAs are released by tumour and host cells into the blood by apoptosis/necrosis. Different kinds of RNAs have various functions. For example, miRNAs and small interfering RNAs (siRNAs) mediate post-transcriptional RNA silencing; small nuclear RNAs (snRNAs) regulate splicing; small nucleolar RNAs (snoRNAs) are involved in ribosomal RNA (rRNA), transfer RNA (tRNA), and snRNA processing; and P-element-induced-wimpy testis (piwi)-interacting RNAs (piwiRNAs) regulate chromatin modification and transposon repression. Circulating RNA can be enriched in the circulation. However, they are unstable and easy to be degraded by circulating RNase.

### 1.2.4 Circulating Proteins

Circulating protein markers are indicative of tumour progression and can be analysed. They perform various functions within organisms, including catalysing metabolic reactions, gene replication, responding to stimuli, providing structure to cells and organisms, and transporting molecules from one location to another. But they are of low-specificity and can be present in patients without cancer.

### 1.2.5 Circulating extracellular vesicles

EVs are membrane-bound phospholipid vesicles actively secreted by most cells and existing in almost all kinds of body fluids, like blood<sup>7,8</sup>, ejaculates<sup>9,10</sup>, urine<sup>11,12</sup>, cerebrospinal fluid<sup>13,14</sup>, saliva<sup>15</sup>, and breast milk<sup>16,17</sup>. EVs carry specific cargos such as mRNA, miRNA and gDNA fragments, and a myriad of different proteins depending on the cell of origin (**Fig. 1-3b**). They are stable in circulation as they are protected by lipid bilayer membrane. However, there are technical challenges for the isolation, purification, quantification of EVs and their contents.

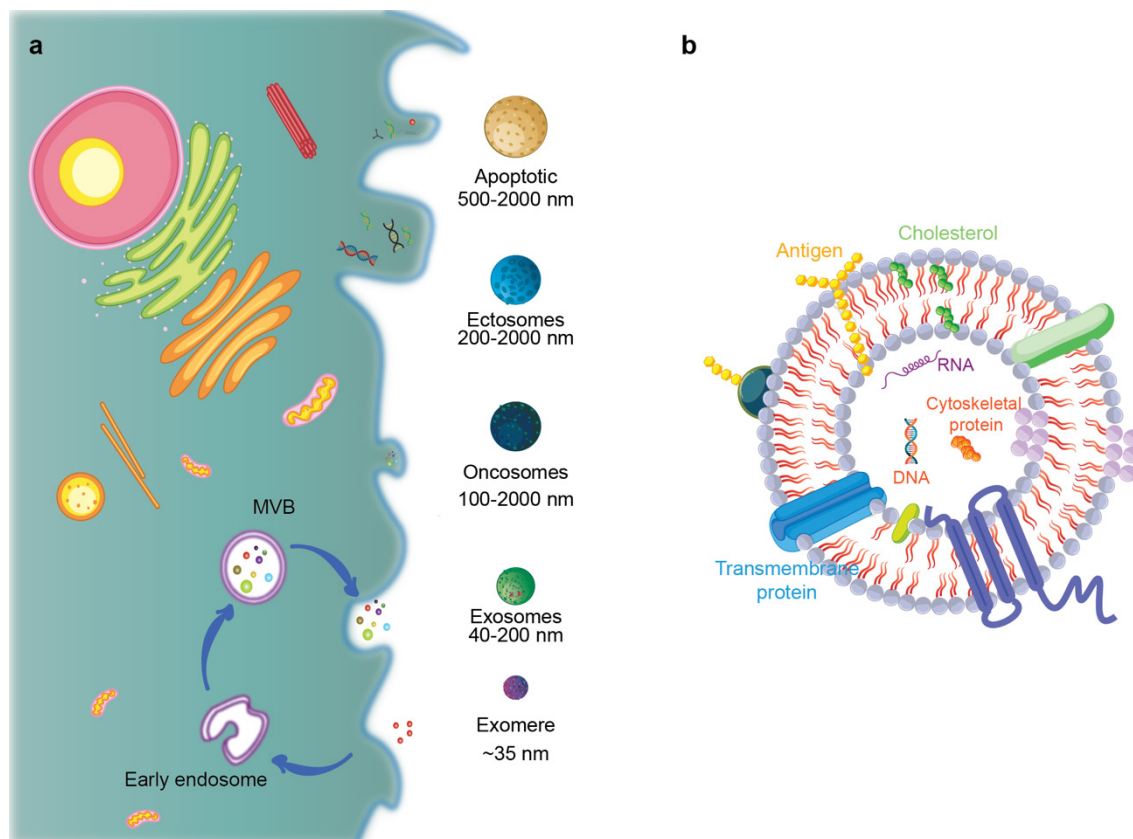


**Figure 1-3 | Extracellular vesicles and their compositions.** (a) Schematic illustration of vesicle subpopulations that comprise the cellular communication milieu. (b) EVs carry a wealth of proteomic and genetic information including proteins, lipids, miRNAs, mRNA, non-coding RNA and other molecules from parent cells. Reprinted from Reference<sup>18</sup>.

Based on biogenesis and biophysical characteristics, EVs have been classified into three major subtypes (**Fig. 1-3a**): (I) exosomes - generated within multivesicular endosomal compartments and are secreted when these compartments fuse with the plasma membrane (PM), with sizes in the range of 40-200 nm; (II) ectosomes or shedding microvesicles (MVs) - directly formed and released from the cells' PM, with sizes in the range of 200-2000 nm; (III), apoptotic bodies - formed as a consequence of apoptotic disintegration, with sizes in the range of 500-2000 nm<sup>19-22</sup>.

### **1.3 Role of EVs in liquid biopsy**

The functions of EVs can vary greatly depending on their inherent compositions of each class. Exosomes are known for intercellular communication in both normal and diseased tissue<sup>13,14</sup>, and its biogenesis starts within the endosomal system, and the release of exosome involves several cellular steps<sup>19-21</sup>. MVs are involved regulating programmed cell death<sup>23</sup>, modulation of the immune response<sup>24</sup>, inflammation<sup>25</sup>, angiogenesis<sup>22</sup>, and coagulation<sup>26</sup>. Oncosomes are cancer-specific MVs transferring oncogenic messages and protein complexes across cell borders<sup>27</sup>. The apoptotic bodies are known for facilitating phagocytosis and are formed only during programmed cell death<sup>28</sup>. Due to the above specific characteristics, EVs are promising biomarkers in cancer diagnostics and mediators in drug delivery<sup>25,26</sup>.

Cancer-derived EVs are regarded as promising potential to be used as therapeutics and disease biomarkers<sup>29</sup>. The role of EVs in cancer is diverse and they contribute to many of the hallmarks of cancer<sup>30,31</sup>, including cell proliferation and migration, angiogenesis, evasion of cell death, and invasion and metastasis<sup>29</sup> (**Fig. 1-4**). The non-invasive nature of obtaining cancer-derived EVs allows the sequential sampling of patients over time, thereby assisting clinical decision-making with regard to early diagnosis, prognosis, detecting cancer recurrence, and therapy resistance or alterations of the cancer oncogenic repertoire in potentially all cancers<sup>32</sup>.



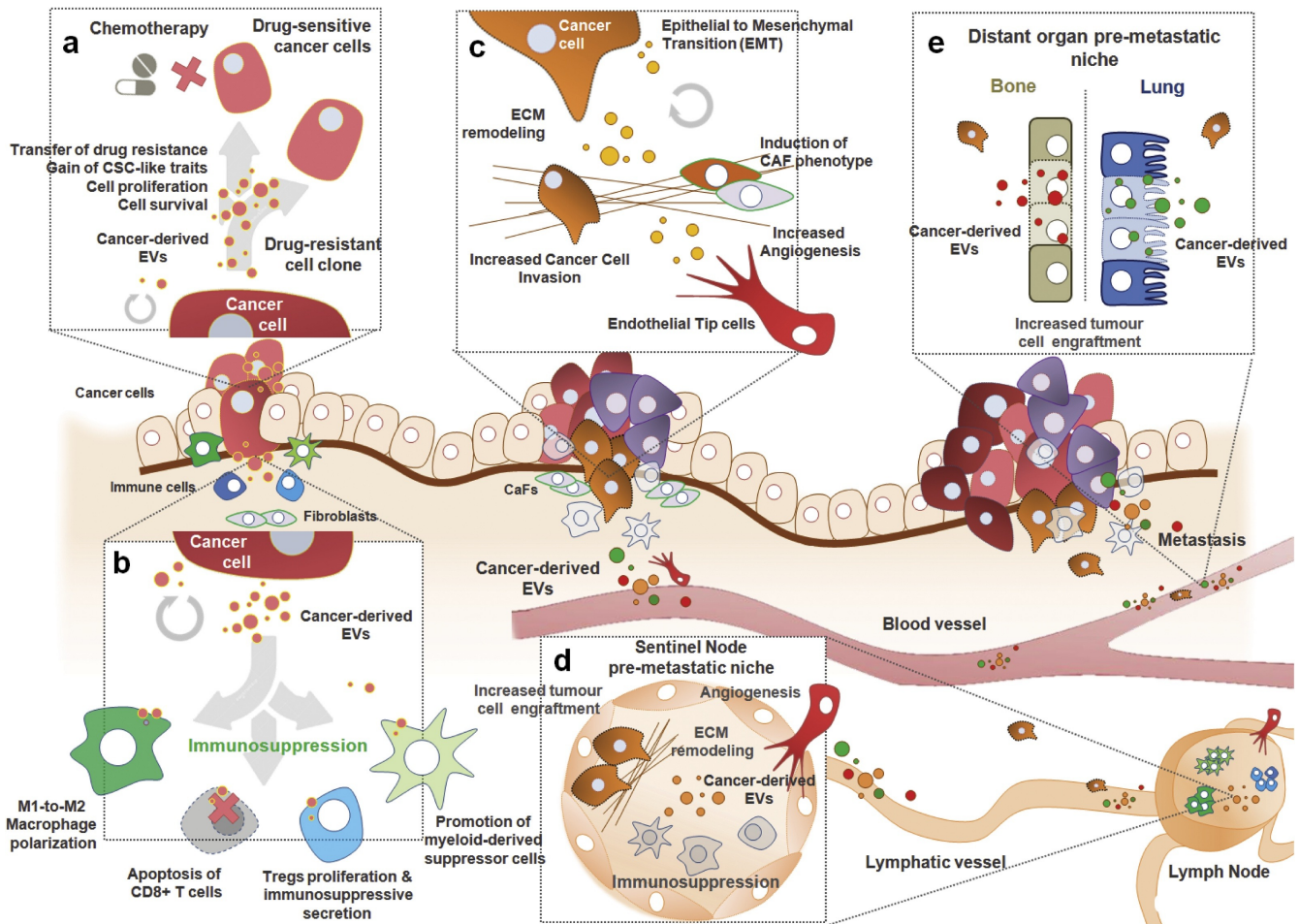


**Figure 1-4 | Contribution of cancer-derived EVs to cancer progression and drug resistance.** (a) Transfer of aggressive phenotype from drug-resistant cancer cells to neighbouring cells via EV shedding. (b) Cancer-derived EVs can modulate the local immune and/or inflammatory response. (c) EV-mediated tumour-promoting microenvironment will grant the tumour cells the ability to evade the immune system. Importantly, these circulating EVs are selectively taken up in the (d) lymph nodes and/or at (e) distant organs such as the lungs or bone, accordingly to their EV-surface integrin specificity. Reprinted from Reference<sup>33</sup>.

#### 1.4 EV separation and concentration techniques

The release of extracellular vesicles in the extracellular space allows for their recovery from cell culture supernatants and liquid biopsy samples. In order to analyse the EV cargo, first EVs of interest must be isolated in high purity and high yields. Currently used EV separation and concentration techniques are summarized in **Figure 1-5**. Combining multiple isolation procedures is encouraged to clearly separate subpopulations of vesicles based on their size, density or composition.

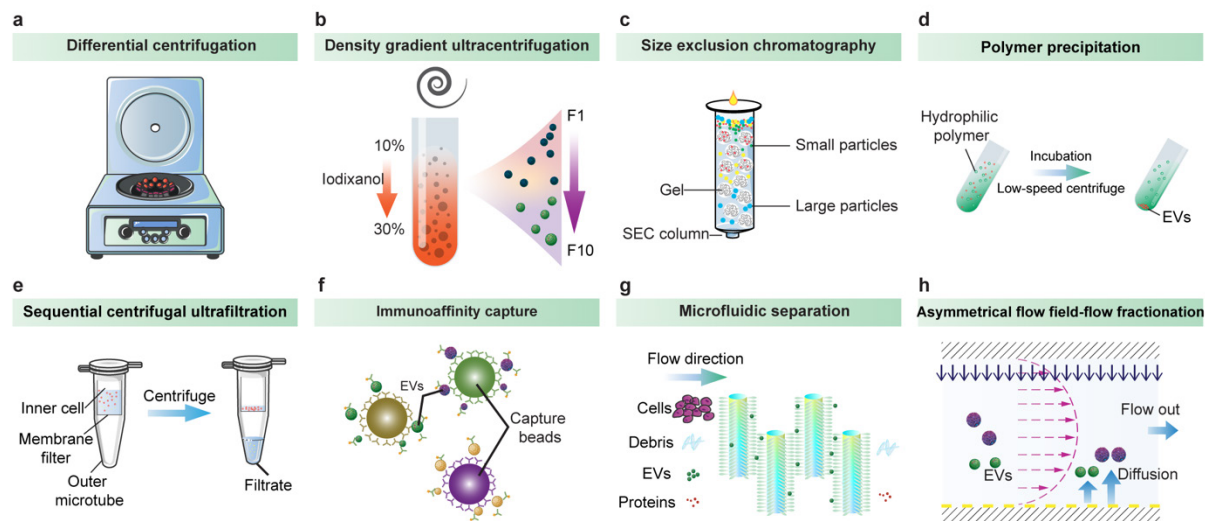


**Figure 1-5 | The methods for EV isolation.** (a) Differential centrifugation. (b) Density gradient ultracentrifugation. (c) Size exclusion chromatography. (d) Polymer precipitation. (e) Sequential centrifugal ultrafiltration. (f) Immunoaffinity capture. (g) Microfluidic separation. (h) Asymmetrical flow field-flow fractionations.

### 1.5 EV characterisation techniques

Once EVs are isolated by one of the methods described above, the isolated EVs need to be analyzed by downstream assays. Isolated samples of EVs also often contain a mixture of contaminants consisting of small organelles, lipids, cholesterol, and other undesired microparticles. It is possible that contamination of isolated EVs may lead to abnormal or misleading data, therefore, checking the sample purity is a crucial step in properly analysing EVs. Several analytical methods are available and should be combined to first assess the purity, integrity and concentration of extracellular vesicles before further analysis or other experiments are performed. Some of current EV analytical techniques are summarized in **Table 1-1**.

**Table 1-1. Summary of main techniques for the characterization of EVs physical properties<sup>34</sup>.**

Physical property and technique	Measurement principle	Single particle detection	Targeting surface marker
<i>Structure and morphology</i>			
Electron microscopy (EM)	Images sample with electrons	Yes	Yes
Atomic force microscopy (AFM)	Measures the interaction between AFM tip and sample	Yes	Yes
Small angle X-ray scattering	Detects the scattering of X-rays at small angles	No	No

(SAXS)			
<b>Size</b>			
Dynamic light scattering (DLS)	Analyses the fluctuations of scattering intensity of particles in Brownian motion	No	No
Nanoparticle tracking analysis (NTA)	Tracks the Brownian motion of the particles in scattering or in fluorescence mode	Yes	Yes
Resistive pulse sensing (RPS)	Measures the change in conductance across a sensing pore upon passage of a particle	Yes	No
Flow cytometry	Measures scattering or fluorescence intensity of particles illuminated by a laser	Yes	Yes
<b>Refractive index</b>			
Nanoparticle tracking analysis (NTA)	Measures the scattering intensity of single particles and correlates with the size determined by NTA	Yes	No
<b>Buoyant density</b>			
Density gradient	Material floats at a density equal the one of the surrounding medium	No	No
<b>Buoyant mass</b>			
Suspended channel resonator	The change of the resonance frequency upon passage of a vesicle is related to the vesicle mass	No	No
<b>Zeta potential</b>			
Electrophoretic light scattering	Electrophoretic mobility is measured in an oscillating electric field; in conjunction with DLS size measurement	No	No
Zeta potential nanoparticle tracking analysis (Z-NTA)	Tracks the motion of the particles in an electrical field; in conjunction with NTA size measurement	Yes	No
Resistive pulse sensing (RPS)	Quantification of the passage velocity of particle through the pore in presence of an electric field; in conjunction with RPS size measurement	Yes	No
On chip microcapillary electrophoresis	The motion of the particle in an electric field is detected in dark-field microscopy	Yes	No

## 1.6 Strengths of circulating EVs in liquid biopsy

Circulating EVs show significant superiority over other sources of liquid biopsy<sup>35</sup> (**Fig. 1-6**). First, circulating EVs exist in almost all body fluids and possess high stability encapsulated by lipid bilayers, protecting their cargo against degradation<sup>36</sup>. The high biological stability can reduce the cost of sample short-term storage and the difficulty of transportation, which greatly enhances the clinical applicability of circulating EVs. Second, the biological information of circulating EVs is more representative than ctDNA. Third, circulating EVs express specific proteins, which can be used as markers to effectively distinguish them from other vesicles. Fourth, circulating EVs can present specific surface proteins from parental cells, which can realize the isolation of origin-specific EVs and predict organ-specific metastasis. Fifth, compared with CTCs, circulating EVs are much more abundant in biofluids than CTCs and

relatively convenient to obtain from almost body fluid. In particular, EVs are a valuable source of cancer biomarkers since they are much more abundant in biofluids than CTCs. Additionally, there are many recognized classic extraction methods and a considerable number of novel methods under development for EVs, while CTC collection is still challenging. Meanwhile, the detection sensitivity and specificity of EV-DNA mutation frequency are higher than those of ctDNA<sup>37</sup>.

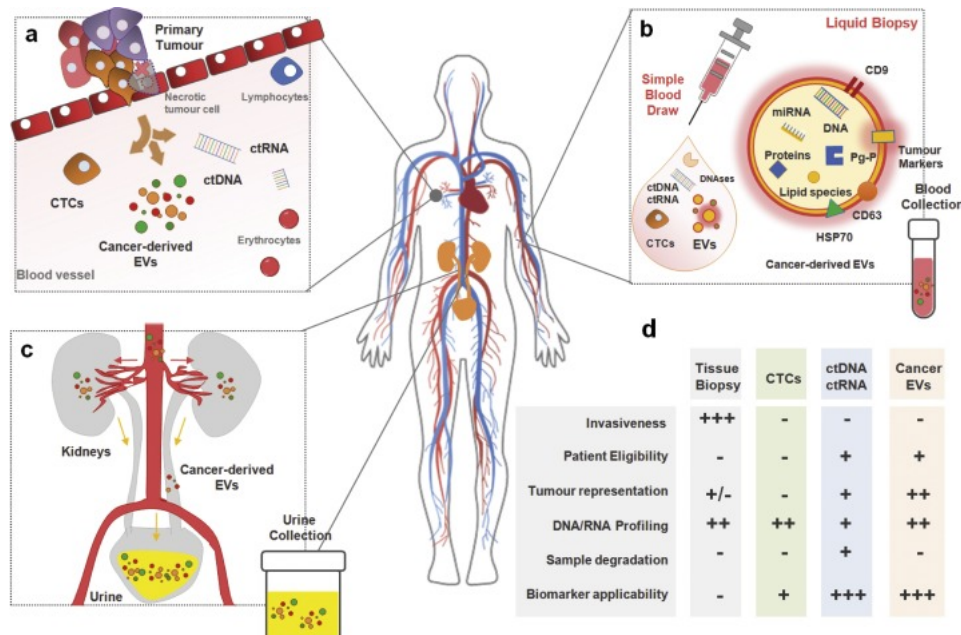


**Figure 1-6 | EV-based analytes of liquid biopsies.** (a) At the primary tumour site, living cancer cells release high amounts of tumour-analytes into the bloodstream. (b) These tumour-derived analytes can be easily accessed in liquid biopsies through multiple longitudinal sampling of (b) peripheral blood or (c) urine to interrogate the tumour landscape. (d) Comparative table illustrating the advantages of liquid biopsies (CTCs, ctDNA/RNA and cancer-derived EVs) over the traditional tissue biopsy. Reprinted from Reference<sup>33</sup>.

### 1.7 Limitations of circulating EVs in liquid biopsy

Current limitations of EV-based liquid biopsy are discussed as well<sup>38,39</sup>. A critical limit to the clinical application of EVs as liquid biopsies is the lack of standardized protocols for sample handling and EV isolation and analysis, which could impact reproducibility in the clinical setting. Currently used EV isolation procedures often comprise many biospecimen-handling steps and can subject EVs to different types of physical and chemical insults, which may damage EVs and/or change their biological and physical properties. Another factor influencing the reproducibility of EV studies is the lack of standardized guidelines defining EV nomenclature and definition, and the control experiments needed

for validation. In addition, more knowledge of the specific markers of the EV subtypes and fundamental roles of each type of EV is required before their applications in various disease setting.

### 1.7.1 Heterogeneity - A hidden world beneath population averages

It has become clear that most methods used to isolate exosomes co-isolate heterogeneous populations of EVs of diverse biogenic origin. The existing heterogeneity beneath the EV population is why there is no standardized protocol for sample handling and EV isolation and analysis. And the heterogeneity is the factor that influences the reproducibility of EV studies, thereby limiting the clinical application of EVs as liquid biopsies.

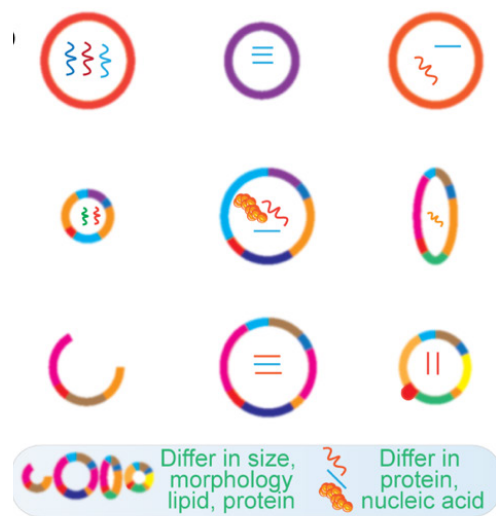


**Figure 1-7 | Schematic representation of EVs heterogeneity.** Different subpopulations exist within EVs isolated from the same batch of cells. EVs can differ with regard to size, morphology, lipid, protein, and nucleic acid composition.

At the current stage, one of the biggest challenges for EVs is to address the heterogeneity within EV populations. For one thing, according to the latest consensus of the International Society for Extracellular Vesicles (ISEV), assigning an EV to its biogenesis pathway is extraordinarily difficult. Currently, no isolation methods can separate EVs based on their biogenesis, and the isolation fractions overlap when using current isolation methods<sup>40</sup>. Growing evidence shows that within the biogenesis classifications of EVs, various subpopulations may exist, even with EVs originating from the same parental cells<sup>41-46</sup>. Their physical characteristics (size, density, morphology), cargos (protein, lipid content, nucleic acids) vary substantially, and biological properties may diverse accordingly. In this way, all above contribute to the heterogeneity of EVs (**Fig. 1-7**)<sup>40</sup>.

EVs have a diversity of physical characteristics. It is well known that EVs have diverse sizes, diverse densities, and even similar sizes could have different densities<sup>47</sup>, as discussed in more detail in many previous reviews<sup>44,48,49</sup>. To be emphasized here are that the size and density of varying EV subpopulations may significantly overlap even from the same parental cells due to current technology limitations. More interestingly, various morphologies of EVs have been confirmed by electron microscopy techniques. It has been shown that non-spherical EVs exist, and EVs can be featured with different shapes (such as long tubule-like, round, protrusions on surface, an incomplete round structure and so on) even they are produced by a single cell type<sup>50-53</sup>. The protrusions could be made up of proteins with specific functions, e.g. facilitating membrane fusion, which could allow cargo delivery into the cytoplasm of a potential target cell<sup>54</sup>. The variations in the morphologies of the EVs are indicative of the existence of different subpopulations that may have different functions.

Moreover, EVs also have a diversity of cargos. Too much overlap in the size of isolated EVs prohibits clear-cut differentiation by proteomic quantitation and complicates the study of EV heterogeneity in biological properties<sup>55-57</sup>. Different EV subpopulations secreted by neuroblastoma cells were reported to differ in the mutually exclusive presence of tetraspanin CD63 and amyloid precursor protein, which result in their different capabilities to target different cells<sup>24</sup>. Compared to proteomics, researches on lipid contents in EVs are under inadequate representation<sup>58</sup>. Lipid bilayer consists of two chains of the hydrophilic phosphate head and hydrophobic tail, with a variety of possible modifications and configurations, which could lead to heterogeneity in lipid contents<sup>59</sup>. The main limitation in EV proteomics and lipidomics are largely depends on the isolation techniques<sup>60</sup>. Similarly, profiling nucleic acid content of EVs face the same challenges<sup>46,61</sup>.

EVs' content was generally thought of as stochastically packaged. Evidence has proven that the uptake of cytoplasmic components during the classical exosome biogenesis is not random, and the exosome loading can be a highly regulated process<sup>61</sup>. RNA sorting into exosomes is unlikely to be random as well<sup>62-64</sup>. EVs' cargo is a reflection of what the cell is experiencing in response to different physiological and pathological conditions. EVs is a promising disease biomarker and could serve as a potential therapeutic tool. The main obstacle of understanding "disease-specific" EVs is lacking sufficient tools to reveal the mysteries of EVs heterogeneity among overlapped populations.

### **1.7.2 Current Approaches for EV Heterogeneity Analysis**

The limited capabilities of current EVs isolation and analysis techniques can only reveal a tip of iceberg of EV heterogeneity<sup>65</sup>. Most isolation methods, including ultracentrifugation, commercial precipitation kits or size-exclusion chromatography, can only yield an overlapped population of EVs based on the underlying physical mechanisms such as size, density and solubility. In addition, the isolated EVs are easily contaminated by protein aggregates as well as lipoprotein particles, which could lead to artefacts and complicate downstream analysis<sup>23,66</sup>. In this part, we will specifically discuss a few representative physical separation approaches that can fractionate different populations with innovative findings contributed to EVs heterogeneity study.

Ultracentrifugation is the most popular method to separate EVs with specific size range. Recently, a novel population of EVs (P200 fraction) smaller than exosomes promotes cell proliferation was identified, distinguishing from exosomes in size, protein, and biogenesis pathway<sup>45</sup>. However, ultracentrifugation is not a good choice for separating heterogeneous EVs subpopulation, but density gradients can move one step further. Density gradients, either of sucrose or iodixanol, are a classic method to separate EVs according to their floatation speed and equilibrium density. Protein aggregates sediment into a sucrose or iodixanol gradient, whereas lipid-containing vesicles with different densities float upward to the different positions of equilibrium buoyant density fractions (**Fig. 1-8a**). Such an approach, when combined with ultracentrifugation, has allowed for the first time the identification of mutant proteins that can be secreted via exosomes and ectosomes<sup>67</sup>. Parallel quantitative proteomics analysis on the EV subtypes has further revealed that CD81 and MMP2 can be used as exosomal and ectosomal markers, respectively. With the same method, different types of EVs, specific exosomal (CD63, CD81, or CD9) and non-exosomal subpopulations within small EVs from a single cell type can be isolated (**Fig. 1-8b**)<sup>41</sup>. This approach represents one of the earliest attempts to address the EV heterogeneity. Recently, a high-resolution iodixanol density gradients method was utilized to isolate small EVs from non-vesicular gradient. The study found that Argonaute 1- 4 and major vault protein are released free of small EVs and annexin A1 is a specific marker of MVs shed from the PM<sup>41</sup>. The progress would benefit the proper evaluation of the molecular mechanisms of biogenesis and the respective functions of subtypes of EVs.

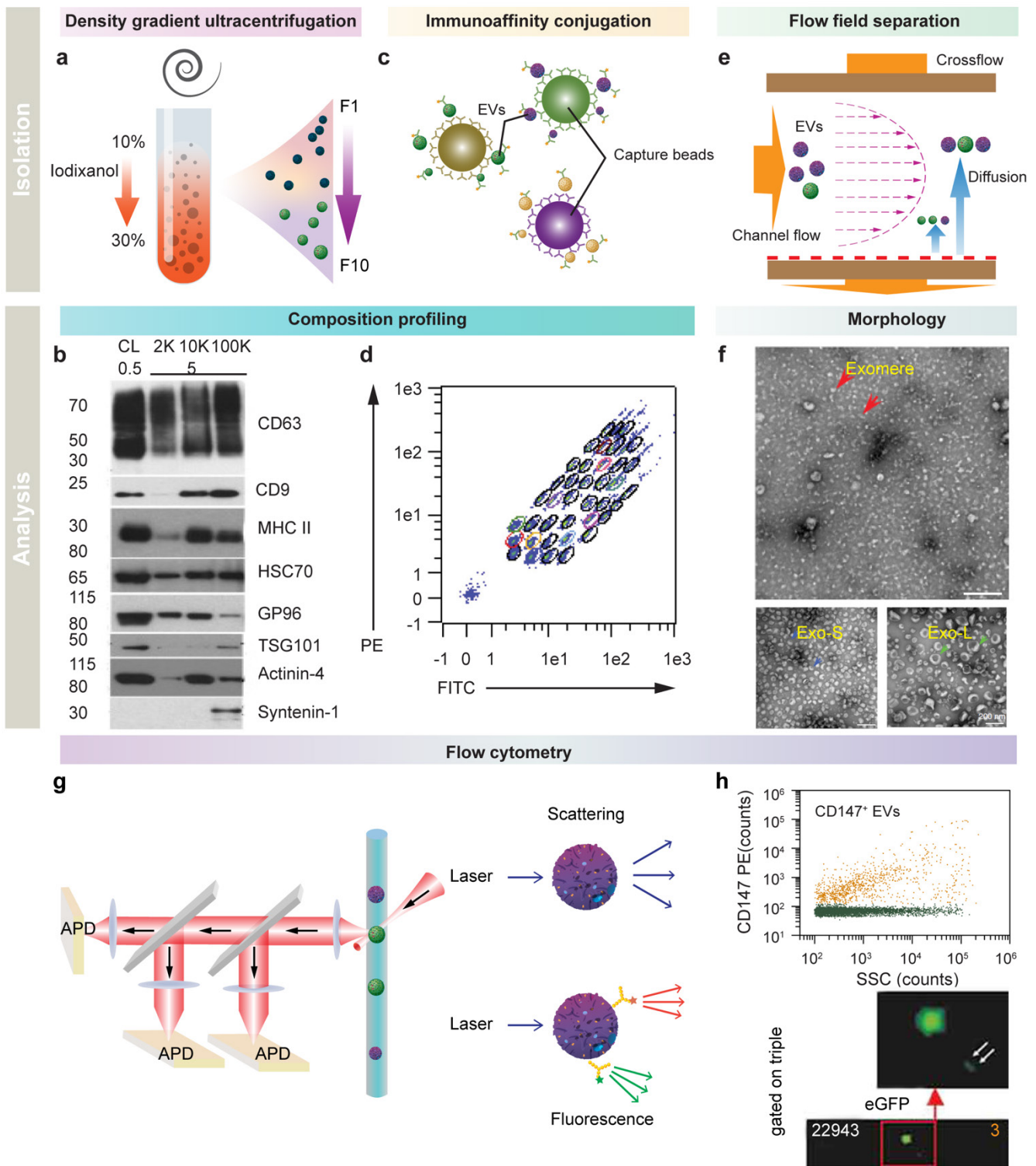


**Figure 1-8 | Representatives of current approaches for EV isolation with innovative discoveries in heterogeneity.** (a) Overview of iodixanol density gradient ultracentrifugation. (b) Western blot analysis of different proteins in EVs isolated from mouse bone marrow-derived dendritic cells<sup>41</sup>. Syntenin-1, TSG101 are only present in the 100K pellet. GP96 are mainly present in 2K and 10K pellets. HSC70, actinin-4 and MHC II are present in all EVs. Small EVs (100K pellet) are coenriched in CD63 and CD9 tetraspanins. (c) Schematic of immunoaffinity capture method. (d) Isolated EVs are incubated with 39



different bead populations<sup>68</sup>. Each bead population is coupled to a different capture antibody which is distinguishable by flow cytometry. Positive bead populations are highlighted in colors. (e) Principle of EVs isolation by asymmetric flow field fractionation. (f) TEM imaging analysis of fractionated exomeres, small exosomes and large exosomes subpopulations<sup>69</sup>. (g) Flow cytometry for EV heterogeneity analysis. Conventional flow cytometers enabled by scattered light signals, fluorescence staining, signal amplification<sup>70</sup>, higher laser power and slower flow<sup>71,72</sup> can be used for EV heterogeneity analysis. (h) High-sensitivity nanoparticle flow cytometry analysis of EVs at the single-particle level<sup>67,72,73</sup>. Upper: bivariate dot-plot of the PE orange fluorescence *versus* side scatter for EVs isolated from a patient sample upon immunofluorescent staining with PE-conjugated MAb against CD147<sup>72</sup>. Lower: enlarged image demonstrate that even faint spots being very close to each other are counted correctly as distinct spots/EVs<sup>73</sup>.

Sequential centrifugal ultrafiltration (SCUF) allows for the separation of EVs subtypes by utilizing the centrifugal force that allows substances of specific relative molecular mass to pass through or to be intercepted on the ultrafiltration membrane<sup>74,75</sup>. It typically requires centrifugation at 100,000×g for 1-2 h to obtain nanometer-sized EVs from the filtrate. Solvent and small molecules can be filtered through the membrane, while the molecules with higher relative molecular masses can be trapped in the ultrafiltration membrane, thereby achieving separation. SCUF is usually used in combination with size-exclusion chromatography to achieve a higher yield and purity<sup>76</sup>. A series of different pore-sized polyvinylidene fluoride ultrafilters has been applied for isolating both small EVs and large EVs from LIM1863 colon cancer cells<sup>77</sup>. Notably, it was found that the large EVs promote invasion to recipient NIH3T3 cells more significantly (3-fold more) than small EVs. However, a critical limitation of ultrafiltration is that it cannot separate dissolved low molecular weight species. In addition, efficient fractionation by ultrafiltration is only possible if the species differ in molecular weight by a factor of 10 or more. In fact, no new discovery on EVs heterogeneity has been found with this approach in recent three years.

Asymmetric flow-field flow fractionation (AF4) can be used to separate different sizes of EVs based on their density and hydrodynamic properties (**Fig. 1-8e**). By using two perpendicular flows: forward laminar channel flow and variable crossflow in AF4, two exosomes subpopulations have been identified recently. Importantly, the technique has led to the discovery of an abundant subpopulation of even smaller non-membranous nanoparticles (~35 nm, named exomeres) (**Fig. 1-8f**)<sup>69</sup>. Different populations show unique N-glycosylation, protein, lipid, DNA and RNA profiles and organ biodistribution.

Compared with traditional centrifugation methods, AF4 relies on more specialized fractionation equipment and requires highly trained personnel to operate.

**Immunoaffinity capture.** Most of the above physical isolation approaches rely on the specific physical properties of EVs to passively select subpopulations of EVs. They don't allow the purification of EVs with desired biochemical properties. For this, the use of capture antibodies attached to different matrices such as microbeads, nanoparticles, membranes or chip surface allows the analysis of a specific subgroup of EVs expressing the surface markers recognized by the capture antibodies. With a combination of capture and detection antibodies the immunoaffinity capture method enables an easy screening of surface markers on populations of EVs. Among them, specific antibody coated microbeads are especially popular, and several relevant products have come into the market (**Fig. 1-8c**). In recent years, several interesting discoveries have been found using the immunoaffinity capture approach. A novel multiplexed bead-based platform has been demonstrated to investigate up to 39 different surface markers in one sample (**Fig. 1-8d**). It has been found that NK cell-derived EVs and platelet-derived EVs are devoid of CD9 or CD81, and that EVs isolated from activated B cells comprise different EV subpopulations<sup>68</sup>. Furthermore, the contents of EVs can be analyzed by a subsequent lysing of EVs captured on the matrices, but correlating the inner contents to individual isolated EVs remains elusive. More recently, it was found small EVs do not contain DNA and active secretion of cytosolic DNA occurs through an amphisome-dependent mechanism<sup>41</sup>. The progress takes one step forward to understand how nucleic acid contribute to EVs heterogeneity. However, compared with label-free methods, the immunoaffinity capture method only detects EVs with known surface markers, thus EVs not expressing known markers or with unknown markers will be lost. The EVs captured by the microbeads can be further analyzed by conventional flow cytometry, but the approach cannot profile individual EVs because many EVs are captured on a bead.

Flow cytometry is one of the most popular techniques for detecting heterogeneous mixtures of single particles (**Fig. 1-8g**). Conventional flow cytometry uses light scattering as a trigger parameter and is limited to analyzing particles  $\geq 300\text{nm}$ <sup>71</sup>. The small size of EVs makes it difficult to measure EVs directly using conventional flow cytometry as the scatter intensity by EVs drops off rapidly with the decrease of the particle size. Single EV analysis in conventional flow cytometers can be enabled by applying signal amplification methods. For instance, target-initiated engineering of DNA nanostructures on individual EVs allows an increase of the fluorescence signals from single EVs<sup>70</sup>. This technique employed a conformation-switchable DNA probe to bind to the EV surface marker, which triggers a hybridization

chain reaction (HCR) of DNA nanostructures. The HCR method can enlarge the overall size of single EVs to beyond 500 nm, where multiple fluorophores can be bound to amplify the signal, enabling the visualization of single EVs in a conventional flow cytometer and greatly simplifying the measurement of multiple markers on the same EV. Compared with light scattering, fluorescence has some advantages as a trigger parameter, including an improved resolution against the background and well-established fluorescence calibration protocols.

In addition to the chemical methods for signal amplification, advances in optical engineering have enabled the detection of single EVs. Recently, a two-color high-sensitivity flow cytometer (HSFCM) has been demonstrated by using higher laser power and slower flow rates than what are typically used in conventional instruments<sup>71</sup>. The higher laser power can excite more fluorophores into higher states, and the slow flow rates allow more emitted photons being collected by using a high-sensitivity single photon counting avalanche photodiode with a high quantum yield. HSFCM allows the enumeration and estimation of the size of individual EVs down to 40 nm, as well as the measurement of the presence of surface markers to identify phenotypic subsets of EVs (**Fig. 1-8h**)<sup>67,72</sup>. Moreover, HSFCM could offer a rapid approach for quantitative multi-parameter analysis of single EVs with an analysis rate up to 10,000 particles per minute. Imaging flow cytometry is a technique complementary to conventional flow cytometry based on intensity measurement. It allows imaging samples in a flow, and all HSFCM signals are collected through the microscope objectives and quantified based on images detected by a charge-coupled-device camera. More acquisition and analysis parameters including the morphology and size of EVs could be defined and optimized for the analysis of single EVs (**Fig. 1-8h**)<sup>73</sup>. When analyzing the function of a single type of EV (e.g., sEVs or m/IEVs) exclusively, one may overlook a potentially important function of an EV subtype due to the presence of the other subpopulations if they are studied in a mixture. The methods above are usually combined together to isolate heterogeneous EVs<sup>78</sup>.

Microfluidic-based EV isolation approaches have become a research focus in the field of EV research. In general, microfluidic techniques have been used in the separation of different types of particles with sizes ranging from a few nanometers to a few hundreds of micrometres<sup>79</sup>. There have been many recent review articles summarizing microfluidic methods to separation subpopulations of EVs, involving size-based separation, membrane-based filtration, nanowires trapping, nanoscale deterministic lateral displacement sorting, acoustic isolation and viscoelastic flow sorting<sup>80,81</sup>. Hence, we don't go into details of these approaches but would like to emphasize that these approaches are mainly based on generating

novel hydrodynamic effects at the micro- and nanoscale with rationally designed micro- and nanostructures or through the integration of the structures with external actuation principles. They can be readily used to sort EVs of different properties, primarily based on size and shape. Apart from the traditional sorting capability, the concept of digital microfluidics can be also translated to EV research. For instance, the digital qualification of target exosomes can be realized by using droplet microfluidics, taking the format of digital PCR. To achieve the digital quantification, magnetic beads are used to capture exosomes through sandwich ELISA complexes. They are subsequently encapsulated in micro-droplets to ensure not more than one bead per droplet<sup>82</sup>. A limit of detection down to 10 enzyme-labelled exosomes complexes per microliter ( $\sim 10^{-17}$  M) can be achieved.

### 1.7.3 Single-vesicle analysis methods

In recent years, researchers have made a lot of progresses in single-vesicle analysis. Here, we discuss the benefits and challenges of current methods. Some of these methods utilize labelling techniques (such as fluorescence or nanoparticle coating) to visualize the EVs, and others work as label-free systems. Ten different methods are summarised in **Table 1-2**, including label free methods – cryogenic transmission electron microscopy (cryo-TEM), nanoparticle tracking analysis (NTA), raman tweezer microspectroscopy (RTM), atomic force microscopy (AFM), single-particle interferometric reflectance imaging sensor (SP-IRIS); and label-based methodologies – total internal reflection fluorescent (TIRF), high-resolution flow cytometry (hrFC), super-resolution microscopy (SRM) and digital method.

**Cryo-EM** is a useful technique for high-resolution visualization of EVs with less sample damage and artifact effects compared with TEM. The main problem of cryo-EM is it can provide only limited information regarding EV composition. To overcome this problem, nanoparticles functionalized with immunogold-labelled antibodies targeting markers of interest have recently been employed to characterize the biochemical composition of the EV surface<sup>83</sup>. **NTA** is used to determine the concentration and size distribution of EVs based on the Brownian motion of microparticles in suspension. However, accurate detection of particles with a diameter less than 60 nm is challenging and protein aggregates cannot be discriminated<sup>84</sup>. Fluorescence labelling have enabled NTA capability to phenotype EV down to  $\sim 50$  nm, help improve the resolution<sup>85</sup>. **RTM** is an inelastic scattering-based method, which can be employed to investigate the vesicle shape and size of single EVs qualitatively and quantitatively<sup>86</sup>. Using this method, it was found that a decrease in cholesterol concentration increases the local membrane curvature and stretches the vesicle<sup>87</sup>. The main disadvantage is that the scattering efficiency is very low.

**Surface enhanced Raman spectroscopy (SERS)** has been reported to overcome the disadvantage, EVs

can be exposed to various signal-enhancing nanoparticles and/or substrates to obtain a strengthened biomolecular signal<sup>88</sup>. **SP-IRIS** can detect several surface biomarkers and simultaneously measure the size of individual EVs. It can be used to accurately count and distinguish individual vesicles<sup>89</sup>. However, as the lateral resolution of the microscope (~400 nm) could accommodate several small vesicles, some detected signals could be erroneously assigned and categorized as larger vesicles instead of several smaller vesicles. This could be an issue especially in highly concentrated sample preparations<sup>90</sup>. **AFM** allows an accurate morphological and mechanical characterization of EVs. To characterize the biochemical properties of an EV surface, either the probing tip or the surface itself can be further immune-functionalized<sup>91</sup>.

Compared with light scattering, fluorescence has some advantages as a trigger parameter, including an improved resolution against the background and well-established fluorescence calibration protocols. **TIRF** is a commonly used fluorescence microscopy in the single-EV field, directly localizes fluorescently labelled molecules in EV preparation<sup>92</sup>. The fluorophores can be excited only within a few hundred nanometres from the solid substrate. The properties of fluorophores (instability and gradual photobleaching) are the main problem that limits the TIRF technology. Single EV analysis in conventional flow cytometers can be enabled by applying signal amplification methods and optical engineering. For instance, target-initiated engineering of DNA nanostructures on individual EVs allows an increase of the fluorescence signals from single EVs<sup>70</sup>. Recently, **high-sensitivity flow cytometer (HSFCM)** has been demonstrated by using higher laser power and slower flow rates than what are typically used in conventional instruments<sup>71</sup>. HSFCM allows the enumeration and estimation of the size of individual EVs down to 40 nm, as well as the measurement of the presence of surface markers to identify phenotypic subsets of EVs<sup>67,72,73,78</sup>. **FRET imaging** offers unique opportunities for the assessment of kinetic and structural dynamics and studies of the interaction and fusion events between EVs and cells<sup>93</sup>. However, fluorescent signal fluctuations due to a low signal-to-noise ratio and poor photostability of certain dyes might lead to changes in the FRET signal that are unrelated to the biological processes. **Super-resolved microscopy** would break the diffraction limit in revealing the fine structure of EVs<sup>94</sup>. **Digital methods**, including digital PCR and digital ELISA methods, improve the diagnostic performance for early detection. Droplet digital PCR is a highly sensitive method for mutant sequence detection<sup>95-97</sup>. It has been used to detect and quantify rare mutations in EV mRNAs and observed mutant *IDH1* mRNA in cerebrospinal fluid-derived EVs whereas not in serum-derived EVs<sup>57</sup>. Digital ELISA is a recently developed immunoassay methodology which is capable of robust, multiplexed protein

biomarker measurement in individual vesicles. With digital ELISA, glioblastoma EV was profiled and discovered surprising variations in putative pan-EV as well as tumour cell markers on EV<sup>98</sup>. Digital methods are usually combined with microfluidic device and/or aptamers<sup>99–102</sup> enable high-throughput quantitative analysis of EV content and can be used for the identification of biomarkers<sup>82,103</sup>.

It is important to note from following discussion, **label-free approaches** might hinder the detection of EVs because they often produce weak signals. label-free approaches can couple with labelling allowing signal increasement. Moreover, **label-based methodologies** demand new luminescent nanomaterial that is photo-stable and anti-photobleaching that suitable for alternative to fluorescent molecular probes.

**Table 1-2 | Comparison of single-vesicle analysis techniques**

Technique	Principle	Properties	Limitations	Improvements
<b>Cryo-TEM</b>	Transmission electron	High-resolution visualization of morphology, size	Limited EV composition information	Immunogold-labelled antibodies <sup>83</sup>
<b>NTA</b>	Brownian motion	Concentration, size distribution	Difficulty in accurate detection	Fluorescent labelling <sup>85</sup>
<b>RTM</b>	Raman scattering	Biochemical characterization	Time consuming	Surface-enhanced Raman spectroscopy (SERS) <sup>88</sup>
<b>AFM</b>	Interaction between a probing tip and a sample surface	Accurate morphological and mechanical	Labour- and time-consuming	High-throughput AFM-base method; the probing tip or the surface itself can be further immune-functionalized <sup>91</sup>
<b>SP-IRIS</b>	interferometric imaging	Surface biomarkers and size	signals could be erroneously assigned	Highly concentrated sample preparations <sup>90</sup>
<b>Label-based methodologies</b>				
<b>TIRF</b>	Reflection of an excitation light beam at a high incident angle	Localize fluorescently labelled	Incident angle and fluorophore	Technical improvement and fluorophore improvement

molecules with EV				
<b>High-resolution flow cytometry</b>	scattered light and fluorescence emitted by the labeled fluorophores	Surface marker, size	Laser power, flow rates, fluorophore	Technical improvement and fluorophore improvement
<b>FRET</b>	The excitation energy from a fluorophore is transferred nonradiatively to another fluorophore	kinetic and structural dynamics and studies	low signal-to-noise ratio and poor photostability of certain dyes	Technical improvement and fluorophore improvement
<b>SRM</b>	(i) spatial patterning of the excitation light and (ii) single-molecule localization	Visualize biological features smaller than the optical diffraction limit <sup>104-106</sup>	Technique, fluorophore	Technical improvement and fluorophore improvement
<b>Digital methods</b>				
<b>Digital PCR</b>	Amplification and characterization of nucleic acid	High-throughput, multiplexing, high sensitivity <sup>91-99</sup>	Large Coefficient of Variation value	More number of EVs to be analysed
<b>Digital ELISA</b>	Amplification and characterization of membrane proteins	High-throughput, multiplexing, high sensitivity <sup>82</sup>	Large Coefficient of Variation value	More number of EVs to be analysed

## 1.8 Nanomaterials for EV detection

We note that a majority of current tools have focused on presenting new assay methodologies. Nanomaterial provides high sensitivity, specificity, and multiplexed measurement capacity and has

therefore been investigated for the detection of extracellular cancer biomarkers and cancer cells, as well as for in vivo imaging. Materials on the nanometre scale have unique optical, electronic, and magnetic properties.

### 1.8.1 Magnetic nanoparticles (MNPs)

MNPs comprise aggregates of iron oxide (FeO, Fe<sub>2</sub>O<sub>3</sub>, and Fe<sub>3</sub>O<sub>4</sub>) or ferrite particles (which contain iron oxide as the main component) in the nanometre order. MNPs can be processed to furnish their surface with a variety of functions. Recognition sites, such as functional groups and biomolecules, are immobilized on the surface of the beads and are used to recognize targets for separation or detection<sup>107</sup>. ExoCounter system is a unique assay system that uses ferrite and glycidyl methacrylate beads to count the absolute number of EVs and analyse surface proteins simultaneously<sup>108</sup>. The ExoCounter system has been used to analyse 99 samples from pancreatic cancer patient serum and 77 negative control serum samples. Fluorescent signals can be amplified by metal-enhanced fluorescence (MEF). For example, Lee et al. reported an antibody-conjugated multifunctional magneto-plasmonic nanorod. EVs could be captured by the magnetic nanorods with antibody affinity, and the released miRNAs could be detected by the molecular beacons binding to the nanorods. The MEF effects of the Au plasmon could further amplify the fluorescent signals (**Fig. 1-9a**)<sup>109</sup>. This MEF system was used to analyze EV-derived miRNAs in a conditioned medium to control stem cell differentiation.

### 1.8.2 Graphene oxide (GO)

GO is the first reported 2D material with fluorescence quenching ability. The  $\pi$ - $\pi$  stacking interaction strongly binds the aptamers on the surface of GO, and the fluorescence is quenched by fluorescence resonance energy transfer between the conjugated dyes and GO<sup>110</sup>. Graphene-based field effect transistor biosensors have the advantages that include fast response, low detection limit, rapid detection, etc<sup>111</sup>. It was reported that a CD63-functionalized reduced graphene oxide (RGO) FET biosensor was used to directly quantify exosomes in a label-free and sensitive manner<sup>112</sup>. The method achieved a low limit of detection down to 33 particles  $\mu\text{L}^{-1}$ . A nanointerfaced microfluidic EV (nano-IMEX) platform was developed based on layer-by-layer coating the surface of the channel and the Y-shaped microposts with antibody-functionalized GO-induced nanostructured polydopamine (PDA) (**Fig. 1-9b**)<sup>113</sup>. This GO/PDA coating 3D nanostructured interface enhances the capacity for EV detection, and allows for the subsequent ultrasensitive enzyme-linked immunosorbent assays (ELISA) of the captured EV, achieving a very low detection limit of 50  $\mu\text{L}^{-1}$  with a 4-log dynamic range.

### 1.8.3 Gold nanoparticles (AuNPs)



have been used to develop biosensors taking advantages of their plasmonic features and their aggregation strategies for biotarget detection. Nanoplasmonic electrical field-enhanced resonating device (NE<sup>2</sup>RD) was created based on gold nanoparticle (10 nm diameter)-modified polystyrene surfaces where the inter-nanoparticle distance is reduced by 3D self-assembly. The gold nanoparticle-modified surface was functionalized with antibodies for immunodetection of the biological targets. NE<sup>2</sup>RD yielded a label-free optical readout by precisely measuring collective oscillations of the self-assembled gold nanoparticles on the surface (**Fig. 1-9c**)<sup>114</sup>. This device was able to detect multiple biotargets (i.e., protein biomarkers, drugs, protein allergens, bacteria, eukaryotic cells, and distinct viruses) from distinct clinical matrices such as saliva, serum, and the whole blood, and could be used as a disposable fluidic chip format for diagnostic applications in the POCT settings. Nanoscale Au particles exhibit a redshift in their plasmonic absorbance spectra when their size increases. For instance, Wu et al. enabled in situ growth of Au nanoshells on EVs, resulting in a large redshift in Au-based plasmonic resonance and quenching of fluorescent probes targeted to EV membrane proteins<sup>102</sup>. This system exhibited an LoD of  $\approx$ 1500 EVs and was utilized in the prognosis of both gastric and colorectal cancers. Lin et al. integrated Au@Pd nanosphere redshift effect sensors with aptamer nanoclusters for EV capture on an LFA strip and enabled a thermal signal readout (**Fig. 1-9d**)<sup>109</sup>. The Au@Pd nanosphere and aptamer nanocluster-assisted lateral flow strip device can detect EVs from serum and exhibit a balance between sensitivity and portability.

#### **1.8.4 Quantum dots (QDs)**

QDs are inorganic nanocrystals with unique optical properties. Compared to common fluorescent dyes, QDs show a broad and intense absorption, enabling unique flexibility in excitation and a higher fluorescence quantum yield<sup>115</sup>. Rodrigues et al. labeled a series of antibodies with different QDs and quantified the multiplex EV surface proteins (**Fig.1-9e**)<sup>116</sup>. The new method showed an improved ability to detect two pancreatic cancer associated EV biomarkers (EpCAM and EphA2).

#### **1.8.5 Semiconducting polymer dots (Pdots)**

Pdots exhibits spontaneous blinking with <5 nm localization error and a broad range of optical-adjustable duty cycles. An approach was described for high-throughput counting and super-resolution mapping of surface proteins on exosomes, using a combination of a single-molecule sensitive flow technique and an adaptive super-resolution imaging method enabled by a new class of transistor-like, photo-switching polymer dots (**Fig. 1-9f**)<sup>117</sup>. The method combines a single-molecule sensitive flow technique and an adaptive superresolution imaging method. Exosomes stained with membrane dye and dye-conjugated antibodies were analyzed using a microfluidic platform to determine size and protein copy number.

Super-resolution mapping was performed with exosomes labelled with Pdots. Based on the copy numbers extracted from the flow analysis, the switch-on frequency of the Pdots were finely adjusted so that structures of hundreds of exosomes were obtained. The high throughput and high sensitivity of this method offer clear advantages for characterization of exosomes and similar biological vesicles.

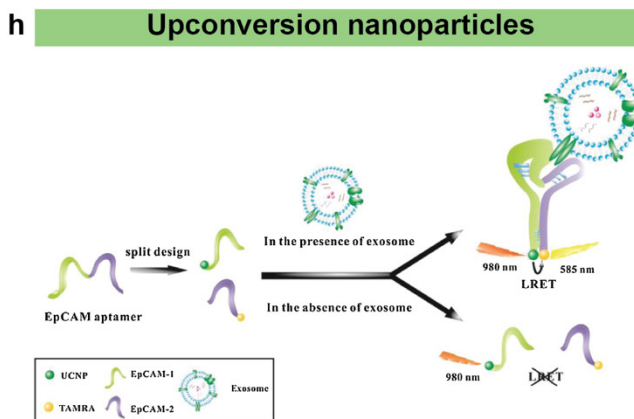
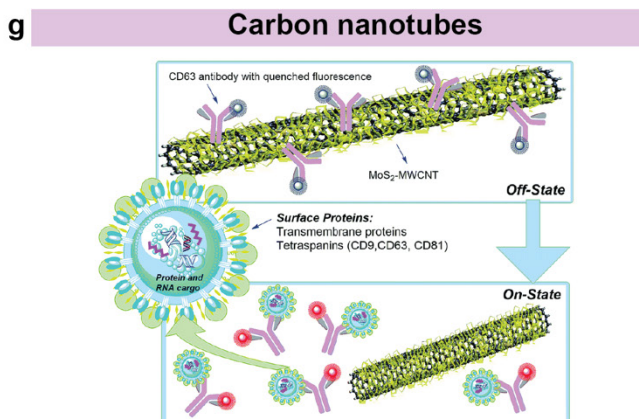
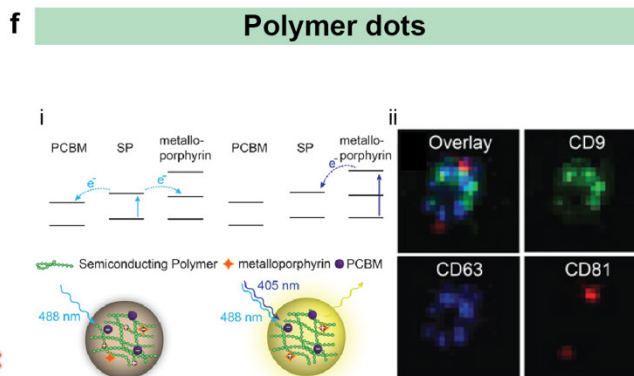
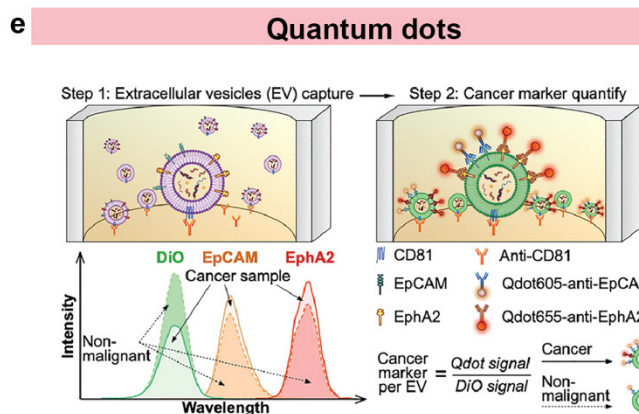
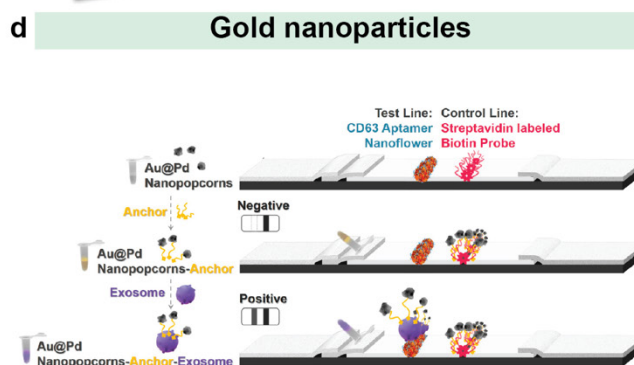
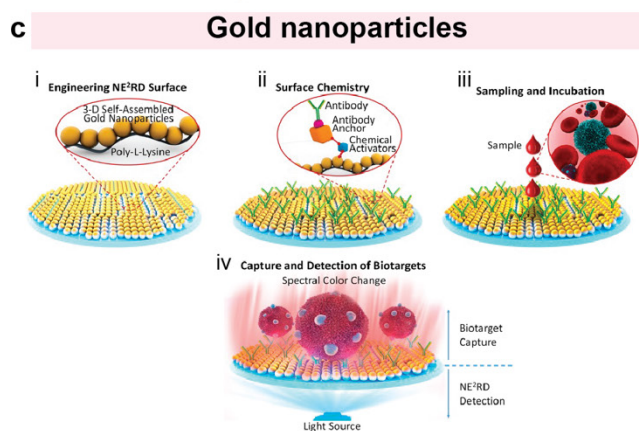
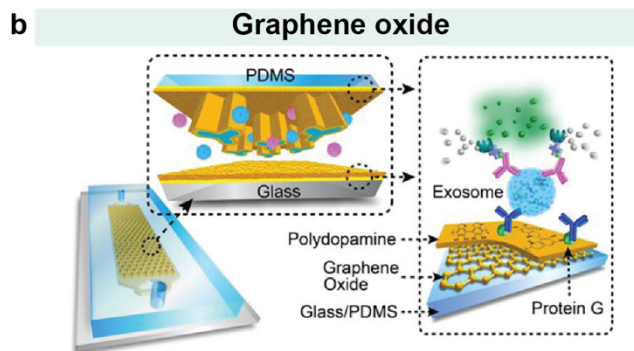
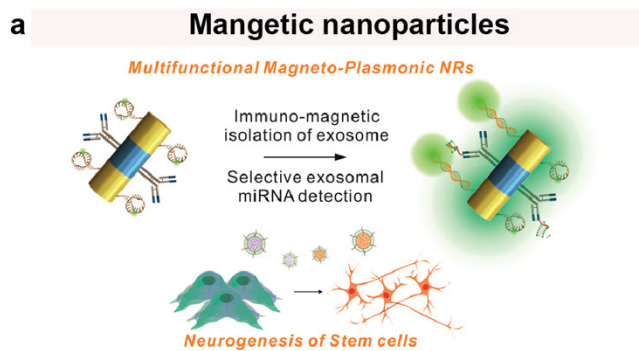


**Figure 1-9 | Nanomaterial for the detection of EVs.** (a) Metal-enhanced fluorescence. Reproduced from reference<sup>109</sup>. (b) Scheme of the nanointerfaced microfluidic EV platform (nano-IMEX). The glass/PDMS surface of the channel was coated with antibody-functionalized graphene oxide/polydopamine-nanostructured interface for the detection and subsequent sandwich ELISA of EVs. Reproduced from reference<sup>113</sup>. (c) Representation of the NE2RD platform. AuNPs are immobilized on the polystyrene surfaces via poly-l-lysine. Several activators and antibody anchors are used to immobilize antibodies onto the surface for immunodetection. Reproduced from reference<sup>114</sup>. (d) Schematic Illustration of the Strategy of Integrating an ANAN-LFS with a Smartphone-Based Thermal Reader. Reproduced from reference<sup>109</sup>. (e) Schematic of the quantum dot assay. EVs captured by an antibody to an EV-specific surface are stained with the lipophilic fluorescent dye DiO and then hybridized with antibody-conjugated quantum dot probes specific for biomarker targets on the EV membrane (e.g., EpCAM and EphA2). DiO signal from the captured EVs functions as a surrogate marker of EV abundance and allows direct normalization of quantum dot probe signal to permit quantification of mean biomarker levels in a captured population without the need for an independent EV isolation and quantitation procedure. This allows direct comparison of relative EV biomarker levels among different cohorts for disease diagnosis (e.g., cancer patients vs healthy subjects with suspected malignancy). Reproduced from reference<sup>116</sup>. (f) Optical properties of the superresolution Pdot probes. (i) Energy level alignment and working principle of the transistor-like Pdots. (ii) Three-color superresolution imaging of CD63 (blue), CD81 (red), and CD9 (green) on seminal exosomes. Reproduced from reference<sup>117</sup>. (g) Schematic illustration of the MoS<sub>2</sub>-MWCNT based nano-sensor for exosome detection and quantification. Reproduced from reference<sup>118</sup>. (h) The strategy diagram of the aptasensor based on LRET between UCNPs and TAMRA. Reproduced from reference<sup>119</sup>.

### 1.8.6 Carbon nanotubes (CNT)

CNT have outstanding electronic properties. A rapid sensitive platform was developed for exosome detection and quantification by employing MoS<sub>2</sub>-multiwall carbon nanotubes (MoS<sub>2</sub>-MWCNT) as a fluorescence quenching material (Fig. 1-9g)<sup>118</sup>. MoS<sub>2</sub>-MWCNT is a three-dimensional hierarchical nanostructure, which has one-dimensional MWCNT backbones with two-dimensional MoS<sub>2</sub> nanosheets grown on the surface of MWCNTs and also possesses partially standing branch features<sup>120</sup>. This exosome biosensor shows a sensitive and selective biomarker detection. This MoS<sub>2</sub>-MWCNT based fluorometric nanosensor technique is able to quantify exosomes with different surface biomarker expressions and has

revealed that exosomes secreted from MCF-7 breast cancer cells have a higher CD24 expression compared to CD63 and CD81.

### 1.8.7 Upconversion nanoparticles (UCNPs)

UCNPs coupled to aptamers have been used as energy donors in the development of aptasensors based on Luminescence Resonance Energy Transfer (LRET) in combination with other fluorophores or NPs that act as acceptors. Tetramethyl rhodamine (TAMRA) and UCNPs functionalized with two DNA aptamers were used to target the epithelial cell adhesion molecule (EpCAM) present on the exosome membrane of some cell lines<sup>119</sup>. After the aptamer–exosome binding, both DNA strands got closer and the distance between the energy donor (UCNPs) and the acceptor (TAMRA) was reduced, promoting the LRET process (**Fig. 1-9h**). Due to the coincidence between the emission wavelength of the donor and the excitation spectrum of the acceptor, the excitation of UCNPs by IR light produces a UV emission that excites the TAMRA molecule, leading to a yellow emission (585 nm) that is linearly correlated with the exosome concentration. This LRET sensor reached a LOD of  $8 \times 10^4$  particles per mL.

## 1.9 UCNPs in bio-applications

The development of new luminescent nanoparticles has been strongly driven by the needs in cancer diagnosis and treatment as they are chemically and physically stable and their properties can be tuned by physical, chemical and biology properties with enhanced performance. Among nanomaterials, fluorescent UCNPs have attracted attentions due to their superior optical properties, including large anti-Stokes shifts, sharp emission bandwidth, low toxicity, tunable excitation dynamics, great photostability, and high chemical stability<sup>121,122</sup>.

### 1.9.1 Mechanism of UCNPs

UCNPs are typically made up of inorganic host crystals and a lanthanide dopant that embedded within the host's lattice. Compared with most other luminescence processes involve a single electron that is excited from the ground state to the excited state, UCNPs use the multiple low energy photons to generate high energy emissions (**Fig. 1-10**)<sup>123</sup>.

**Figure 1-10 | Schematic representation of the conventional luminescence and upconversion luminescence processes.** In conventional luminescence, the absorption of a high-energy photon ( $h\nu_1$ ) by a system in the ground state (1) can lead to promotion of the system to the excited state (3). The system can then undergo nonradiative decay to a lower-excited state (2), followed by relaxation to the ground state accompanied by the emission of a lower-energy photon ( $h\nu_2$ ). In the upconversion luminescence process, the system in the ground state is initially promoted into the first excited state by an excitation photon or an energy transfer process from a sensitizer. The system is then further excited into level 3 by receiving energy from another excitation photon or energy transfer process. Radiative transition of the excited state into the ground state or another low-energy state leads to UCL emission, in which the emitted photon has a higher energy than the individual excitation photons and achieves anti-Stokes luminescence ( $h\nu_3$ ). Reprinted from reference<sup>123</sup>.

The two most common processes by which upconversion can occur in lanthanide-doped nanoparticles are excited state absorption (ESA) and energy transfer upconversion (ETU). Amongst the lanthanide ions,  $\text{Er}^{3+}$ ,  $\text{Tm}^{3+}$  and  $\text{Ho}^{3+}$  are mostly used as activators due to their ability to generate visible optical emissions under low excitation power densities. The most frequently used lanthanide sensitizer is the trivalent Ytterbium ion ( $\text{Yb}^{3+}$ ), which constitute a simple two energy level system, and has a large absorption cross-section at wavelengths around 975 nm. A schematic illustration of the energy transitions between the sensitizer and the activator, the emission is show in **Figure1-11**<sup>124</sup>.

**Figure 1-11 | Energy level diagram of typical showing the excitation and emission lines for a system containing Yb<sup>3+</sup>-sensitized, Er<sup>3+</sup> and Tm<sup>3+</sup> -activated UCNPs.**

### **1.9.2 Synthesis of UCNPs**

A variety of synthetic methods have been developed and reported in the literature to synthesize efficient and monodisperse UCNP with controlled size, such as: co-precipitation, hydro(solvo-)thermal synthesis, thermal decomposition, ionic liquid-based synthesis and microwave synthesis<sup>125</sup>. The choice of the synthesis method affects the produced nanoparticles' size, crystallinity, and monodisperse. The work discussed in this project is based on the use of NaYF<sub>4</sub>:20%Yb<sup>3+</sup>, 2%Er<sup>3+</sup> and NaYF<sub>4</sub>:40%Yb<sup>3+</sup>, 4%Tm<sup>3+</sup> that are synthesized following a general procedure for the synthesis of monodisperse nanoparticles using co-precipitation. The advantage of this method is highly uniform size, low cost, benignancy to environment and synthetic convenience.

### **1.9.3 Surface modification of hydrophobic UCNPs**

However, most UCNPs are stabilized by oleic acid and are hydrophobic only dispersible in organic solvents such as chloroform and hexanes. Subsequently, appropriate surface modification is desired to form a hydrophilic surface composition prior to their use in biomedical applications. As a result, the UCNPs gain functional groups or become strongly charged on the nanoparticle surface and become suitable for conjugation with antibodies, small molecules, peptides, aptamers, and other moieties. These moieties can bind and recognize specific cancer molecules. Surface modification enhances photostability of the nanoparticles and facilitates the platform for conjugating biomolecules for various bio-medicinal applications.

Ideally, the surface modification should impart colloidal stability in water, minimize interactions with cells and provide functionality for the covalent attachment of biomarkers for active targeting. Several strategies for the surface modification of UCNPs including: ligand oxidation, ligand exchange, ligand removal, polymer encapsulation, lipid encapsulation and silica encapsulation (Fig. 1-12).

### 1.9.3.1 Ligand exchange

Ligand exchange is the most common method for removing the original oleate ligands on the surface and then coat them with a hydrophilic organic ligand. Surface modification on this project following the ligand exchange procedures allow the hydrophobic ligands to be replaced with bifunctional polymers.

### 1.9.3.2 Ligand Oxidation

The ligand oxidation technique includes a carbon–carbon double bond oxidation by Lemieux-von Rudloff reagent. Usually, the carbon–carbon double bonds are transformed into carboxylic groups to facilitate reactive functional moieties. The oxidized UCNPs can be directly conjugated with proteins in the presence of free carboxylic groups and a DNA sensor was fabricated by this technique.

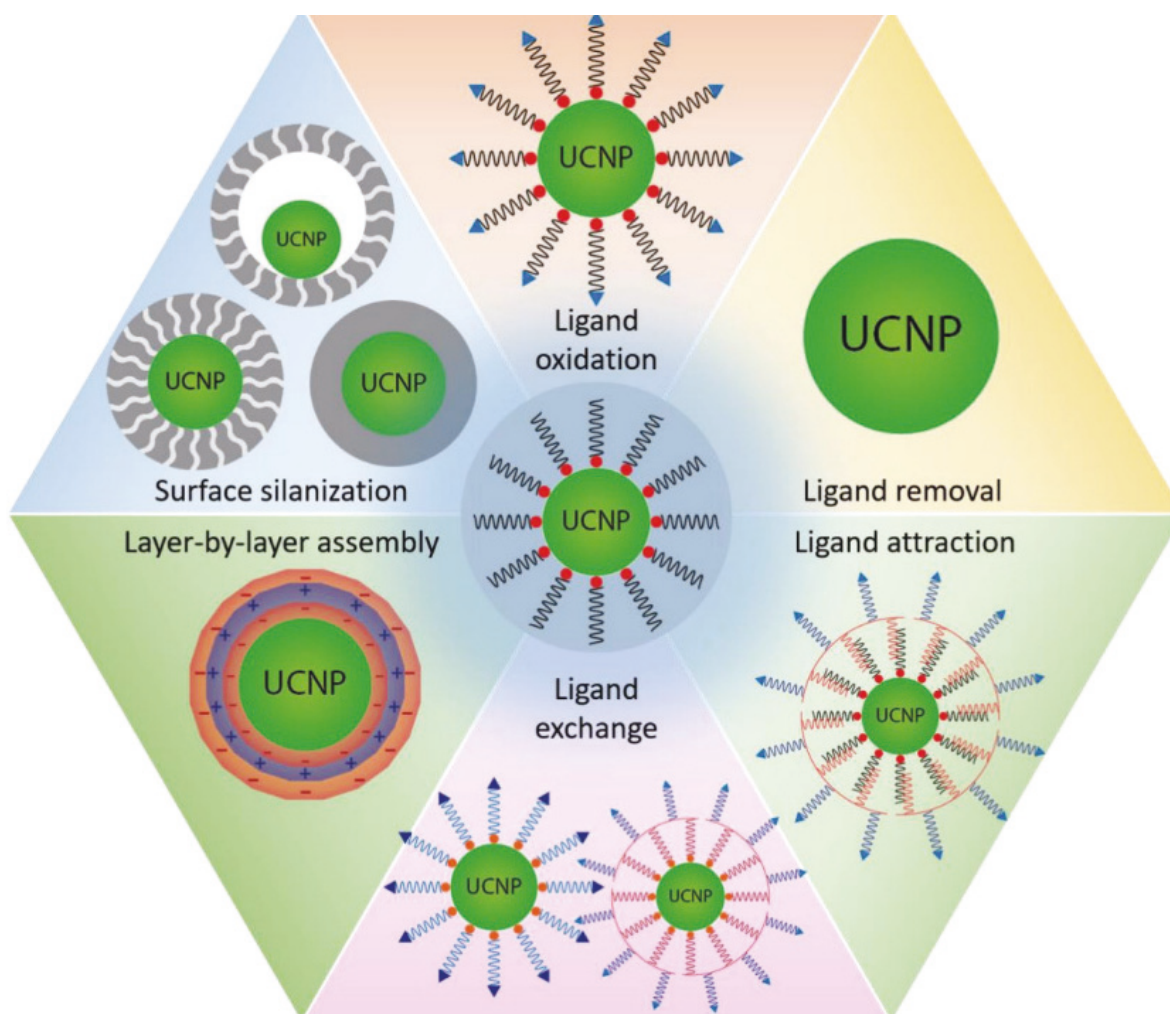


**Figure 1-12 | A diagram of surface modification methods used to alter the surface chemistry of UCNPs.** Reprinted from reference<sup>126</sup>.

### **1.9.3.3 Ligand Removal**

One novel method of surface modification is to remove oleate ligands by acid treatment. The motivation behind this approach is to facilitate the conjugation of electronegative ligands without any steric hindrance. This process rendered the nanoparticles negatively charged and colloiddally stable via electrostatic forces, but it was not able to impart long term colloidal stability in water or buffers.

### **1.9.3.4 Lipid encapsulation**

Lipid encapsulation is a specific type polymer encapsulation. The encapsulation is driven by the hydrophobic interaction between the oleate ligands and the hydrophobic tail of the lipids. One advantage of using lipids is that they can coat the NPs and provide functional groups on the surface of the NPs in a one-step encapsulation strategy. Sometimes, a layer of silica shell makes it a more accessible platform for conjugating various functional groups. On the other hand, binding silver or gold nanoparticles on the surface of UCNPs can facilitate thiol-containing ligands. Several surface modification techniques also depend on the intermolecular interactions of the UCNP surface and the ligand. For instance, the hydrophilic ligands can replace the hydrophobic surface ligands through a ligand exchange reaction. The hydrophobic surface can be oxidized partially to obtain a hydrophilic surface and a further modification is performed to bind biomolecules on the UCNP's surface.

### **1.9.3.5 Polymer encapsulation**

Amphiphilic copolymers containing both a hydrophobic and hydrophilic component have also been used to stabilize OA capped UCNPs. The nanoparticles are stabilized by the interdigitation of the hydrophobic component of the ligand with the oleates while the hydrophilic component of the ligand renders the nanoparticle colloiddally stable in water. The advantages of this method are that it does not perturb the surface and it retains the native ligands.

### **1.9.3.6 Silica encapsulation**

Additionally, silica coatings have been used to render UCNP water dispersible. This also enables further surface functionalization, such as the covalent attachment of fluorescent dyes for biotechnological applications, or the specific modification of silica nanoparticles for targeted drug delivery or for their use as biosensors.



#### 1.9.4 UCNPs in biosensing

UCNPs show an outstanding fluorescence intensity and photostability, a strong light absorption, high fluorescence quantum yield and good water solubility and can be used for fluorescence microscopy, fluorescent in situ hybridization (FISH), fluorescence correlation spectroscopy (FCS) and microarrays (protein, DNA). Over the past decade, researchers on UCNPs have made tremendous progress, particularly in the realm of bio-applications, such as imaging, sensing and cancer therapy<sup>121</sup>. Compared with the currently available cancer diagnostics in the clinic, such unique luminescent nanoprobe potentially offer a reliable alternative to traditional approaches for EV research in terms of selectivity and sensitivity.

After tuning the surface coating, for many applications, it is necessary to conjugate biomolecules, such as antibodies or oligonucleotides, to the UCNP's surface. Hydrophilic UCNPs are often subjected to further modification, such as conjugation of functional polymers with anchoring groups, small organic/dye molecules, biomolecules (e.g. ssDNA, antibodies, enzymes, etc.), or via incorporation into hybrid structures with various other nanomaterials (e.g. QDs, C-structures, plasmonic nanoparticles, MnO<sub>2</sub>, MOS<sub>2</sub>, MOFs, COFs, etc.) for the development of functional analytical platforms.

Organic dyes are classical LRET acceptors in UCNP-based probe design, which exhibit spectral overlap with UCNPs. Functional moieties of the surface-attached molecules can be utilized to conjugate UCNPs conjugated with a wide range of organic dyes have been utilized to construct LRET pairs for developing sensing probes. An ultrasensitive nanoprobe for *in vivo* monitoring of methylmercury (MeHg<sup>+</sup>) in mice was developed (**Fig. 1-13a**)<sup>127</sup>. When used with UCNPs, QDs can be prepared into hybrid nanostructures that can undergo LRET for transducing biochemical or biomolecular interactions. LRET based interactions between UCNPs and QDs as the basis have been used for sensing lead ions in human serum (**Fig. 1-13b**)<sup>128</sup>. Plasmonic nanostructures, such as AuNPs, AgNPs, AuAg hybrids, and palladium nanoparticles (PdNPs), have been extensively utilized in conjunction with UCNPs owing to their excellent photophysical properties with broad absorption spectra, surface plasmon resonance (SPR) activity, facile surface modifications, exceptional biocompatibility. AuNRs along with UCNPs has been used for intracellular detection of mRNA (**Fig. 1-13c**)<sup>129</sup>. GO is one of the most exploited 2D carbon structures utilized as a LRET acceptor for UCNPs. It was reported that UCNP–CNP hybrid construct for the detection of the tumour biomarker matrix metalloproteinase 2 (MMP-2) on fluorescence recovery principle(**Fig. 1-13d**)<sup>130</sup>. Carbon-based nanostructures including 0D carbon nanoparticles (CNPs), graphene and its oxidized derivative (i.e. graphene oxide (GO)) have gained enormous attention as LRET

acceptors for UCNPs because of their complementary photophysical properties, remarkable electronic behaviour, low toxicity, simple synthetic preparation, low cost and environment-friendly nature. MnO<sub>2</sub> nanosheet modified NaYF<sub>4</sub>:Yb/Tm UCNPs were utilized, in which the MnO<sub>2</sub> nanosheets acted as LRET acceptors to detect glutathione (GSH) in aqueous solutions and in cancerous cells(**Fig. 1-13e**)<sup>131</sup>. Metal-organic frameworks (MOFs) as energy acceptors in the fabrication of UCNP-based analytical platforms was used for the quantification and selective bioimaging of reactive oxygen species (ROS) *in vivo* (**Fig. 1-13f**)<sup>132</sup>. COFs are primarily crystalline porous polymer materials with covalently connected organic building blocks of lighter elements. These covalent structures have also been demonstrated in bioanalytical applications as a hybrid assembly with UCNPs due to their interesting structural properties, including high surface area, high porosity, low density, remarkable thermal and chemical stability, along with photophysical characteristics suitable for pairing with UCNPs. UCNP–COF hybrid nano-assembly was reported to assess therapeutic responses via monitoring of singlet oxygen generation *in vivo* (**Fig. 1-13g**)<sup>133</sup>.

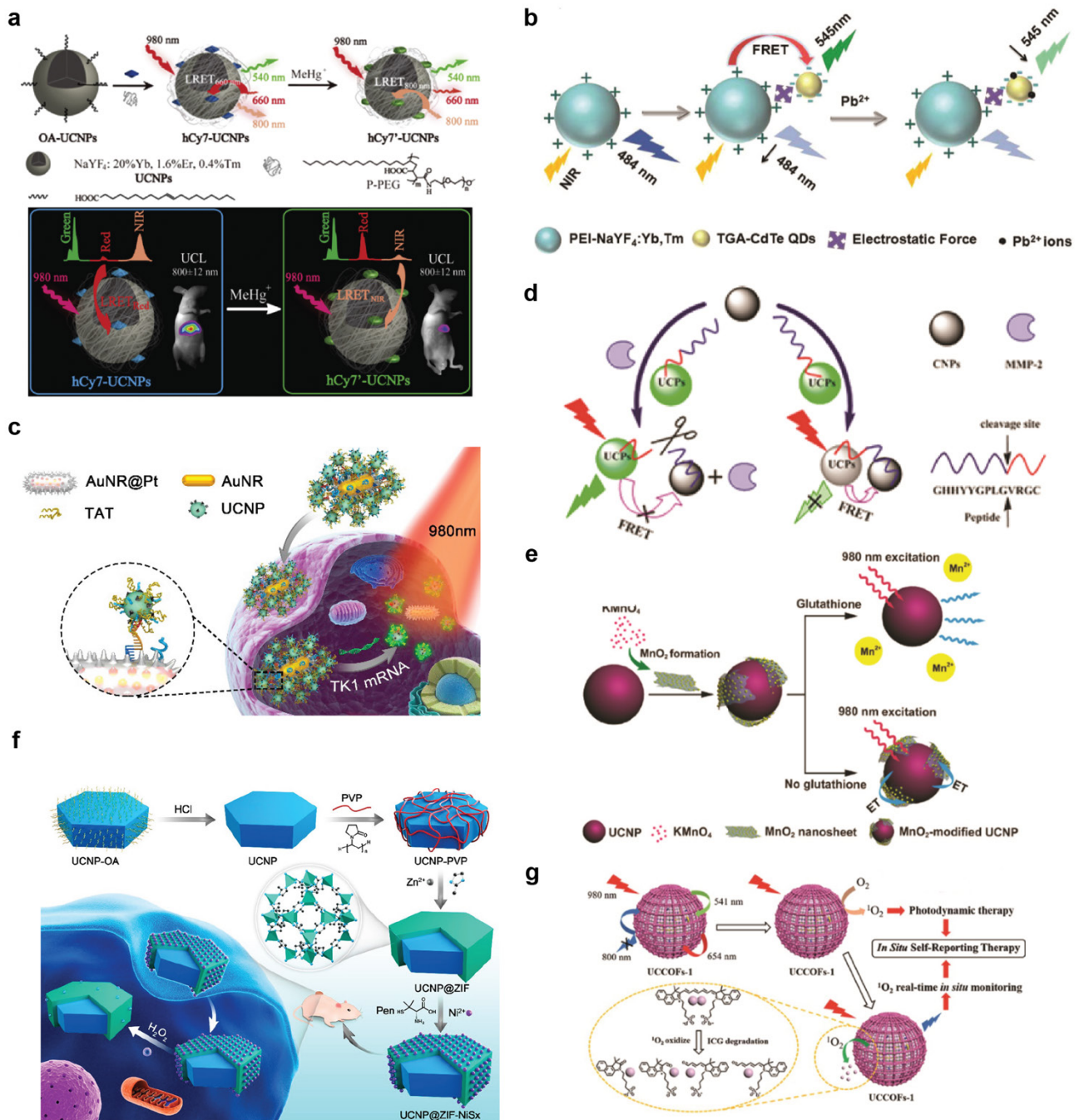


**Figure 1-13 | UCNP-based Hybrid platform.** (a) Schematic Illustration of the Synthesis of UCNPs-hCy7 and Its Sensing to MeHg<sup>+</sup> with a Change in UCL Emission. *In vivo* UCL images of 40 μg hCy7-UCNPs-pretreated living mice injected intravenously with 0.2 mL normal saline (left mouse) or 0.1 mM MeHg<sup>+</sup> solution (right mouse). Reproduced from reference<sup>127</sup>. (b) Schematic representation for UCNP–CdTe QDs hybrid nanoassembly mediated sensing of lead ions in human serum. Reproduced from reference<sup>128</sup>. (c) Schematic representations for UCNP-plasmonic structures nanoassembly mediated sensing probes in the detection of intracellular mRNA using AuNRs. Reproduced from reference<sup>129</sup>. (d) Schematic representations for UCNP-carbon-based structures nanoassembly mediated sensing probes in the detection of (a) MMP2 via “turn-on” mechanism using 0D CNPs. Reproduced from reference<sup>130</sup>. (e)

Schematic representations for UCNP-other hybrid structures nanoassembly mediated sensing probes in the detection of glutathione via “turn-on” mechanism using 2D MnO<sub>2</sub> nanosheets. Reproduced from reference<sup>131</sup>. (f) Schematic representations for UCNP-other hybrid structures nanoassembly mediated sensing probes in the detection of biii) Hydrogen peroxide using MOFs. Reproduced from reference<sup>132</sup>. (g) Real-time <sup>1</sup>O<sub>2</sub> and self-reporting therapy using COFs. Reproduced from reference<sup>133</sup>.

UCNP nanoprobe have been successfully fabricated into four broad classes of heterogeneous detection (or sandwich assay) formats in point-of-care testing (POCT) applications. Paper-based analytical devices (PADs) represent sensing systems wherein the assay components are fabricated on or within the 3D networks of cellulose fibres in papers. With regards to the use of UCNPs in PADs, PAA-modified UCNPs was utilized as a nanoprobe to detect target DNA sequences (**Fig. 1-14ai**)<sup>134</sup>. An assay for sensitive detection of telomerase activity in different cell lines demonstrated the feasibility of recording assay results using a cell phone camera, and even by naked eye observation, following irradiation with a hand-held NIR laser. (**Fig. 1-14aii**)<sup>135</sup>. Lateral flow assays (LFAs) rely upon the movement of reagents and sample components via capillary action and subsequent immune reactions to allow for analyte detection. Our group reported UCNPs were utilized in the fabrication of LFIA devices for detection of prostate-specific antigen (PSA) and ephrin type-A receptor 2 (EphA2) biomarkers (**Fig. 1-14b**)<sup>136</sup>. Microfluidic devices allow for easy customization of design to suit the need for multiplexing within the analytical platform. Wang et al. prepared a microfluidic nanoplatform with incorporated magnetic UCNPs was fabricated for the detection of CTCs (**Fig. 1-14c**)<sup>137</sup>. Microarray technology has allowed high-throughput and multiplexed detection from small-volume samples. Two different UCNPs was utilized to develop a spectrally and spatially multiplexed serological assay in an array-in-well format for the detection of adenovirus and influenza virus along with several other antigens (**Fig. 1-14d**)<sup>138</sup>.

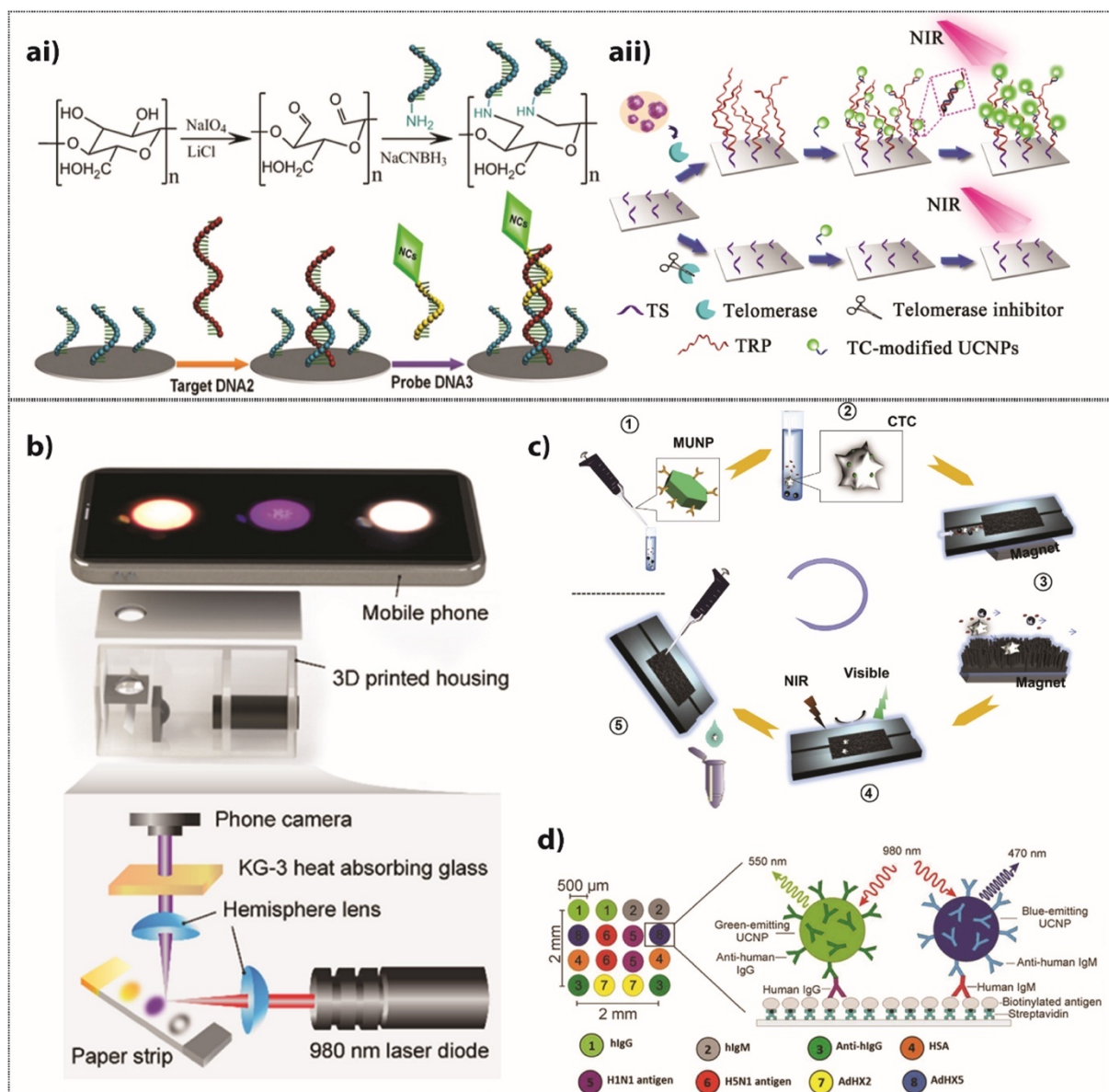


**Figure 1-14 | Various heterogeneous (sandwich) assay modes using UCNPs.** (a) Paper based sandwich assay modes using UCNPs in the detection of ai) target DNA<sup>134</sup>, aii) telomerase<sup>135</sup>. (b) Lateral flow assay in the detection of PSA and EphA2 biomarkers with a simplified optic module employing a low cost laser diode and collection optics, to allow the recording of the results using a mobile phone camera<sup>136</sup>. (c) Microfluidic device based integrated platform for effective capture and sensitive detection of CTCs in blood samples utilizing UCNPs as signal reporter<sup>137</sup>. (d) Microarray platform for spectrally and spatially multiplexed serological array-in-well assay utilizing anti-hIgG/hIgM coated-two-colour UCNPs<sup>138</sup>. Reprinted from Reference<sup>139</sup>.

### 1.10 EVs and super-resolution microscopy

Current methods cannot profile the inherent differences between individual EVs. Addressing this issue may require the development of single-vesicle analysis tool rather than bulk analysis (Fig. 1-15).

### 1.10.1 Single EV imaging technique

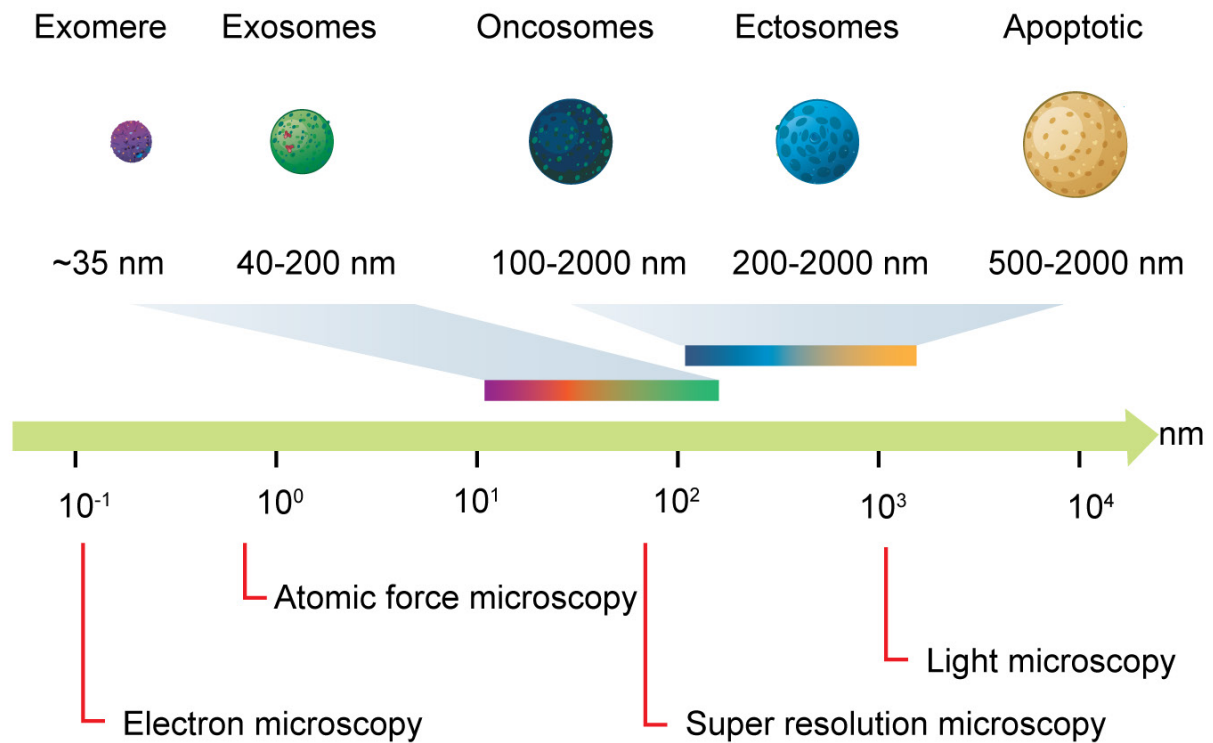


**Figure 1-15 | Microscopies for imaging single EVs.** Reprinted from reference<sup>18</sup>.

The development of super-resolved microscopy enables the study of the fine structure of EVs within diffraction limit (**Fig. 1-16b**)<sup>94</sup>. Currently available super resolution microscopy techniques include Structure Illumination Microscopy, Stimulated Emission Depletion microscopy, Photoactivation Localization Microscopy (PALM), Stochastic Optical Reconstruction Microscopy (STORM) and Single Molecule Localization Microscopy (SMLM), with resolutions in the range of a few tens of nanometres<sup>140,141</sup>. SMLM has been recently applied to image quantum dot-labelled EVs with a spatial resolution of 30 nm<sup>104</sup>. PALM and d-STORM were used to study the interactions of EVs with neurons in Alzheimer's disease with a precision of 25 nm<sup>105</sup>. A current technical trend under development is focused on using super-resolution microscopy to study EV uptake and sizing (**Fig. 1-16a**)<sup>142</sup>. Apart from quantum dots, a range of luminescent nanoparticle probes are available, such as lanthanide-doped nanocrystals and carbon dots<sup>106</sup>. They would be suited for long-term tracking of individual EVs, but innovative functionalization strategies are needed to selectively label EVs with these nanoprobe.

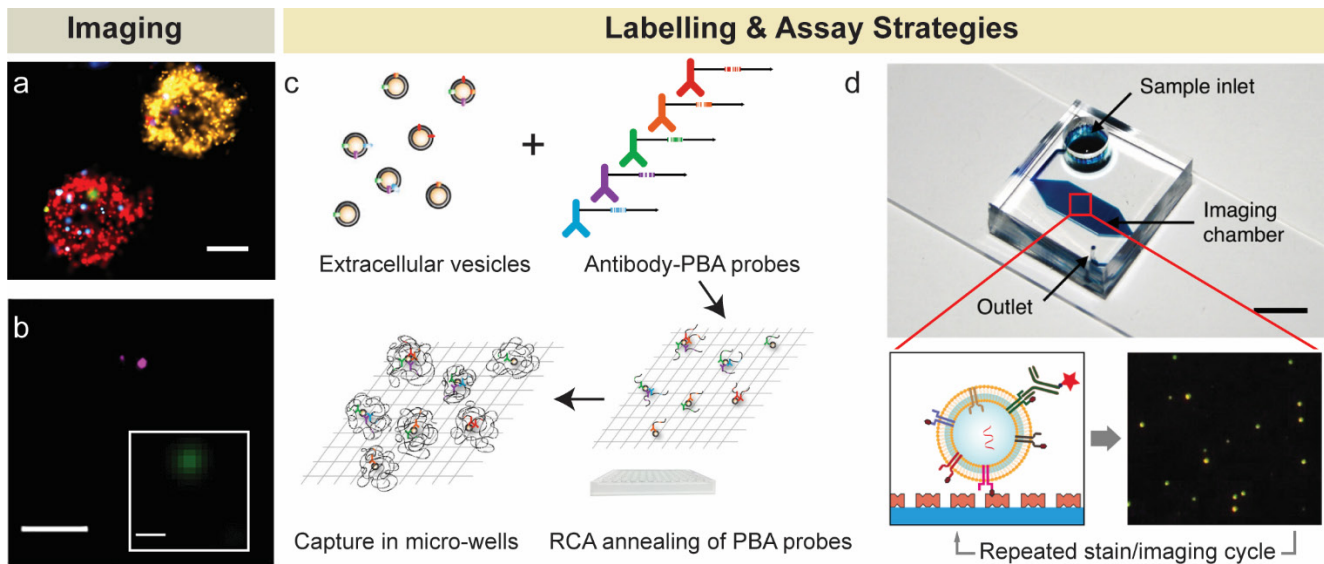


**Figure 1-16 | Single EV imaging.** (a) An excellent example of the application of Nanoimager (dSTORM) to investigate EVs<sup>142</sup>. Nanoimager is the world's first desktop-compatible microscope able to easily visualize EVs with a resolution reaching 20 nm. The ability to track in two colors simultaneously allows it to characterize and compare two different biomolecules on the EV simultaneously. (b) d-STORM imaging of DiD-labelled EVs<sup>94</sup>. d-STORM (magenta) and reconstructed standard wide-field image (green). Scale bar: 500 nm. (c) Design and workflow of proximity-dependent barcoding assay (PBA)<sup>143</sup>. Exosomes are first incubated with PBA probes, hybridizing to a unique rolling circle amplification primer. Then, the complex tag incorporates a standard sequence motif for enzymatic extension. The identities of proteins on individual exosome is revealed by analysing PCR product. (d) Microfluidic chip for single EV analysis<sup>98</sup>. EVs are first biotinylated and captured on neutravidin-coated surface. EVs are then stained by fluorescent antibodies (three colours per step) and imaged by microscopy.

Apart from that, it is still challenging to profile the composition of single EVs, which is beyond the capabilities of state-of-the-art super-resolution microscopy techniques with existing functional probes. Many existing high-resolution microscopies have been applied to resolve the fine subcellular structures. However, small EVs with a much smaller scale of a few tens of nanometers are difficult to be resolved with current microscopy techniques. Promising solutions include signal amplification methods such as DNA assisted ligation or extension assays which combine affinity probes (e.g. proteins) with amplifiable oligonucleotides<sup>144-146</sup>. This allows converting protein identities to DNA sequences for protein detection at the level of single molecules or molecular complexes. Very recently, such DNA ligation assays have shown potential for profiling surface proteins on EVs (**Fig. 1-16c**)<sup>143</sup>. Up to 38 different surface proteins on EVs originating from 18 different sources have been analyzed with this approach. The approach is

ultimately limited by the specificity of a given protein combination, the coverage and depth of sequencing and the density of surface proteins that may affect the affinity binding of antibodies. Despite that DNA-assisted technologies shine some light on the analysis of surface markers of EVs, profiling the inner content of EVs remains elusive. Research along this direction has been devoted to the advancement of instrumentation and labelling strategies to achieve highly sensitive single-EV detection. The microfluidic and nanofluidic technologies can be combined with imaging to achieve more sensitive single EV imaging and tracking (**Fig. 1-16d**)<sup>98</sup>. Microfluidic and nanofluidic devices can enable imaging and characterization of small vesicles on a single particle basis<sup>147</sup>. For instance, individual vesicles can be visualized by fluorescence microscopy while passing through parallel nanochannels in a pressure-driven flow. It requires very small amounts of sample volume to quantify both the vesicle content and the fluorescence signals emitted by individual vesicles. Future advances of micro and nanofabrication would enable the study of EVs transport and the roles of EVs in cell communications by combining microfluidic and nanofluidic devices with fluorescence imaging techniques.

### 1.10.2 UCNPs in super-resolution techniques

Organic dyes and fluorescent proteins are too dim to offer enough signal in fast imaging and can be rapidly photobleached under the excitation light. Therefore, the super-resolution community seeks alternative probes with intense brightness and resistance to photobleaching. UCNPs with thousands of emitters per nanoparticle can serve as suitable single-molecule probes, enabling bright emission in super-resolution imaging<sup>148</sup>. Recent years, UCNPs has been developed as an important part witness several breakthroughs in super-resolution imaging (**Fig. 1-17**). To date, the optimal resolution reached 28 nm ( $\lambda/36$ ) for single nanoparticles and 82 nm ( $\lambda/12$ ) for cytoskeleton structures with UCNPs. Compared with conventional probes such as organic dyes and quantum dots, UCNP-related super-resolution microscopy is still in the preliminary stage, and both opportunities and challenges exist.

A UCNP-assisted STED nanoscopy with low saturation intensity has achieved sub-30 nm optical resolution and reduced two orders of magnitude power than conventional dye-based STED (**Fig. 1-13**)<sup>149</sup>. With the excitation orthogonalized UCNPs, one-scan fluorescence emission difference (FED) microscopy eliminates the sample drifting issue by using two synchronized Gaussian and doughnut beams<sup>150</sup>. The progress made in nonlinear SIM using UCNPs lies in the improved resolution under a low excitation power, particularly for single nanoparticles dynamic tracking through deep tissues<sup>151,152</sup>.

### 1.10.3 Diffraction limit in microscopy



Abbe described the transverse dimension of the far-field microsystem focal spot as follows with this equation (1-1):

$$\Delta r \approx \frac{\lambda}{2n \sin \alpha} = \frac{0.61\lambda}{NA} \quad (1-1)$$

Where  $\lambda$  represents the wavelength,  $n$  is the refractive index of the medium between the sample and the objective,  $\alpha$  is the semi-objective aperture angle, and  $NA$  represents the numerical aperture. The size of the refractive index  $n$  and the aperture half-angle  $\alpha$  are constrained by objective technical conditions. The resolution of the optical microscopy was limited to approximately half wavelength of the light, even with perfect lenses and optimal alignment.

#### 1.10.4 UCNP-based STED-like super-resolution nanoscopy

UCNPs have been recently discovered as being suitable for STED-like super-resolution nanoscopy with sub-30 nm optical resolution in resolving the cluster of single UCNPs<sup>149</sup>. STED microscopy is one type of PSF engineering technique that sharpens the size of the focal spot, equivalent to expanding the microscope spatial frequency passband. The nonlinear depletion of the excited fluorescent state by the STED beam constitutes the basis for achieving images with resolution under the diffraction limit. When two laser pulses are superimposed, only probes that sit in the centre of the STED beam can have the fluorescence emission, significantly restricting the emission and narrowing the size of the effective point spread function (PSF). The full width at half maximum (FWHM) of the remaining effective PSF is well approximated by an expanded form of Equation (1-2):

$$\Delta r \approx \frac{\lambda}{2n \sin \alpha \sqrt{1 + \left(\frac{I_{max}}{I_{sat}}\right)}} \quad (1-2)$$

where  $I_{sat} = \frac{h\nu}{\tau_{fl}\sigma}$  is defined as the characteristic threshold intensity at which half of the  $\tau_{fl}\sigma$  maximal fluorescent signal is elicited,  $I_{max}$  is the maximum STED beam power,  $h\nu$  is the photon energy,  $\sigma$  is the cross-section of excitation, and  $\tau_{fl}$  is the fluorescence lifetime of the excited state.

Underlying Equation (1-2), the effective resolution increase with STED is proportional to the power of the depletion laser. One of the advantages of STED microscopy is that effective resolution increase is entirely dictated by the experimental configuration and the laser beam powers applied to the sample.

#### 1.10.5 Photon transition system in UCNPs

The FWHM of two-photon negative upconversion STED with a fluorophore that contains two energy levels can be represented as:

$$\Delta x = \frac{h_0}{\sqrt{\zeta}} \quad (1-3)$$

Here  $H_0$  denotes the FWHM of confocal point spread function (PSF).  $\zeta = \frac{I_{STED}^{Max}}{I_s}$  denotes the saturation factor.  $I_s$  referred to as the saturation intensity where the emission intensity decreases to half of the maximum.  $I_{STED}^{Max}$  represent the maximum amplitude of the STED beam profile.

### 1.10.6 Saturation effect with doughnut-shaped beam

The effective point spread function (PSF) of the super-resolution as:

$$h_{eff}(x) = h_{em} \times h_c(x) \quad (1-4)$$

$$h_{em}(x) = \eta(i) \times h_{exc}(x) \quad (1-5)$$

Here  $h_{em}(x)$  is the PSF of emission;  $h_{exc}(x)$  is the PSF of the excitation beam (doughnut beam for nanoscopy);  $\eta$  is excitation power-dependent emission intensity curve; and  $h_c(x)$  is the PSF of the confocal collection system. The FWHM of the intensity dip in  $h_{eff}$  represents the resolution for nanoscopy.

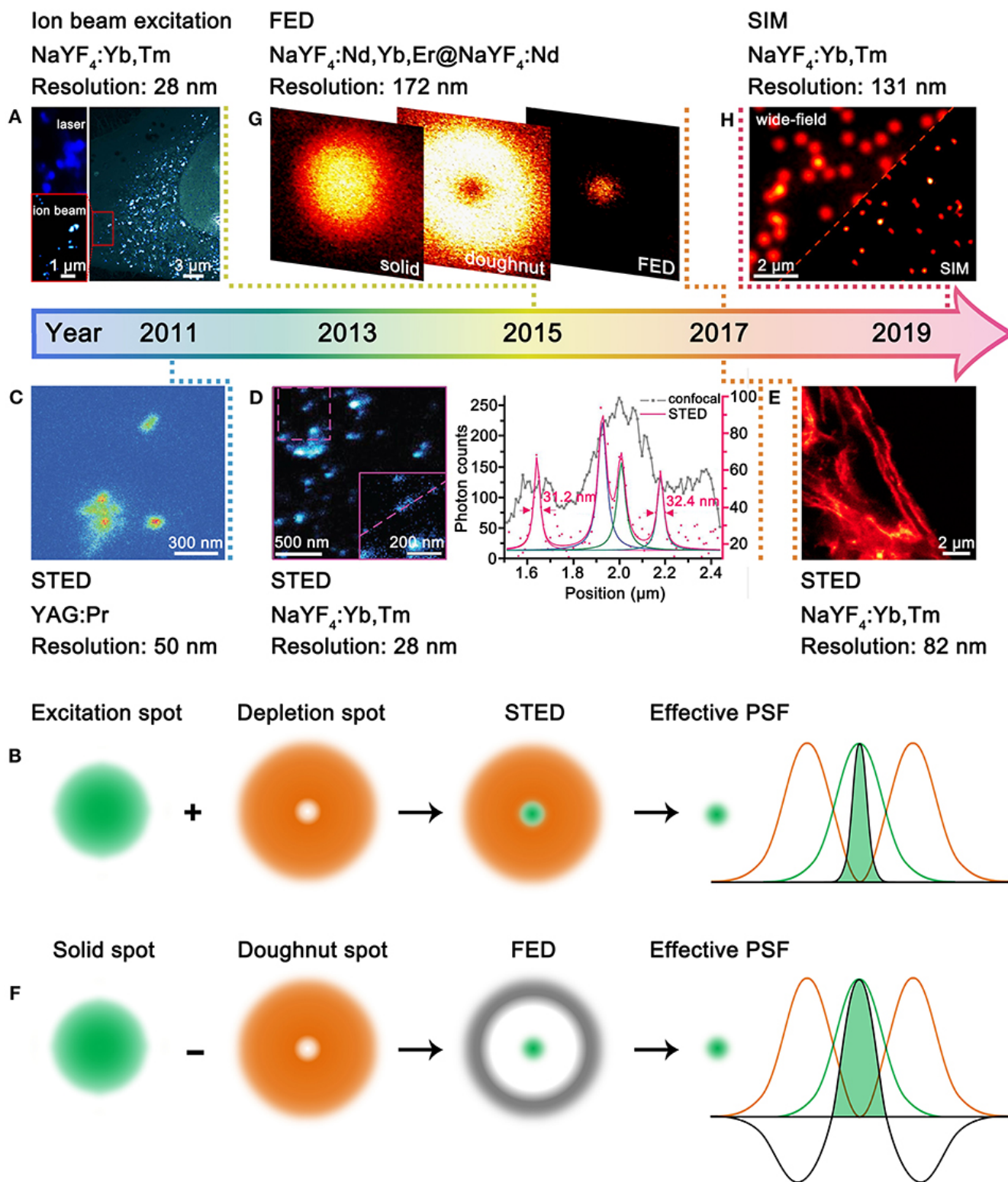


**Figure 1-17 | Development of UCNP for super-resolution microscopy.** (a) Comparative photoluminescence imaging under 980-nm excitation (top left) and ionoluminescence imaging under helium ion beam excitation (bottom left) of  $\text{NaYF}_4:\text{Yb,Tm}$  UCNP in a HeLa cell (right). (b) Schematic illustration for STED microscopy. (c) STED imaging of YAG:Pr nanoparticle clusters. (d) STED imaging of ca. 13 nm  $\text{NaYF}_4:\text{Yb,Tm}$  UCNP (left) and the intensity profiles along the dashed line (right). (e) STED imaging of cytoskeleton structures and desmin proteins in HeLa cancer cells with

NaYF<sub>4</sub>:Yb,Tm UCNPs. (f) Schematic illustration for FED microscopy. (g) FED imaging of a single NaYF<sub>4</sub>:Nd,Yb,Er@NaYF<sub>4</sub>:Nd UCNPs. (h) Comparative wide-field and SIM imaging of NaYF<sub>4</sub>:Yb,Tm UCNPs. Reprinted from reference<sup>149</sup>.

### 1.10.7 Emission saturation enabled sub-diffraction resolution

STED-like super-resolution nanoscopy takes advantages of multi-intermediate ladder-like energy levels of UCNPs (Fig. 1-18a), easily converting 980 nm photons into 800 nm photons. The emission saturation curve of the two-photon state <sup>3</sup>H<sub>4</sub> (800 nm) (Fig. 1-18b) shows an early onset of upconversion emissions at low excitation power density and sharp rising-up slope, reflecting its nonlinear energy transfer assisted photon upconversion process. 800 nm emission band has smaller  $I_s$ ,  $I_{MAX}$ , larger  $\zeta$  than 455 nm emission band. Underlying Equations (1-3, 1-4, and 1-5), 800 nm emission band improves the resolution compared with 455 nm emission peak under the fixed excitation power. UCNPs unlock a STED-like super-resolution nanoscopy for super-resolution imaging, with much lower excitation intensity than that required in conventional dyes.

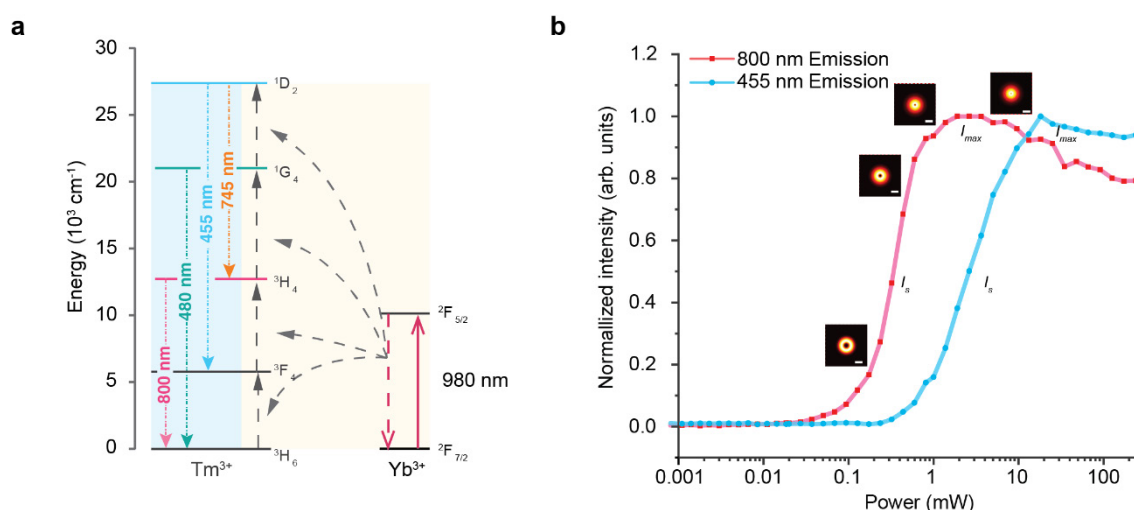


**Figure 1-18 | The principle of NIR super-resolution microscopy using UCNPs as multiphoton probe for imaging.** (a) Energy level diagram of Tm<sup>3+</sup> and Yb<sup>3+</sup> doped UCNPs. (b) 800 nm and 455 nm emission saturation curves obtained from UCNPs (39.3 ± 1.6 nm NaYF<sub>4</sub>:40%Yb<sup>3+</sup>,4%Tm<sup>3+</sup>) under 980-nm excitation. Scale bar: 250 nm.

### 1.11 Aim

Quantification of low concentration of specific EVs present in very small volumes of clinical samples may be used for non-invasive cancer diagnosis and prognosis. Currently available and clinically viable diagnostics are all based on “bulk measurements” requiring 10<sup>5</sup> - 10<sup>6</sup> EVs per biomarker to measure protein (e.g., Western, ELISA) or 10<sup>2</sup> -10<sup>3</sup> EV for the more sensitive methods (μNMR, nPLEX)<sup>131,132</sup>.

Each single EVs could be extremely valuable in studying tumour heterogeneity, rare tumour subtypes, phenotypic changes occurring during therapy, and tumoral changes. To quantitate such low abundance markers, the required sensitivity for detection needs to be at the single EVs level. The aim of this thesis is to develop new detecting capabilities for ultrasensitive and specific analysis of disease-associated EVs subtypes in the complex biofluid background. In this thesis, we explore applying UCNPs as an alternative to traditional approaches for EVs research, especially in the field of EV-based liquid biopsy and EVs heterogeneity. Specially, this thesis develops platforms for single EVs imaging by: (i) UCNPs labelling and imaged by a TIRF microscopy; (ii) UCNPs labelling and imaged by a STED-like super-resolution microscopy.

## Statement of Contribution of Authors for Chapter 2

[2] **G. Huang**, Y. Zhu, S. Wen, H. Mei, Y. Liu, D. Wang, M. Maddahfar, Q. P. Su, G. Lin, Y. Chen and D. Jin. Single Small Extracellular Vesicle (sEV) Quantification by Upconversion Nanoparticles. *Nano Lett.* 22, 3761–3769 (2022).

	G. H	Y. Z	S.W	H.M	Y.L	D.W	M.M	Q.S	G.L	Y.C	D.J
Experiment Design	▪									▪	▪
Sample preparation	▪		▪	▪	▪	▪	▪	▪		▪	
Data collection	▪	▪	▪	▪			▪				
Analysis	▪								▪		▪
Manuscript	▪	▪	▪				▪		▪	▪	▪

The concept of this paper was developed by my supervisor Dayong Jin. I designed the experiments and conducted the majority of experimental work, including modification of UCNPs, Characterization of UCNPs, EV isolation, LENS assay, ELISA assay, flow cytometry, data collection, data analysis, and manuscript writing.

---

## Chapter 2 Single small extracellular vesicle (sEV) quantification by upconversion nanoparticles

---

### Abstract

Cancer-derived small extracellular vesicles (sEVs) are the potential circulating biomarkers in liquid biopsy. However, their small sizes, low abundance and heterogeneity in molecular makeups, pose the major technical challenges to detecting and characterizing them quantitatively. Here, we demonstrate a single-sEV enumeration platform using lanthanide-doped upconversion nanoparticles (UCNPs). Taking advantage of the unique optical properties of UCNPs and the background-eliminating property of Total Internal Reflection Fluorescence imaging (TIRF) technique, single-sEV assay recorded a limit of detection  $1.8 \times 10^6$  EVs/mL, which was nearly three orders of magnitude lower than the standard enzyme-linked immunosorbent assay (ELISA). Its specificity was validated by the difference between EpCAM-positive and EpCAM-negative sEVs. The accuracy of the UCNP-based single-sEV assay was benchmarked with immunomagnetic-beads flow cytometry, showing a high correlation ( $R^2 > 0.99$ ). The platform is suitable for evaluating the heterogeneous antigen expression of sEV and can be easily adapted for biomarker discoveries and disease diagnosis.

### 2.1 Introduction

Extracellular vesicles are ubiquitous and readily accessible in all body fluids<sup>153</sup>, carrying on a wealth of proteomic, lipidomic and genetic information from parent cells<sup>154–156</sup>. In particular, accumulating evidence indicated that cancer-derived small EVs (sEVs) are unique and reflect heterogeneous biological changes associated with the progression of growing tumors<sup>5–7</sup>. They have been found as promising circulating biomarkers for a variety types of cancers, such as breast<sup>160–164</sup>, colon<sup>165</sup>, prostate<sup>166,167</sup>, pancreatic<sup>168</sup>, ovarian<sup>169,170</sup>, colorectal cancers<sup>171</sup> and glioblastoma<sup>172</sup>, especially in the early detection of cancer<sup>173</sup>.

Because of the small sizes (40-200 nm) and low abundance of sEVs in early stages of cancer<sup>174,175</sup>, conventional methods, such as western blotting and enzyme-linked immunosorbent assay (ELISA), with limited sensitivity, require large amounts of samples to only report the ensemble averaging results with the significant heterogeneity information covered. The new development of flow cytometry can analyze single sEV, but with limited capability in revealing their heterogeneity distributions<sup>67,72,73,78</sup>.

Nanoparticle tracking analysis is a commonly used method for quantifying the numbers of EVs, but it lacks specificity<sup>84</sup>. Several imaging techniques have been applied for the analysis of single sEVs, including an interferometric reflectance imaging sensor that has been commercialized and widely used in the EV community<sup>176</sup>. However, the use of fluorescence dyes has limited the signal intensity for fast imaging, not mentioning the photobleaching issue<sup>18</sup>. The technical bottlenecks prevent sEVs to be clinically applied for diagnosis<sup>177</sup>.

Luminescent nanoparticles, with outstanding brightness and resistance to photobleaching, may offer an alternative as the single-molecule probes. Semiconductor quantum dots (QDs) have been used for single EV imaging but have inherently random and unpredictable “blinking” problem. Semiconductor polymer dots (Pdots) combined with super-resolution imaging method have been used to image tetraspanins on EVs<sup>117</sup>. Lanthanide-doped upconversion nanoparticles (UCNPs) with unique optical features, including their non-bleaching, non-blinking, and anti-Stokes emissions, make them ideal for single-molecule fluorescent probes<sup>122</sup> and their tunable colors and lifetimes are ideal for multiplexed detection.

Here we present a strategy (**Figure 2-1**) for immunoassay of single sEVs, based on a set of Lanthanide-doped EV-targeting Nanoscopic Signal-amplifiers (LENS) and a total-internal-reflection-fluorescence (TIRF) microscope. EV-specific CD81, CD63 and CD9 antibodies are functionalized on the surface of glass slides, where immunosorbent assays are conducted to capture sEVs and subsequently detected by LENS labelled with anti-epithelial cell adhesion molecule (EpCAM) antibody. LENS are made of uniform, bright and photostable UCNPs highly doped with tens of thousands of lanthanide ions<sup>122,178,179</sup>, which can significantly amplify the optical signal of single molecules and in a background-free condition under the near infrared excitation, so that the presence of single sEVs can be directly counted by counting the bright spots. EpCAM is a cancer biomarker widely used for various epithelial cancers<sup>180,181</sup> and clinically approved for liquid biopsy (CellSearch<sup>®</sup> CTCs test)<sup>182</sup>, thus the detection of EpCAM positive EVs can be used to diagnose cancer-specific EVs.



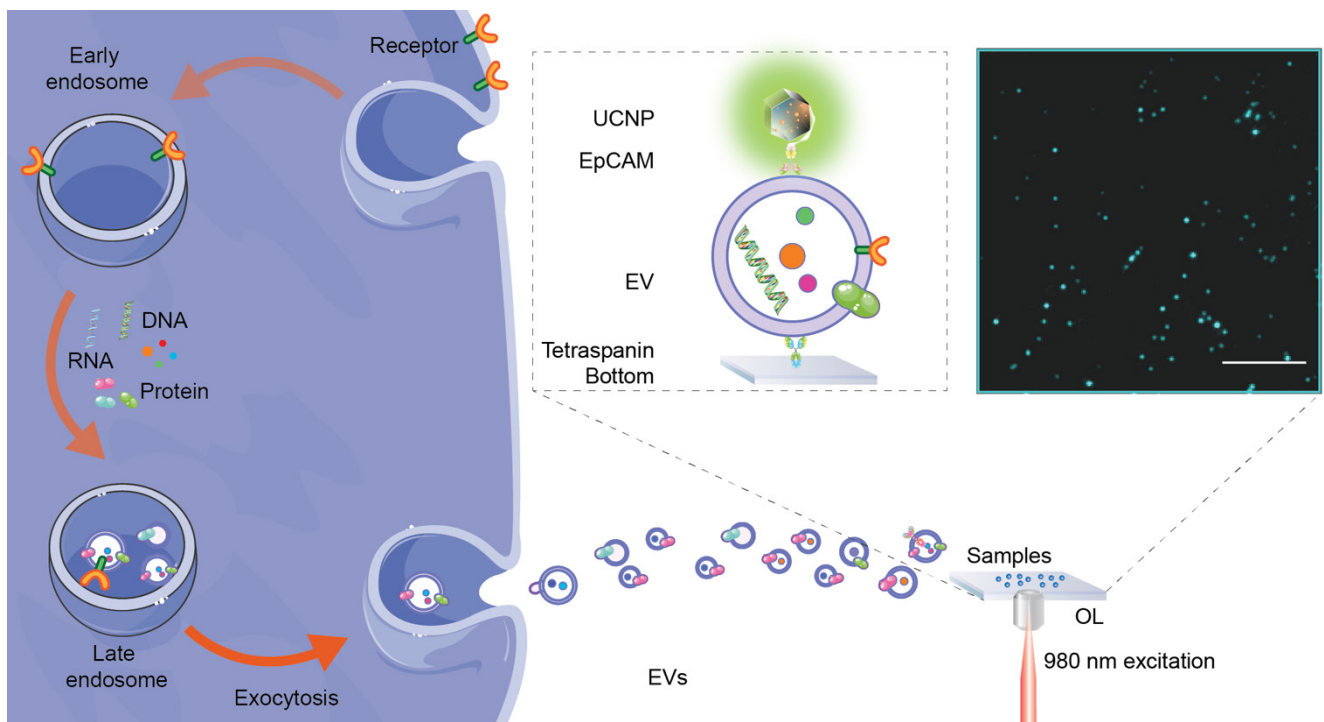


**Figure 2-1 | Schematic illustration of quantitative analysis of single cancer cell-derived small EVs labelled by LENS.** Scale bar: 10  $\mu\text{m}$ .

## 2.2 Methods

**2.2.1 Cell culture.** The human colorectal adenocarcinoma cell line (HT-29) and human embryonic kidney cell line (HEK 293T) were provided by Professor Wei Duan, School of Medicine, Deakin University. The cells were cultured in Dulbecco's modified eagle medium (DMEM, Gibco, Invitrogen, Waltham, USA) supplemented with 10% fetal bovine serum (FBS, Gibco, Invitrogen, Waltham, USA), 100 U/mL penicillin G, 100 U/mL streptomycin and 2mM glutamine at 37 °C with 5% CO<sub>2</sub>. Cell lines were tested negative for mycoplasma.

**2.2.2 EVs isolation from Cell culture medium.** Make sure cells are in good conditions and Cell culture medium was collected after cells were incubated in DMEM supplemented with 5% exosome-depleted FBS (Gibco, Invitrogen, Waltham, USA) for 48 h. Cell culture medium was centrifuged at 300  $\times$  g for 5 min, 2000  $\times$  g for 20 min and 10,000  $\times$  g for 20 min at 4 °C to remove cells and cellular debris. Supernatant was then filtered using 0.2  $\mu\text{m}$  pore filter and incubated with total exosome isolation reagent (Gibco, Invitrogen, Waltham, USA) overnight with a ratio 2:1 v/v at 4 °C. The medium was centrifuged at 10,000  $\times$  g for 1 h at 4 °C. The EV pellet was suspended in 0.22  $\mu\text{m}$  filtered PBS, stored in -80 °C freezer before use.

**2.2.3 Cryogenic Electron Microscopy.** Cryogenic electron microscopy (cryo-EM) was used for the direct visualization of EVs. Prior to sample preparation for cryo-EM, sample grids (Quantifoil R2/2, Quantifoil Micro Tools) were glow-discharged to make the carbon film hydrophilic. 4  $\mu$ L of EVs was loaded onto a grid and any excess solution was removed by blotting with filter paper for 3 seconds at 4 °C. The grid was plunged into the precooled liquid ethane with a EM GP freeze plunger (Leica Microsystems, Wetzlar, Germany) and stored in liquid nitrogen (-196 °C). Electron micrographs of EVs were obtained with a FEI Talos Arctica cryo-EM (ThermoFisher Scientific, Waltham, USA) operating at 200keV.

**2.2.4 Nanoparticle tracking analysis.** To determine the size distribution and concentration of EVs, semi-automated nanoparticle tracking analysis (NTA) was performed using a NanoSight LM14 system (Nanosight Technology, Malvern, UK). In brief, 10  $\mu$ L isolated EVs were diluted with freshly 0.22  $\mu$ m filtered PBS to provide counts within the linear range of the instrument ( $1.19 \times 10^8$  to  $10^9$  per mL)<sup>183,184</sup>. The diluted EV samples were loaded into the detection chamber by syringe. The parameter settings for EV sample measurements: camera level, 12; detect threshold, 8; capture, 60s; number of capture, 5; temperature, 22 °C. Particle movement was analysed by NTA software (NTA version 3.3; Malvern Instruments, Malvern, UK).

**2.2.5 Western blotting.** Western blotting was performed using the Bolt™ Bis-Tris system (Invitrogen, Thermo Fisher Scientific), following the manufacture's instruction. The EV pellets and cells are lysed by RIPA Lysis and Extraction Buffer (Invitrogen, Thermo Scientific) with 1% Halt™ Protease & Phosphatase Inhibitor Cocktail (Invitrogen, Thermo Fisher Scientific, Waltham, USA).

Equal amount of each protein sample (10ug, quantified by Micro BCA Protein Assay Kit [Invitrogen, Thermo Scientific, Waltham, USA) were mixed with Bolt™ Sample Reducing Agent (Invitrogen, Thermo Fisher Scientific, Waltham, USA) and Bolt™ LDS Sample Buffer (Invitrogen, Thermo Fisher Scientific, Waltham, USA), and heated at 70°C for 10 minutes. The mixture is then loaded into Bolt 4-12% Bis-Tris Plus 1.0mm Gel (Invitrogen, Thermo Fisher Scientific, Waltham, USA) and run at 100V in Bolt™ MES SDS Running Buffer (Invitrogen, Thermo Fisher Scientific, Waltham, USA) containing 0.25% Antioxidant (Invitrogen, Thermo Fisher Scientific, Waltham, USA) for 1.5-2 hours. The proteins on the gel are transferred onto a PVDF membrane by using Mini Bolt Module (Invitrogen, Thermo Fisher Scientific, Waltham, USA) in Bolt™ transfer buffer (Invitrogen, Thermo Fisher Scientific, Waltham, USA) for 1 hour. The PVDF membrane was then blocked with 5% BSA blocking buffer (Sigma) in 0.1% TBST overnight at 4°C with gentle shaking. When the blocking is complete, the PVDF is incubated

overnight at 4°C in primary antibody solution (CD81 [1:500 dilution, 10630D, Thermo Fisher Scientific];  $\beta$ -Actin [1:2000, MA5-15739, Thermo Fisher Scientific]; Flottlin-1 [1:2000, PA5-18053, Thermo Fisher Scientific]; Calnexin [1:2000, PA5-34665, Thermo Fisher Scientific]; TSG101 [1:500, MA1-23296, Thermo Fisher Scientific]; EpCAM for cell [1:200, MA5-13917, Thermo Fisher Scientific]; EpCAM for EV [1:400, MA5-13917, Thermo Fisher Scientific]. The PVDF is washed by 1x 0.1% TBS-T 5 times and 5 minutes each washing followed by secondary antibody incubation (Goat Anti-Mouse IgG (H+L) HRP conjugate, Thermo Fisher Scientific G21040 for CD81 [1:10,000 dilution],  $\beta$ -actin [1:20,000 dilution], TSG101 [1:2000 dilution] and EpCAM for EV [1:10,000 dilution], EpCAM for cell [1:2000 dilution]; Goat Anti-Rabbit IgG (H+L) HRP conjugate (Thermo Fisher Scientific) for Calnexin [1: 2000 dilution]; Rabbit Anti-Goat IgG (H+L) HRP conjugate (Thermo Fisher Scientific) for Flottlin-1) [1:2000 dilution] for 1 hour at room temperature with moderate shaking. Membranes were washed with 0.1% (CD81,  $\beta$ -actin, Flottlin-1, Calnexin, EpCAM for EV) or 0.05% (EpCAM for cell) 1x TBS-T for 5 min and 5 times. Finally, the membranes were incubated in SuperSignal™ West Pico PLUS chemiluminescent substrate (Invitrogen, Thermo Scientific) in dark for 3 minutes and visualized on Amersham Imager 600 system.

**2.2.6 Flow cytometry.** Surface biomarkers of EVs were quantified by flow cytometry (CytoFLEX LX, Beckman Coulter, Australia). Capturing beads: anti-CD9 magnetic beads (2.7  $\mu$ m, ThermoFisher Scientific, Waltham, USA), anti-CD81 magnetic beads (2.7  $\mu$ m, ThermoFisher Scientific, Waltham, USA) and anti-63 magnetic beads (4.5  $\mu$ m, ThermoFisher Scientific, Waltham, USA). In brief, 10- $\mu$ L antibody coated magnetic beads (exosome human CD9/CD63/CD81 Isolation) were washed with 100  $\mu$ L isolation buffer (PBS with 2% BSA) once. 100  $\mu$ L diluted EV sample was added and incubated at 4 °C on the shaker overnight. Beads were washed twice with isolation buffer and stained with allophycocyanin (APC) conjugated EpCAM (Invitrogen, ThermoFisher Scientific, Waltham, USA) for flow cytometry. After staining for 30 min at 4 °C, the beads were washed twice with 100  $\mu$ L isolation buffer to remove residue stains. 600  $\mu$ L isolation buffer was added and suspended for the analysis on flow cytometry (CytoFLEX LX, Beckman Coulter, Brea, USA). APC conjugated Immunoglobulin G (IgG1, Invitrogen, ThermoFisher Scientific, Waltham, USA) was used as isotype control for non-specific labelling. 20,000 events were collected for each sample and the data was analysed by FlowJo™ Software. The number of EVs used in each one of the assays was kept consistent. The concentration of sEVs used in each assay was kept consistent. 20,000 events were collected for each sample. Each signal value was normalized using the value of Isotype. The flow cytometry-based detection provides the relative

fluorescence intensity (RFI) value for EVs carrying the antigen. The RFI was calculated according to the formula,  $RFI = \frac{MFI\ positive}{MFI\ isotype}$ , where MFI is mean fluorescence intensity.

**2.2.7 Synthesis of NaYF<sub>4</sub>:20%Yb<sup>3+</sup>,2%Er<sup>3+</sup>.** NaYF<sub>4</sub>:20%Yb<sup>3+</sup>,2%Er<sup>3+</sup> nanocrystals were synthesized according to our previously reported method<sup>149</sup>. 1 mmol RECl<sub>3</sub> (RE=Y, Yb, Er) with the molar ratio of 78:20:2 were mixed with 6 ml oleic acid (OA) and 15 ml 1-Octadecene in a three-neck flask. The solution was heated to 160 °C under flowing argon for 30 min to obtain a clear solution and was cooled down to room temperature. Then, 5 mL methanol solution of NH<sub>4</sub>F (4 mmol) and NaOH (2.5 mmol) were quickly injected into the flask and stirred for 30 min at room temperature. Subsequently, the mixture was heated to 80 °C under flowing argon for 20 min to remove methanol, and was further heated to 300 °C for another 90 min. The solution was cooled down to room temperature, and nanocrystals were precipitated by ethanol. The nanoparticles were washed thrice with cyclohexane, ethanol and methanol, respectively. The final products were re-dispersed in cyclohexane with the concentration of 20 mg mL<sup>-1</sup>.

**2.2.8 Transmission electron microscopy.** The morphology of the formed materials was characterized via transmission electron microscopy (TEM) imaging (Philips CM10 TEM with Olympus Sis Megaview G2 Digital Camera) with an operating voltage of 100 kV. The samples were prepared by placing a drop of a dilute suspension of nanocrystals onto copper grids. High-angle annular dark-field (HAADF) scanning transmission electron microscope (STEM) images were collected with a Talos F200X S/TEM (Thermo Scientific™).

**2.2.9 Synthesis of POEGMEA<sub>13</sub>-b-PMAEP<sub>7</sub>.** POEGMEA with different numbers of repeating OEGMEA units were used as POEGMEA macro-RAFT agent for further extension of the polymer to produce diblock copolymers for surface modification of LnNPs. According to our previous paper, monoacryloxyethyl phosphate monomer was chosen because of the high affinity of phosphate ligand toward the positively charged lanthanide ions in comparison with the carboxylic group. In detail, (1.4 M) POEGMEA (6, 13, 35, 55 OEGMEA units), (0.4 × 10<sup>-2</sup> M) AIBN, and (1.43 × 10<sup>-1</sup> M) MAEP were dissolved in (5 mL) acetonitrile in a one-necked round-bottom flask equipped with a magnetic stirrer. The reaction solution was sealed by a rubber septum and purged with argon gas for 30 min. The mixture was then placed into the preheated oil bath at 70 °C for 17 h. The polymerization was quenched by ice-bath after 70% MAEP monomer conversion. The final 6 and 13 OEGMEA unit polymers were dialyzed (3 kDa cutoff) against methanol for 48 h, while dialysis of the 35 and 55 OEGMEA unit polymers used a 14 kDa cutoff dialysis membrane. The presence of seven repeat units of the MEAP

(second block) was confirmed by  $^1\text{H}$  NMR. The narrow molecular weight of the final polymers was confirmed by gel permeation chromatography (GPC).

**2.2.10 Surface modification of UCNPs.** Surface modification of oleic acid-capped UCNPs (UCNPs@OA) was performed to get water-soluble UCNPs via ligand exchange with block copolymer composed of hydrophilic block poly (ethylene glycol) methyl ether acrylate phosphate methacrylate (POEGA<sub>13</sub>-b-PMAEP<sub>7</sub>, *PbP*), containing phosphate and carboxyl groups (-COOH). Streptavidin (SA, Sigma-Aldrich, St. Louis, USA) was conjugated to UCNPs@*PbP* via 1-ethyl-3-(3-dimethylaminopropyl) carbodiimide hydrochloride carbodiimide (EDC, Sigma-Aldrich, St. Louis, USA) crosslinker. In brief, 1 mL of OA-UCNPs (20 mg/mL) kept in cyclohexane, solvent was evaporated to be re-dispersed in THF. Furthermore, OA-UCNPs in THF were mixed with 10 mg of *PbP* in 2 mL of THF. The reaction was kept overnight at room temperature. *PbP* coated UCNPs were purified by centrifugation at 14,680 rpm cycles twice with water to obtain carboxyl-UCNPs (UCNPs@*PbP*, 5 mg/mL). UCNPs@*PbP* (5 mg/mL) were re-suspended in water. (1.7 pmole, 100  $\mu\text{g}$ ) UCNPs@*PbP* ( $M_w = 60$  MDa, calculated from reference<sup>185</sup>) and 1 mg EDC were dissolved in 90  $\mu\text{L}$  HEPES buffer (Sigma-Aldrich, St. Louis, USA), mixed with shaker for 30 min. The mixture was centrifuged at 10,000rpm for 7 min and discarded the supernatant. Then, (83.3 pmole, 5  $\mu\text{g}$ ) SA (60 kDa, Sigma-Aldrich, St. Louis, USA) was added into 195  $\mu\text{L}$  HEPES buffer, mixing with shaker for 2 h. UCNPs@*PbP*@SA was purified by centrifugation at 10,000 rpm for 7 min thrice. Finally, the pellet was resuspended in 100  $\mu\text{L}$  Tris buffer (Sigma-Aldrich, St. Louis, USA). Stored at 4 °C before use.

**2.2.11 Characterization of functionalised UCNPs.** Transmission electron microscopy (TEM) images were captured by Tecnai T20, FEI, (Thermo Fisher Scientific, Waltham, USA) to visualize the size and morphology of nanoparticles. Dynamic light scattering (DLS) was conducted by Zetasizer Nano series (Malvern Panalytical, Malvern, UK) to confirm the hydrodynamic size of nanoparticles. Fourier transform-infrared spectroscopy (FTIR) spectra experiments were carried out using a Nicolet 6700 FTIR spectrometer (ThermoFisher Scientific, Waltham, USA) to determine the surface ligands of nanoparticles. Upconversion luminescence intensity spectra were performed by an iHR550 spectrometer (HORIBA Scientific Instruments Inc.) with a modified external 980 nm laser. Nanodrop was conducted to confirm the successful coupling of UCNPs and SA.

**2.2.12 TIRF setup and imaging.** EVs were localized in TIRF using fluorescent signal from the UCNPs. Imaging was performed on a purpose-built TIRF microscope. Images were taken with a 100 $\times$  objective

(NA = 1.40, UPlanSApo, Olympus, Tokyo, Japan) and a back-illuminated electron multiplying charge-coupled devices (EMCCD) Camera (iXon Ultra 897, Andor Technology, South Windsor, CT). A compact laser diode driver with temperature controller and mount (CLD1015, Thorlabs, Newton, USA) was used to control the laser power. The optical filter set included a long-pass excitation filter ( $\lambda_{\text{cut-on}} = 830$  nm, Chroma, USA), a multiphoton long-pass dichroic mirror ( $\lambda_{\text{cut-on}} = 875$  nm, Chroma, Bellows Falls, USA), and a short-pass emission filter ( $\lambda_{\text{cut-on}} = 842$  nm, Chroma, , Bellows Falls, USA). Fluorescent localizations were extracted from raw image data using Andor SOLIS. Images of  $512 \mu\text{m} \times 512 \mu\text{m}$  were collected with an exposure time of 500 ms. To activate Er-doped UCNPs, the 980 nm laser power was set to 150 mW. Electron multiplier gain was 100. 50 frames were acquired for each field of view.  $100\times$  microscope objective was chosen for counting single UCNPs. To account for the small field of view of the  $100\times$  objective, we acquired consecutive images of eight areas per well to reduce the Poisson noise.

**2.2.13 LENS assay.** Antibodies: anti-human CD81 monoclonal antibody (M38, ThermoFisher, Waltham, USA), anti-human CD63 monoclonal antibody (Ts63, ThermoFisher, Waltham, USA), anti-human CD9 Monoclonal Antibody (eBioSN4 (SN4 C3-3A2), ThermoFisher, Waltham, USA), biotinylated anti-human CD326 (EpCAM, ThermoFisher, Waltham, USA), biotinylated anti-mouse CD326 (Ep-CAM, Clone: G8.8, Australian biosearch, Wangarran, AU), anti-mouse CD9 (Clone: MZ3, Australian biosearch, Wangarran, AU), anti-mouse CD63 (Clone: NVG-2, Australian biosearch, Wangarran, AU), Panti-mouse CD81 (Clone: Eat-2, Australian biosearch, Wangarran, AU). In brief, a 96-well polystyrene microplate with  $190 \mu\text{m}$  thick bottom foil ( $\mu\text{CLEAR}$ , Greiner, Germany) was coated with anti-CD9, CD63, or CD81 antibody ( $10 \mu\text{g/mL}$ ) at  $4^\circ\text{C}$  overnight. All subsequent steps were carried out at room temperature. The microtiter plate was then blocked with blocking buffer (2% Casein in Tris-buffer) for 1 h. On each well,  $100 \mu\text{L}$  of the EVs dilution was incubated for 2 h. After four washing steps (0.1% Casein in Tris-buffer), the microtiter plate was incubated with biotin-EpCAM antibody ( $1 \mu\text{g/mL}$ ) for 1 h. After four washing steps (0.1% Casein in Tris-buffer),  $100 \mu\text{L}$  of LENS ( $50 \mu\text{g/mL}$ ) was applied to each well for 1 h. The microtiter plate was washed four times and was ready for imaging.

**2.2.14 Image and data processing.** For each concentration, the mean and standard deviation were calculated from three replicate wells. Four parameter logistic model was used to characterize the fitting curve of LENS and ELISA, which can reflect the relationship between concentration and absorbance accurately. Responds is calculated as:

$$Responds = Top + \frac{(Top - Bottom)}{1 + \left(\frac{C_{EV}}{EC_{50}}\right)^s} \quad (2-1)$$

Here,  $C_{EV}$  is the concentration of EVs. Responds is the computed number of LENS or the optical density (OD<sub>450</sub>) by ELISA. The equation yields the maximum (Top) and the minimum (Bottom) number of LENS or OD<sub>450</sub> that are experimentally determined,  $EC_{50}$  is the half-maximum effective concentration of EVs that reduces (Top - Bottom) by 50%, and  $s$  is the slope at the inflection point.

## 2.3 Results

### 2.3.1 Production and isolation of cancer cell-derived EVs

We chose a pair of cells including human colon cancer HT29 cells that express EpCAM-positive (EpCAM<sup>+</sup>) EVs and human embryonic kidney HEK293T cells that express EpCAM-negative (EpCAM<sup>-</sup>) EVs. HT-29 is a human colorectal adenocarcinoma cell line with epithelial morphology, express 2 million epcam per cell. When Grown in Dulbecco's modified Eagle's medium (DMEM), HT29 cells grow as a multilayer of unpolarised undifferentiated cells<sup>186</sup> (**Fig. 2-2a**). HEK293T cells are derived from HEK293 cells expressing the simian virus 40 (SV40) large T antigen, which allows for the replication of plasmids containing the SV40 origin of replication, leading to high expression of protein. HEK293T cells adhere to the polystyrene dishes for adherent culture (**Fig. 2-2b**), expressing no EpCAM per cell. To obtain small EV (sEV) from cell culture medium, commercial precipitation kits and differential centrifugations were employed (**Fig. 2-2c**). Although FBS is necessary for cell growth, FBS contains large number of bovine EVs. EV depleted FBS other than FBS was applied to the cell culture medium.

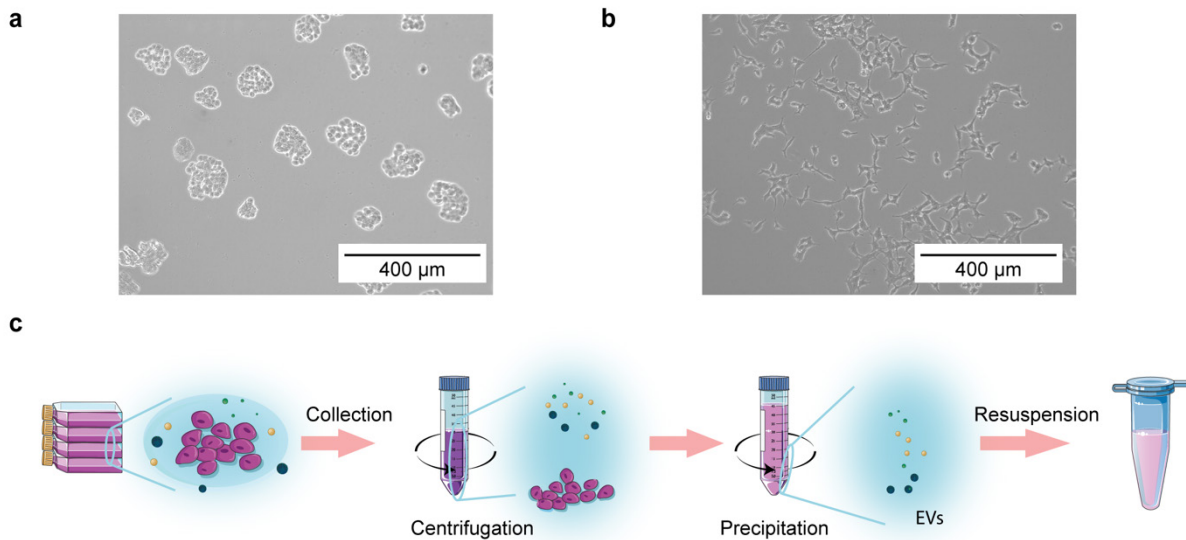


**Figure 2-2 | Cell culture and EV isolation.** (a) Representative phase-contrast image of HT29 cells. (b) Representative phase-contrast image of HEK293T cells. (c) Schematic of EV isolation by commercial precipitation kits.

### 2.3.2 Characterization of Cancer cell-derived EVs

To characterize the successful collected sEVs, various orthogonal technologies, including cryo-electron microscopy (cryo-EM), nanoparticle tracking analysis (NTA), membrane lipid dye staining, and western blotting were conducted following Minimal Information for Studies of Extracellular Vesicles (MISEV) guidelines<sup>40</sup>.

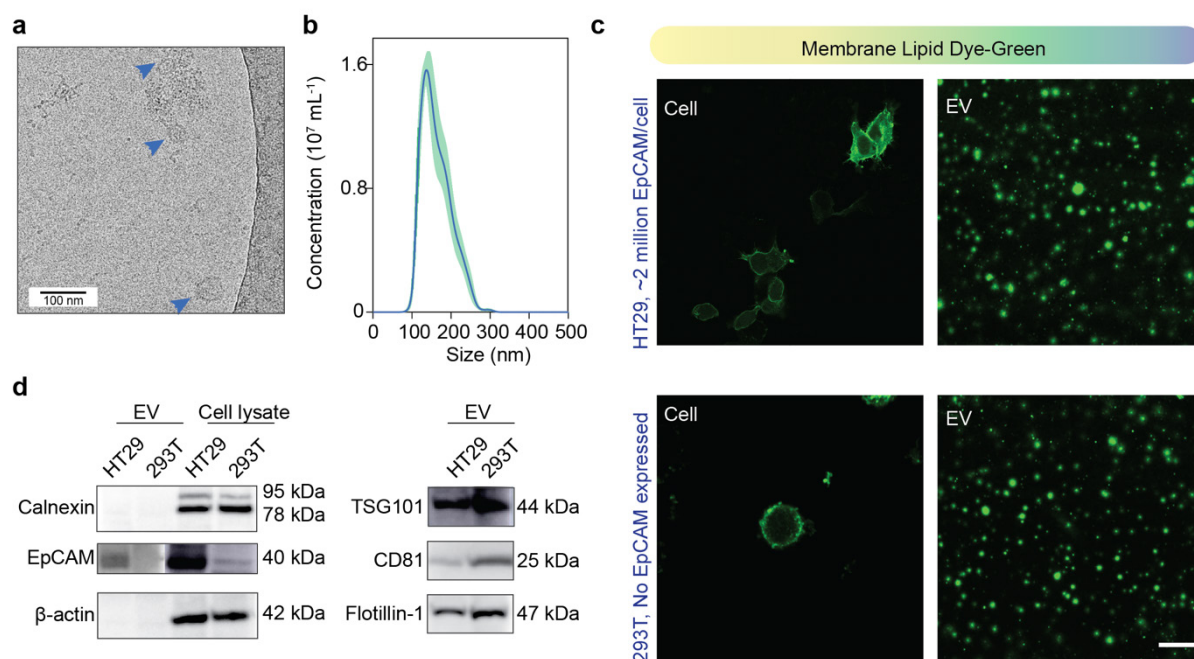


**Figure 2-3 | Characterization of cancer-cell derived EVs.** (a) Cryo-EM image of HT29-derived EVs. The blue arrows point to vesicles. (b) Representative modal size (nm) and concentration of HT29-derived EV samples according to 5 measures of NTA. (c) Representative images of PHK67 (green) labelled HT29 cells, HEK293T cells, HT29-derived EVs, and HEK293T-derived EVs. Scale bar: 10  $\mu$ m. (d) Characterisation of the EVs using western blot analysis of the cell marker ( $\beta$ -actin, Calnexin), EV markers (Flotillin-1, TSG101 and CD81) and cancer marker (EpCAM).

Morphological characteristics of EVs were conducted via cryo-EM. Cryo-EM allowed us to directly visualize morphology of with no additional fixative chemicals of any sort. The cryo-EM images confirmed the isolated EVs had lipid bilayers and vesicle internal structures (**Fig. 2-3a**).

Size and concentration profiles for the samples of HT29-derived EVs were obtained by NTA and are shown in **Figure 2-3b**. Sizes and hydrodynamic diameters were calculated based on the Brownian motion



of particles in solution. The NTA results presented the modal size of the obtained HT29-derived EVs was around  $133.8 \pm 4.8$  nm (ave  $\pm$  stdev).  $>83\%$  particles are below 200 nm, which are in the definition range of sEVs. The concentration of EVs was  $1.31 \times 10^9$  ( $\pm 0.146 \times 10^8$ ) particles  $\text{mL}^{-1}$ . Lipophilic membrane dye labelling was carried out to stain the lipid structure of EVs. EVs are comprised of a lipid membrane containing membrane-bound proteins. Lipophilic membrane dye can incorporate into the lipid structure of EVs. PKH dyes can be incorporated into the lipid structure of EVs and were successfully used to label the lipid membrane of cells and EVs (**Fig. 2-3c**). But it will stain any lipid bilayer, not specific to EV labelling.

Western blotting analysis was performed to detect the presence of different protein markers from EV samples. Western blotting analysis showed the presence of tetraspanin marker CD81 and cytosolic protein TSG101. The absence of non-sEV marker calnexin confirmed that there were no other large EVs in our sample (**Fig. 2-3d**). In addition, the expression of EpCAM was observed in both HT29 cells and its derived EVs, whereas not in HEK293T-EVs and only slighted in HEK293T cells. This result confirmed that HT29 cells express  $\text{EpCAM}^+$  EVs and HEK293T cells express  $\text{EpCAM}^-$  EVs.

Furthermore, immunomagnetic beads-based flow cytometry was performed to quantitatively evaluate the expression level of EpCAM in three EV subpopulations (captured by CD9, CD81 and CD63 beads). For all three subpopulations, the level of  $\text{EpCAM}^+$  EVs from HT29 were significantly higher than HEK293T (**Fig. 2-4**). The consistent results from western blotting and flow cytometry confirmed that HT29 EVs and HEK293T EVs can be used a pair to evaluate the analytical performance of the LENS assay, especially the specificity of LENS labelling.

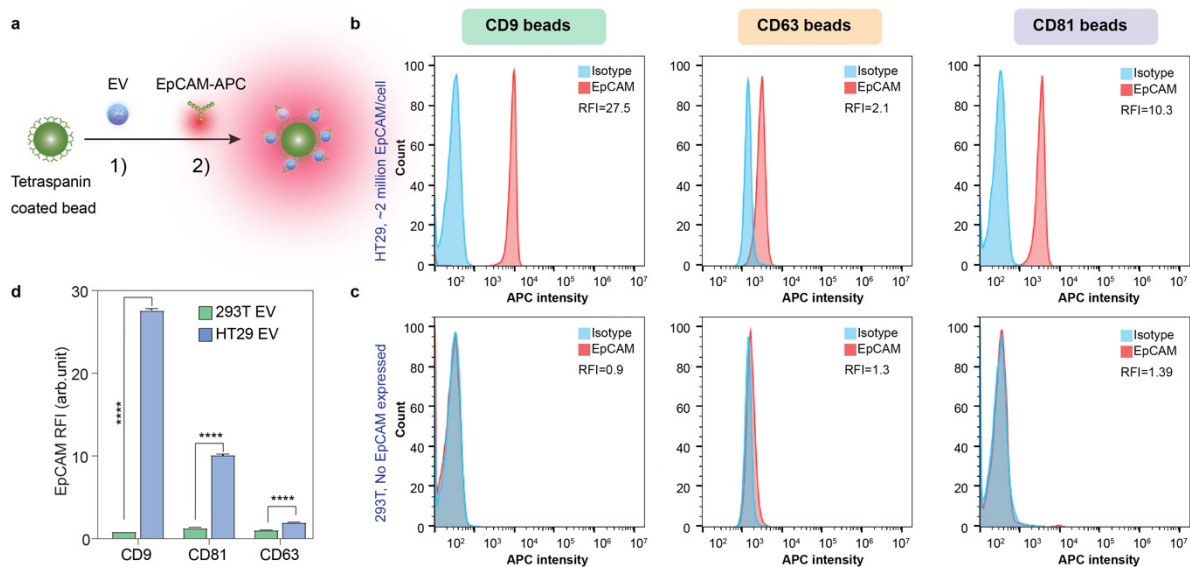


**Figure 2-4 | EpCAM expression profile of cancer-cell derived sEVs.** (a) Schematic of the detection of EVs immunocaptured on beads by flow cytometry. EVs were captured onto anti-CD9, CD63, or CD81 magnetic beads followed by detection with allophycocyanin (APC) conjugated anti-EpCAM antibody. (b,c) Representative fluorescence histogram data for HT29 EVs stained with red trace - APC conjugated EpCAM; blue trace - APC conjugated IgG1 isotype. (d) Flow cytometry analysis of EpCAM expression level from EVs captured by CD9, CD81 and CD63 beads for both HT29 cells and HEK293T cells. The data points are Mean  $\pm$  s.d. of 3 independent experiments. Unpaired Student's *t*-test, \*\*\*\**P* < 0.0001. In Summary, the characterisation results above proved that the methods for EV isolation was effective and reliable, could be used for further study.

### 2.3.3 Preparation and characterisation of LENS

To prepare a set of well-dispersed and stable LENS in physiological buffers, the co-polymer POEGMA-*b*-PMAEP (**Fig.2-5b**) was used as a hydrophilic ligand to make the nanoparticles biocompatible via a ligand exchange process. UCNPs@PbP provides carboxylic groups for further conjugation of streptavidin (SA) via a standard EDC method. UCNPs@PbP and UCNPs@PbP@SA were characterized using TEM, FT-IR, and DLS.

Reversible Addition–Fragmentation Chain Transfer (RAFT) polymerization was used to synthesis diblock copolymers composed of 7 monoacryloxyethyl phosphate (MAEP) units and 13 OEGMEA units<sup>187</sup>. The two-step synthesis procedure of the deblock copolymer is illustrated in **Figure 2-5a**.

Polymer characterization Proton Nuclear Magnetic Resonance (<sup>1</sup>H NMR):<sup>1</sup>H NMR spectra of the polymer were characterized by a 500 MHz Agilent instrument at 25°C in d<sub>6</sub>-DMSO and D<sub>2</sub>O. The percentage of monomer conversion to the polymer POEGMEA and molecular weight was calculated by <sup>1</sup>H NMR signals followed by sequencing equations.

$$\alpha^{POEGMEA} = \left[ \frac{\int_{4.1}}{\int_{4.1} + \int_{4.2}} \right] \quad (2-2)$$

In the above equation,  $\int_{4.2}$  ppm and  $\int_{4.1}$  ppm represent the integral of the signal of polymer and monomer at 4.1 and 4.2 ppm, respectively. Monomer conversion of the second block was measured also by <sup>1</sup>H NMR spectra of the reaction mixture before and after polymerization by comparing the integral ratio of the vinyl protons of monomer and the unchanged methylene protons of the POEGMEA adjacent to the ester bond at 4.1 ppm.

$$\alpha^{PMAEP} = \left[ \frac{\int_{6.2(0)h} - \int_{6.2(t)h}}{\int_{6.2(0)h}} \right] \quad (2-3)$$

$$M_{n,NMR}^{POEGA-b-PMAEP} = \alpha^{PMAEP} \times \left( \frac{[POEGMEA]}{[RAFT]} \right) \times M_W^{POEGMEA} + M_W^{RAFT} \quad (2-4)$$

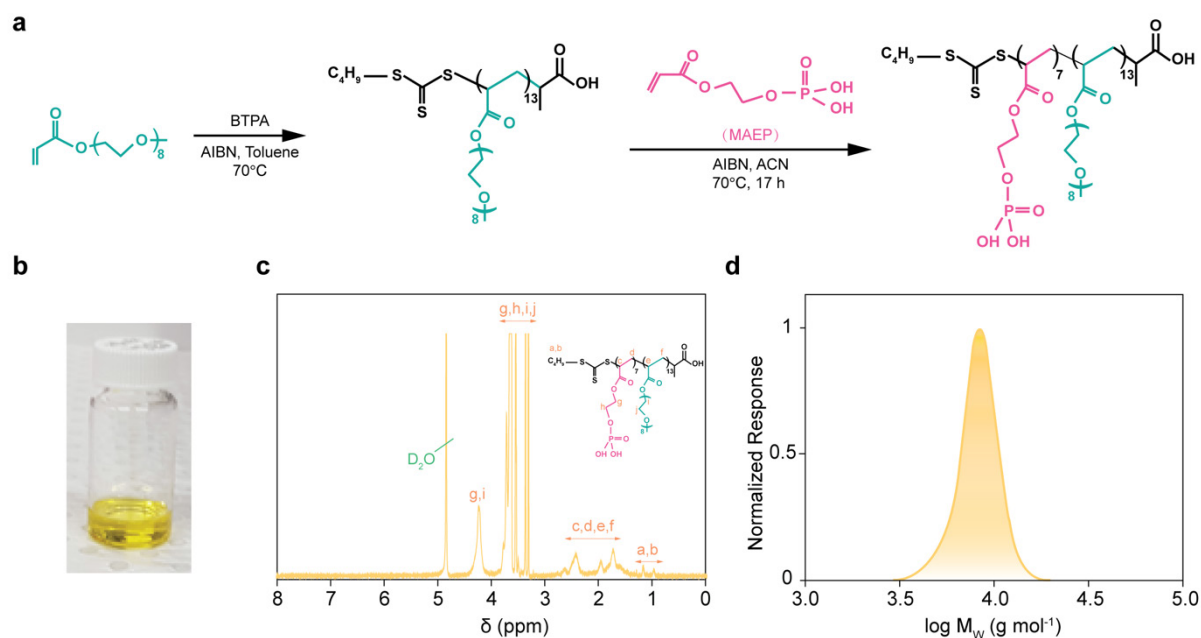


**Figure 2-5 | Synthesis and characterization of POEGMEA<sub>13</sub>-*b*-PMAEP<sub>7</sub> copolymer.** (a) Two-step synthesis procedure of the deblock copolymer. (b) A photo of synthesized deblock copolymer. (c) <sup>1</sup>H NMR spectrum of POEGMEA<sub>13</sub>-*b*-PMAEP<sub>7</sub>. <sup>1</sup>H NMR spectra confirmed the presence of ester, phosphate, amide and sulphonic acid. (d) GPC curves of POEGMEA<sub>13</sub>-*b*-PMAEP<sub>7</sub>. The POEGA macro-RAFT agent was measured to be ~13 repeating units.

<sup>1</sup>H NMR spectrum analysis confirmed the presence of methylene, ester, and the methylene group adjacent to the phosphate groups of the 13 POEGMEA polymer (**Fig. 2-5c**). Gel permeation chromatography (GPC) analysis was used to confirm the molecular weight of the formed polymers (**Fig. 2-5d**). The molecular weight of the PEG polymers with 13 POEGMEA repeating units and 7 PMAEP repeating units were 6500 g mol<sup>-1</sup>. The narrow molecular weight distribution ( $M_w/M_n$ ) is 1.06. This confirms the successful polymerization and chain extension with the designed molecular weight and chain length of the POEGMEA, without any evidence of dead polymers.

Transmission Electron microscopy (TEM) is used for 2D size and shape determination of the synthesized samples. **Figure 2-6a, b, c** shows TEM images of the UCNP@OA, UCNP@PbP and

UCNPs@PbP@SA, respectively. The size of the synthesized UCNPs@OA is uniform with a diameter of  $40.0 \pm 2.1$  nm (**Fig. 2-6d**). The TEM results confirmed that the surface modifications did not change the morphology of UCNPs, and the size of particles remains uniform with a diameter around  $41.5 \pm 2.1$  nm after two-step surface modifications (**Fig. 2-6e, f**). It should be noted that the distances between the nanoparticles increased after the surface modification. Quantitatively, the distances between each particle are increased from  $40.4 \pm 1.8$  nm (UCNPs@OA, **Fig. 2-6g**) to  $52.1 \pm 3.3$  nm for (UCNPs@PbP, **Fig. 2-6h**) and  $59.3 \pm 7.9$  nm (UCNPs@PbP@SA, **Fig. 2-6i**).

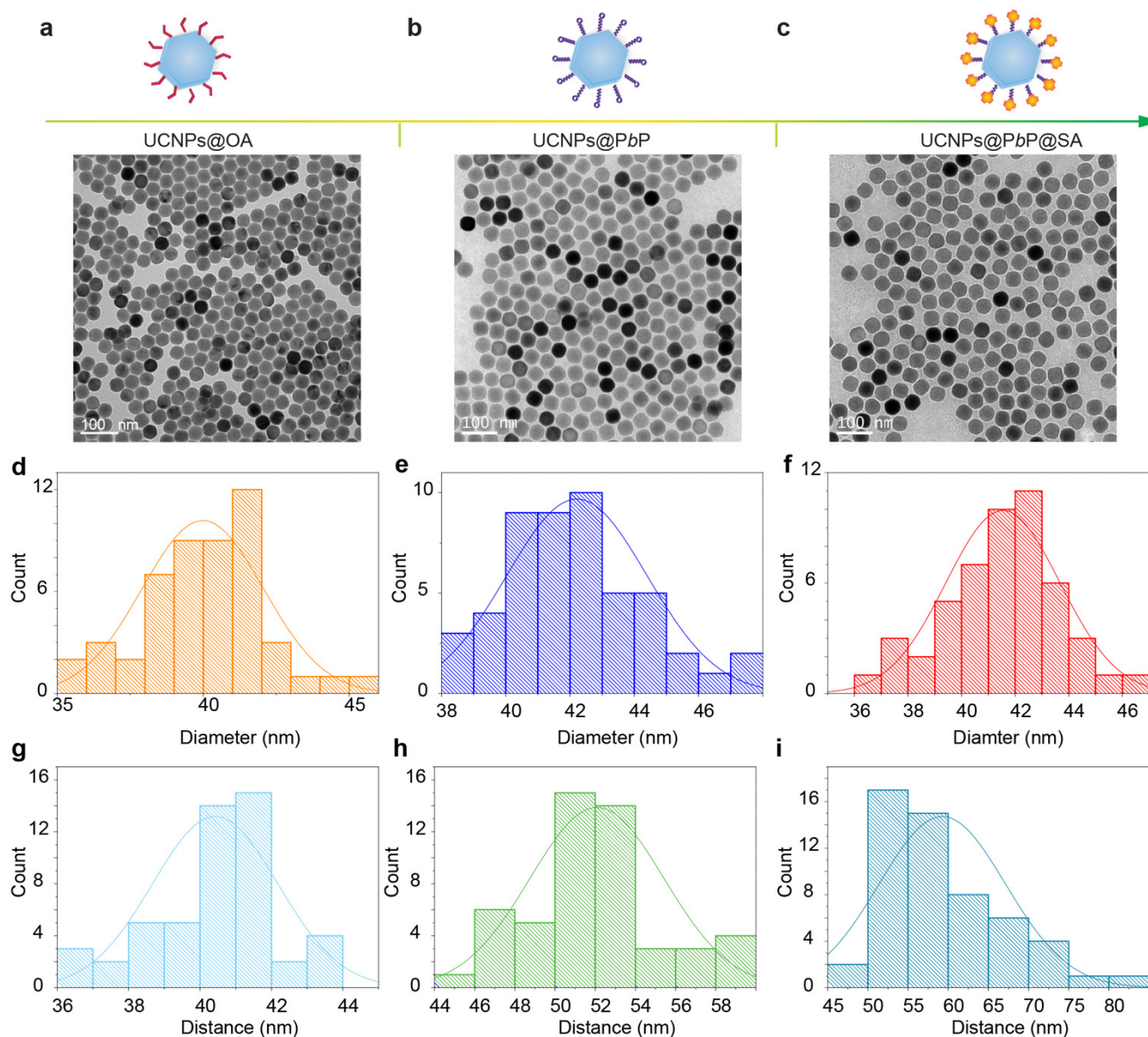


**Figure 2-6 | TEM results.** (a) TEM image of UCNPs@OA. (b) TEM image of UCNPs @PbP. (c) TEM image of UCNPs@PbP@SA. (d) Size distribution of UCNPs@OA. (e) Size distribution of UCNPs@PbP. (f) Size distribution of UCNPs@PbP@SA. (g) Distances profile between each UCNPs@OA nanoparticle.

(h) Distance profile between each UCNPs@PbP nanoparticle. (i) Distance profile between each UCNPs@PbP@SA nanoparticle.

Typical FT-IR peaks of OA-UCNPs at  $3003\text{ cm}^{-1}$  and  $1625\text{ cm}^{-1}$  confirmed carbon-carbon double bond (C=C) and carbon-oxygen bond (C-O) vibration stretch of OA ligands, respectively (Fig. 2-7). The peaks at  $1732\text{ cm}^{-1}$  and  $1101\text{ cm}^{-1}$  represent the carboxylic group (C=O) and phosphine oxides (P=O) vibration stretches of the polymer confirmed the successful ligand exchange.

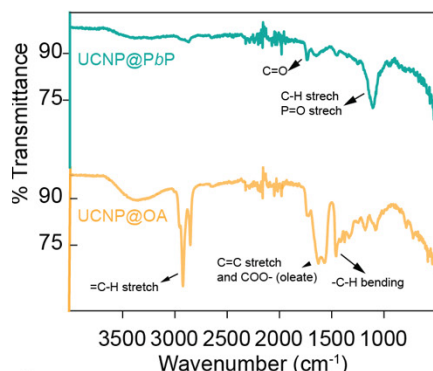


**Figure 2-7 | FT-IR spectra of UCNPs.**

DLS analysis was performed to obtain information on the particle size after surface modification. DLS is a technique used to measure the Brownian motion of particles in a dispersion to determine their hydrodynamic diameter accordingly. The DLS data showed a stepwise increase in the average size of particles from 41.93 nm to 48.01 nm, and 52.38 nm after two steps' modification. (Fig. 2-8).

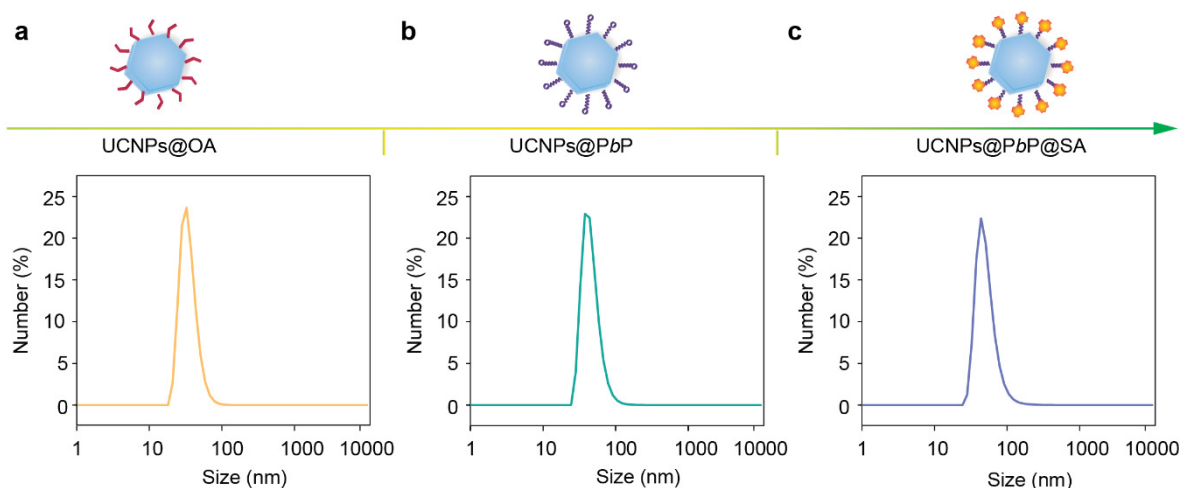


**Figure 2-8 | DLS analysis of UCNPs. (a) UCNPs@OA. (b) UCNPs@PbP. (c) UCNPs@PbP@SA.**

The fluorescence emission of UCNPs was further determined by fixing the emission wavelength and scanning the excitation monochromator over a wavelength range from 400 nm to 800 nm. Under the 980 nm excitation, the formed UCNPs@PbP@SA. display multiple emission bands. which has emission

bands at 525nm, 541 nm and 654 nm corresponding to the  ${}^2H_{11/2} \rightarrow {}^4I_{15/2}$ ,  ${}^4S_{3/2} \rightarrow {}^4I_{15/2}$ ,  ${}^4F_{9/2} \rightarrow {}^4I_{15/2}$  transitions of  $Er^{3+}$  (Fig. 2-9a). The luminescence emission spectra results confirmed that the luminescence properties of UNCPs were stable after surface modification (Fig. 2-9b).

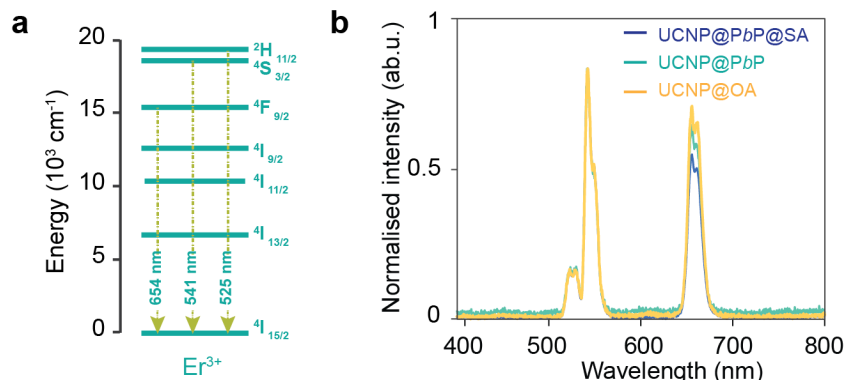


**Figure 2-9 | Luminescence properties of UNCPs.** (a) Energy transfer diagram of  $Yb^{3+}$ – $Er^{3+}$  multiphoton upconversion under 980 nm excitation. (b) upconversion luminescence spectra of UNCPs@OA , UNCPs@PbP, and UNCPs@PbP@SA under 980 nm excitation.

To measure the amount of coupled SA, we used UV 280nm (A280) absorbance to estimate the SA concentration remaining in the supernatants of the reactions after bioconjugation and centrifugation. The experimental calculation of mole ration SA per single UNCPs follows the equations below<sup>185,187</sup>:

$$Con_{SA \text{ in sampe}} = Initial \ Con_{SA} - S/N \quad (2-5)$$

As shown in **Figure 2-10**, the A280 measurements of the initial concentration of SA and supernatants were 0.107, 0.06, respectively. According to equation (2-5),  $Con_{SA \text{ in sample}}$  was calculated to be 0.047.

$$\% \ SA = \frac{Con_{SA \text{ in sample}}}{Initial \ Con_{SA}} \times 100 \quad (2-6)$$

According to equation (2-6), 44% of the SA was coupled to the UNCPs@PbP.

$$Mole \ ratio \ SA/UCNP = \% \ Ab \times 49 \quad (2-7)$$

The molecular weight of UNCP@PbP is 60 MDa, calculated from reference<sup>185</sup>. 100  $\mu$ g (1.7 pmole) of the UNCP@PbP was used here. The molecular weight of SA is 60 kDa, 5  $\mu$ g (83.3 pmole) of SA was used here. The mole ratio of SA per single UNCPs before reaction was calculated to be 49. After reaction, according to equation (2-7), we calculated that each nanoparticle was conjugated with approximately 22 of SA molecules.

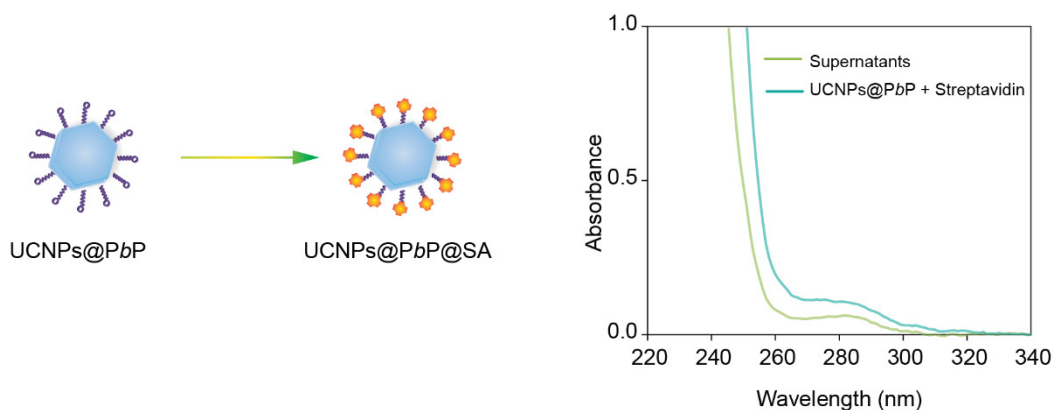


**Figure 2-10 | Absorbance spectra of the original solution and supernatants after bioconjugation and centrifugation of SA with UCNPs@PbP.**

Streptavidin (SA) is a non-glycosylated protein capable of binding biotin or biotinylated molecule with extremely high affinity ( $k_d \sim 10^{-15}$ ), owning a lower non-specific absorption in some biotechnologies than its analog avidin<sup>188</sup>. The activity of UCNPs@PbP@SA was tested using avidin-biotin interaction assay (**Fig. 2-11a, b**). Compared with UCNPs@PbP, UCNPs@PbP@SA showed specific binding to the biotin-Ab which was concentration dependent (**Fig. 2-11c**). The stepwise increasement of the UCNPs and successful validation of avidin-biotin interaction assay indicated that the successful modification of SA on the surface of UCNPs@PbP.

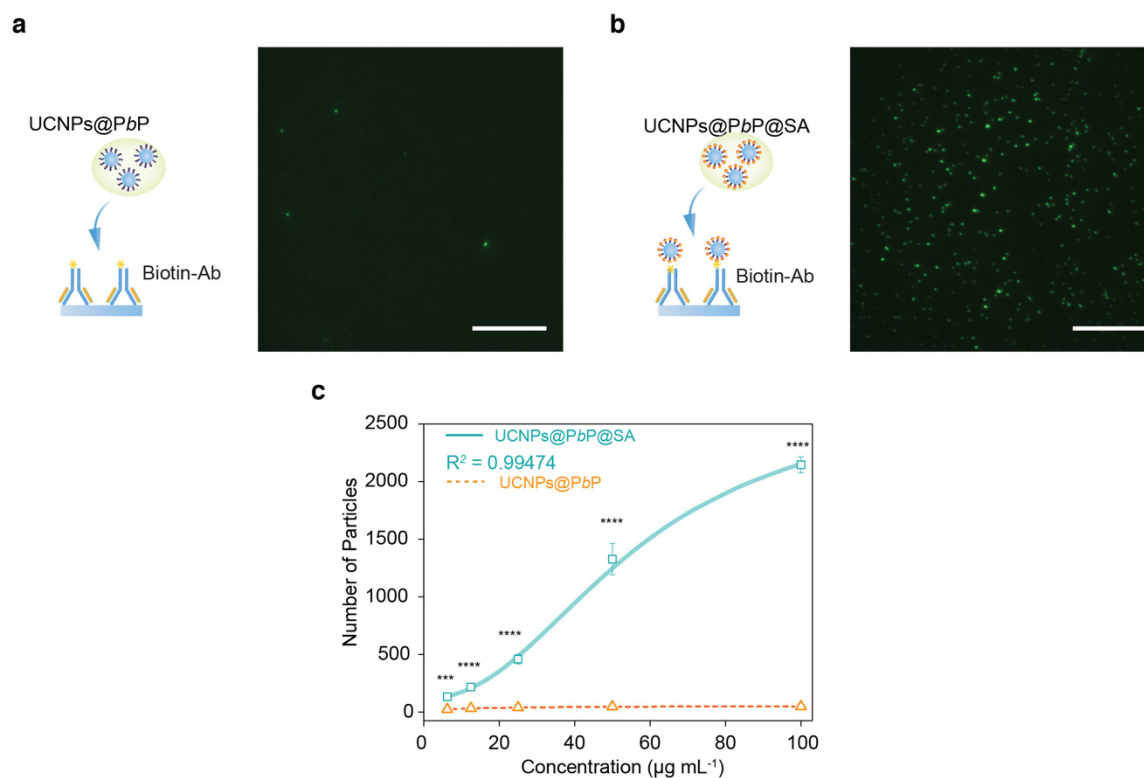


**Figure 2-11 | Binding activity and specificity of UCNPs@PbP (a) v.s. UCNPs@PbP@SA (b) on the detection of immobilized biotin-antibody.** Scale bar, 10  $\mu\text{m}$ . (c) The number of UCNPs@PbP@SA bound to the plate versus its concentration added to the plate. Unpaired two-tailed *t*-tests reveal  $p < 0.0001$  between the two groups of data.

In summary, the experimental results above confirmed the successful coating of the PbP and SA on the surface of nanoparticles. These features allow EV enumeration and subtype profiling. Here, we named the method based on UCNPs@PbP@SA for the following EV enumeration and subtype profiling as Lanthanide-doped EV-targeting Nanoscopic Signal-amplifiers (LENS).

#### **2.3.4 Quantification of $\text{EpCAM}^+$ EVs from cell line model**

We next evaluate the performance of LENS for the quantification of specific EVs and explore the limit of detection (LoD). EVs were firstly captured by CD9, CD81, CD63 antibodies on the well plates, respectively, and detected using biotinylated EpCAM antibodies. TIRF images show that the number of the bright spots increases with the concentrations of added EVs (**Fig. 2-12a, c, and d**). We used  $\text{EpCAM}^-$  EVs derived from HEK293T cell line as negative control to determine the LoD, which is  $1.8 \times 10^6$  EVs  $\text{mL}^{-1}$ , nearly three orders of magnitude lower than that of enzyme-linked immunosorbent assay (ELISA) method (**Fig. 2-12b**). The LoDs for the subpopulations of  $\text{CD63}^+$  and  $\text{CD81}^+$  EVs were also remarkably sensitive, i.e.  $1.1 \times 10^7$  particles  $\text{mL}^{-1}$ , and  $8.9 \times 10^6$  particles  $\text{mL}^{-1}$ , respectively (**Fig. 2-12d, f**).



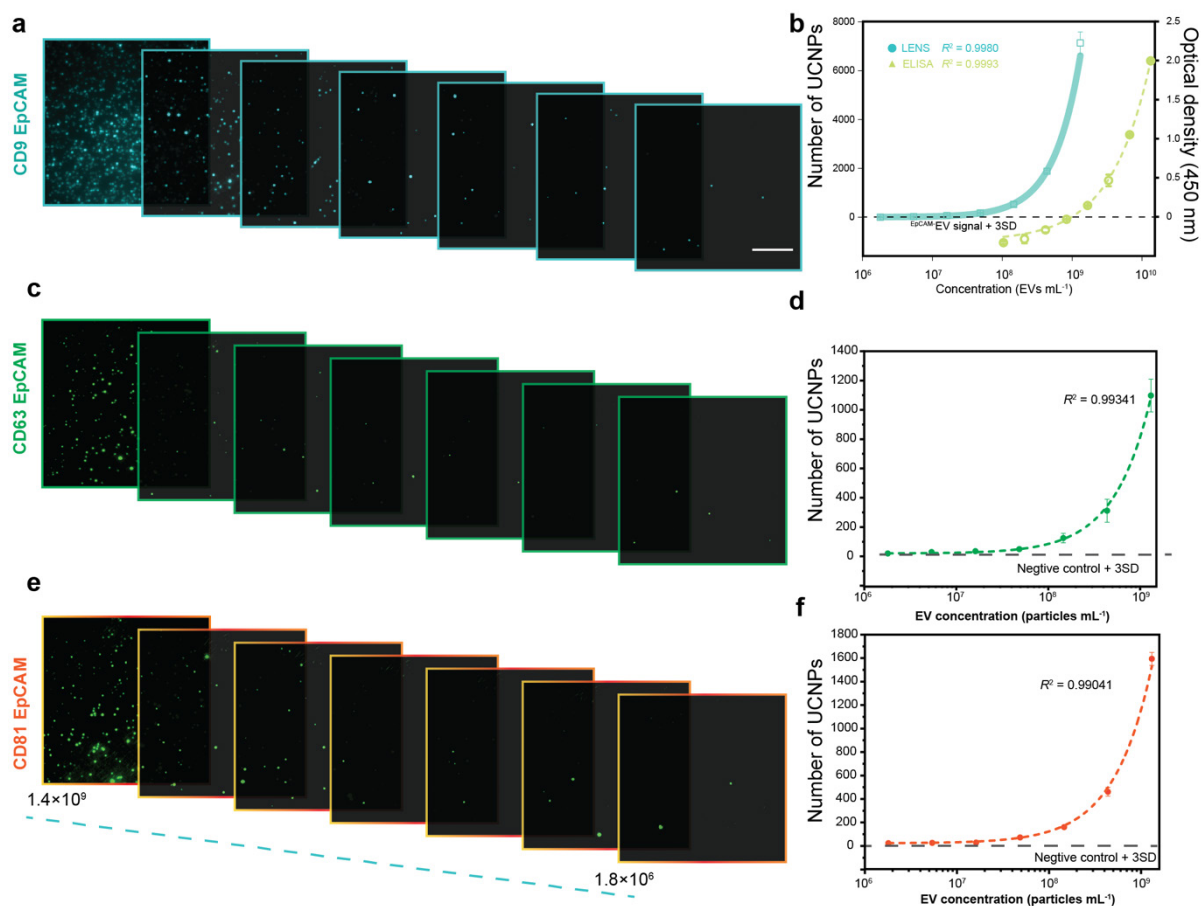


**Figure 2-12 | Ultrasensitive detection of  $\text{EpCAM}^+$ EVs with LENS.** (a, c, e) TIRF images of detecting  $\text{CD9}^+\text{EpCAM}^+$ EVs,  $\text{CD63}^+\text{EpCAM}^+$ EVs and  $\text{CD81}^+\text{EpCAM}^+$ EVs of various EV concentrations using LENS. Scale bar: 10  $\mu\text{m}$ . (b, d, f) Calibration curves of LENS for detecting  $\text{CD9}^+\text{EpCAM}^+$ EVs,  $\text{CD63}^+\text{EpCAM}^+$ EVs and  $\text{CD81}^+\text{EpCAM}^+$ EVs with the concentration ranging from  $1.8 \times 10^6$  to  $1.4 \times 10^9$  EVs  $\text{mL}^{-1}$ . The limit of detection (grey dashed line) was determined by the signal of the  $\text{EpCAM}^-$ EVs plus 3 times the standard deviation.  $\text{EpCAM}^-$ EVs concentration:  $1 \times 10^9$  particles  $\text{mL}^{-1}$ . The data points represent Mean  $\pm$  s.d. of 3 independent experiments.

### 2.3.5 Correlation between Flow cytometry and LENS

The LENS assay result was further systematically validated by flow cytometry method in profiling sEVs from HT29 for various biomarkers. Further, we applied this method to profile EVs from HT29 for various biomarkers. As shown in **Fig. 2-13**, regression analysis of all measured values for surface markers in EVs resulted in a strong linear correlation between the LENS imaging and flow cytometry ( $R^2 > 99\%$ ). But LENS was more sensitive and required smaller sample amounts.

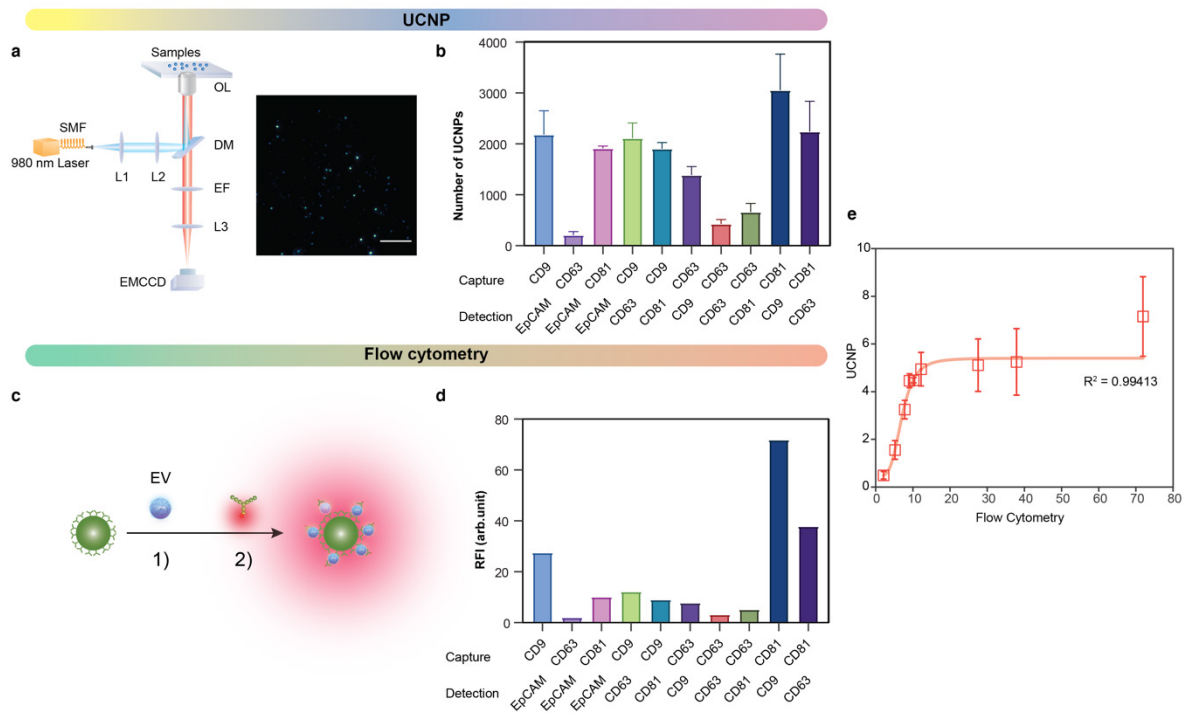


**Figure 2-13 | Correlation between LENS and flow cytometry measurements.** (a) TIRF imaging for various EV identification. EVs isolated from HT29 was used. Scale bar: 10  $\mu\text{m}$ . (b) Protein levels of EVs determined by the UCNP numbers. EVs were captured onto anti-CD9, CD63, CD81, or EpCAM coated plate followed by detection with Biotin -CD9, CD63, CD81, or EpCAM antibody, and subsequently detected by streptavidin coupled UCNPs. (c) Schematic of the detection of EVs immunocaptured on beads by flow cytometry. EVs were captured onto anti-CD9, CD63, CD81, or EpCAM magnetic beads followed by detection with allophycocyanin (APC) conjugated CD9, CD63, CD81, or EpCAM antibody. (d) Protein values of EVs measured from flow cytometry. The flow cytometry-based detection provides the relative fluorescence intensity (RFI) value for EVs. The RFI was calculated according to the formula,  $RFI = \frac{MFI\ positive}{MFI\ isotype}$ , where MFI is mean fluorescence intensity. (e) Correlation between LENS and flow cytometry measurements.

### 2.3.6 LENS assay in EV-spiked plasma

Next, we carried out the LENS assay using human plasma spiked with cell-derived EVs to show that it can be performed in the complex environment of plasma directly without pre-isolation. Specific detection of tumour-derived EVs was assessed by detecting the EpCAM<sup>+</sup> subtype in the HT29 EV spiked in tenfold-diluted healthy plasma. The LoD of  $6.44 \times 10^6$  EVs  $\text{mL}^{-1}$  for the CD9<sup>+</sup>EpCAM<sup>+</sup> subtype (Fig. 2-14), slightly higher, but within the consistency range to the result presented without plasma.

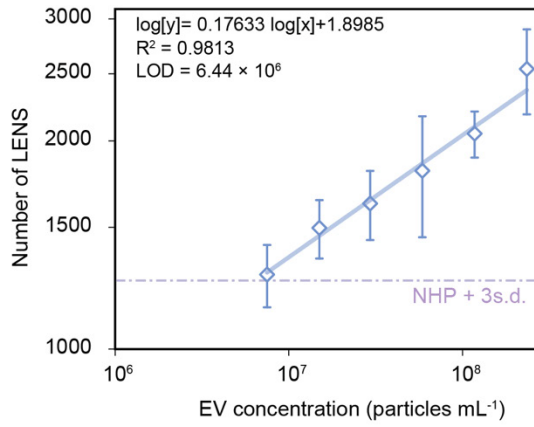


**Figure 2-14 | Calibration curve for detecting  $CD9+EpCAM+$  EVs spiked in tenfold-diluted healthy plasma without pre-isolation.** Error bars represent 1 *s.d.* ( $n = 3$ ).

### 2.3.7 Confirming the single sEV sensitivity

The resolution of our self-setup TIRF imaging is around 424 nm, which is larger than the size of single sEV, therefore, multiple sEVs may present in an optical diffraction-limited spot, particularly when the concentration of sEVs is high. To reconfirm if or not our LENS assay reaches the sensitivity for the detection of single EVs, we provide theoretical analysis. To achieve single EV imaging in our system, theoretical requirement of the upper limit of the EV concentrations, based on Poisson partitioning statistics, were analysed. EVs distributions are assumed as<sup>189</sup>:

$$p(\kappa) = \frac{\lambda^\kappa e^{-\lambda}}{\kappa!} \quad (2-6)$$

Where  $p(\kappa)$  is the probability that a partition will contain  $\kappa$  copies of the EVs.  $\lambda$  denotes the average number of EV per partition defined by the ratio between the number of EVs ( $m$ ) and the partitions ( $n$ ). As the area of the well plate is 0.32 cm<sup>2</sup>, it provides as many as  $1.8 \times 10^8$  partitions ( $n$ ) of optically-diffraction limited zones. To have at least 99% of partitions containing one or zero EVs, the maximum number of EVs is estimated to be  $2.63 \times 10^7$ , corresponding to the upper limit of EV concentration of  $2.63 \times 10^8$  particles mL<sup>-1</sup> for a 100-uL sample volume in the LENS system. This indicates that the majority of bright spots detected for the concentration range of  $1.8 \times 10^6$  to  $2.63 \times 10^8$  EVs mL<sup>-1</sup> could only contain one EV particle (**Fig. 2-15**).

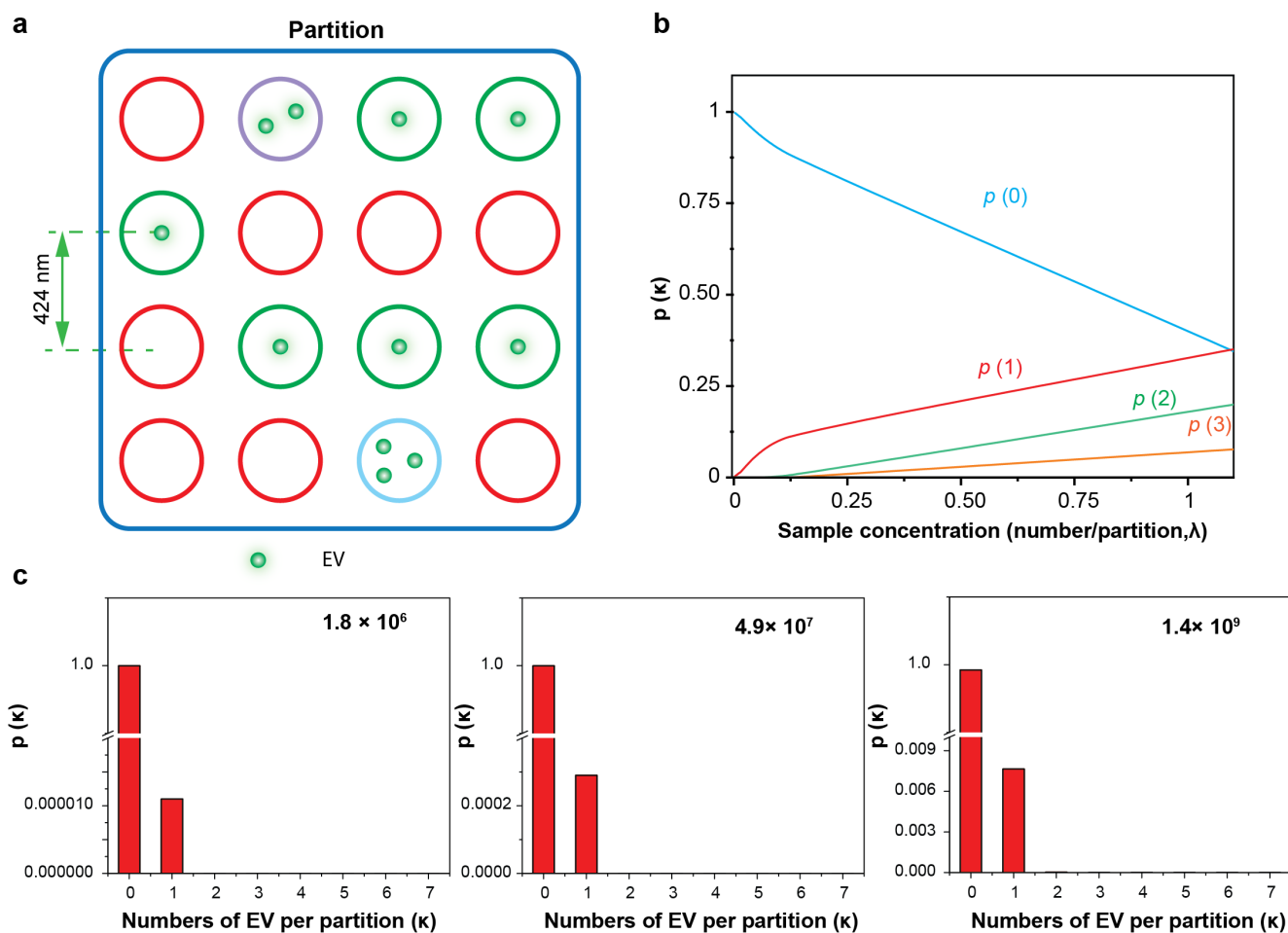


**Figure 2-15 | Poisson distribution showing single EV probability distribution in LENS system. (a)** Illustration of partitioning EVs into small area (resolution limitation) results in a statistical distribution of EVs. **(b)** Probability of zero, one, two, and three entities per partition for various EV concentrations. Probability are calculated using the Poisson distribution. **(c)** Probability that a partition contains  $\kappa$  entities, for various sample concentrations.

## 2.4 Conclusion and discussion

The isolation, detection and quantification of circulating sEVs have attracted rapidly growing interests towards non-invasive diagnosis and the monitoring of patient responses to treatment. Specific detection of disease-associated sEVs that often present in low concentration in biofluids remains challenging for conventional technologies. Here, we established a LENS platform for detection of cancer cell derived sEVs with single sEV quantification achieved. This is particularly promising for the early stage of the diseases (especially cancer) when the subpopulations of disease-specific sEVs are secreted in low abundance. Our method, once the library of LENS caring a diverse range of colours and lifetime barcodes can be specifically labelled with a range of antibodies and biomarker-specific molecules, can be used to

detect multiple EV protein markers. The potential capability of multiplexing detection of different EVs subpopulations will be crucial for investigating the heterogeneous nature of sEVs from cancer patients. Microfluidic device or microarray can be further integrated to increase the throughput.

Nevertheless, sEVs were isolated using a commercial precipitant, which is difficult to avoid coprecipitate contamination of non-EV components like protein complexes and lipoproteins<sup>190,191</sup>, so we combined affinity-based method (CD9/CD63/CD81 capture) to avoid contaminations of non-EV components. In addition, we recommend the use of size-exclusion chromatography for plasma EV isolation<sup>192</sup>. We also suggest removing the buffer from the plate reader once the assay to be completed, so that UCNPs will be firmly attached on the surface-for long-term characterizations, as UCNPs in the dry state will be stable for term use and with high intensity, compared with UCNPs in the buffer.

## Statement of Contribution of Authors for Chapter 3

[3] Guan Huang, Yongtao Liu, Dejiang Wang, Ying Zhu, Shihui Wen, Dayong Jin\*. Super-resolution imaging of single EVs. Nature Communications (Submitted)

	G. H	Y.L	D.W	Y.Z	S.W	D.J
Experiment Design	▪					▪
Sample preparation	▪	▪	▪		▪	
Data collection	▪	▪	▪	▪		
Analysis	▪	▪				▪
Manuscript	▪					▪

The concept of this paper was developed by my supervisor Dayong Jin. I designed the experiments and conducted the majority of experimental work, including modification of UCNPs, Characterization of UCNPs, EV isolation, EV characterisation, LENS assay, data collection, data analysis, and manuscript writing.

---

## Chapter 3 Super-resolution imaging of single sEVs

---

### Abstract

Single small extracellular vesicle (sEV) imaging plays an important role in revealing the heterogeneity of EVs, improving our understandings their molecular biology. Due to their small sizes and low abundance, accurate imaging of single sEV is still a great challenge. Here, we report that highly photostable Lanthanide-doped EV-targeting Nanoscopic Signal-amplifiers (LENS) can be used for single cancer cell derived-EV super-resolution imaging. For different emitters, Er<sup>3+</sup>-doped LENS has better brightness for diffraction-limited imaging, while Tm<sup>3+</sup>-doped LENS has the better resolution for super-resolution imaging. The specificity targeting of LENS to the tumour epitope on single EV is cross validated by comparing antibody labelling to a genetically encoded fluorescent protein. Pearson's R-value for large EVs is 0.83 and a co-localization of double-positive spots (~65%) for small EVs-LENS conjugates confirm a strong co-localization. With targeting specificity, the super-resolution technique clearly resolves single LENS from the clusters and achieves dual-LENS imaging. Furthermore, pushing the size down to 21 nm (limitation), super-resolution imaging allows us to distinguish localization clouds and the theoretical of the maximum number of LENS labelled on the sEVs are 91. Our work may inspire the future direction of LENS field toward single sEVs research.

### 3.1 Introduction

Small extracellular vesicles (sEVs) are nanometre-sized, bilayer lipid carriers that contain a wide variety of cargos such as lipids, proteins, metabolites, RNA and DNA, which play an important role in cancer progression. Single sEV imaging plays an important role in revealing the spatiotemporal property of EVs, improving our understandings their molecular biology<sup>193</sup>. However, considering its size, most methods of optical microscopy are not able to resolve its nanoarchitecture and heterogeneity<sup>18</sup>. In the last decade, new methods of optical super-resolution microscopy have emerged pushing the resolution barrier towards nanometre scales<sup>94,194–197</sup>.

Among these super-resolution concepts, some of the most commonly used techniques are structured illumination microscopy (SIM), stimulated emission depletion (STED), and single-molecule localization microscopy (SMLM) such as stochastic optical reconstruction microscopy (STORM), photoactivated localization microscopy (PALM) (**Table 3-1**)<sup>198,199</sup>. SIM is a useful technique for fast-changing event within live-cell imaging studies, but it does not provide the resolution (ranging from 100 to 140 nm) gains as SMLM or STED. PALM and STORM offer high spatial resolution (20–50 nm), but have low

temporal resolutions ranging from 30 seconds to 30 minutes (a super-resolution image is reconstructed from the multiple image captures). STED microscopy is a powerful direct visualization technique that allows images to be captured at resolutions between that of SMLM and SIM (30-50 nm). STED is quite fast as only a single image is acquired, and no reconstruction is required.

**Table 3-1 | Microscopy methods.** Reprinted from reference<sup>200</sup>.

Modalities	Resolution (XY)	Resolution (Z)	Illumination	Probes	Acquisition time	Post-acquisition processing	Live or fixed
Standard fluorescence microscopy	250 nm	500 nm	Epi, confocal, TIRF	Conventional fluorescent probes	Seconds		Live, fixed
SIM, airyscan	80 nm-150 nm	250 nm-350 nm	Widefield (epi and TIRF)	Conventional fluorescent probes	Seconds	Yes, FTT	Live, fixed
STED	30 nm-80 nm	150 nm	Laser scanning	Limited selection of probes (match depletion laser)	Seconds	No	Live, fixed; optimal for fixed
Cryo-soft X-ray tomography	25 nm-40 nm	30 nm	Widefield	none		No	Fixed (near-native state vitrification)
PALM	20 nm	50 nm	Widefield (epi and TIRF)	Photoactivatable fluorescent proteins	Minutes	Yes (PSF mapping)	Live, fixed
STORM	20 nm	50 nm	Widefield (epi and TIRF)	Photoswitchable dyes	Minutes	Yes (PSF mapping)	Live, fixed
LLSM	100 nm-200 nm	400 nm	Multi-Bessel beam plane illumination	Conventional fluorescent probes	Seconds, minutes or hours	Not necessary, but often tracking dynamic processes	Live, fixed; optimal for live
TEM	<1 nm	70 nm <sup>a</sup>	Electron beam	Contrast reagent, immunochemistry	Seconds	Yes	Fixed
CLEM	<1 nm/150 nm <sup>b</sup>	5 nm <sup>c</sup>	Electron beam, widefield	Contrast reagent, nanodots, and fluorescent proteins	Minutes	Yes (aligning)	Live and/or fixed

Characteristics of imaging methods used to visualize EVs. epi, epifluorescence; FTT, fast Fourier transform; PSF, point spread function; TEM, transmission electron microscopy. <sup>a</sup>Resolution corresponding to the thickness of the section. <sup>b</sup>Resolution gap between electron microscopy and light microscopy data, respectively. <sup>c</sup>Tomography from double-tilted 250 nm sections.

Apart from dedicated imaging set-up, successful labelling strategies are necessary for imaging single small EVs. Most super-resolution techniques rely on dye brightness and photoswitching properties. In single EV imaging, photon budget, contrast and labelling specificity are limiting factors. A single fluorescing molecule generates enough photons to be detected if the background is low. Photoactivation localization microscopy using fluorescent protein Dendra2 and stochastic optical reconstruction microscopy using CellVue® Claret far-red fluorescent membrane dye were applied to study the interactions of EVs with neurons in Alzheimer's disease with a precision of 25 nm<sup>105</sup>. Single molecule localization microscopy has been recently used to image quantum dot-labelled EVs with a spatial resolution of 30 nm<sup>104</sup>. An approach was described for super-resolution technique enabled by a new class of transistor-like, photo-switching polymer dots was described to map of surface proteins on sEVs<sup>117</sup>. Each technique has its strengths and is ideally suited for a certain type of imaging, but also has factors that limit its usefulness.



In our case, site-specific targeting of small-molecule probes to fixed sEVs, STED is a preferable technique to achieve a sub-50 nm resolution<sup>199</sup>. In STED, every increase in optical resolution comes at the expense of more exposures, longer acquisition times and/or higher energy loads, which conversely decreases temporal resolution and increases photobleaching and phototoxicity. Recent years, lanthanide-doped upconversion nanoparticles (UCNPs) has been developed as an important part reaches a 28 nm ( $\lambda/36$ ) optimal resolution in STED-like super-resolution imaging with intense brightness and resistance to photobleaching, and low autofluorescence background<sup>149,201,202</sup>. Here, we present a strategy for super-resolution imaging of single cancer-related EVs (**Fig. 3-1a**), based on Lanthanide-doped EV-targeting Nanoscopic Signal-amplifiers (LENS, made of uniform, bright and photostable UCNPs highly doped with tens of thousands of lanthanide ions) and a STED-like super-resolution microscopy (**Fig. 3-1b**). Prior to our recent ultrasensitive single-EV enumeration platform using UCNPs<sup>203</sup>, we are one step further to investigate the optical performance of LENS doped with different kinds of emitters, the targeting specificity of LENS to tumour epitope (EpCAM) on single sEV, the ability of super-resolution for resolve the portion of single EVs carrying specific number of LENS in a sample and the size related steric hindrance of LENS on single sEV imaging.

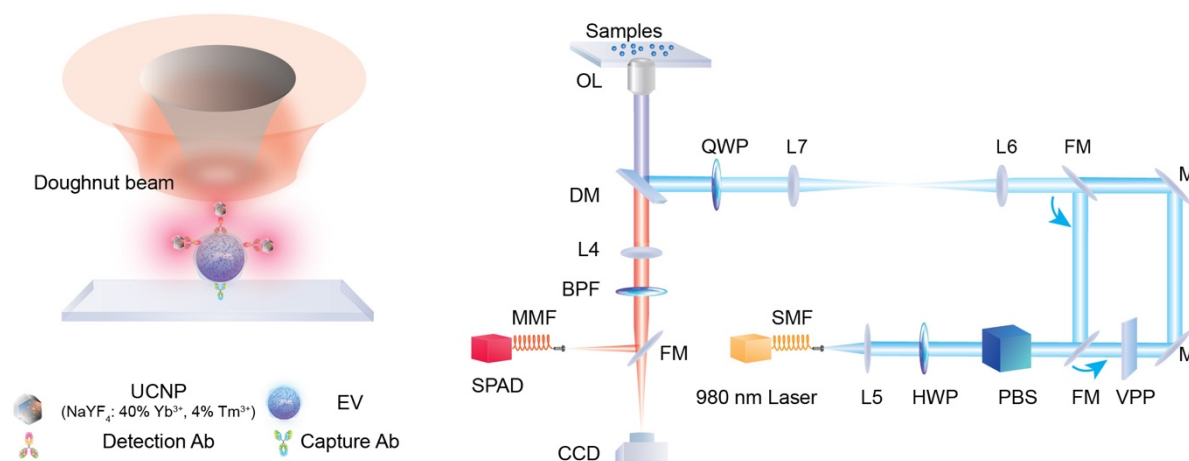


**Figure 3-1 | Schematic illustration of chapter 3.** Left: Super-resolution imaging of single particle on single EVs. Right: Optical setup of the super-resolution microscope for imaging single EVs.

## 3.2 Methods

**3.2.1 Cell transformation.** To produce enough quantities of DNA for transfection experiments, EPCAM (NM\_002354) Human Tagged ORF Clone (RC201989L2, Origene) was transformed into chemically competent cells. Details can be found on reference<sup>204</sup>. The human colorectal adenocarcinoma cell line (HT-29) were seeded in T175 culture flask in Dulbecco's modified eagle medium (DMEM, Gibco, Invitrogen, Waltham, USA) to obtain 50-70% confluence supplemented with 10% fetal bovine serum

(FBS, Gibco, Invitrogen, Waltham, USA) at 37 °C with 5% CO<sub>2</sub>. After 24 h, the cells were transfected with EPCAM (NM\_002354) Human Tagged ORF Clone (15 µg, RC201989L2, ORIGENE) complexed with TurboFectin 8.0 (45 µL, TF81001, ORIGENE) in OptiMEM (4.375 mL, Gibco, Thermo Fisher Scientific). 6 h after transfection, the medium was discarded and changed to Dulbecco's modified eagle medium supplemented with 10% fetal bovine serum. Cells were incubated for 72 before EV isolation.

**3.2.2 EV isolation.** Cell culture medium was centrifuged at 300 × g for 5 min, 2000 × g for 20 min and 10,000 × g for 20 min at 4 °C to remove cells and cellular debris. Supernatant was then filtered using 0.2 µm pore filter and incubated with total exosome isolation reagent (Gibco, Invitrogen, Waltham, USA) overnight with a ratio 2:1 v/v at 4 °C. The medium was centrifuged at 10,000 ×g for 1 h at 4 °C. The EV pellet was suspended in 0.22 µm filtered PBS, stored in -80 °C freezer before use.

**3.2.3 Synthesis of NaYF<sub>4</sub>:40%Yb<sup>3+</sup>,4%Tm<sup>3+</sup> nanocrystals.** NaYF<sub>4</sub>:40%Yb<sup>3+</sup>,4%Tm<sup>3+</sup> nanocrystals were synthesized according to our previously reported method<sup>149</sup>. For the synthesis of NaYF<sub>4</sub>:40%Yb<sup>3+</sup>,4%Tm<sup>3+</sup> : 1 mmol RECl<sub>3</sub> (RE=Y, Yb, Tm) with the molar ratio of 56:40:4 were mixed with 6 ml oleic acid (OA) and 15 ml 1-Octadecene in a three-neck flask. The solution was heated to 160 °C under flowing argon for 30 min to obtain a clear solution and was cooled down to room temperature. Then, 5 mL methanol solution of NH<sub>4</sub>F (4 mmol) and NaOH (2.5 mmol) were quickly injected into the flask and stirred for 30 min at room temperature. Subsequently, the mixture was heated to 80 °C under flowing argon for 20 min to remove methanol, and was further heated to 300 °C for another 90 min. The solution was cooled down to room temperature, and nanocrystals were precipitated by ethanol. The nanoparticles were washed thrice with cyclohexane, ethanol and methanol, respectively. The final products were re-dispersed in cyclohexane with the concentration of 20 mg mL<sup>-1</sup>. Synthesis of NaYF<sub>4</sub>:20%Yb<sup>3+</sup>,2%Er<sup>3+</sup> is same as Methods 2.2.7.

**3.2.4 Fabrication of LENS.** Same as Method 2.2.10.

**3.2.5 GFP-LENS colocalization procedure.** Cells and EVs from transfected HT29 cells were imaged by A1R confocal microscope (Nikon). Vesicles were detected as light diffraction limited GFP fluorescent spots. The GFP-LENS colocalization procedure is the same as Methods 2.2.13, except all the procedures are hidden from light.

**3.2.6 Dual-LENS assay procedures.** Antibodies: anti-human CD9 Monoclonal Antibody (eBioSN4 (SN4 C3-3A2), ThermoFisher, USA), biotinylated anti-human CD326 (EpCAM, ThermoFisher, USA), biotinylated anti-human CD44 (IM7, Biolegend, Australia). In brief, after surface modification, a 96-

well glass bottomed plate (Swissci, Zug, Switzerland) was coated with anti-CD9 (10  $\mu\text{g}/\text{mL}$ ) at 4  $^{\circ}\text{C}$  overnight. All subsequent steps were carried out at room temperature. The microtiter plate was then blocked with blocking buffer (2% Casein in Tris-buffer) for 1 h. On each well, 100  $\mu\text{L}$  of the sEVs dilution was incubated for 2 h. After four washing steps (0.1% Casein in Tris-buffer), the microtiter plate was incubated with biotin-EpCAM antibody (1  $\mu\text{g}/\text{mL}$ ) for 1 h. After four washing steps (0.1% Casein in Tris-buffer), 100  $\mu\text{L}$  of  $\text{Tm}^{3+}$ -LENS (50  $\mu\text{g}/\text{mL}$ ) was applied to each well for 1 h and was washed four times. The microtiter plate was then incubated with biotin-CD44 antibody (1  $\mu\text{g}/\text{mL}$ ) for 1 h. After four washing steps (0.1% Casein in Tris-buffer), 100  $\mu\text{L}$  of  $\text{Er}^{3+}$ -LENS (50  $\mu\text{g}/\text{mL}$ ) was applied to each well for 1 h and was washed four times. The plate was ready for imaging.

**3.2.7 Deconvolution methods for wide-field imaging.** Deconvolution was followed Manual “Parallel spectral deconvolution”, “Diffraction PSF”, “Deconvolution Lab” in ImageJ.

**3.2.8 Super-resolution setup.** Purpose-built multi-photon NIR super-resolution microscopy was built for super resolution imaging. According to activator doping enhanced resolution reported by our group previously<sup>202</sup>. The setup is shown in **Figure 3-1**. A single-mode fibre-coupled 980 nm diode laser (BL976-PAG900, controller CLD1015, maximum output power 900 mW, Thorlabs, Newton, USA) was used as the excitation source. After collimation, the excitation beam was transmitted through the first half-wave plate (HWP, WPH05M-980, Thorlabs) and a polarized beam splitter (PBS, CCM1-PBS252/M, Thorlabs, Newton, USA). Then we can precisely adjust the excitation power by rotating HWP electronically. The vortex phase plate is used to generate a doughnut-shaped point spread function (PSF) at the focal plane. The 4f optical system (L3 and L4) was used to transfer the image plane into the back aperture of the objective lens. The excitation beam was transmitted through a shortpass dichroic mirror (T875spxrxt, Chroma, Bellows Falls, USA), and focused through a high numerical aperture objective (UPlanSApo, 100 $\times$ /1.40 oil, Olympus, Japan) to the sample slide. The quarter-wave plate (QWP, WPQ05M-980, Thorlabs, Newton, USA) was adopted to transform the excitation beam from linear polarization to circular polarization to obtain optical super-resolution images in the excitation beam. Photoluminescence signal from the sample was collected by the same objective and split from the excitation beams by the dichroic mirror. Before being coupled into a multimode fibre (MMF, M24L02, Thorlabs, Newton, USA), the emission signals were filtered by bandpass (BPF, ET805/20M, Chroma, Bellows Falls, USA) or short pass filter (SPF, FF01-842/SP-25, Semrock, Rochester, USA) and coupled into a multi-mode fibre (MMF, M24L02, Thorlabs, Newton, USA). Then the detection part was connected to a single-photon counting avalanche photodiode (APD, SPCM-AQRH-14-FC, Excelitas,

Waltham, USA) which can be time-gated by Labview program. The MMF could also be switched to a spectrometer (Shamrock 193i Spectrograph, Andor, South Windsor, USA) equipped with an EMCCD detector (iXon Ultra, Andor, South Windsor, USA).

### 3.3 Results

#### 3.3.1 Optical performance evaluation of LENS doped with different kinds of emitters

It has been demonstrated that most  $\text{Ln}^{3+}$  ions can exhibit an upconversion process. Among them,  $\text{Er}^{3+}$ ,  $\text{Tm}^{3+}$  ions, with a ladder-like metastable energy level structure, are commonly used emitters in UCNPs. To investigate the effect of emitters on their optical performance, we synthesized  $\text{Er}^{3+}$ -doped LENS ( $39.9 \text{ nm} \pm 2.8 \text{ nm}$ , **Fig. 3-2a**) and  $\text{Tm}^{3+}$ -doped LENS ( $39.3 \pm 1.6 \text{ nm}$ , **Fig. 3-2b**). As shown in **Figure 3-3a**,  $\text{Er}^{3+}$ -doped LENS generate upconverted green and red emission at 550 nm and 650 nm, originating from the transitions  ${}^2\text{H}_{11/2}/{}^4\text{S}_{3/2} \rightarrow {}^4\text{I}_{15/2}$  and  ${}^4\text{F}_{9/2} \rightarrow {}^4\text{I}_{15/2}$ , respectively.  $\text{Tm}^{3+}$ -doped LENS have three main upconversion band at 450, 650, and 800 nm, generated by the transitions of  ${}^1\text{D}_2 \rightarrow {}^3\text{F}_4$ ,  ${}^1\text{G}_4 \rightarrow {}^3\text{F}_4$ , and  ${}^3\text{H}_4 \rightarrow {}^3\text{H}_6$ , respectively.

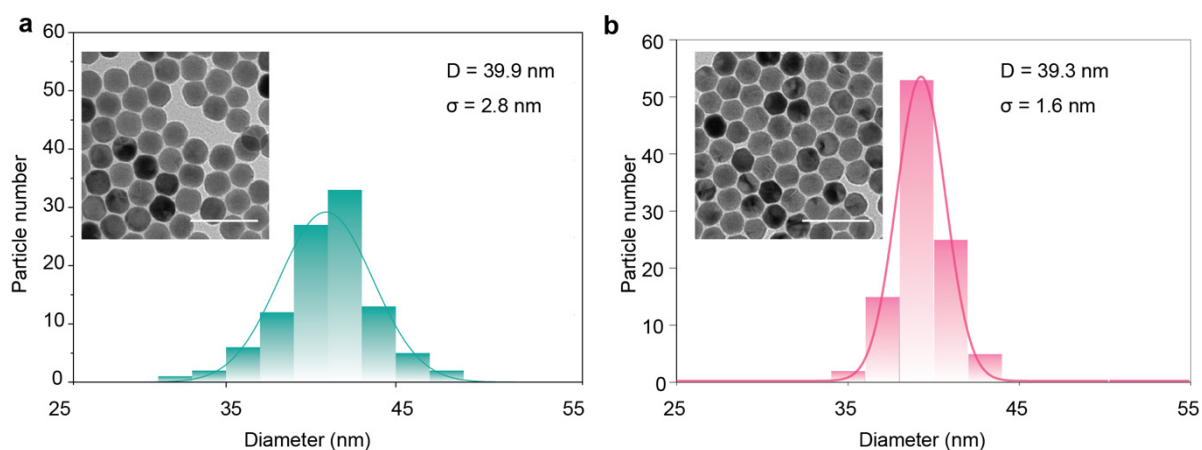


**Figure 3-2. TEM images and size distribution histograms of the synthesized UCNPs. (a)**  $\text{NaYF}_4:20\%\text{Yb}^{3+}, 2\%\text{Er}^{3+}$ . **(b)**  $\text{NaYF}_4:40\%\text{Yb}^{3+}, 4\%\text{Tm}^{3+}$ . Insert: TEM images, scale bar:100 nm. D is the diameter of nanoparticles.  $\sigma$  is the standard deviation. 100 particles were measured for the size distribution.

The similar size of  $\text{Er}^{3+}$ -doped LENS and  $\text{Tm}^{3+}$ -doped LENS guarantees the same amount of optical emitters, which allows us to directly compare their brightness and nonlinear properties in single LENS. As the brightness of the LENS is strongly power-dependent, we measured the brightness of different kinds of LENS under different excitation powers from 0.01 mW to 100 mW (**Fig. 3-3b**). The result presents that  $\text{Er}^{3+}$ -doped LENS are brighter than  $\text{Tm}^{3+}$ -doped LENS under low excitation power (below 5 mW, **Table 3-2**), whereas  $\text{Tm}^{3+}$ -doped LENS are brighter than  $\text{Er}^{3+}$ -doped LENS under relatively high excitation power. Quantitatively, the intensity of  $\text{Er}^{3+}$ -doped LENS is around 141 counts under the

excitation power of 0.01 mW, which is 9.4 times higher than that of  $\text{Tm}^{3+}$ -doped LENS (15 counts). These results indicate that  $\text{Er}^{3+}$ -doped LENS have better brightness due to its high upconverting luminescence under low power excitation.

**Table 3-2.** The upconversion emission intensities obtained from single  $\text{Er}^{3+}$ -doped and  $\text{Tm}^{3+}$ -doped LENS under different excitation power (below 5 mW).

Power (mW)	$\text{Er}^{3+}$ (counts)	$\text{Tm}^{3+}$ (counts)
0.01	141	15
0.05	753	93
0.1	1365	404
0.5	3517	1966
1.0	4763	3201
5.0	6177	4943

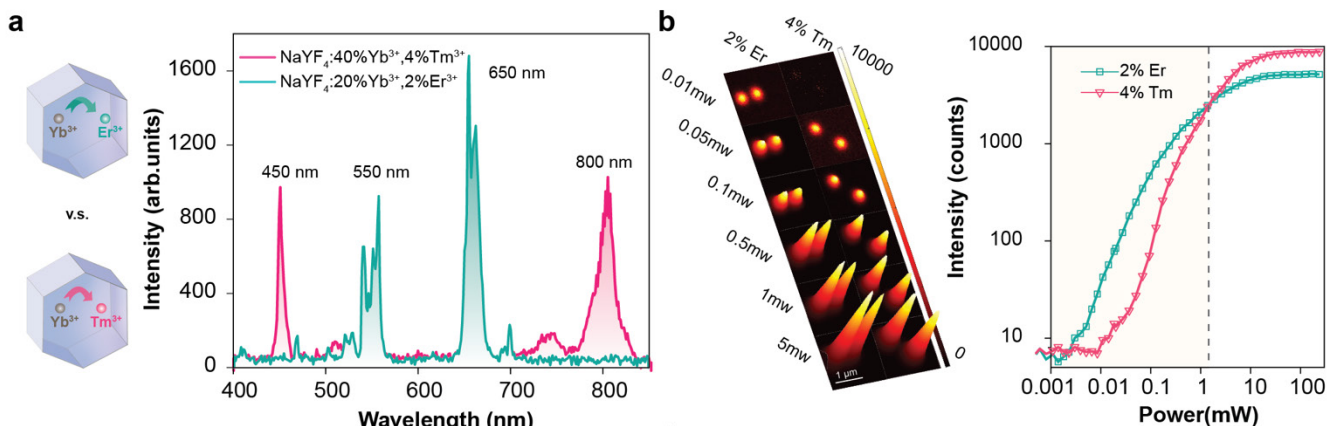


**Figure 3-3.** The intensity properties of  $\text{Er}^{3+}$ -doped and  $\text{Tm}^{3+}$ -doped LENS. (a) The upconversion emission spectra of  $\text{Er}^{3+}$ -doped LENS and  $\text{Tm}^{3+}$ -doped LENS. (b) Left: Confocal images of  $\text{Er}^{3+}$ -doped LENS and  $\text{Tm}^{3+}$ -doped LENS under different excitation power. Right: Total power-dependent upconversion emission intensity obtained from single  $\text{Er}^{3+}$ -doped and  $\text{Tm}^{3+}$ -doped LENS.

Then, we investigated the properties of different emitters for super-resolution imaging. The experimentally measured PSF ( $h_{exp}$ ) of super-resolution nanoscope is the convolution between the  $h_{eff}$  and the spatial profile ( $h_{LENS}$ ) of LENS, defined as equation (3-1):

$$h_{exp} = h_{eff} \times h_{LENS} \quad (3-1)$$

The deconvolution process on  $h_{exp}$  results in a measured  $h_{eff}$ , in which the FWHM of the dip represents the resolution of nanoscopy. The FWHM of the dip at the measured PSF of a single LENS defines the experimental resolution.

The resolution of nanoscopy at a specific excitation power density is primarily determined by the emission saturation curve of LENS. There are three features from the curve affecting the resolution, according to the equations (1-2, 1-3, 1-4, 1-5 and 3-1): 1, The saturation intensity point ( $I_s$ ); 2, The power point ( $I_{MAX}$ ); 3, The onset value of the curve. Lower values of  $I_s$  and/or  $I_{MAX}$  shrink the size of a dark spot in the doughnut emission PSF, thereby enhancing the resolution. The more significant onset of the curve offers a lower depth of the PSF to yield a better resolution.

The emission spectra of the UCNP s were measured on a lab-built confocal microscope. From the fluorescence spectrum profiles of UCNP s under continuous-wave 980 nm excitation laser in **Figure 3-4**. We select two prominent emission peaks at 550 nm and 650 nm of Tm-doped UCNP s and two main emission peaks at 455 nm and 800 nm of Er-doped UCNP s, to investigate the effect of emitters on the imaging resolution.

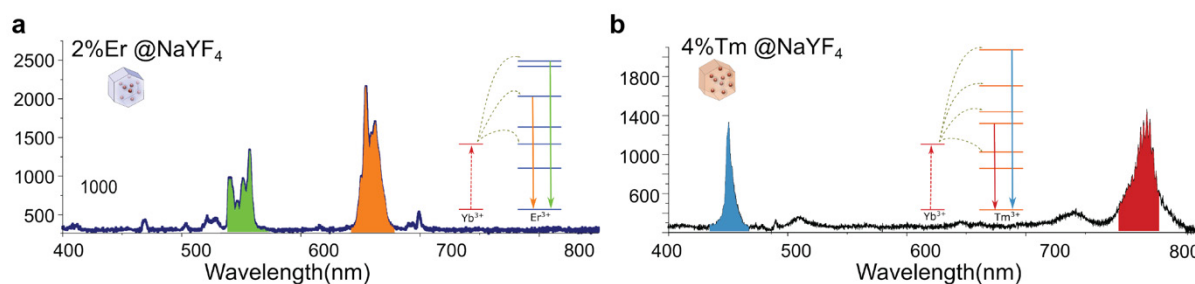


**Figure 3-4 | The upconversion emission spectra from LENS.** (a) 2% Er<sup>3+</sup> doped LENS (size: 40 nm). (b) 4% Tm<sup>3+</sup> doped UCNP s (size: 40 nm).

According to the equations above, the lower values of  $I_s$  and  $I_{MAX}$ , sharp curvature in the onset favour achieving higher resolution. For Er-doped LENS, according to the emission saturation curves in **Figure 3-5a**, 650 nm emission peak improve the resolution than 550 nm emission peak. It is hard for UCNP s in 550 nm emission peak to achieve higher resolution even by increasing the excitation power. For Tm-doped LENS, according to the emission saturation curves in **Figure 3-5b**, 800 nm emission peak improve resolution than 455 nm emission peak. Compared with Er-doped LENS, Tm-doped UCNP s have sharper curvature in the onset of the saturation curves and can quickly reach the saturated point with lower values of  $I_s$  and  $I_{MAX}$  (**Fig. 3-5c**).

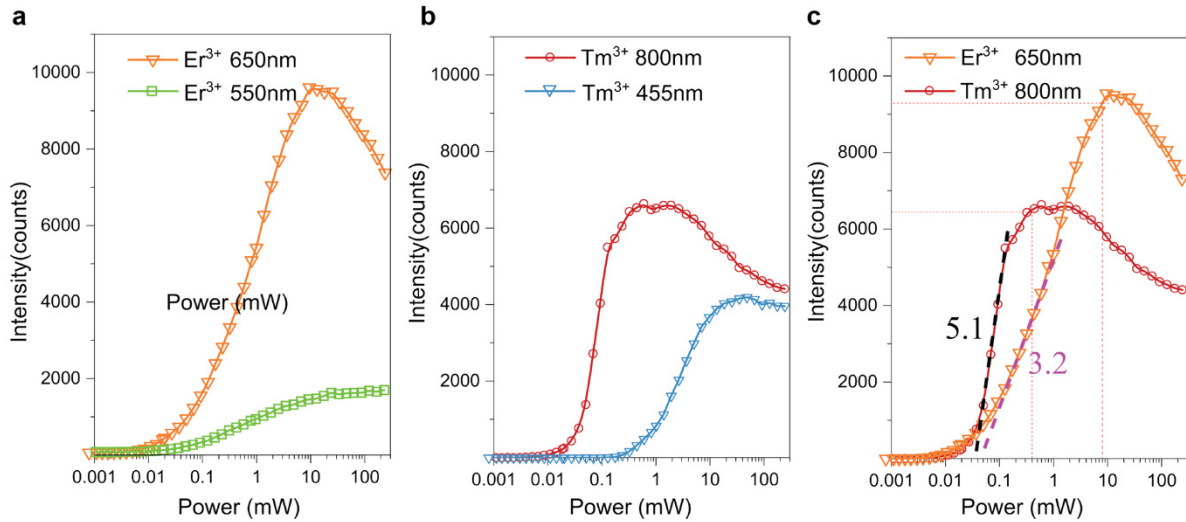


**Figure 3-5 | Optical emission wavelength to achieve high resolution under same excitation power.**

(a) Emission saturation curves obtained for a single UCNP at 650 nm and 550 nm emission. (b) Emission saturation curves obtained for a single UCNP at 800 nm and 455 nm emission. (c) Comparison of Emission saturation curves obtained for a single UCNP at 650 nm (Er-doped LENS) and 800 nm emission (Tm-doped LENS).

A further investigation of the nonlinear properties on the resolution of super-resolution is shown in **Figure 3-6**. We compared Er-doped LENS (650 nm emission) at 5 mW, 15 mW, 25 mW, and 40 mW laser power, and Tm-doped LENS (800 nm emission) at 1 mW, 5 mW, 10 mW, and 18 mW laser power. As a result, the dip size in the Tm-doped LENS is smaller than the Er-doped LENS at the same laser power. The comparison results in **Figure 3-6c** indicated that Er-doped UCNP require higher power to achieve the same resolution as that for Tm-doped UCNP. With that, we chose Tm-doped UCNP for super-resolution imaging. Thus, detecting the signal at 800 nm from Tm-doped UCNP helps achieve high resolution with low excitation power. The comparison results validate the Tm-doped LENS can provide better nonlinear response than Er-doped LENS, which can help achieve higher resolution.

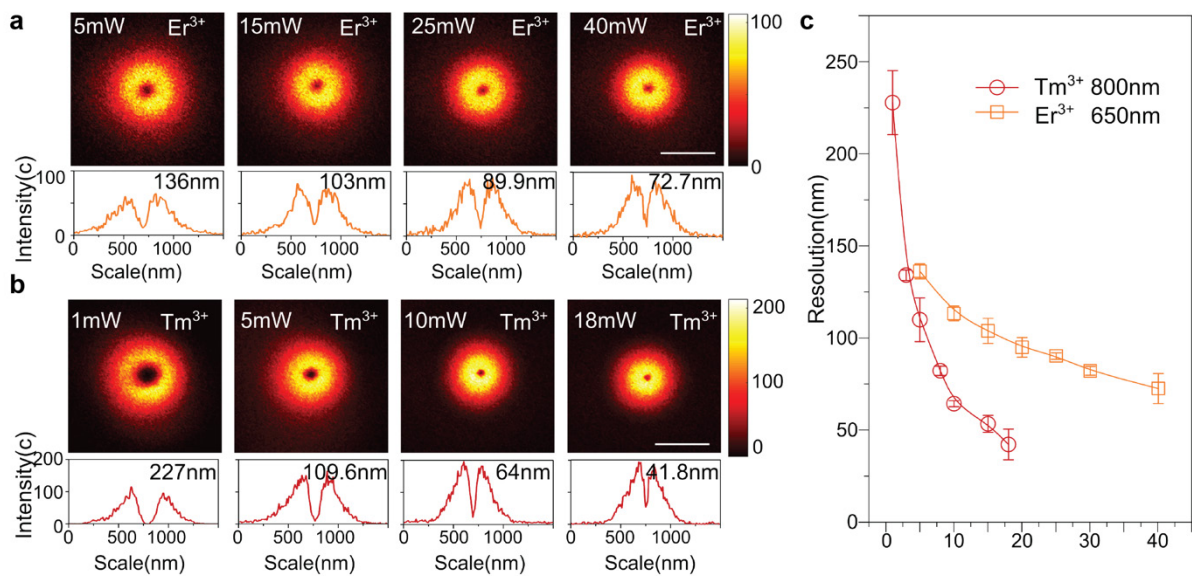


**Figure 3-6 | The nonlinear properties of LENS.** (a) Negative images of single particles (Er-doped LENS) under different excitation power and its corresponding cross-section profile. (b) Negative images of single particles (Tm-doped LENS) under different excitation power and its corresponding cross-section profile. (c) Super-resolution scaling  $\Delta r$  of UCNP as a function of excitation power (intensity). Error bars indicate standard deviations from line profiles of several measurements. Pixel dwell time, 3 ms; pixel size, 10 nm. Scale bar is 500 nm.

### 3.3.2 Co-localization and comparison of EpCAM-mGFP EV with LENS

To further confirm whether LENS was truly targeting the EpCAM epitope on EVs, we conducted colocalization experiments. Firstly, HT29 cells were transfected with an mGFP-tagged EpCAM plasmid. As expected, mGFP-tagged EpCAM were subsequently integrated into EVs. Then LENS assay was conducted to see the colocalization between LENS spot and GFP spot under wide-field imaging.

Epithelial cell adhesion molecule (EpCAM, also known as CD326) represents a good candidate for an EV biomarker as it is overexpressed in many human adenocarcinomas and squamous cell carcinomas, and this expression closely correlates with the epithelial-mesenchymal transition regulating tumor invasion and metastasis<sup>205</sup>. We transiently expressed N-terminal green fluorescent protein (GFP) fusions of EpCAM in HT29 cells (**Fig.3-7**), thereby oriented to the cytosolic side of the EV membrane. The coding sequences were fused to the GFP open reading frame (ORF) and cloned into an expression vector under the control of the cytomegalovirus promoter. The GFP encoding vectors were transiently overexpressed in HT29 cells using transfection for 6 h followed by media change. To examine whether



the EpCAM-mGFP could be successfully expressed in HT29 cells. Cells were imaged by 24-h, 48-h, and 72-h.

The mGFP signal allows us to directly evaluate the expression of EpCAM within HT29 cells. The fluorescent signals of HT29 cells were observed at 24-h, 48-h and 72-h timepoints after transfection. We found that EpCAM-mGFP can be successfully expressed from the plasmid and localized to the surface of cells (**Fig. 3-7c**). Moreover, we witnessed the effective increase of signal intensity in 72-h period.

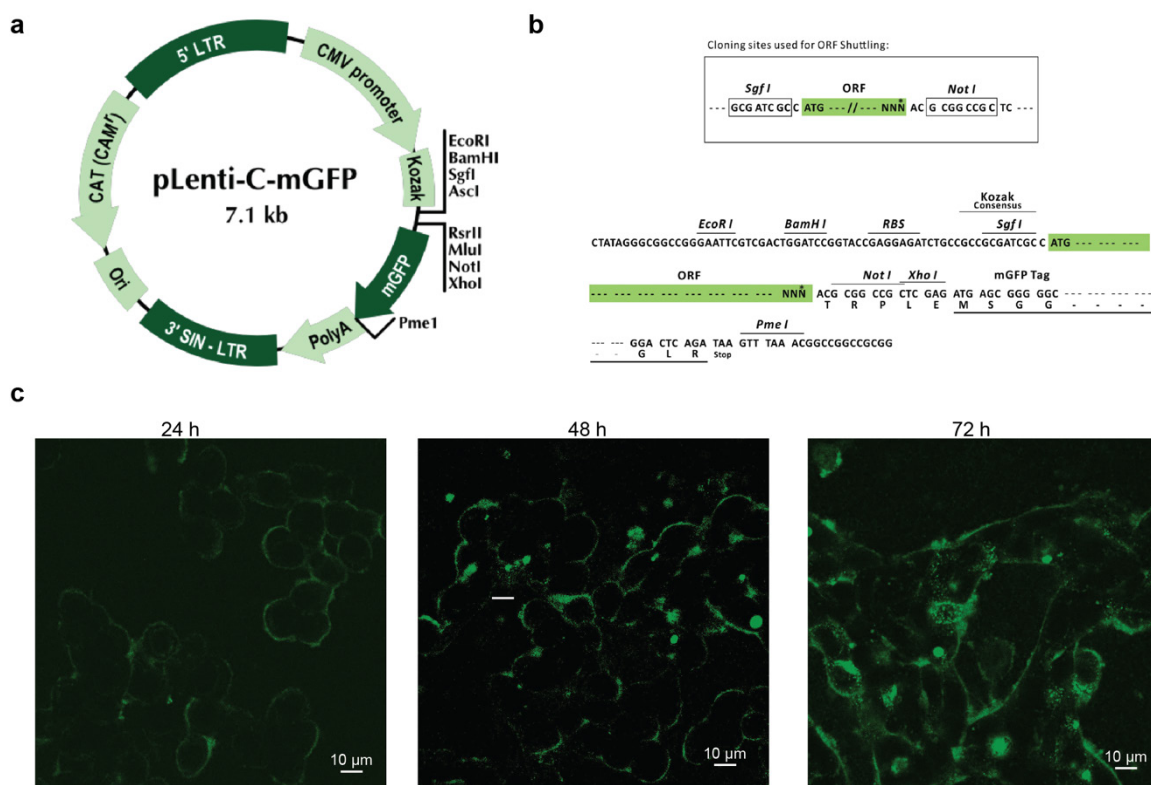


**Figure 3-7 | Overexpression of mGFP-tagged EpCAM in HT29 parental cells.** (a) Lentiviral vectors. (b) Cloning sites are used for ORF shuttling. (c) HT29 cells transfected with EpCAM-mGFP plasmid after 24h, 48, 72h imaged by A1R confocal microscope.

To further confirm whether EpCAM-mGFP were truly integrated into EV compartments. We transiently expressed the GFP-tagged EV EpCAM in HT29 cells and isolated the EVs via commercial precipitation kits by 48-h or 72-h post-transfection of cells. The expression of EpCAM-mGFP in EVs was validated by confocal imaging. EVs were detected as light diffraction-limited GFP fluorescent spots. We found that the fluorescence signal of isolated EVs become stronger at 72-h than 48-h post-transfection (**Fig. 3-8**). Please note that the green fluorescence may represent individual particles or their aggregates, which may not correlate to their true size due to the spatial resolution limit of the fluorescence or confocal microscope.

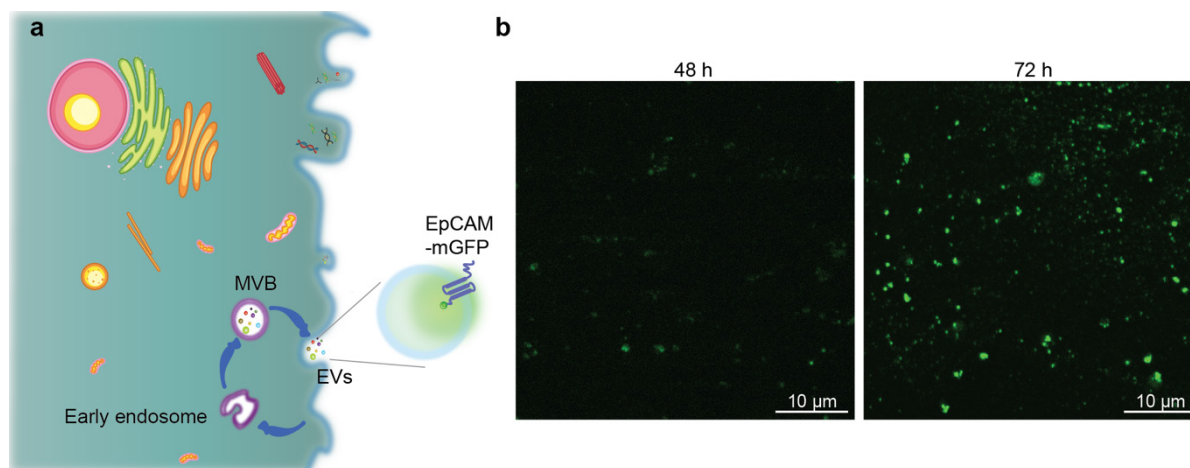


**Figure 3-8 | Overexpression of EpCAM-mGFP in HT29-EVs.** (a) Illustration of EpCAM-mGFP intergrates into EV compartments. (b) Fluorescent images of the isolated EpCAM-mGFP EV by 48-h and 72-h post-transfection.

To further confirm whether LENS was truly targeting to the EpCAM epitope on EVs, we conducted colocalization experiments under wide-field microscope imaging. To validate the approach, The EpCAM-mGFP EVs were first captured by tetraspanin protein (CD9, CD63 and CD81), and subsequently detected using biotinylated EpCAM antibodies and LENSs (**Fig. 3-9a**). The original status of EpCAM-mGFP EVs and LENS prior to the assay are as shown in **Figure 3-9b**. After LENS assay, the EpCAM-mGFP EVs were detected as light diffraction-limited fluorescent spots under 488 nm excitation. The LENS was detected as light diffraction-limited fluorescent spots under 980 nm excitation. Then the co-localization was quantified based on the overlap of the spot spread functions in the two fluorescent channels to derive the GFP and LENS double-positive EVs (**Fig. 3-9c**). Through imaging, a population of double-positive spots confirm a certain degree of vesicle co-localization (~65%).

It is well noting that bleaching and loss of fluorescence intensity for GFP may happen when prolonged exposure to fluorescent light, whereas LENS are also far more resistant to photobleaching than fluorophores and quantum dots. This offers opportunities to create stable detection systems and improved signal quantification in diagnostic platforms.

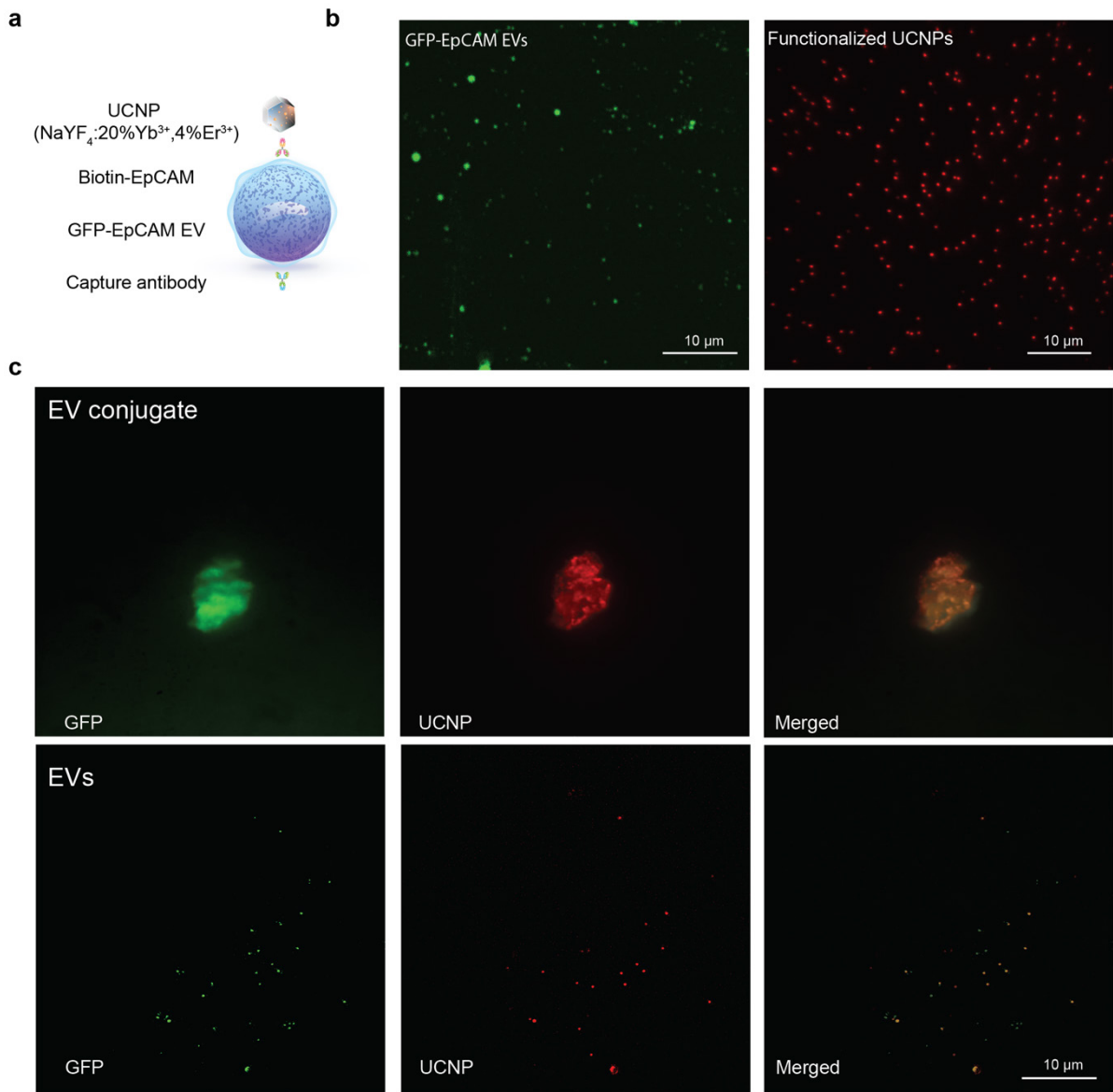


**Figure 3-9 | Co-localization of EpCAM-mGFP EV with LENS.** Red: EpCAM-UCNP; Green: EpCAM-GFP. Scale bar, 10  $\mu\text{m}$ . (a) Illustration of co-localize EpCAM-mGFP EV with LENS. (b) Wide-field images of EpCAM-mGFP EV and LENS prior to co-localize. (c) mGFP/LENS double labelled EpCAM-EVs imaged by widefield fluorescence imaging, confirming a high degree of co-localization. Green, GFP; red, LENS; yellow, double positive.

We conclude that LENS assay can be successfully used to target EVs with high specificity and can be used for following super-resolution experiments.

### 3.3.3 Single EV imaging by super-resolution microscope

Functionalized 4%Tm-doped LENS, the low-power coherent excitation at 980 nm can easily saturate the metastable level that emits NIR emission (800 nm,  $^3H_4 \rightarrow ^3H_6$  transition), so that the sharp nonlinear power-dependent emission curve can be used to super resolve the sub-diffraction-limit images.

Super-resolution imaging techniques depend on high photon intensities, complicating detection of smaller EVs and increasing the risk of photobleaching and phototoxicity. We first investigate the stability of LENS for super-resolution imaging. Time series upconversion confocal images were recorded for the same sample area under continuous laser excitation and scanning for 220 min (**Fig. 3-10**). The results indicated that the LENS is stable enough to enable super-resolution imaging.

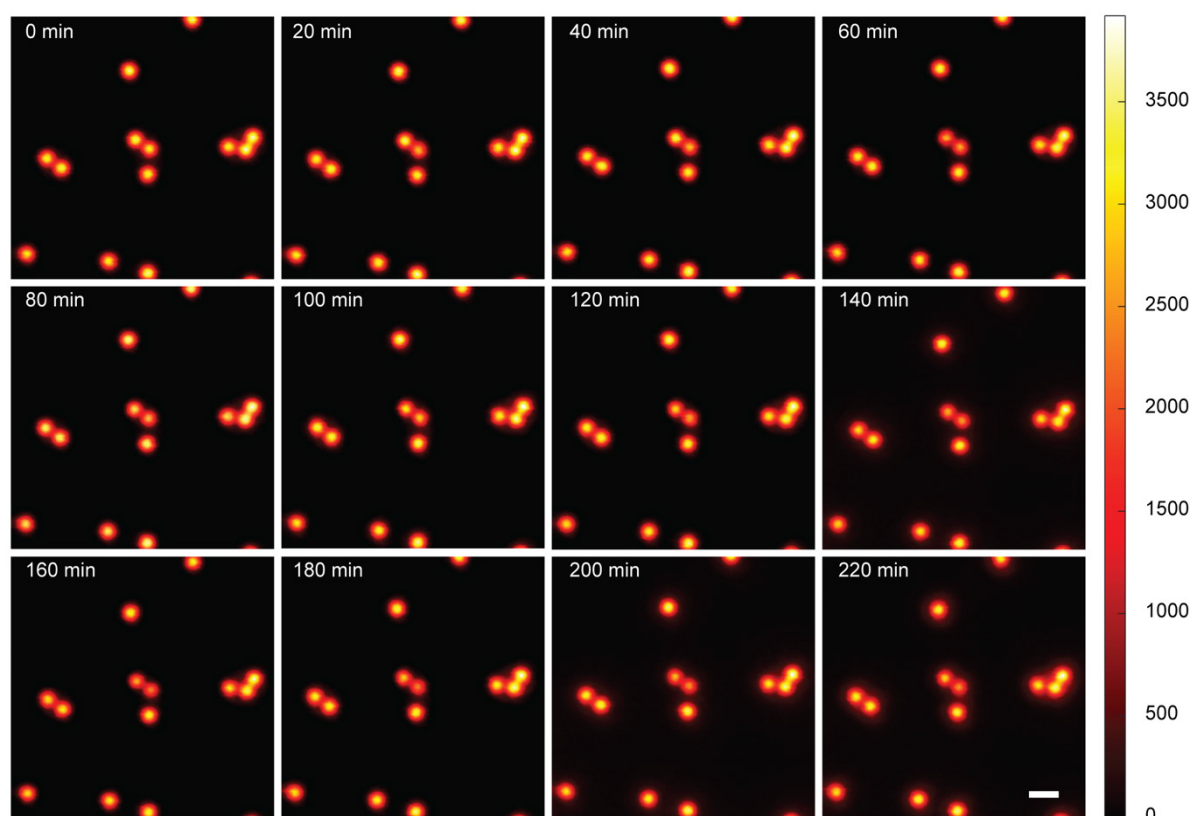


**Figure 3-10 | Time-series upconversion confocal images recorded for the same sample area under continuous laser excitation and scanning.** The sample slide contains 39.3-nm  $\text{NaYF}_4:40\%Yb^{3+},4\%Tm^{3+}$ . The 800 nm upconversion emission photon count is colour coded. The 980 nm laser power at the objective back aperture were 37.86 mW. Scan step: 50 nm, pixel dwell time: 50 ms, scale bar: 1  $\mu\text{m}$ .

For generating a super-resolution image of the single nanoparticle by nanoscopy, we employ a tightly focused doughnut-shaped excitation beam to scan across a sample containing UCNPs (**Fig. 3-11a**). Only when a single UCNP sits in the middle of the doughnut beam, the nanoscopy generates a negative contrast.

To demonstrate the super resolution utility of LENS, **Figure 3-11b** shows two typical areas of EV clusters (in blue and green) in a confocal image, which does not provide sufficient resolution to tell the number or position of LENS on single EVs. In contrast, the super resolution image clearly resolves single LENS from the clusters (**Fig. 3-11c**), e.g. LENS separated by 41.9 nm and 46.7 nm, respectively in **Fig. 3-11d** and **3-11e**.

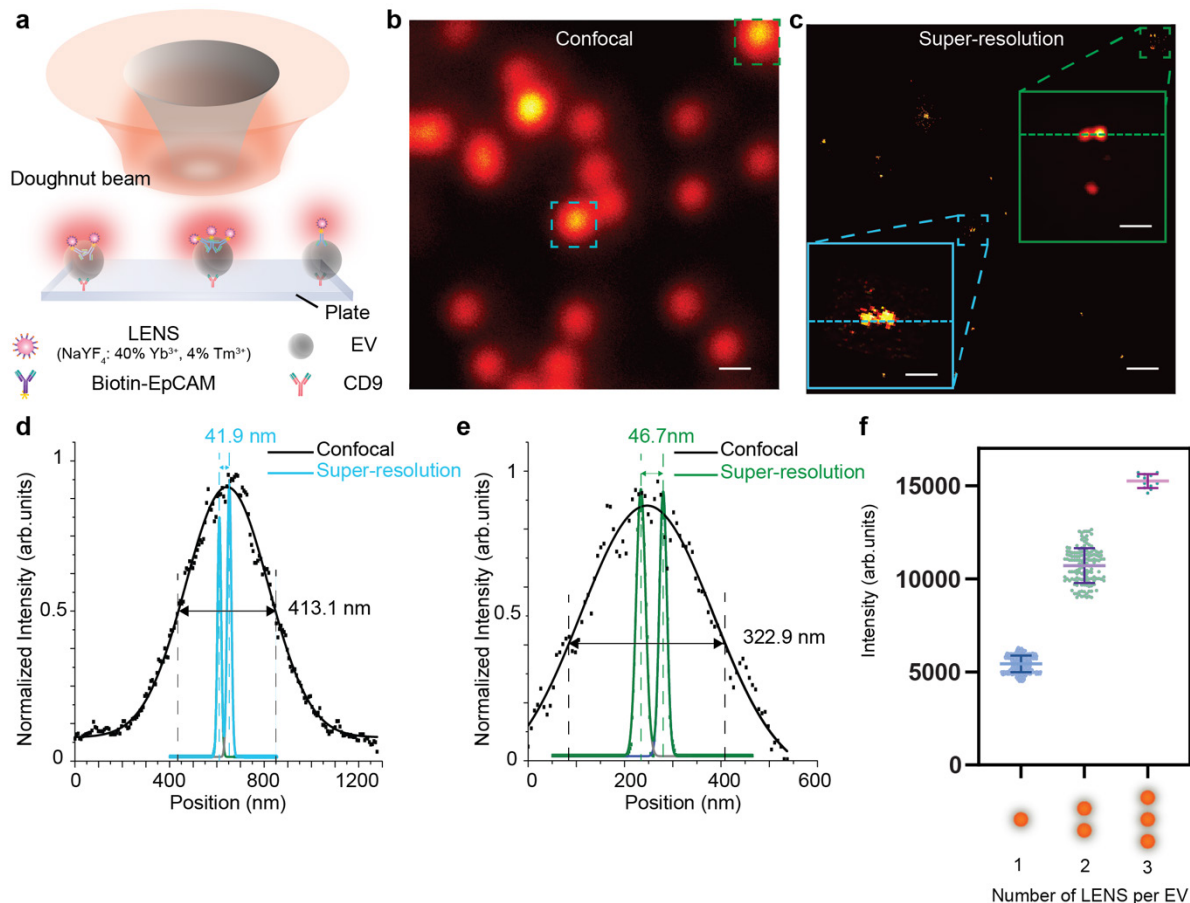


**Figure 3-11 | Super-resolution imaging of LENS on single EVs.** (a) Scanning a doughnut excitation beam to resolve LENS clusters on single EVs. (b) Confocal microscopic image of LENS clusters. Scale bar: 500 nm. (c) Super-resolution image of the same LENS clusters as those in (b). Blue and green dashed boxes mark an area containing closely spaced LENS resolved in super-resolution microscopy, but not in confocal imaging. Scale bars: 500 nm for the main image and 100 nm for the insets. (d,e) Line profiles of the LENS clusters from the confocal image and super-resolution image. Two clusters of doublet LENS can be resolved with the LENS particles separated by 41.9 nm and 46.7 nm, respectively. Pixel dwelling time: 1 ms. Scanning step size: 10 nm. (f) Dependence of the averaged luminescent intensity of bright signal spots on the number of LENS per EV ( $n = 100$ ), showing the three populations of single EVs

carrying one, two, or three LENS. Single-particle intensity:  $5427 \pm 450$  ( $n = 469$ ), Double particles intensity:  $10703 \pm 9376$  ( $n = 141$ ), Triple particle intensity:  $15245 \pm 378$  ( $n = 12$ ).

The super-resolution results allow us to further correlate the number of LENS with their luminescence intensity. **Figure 3-11f** shows that the luminescence intensities of triplet and doublet LENS are three times and twice that of single LENS. The linear correlation also indicates that the luminescent intensity of bright spots in confocal imaging can be directly used to infer the number of LENS on individual EVs. With this capability, we can resolve the portion of single EVs carrying a specific number of LENS in a sample. For instance, in a single testing sample from HT29 cells, there are 75.47% of singlet LENS, 22.64% of doublet LENS, and 1.89% of triplet LENS on single EVs (**Fig. 3-12**).

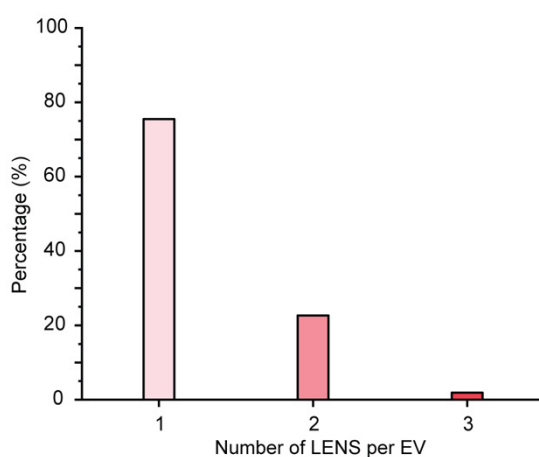


**Figure 3-12 | The percentage of the number of LENS per EV resolved by super-resolution imaging in a single testing sample.** There are 75.47% of singlet LENS, 22.64% of doublet LENS, and 1.89% of triplet LENS on single EVs.

Moreover, LENS approach allows us to further push the resolution to resolve the cluster of LENS on single EVs by employing super-resolution nanoscopy<sup>149,201,202</sup>, so that the number and intensity of LENS on single EVs can be used as new metrics for quantification.

### 3.3.4 Future direction of the technique - Size related steric hindrance

Size is important to super-resolution; not only the labelling density needs to be high to achieve a resolution of tens of nanometer, the ‘disturbance’ on the nanoscale must also allow higher densities to be deduced so that true biological topology can be accurately dissected. Owing to brightness issues, the majority of currently developed UCNPs are relatively large (around 20–50 nm)<sup>178</sup>. It has been challenging to design and fabricate highly doped sub-10 nm UCNPs with emission output comparable with that of quantum dots and organic dyes. To investigate the maximum number of minimum sized LENS for single sEV super-resolution imaging, we firstly calculated the theoretical number of LENS on

the surface of EV. Assuming EV is a large sphere, LENS is a small sphere, surrounding a large sphere (radius is  $R$ ) with smaller spheres (radius is  $r$ ) can be viewed as packing disks on the surface (Fig. 3-13a), which is a heavily studied problem known as the Thomson problem<sup>206</sup>.

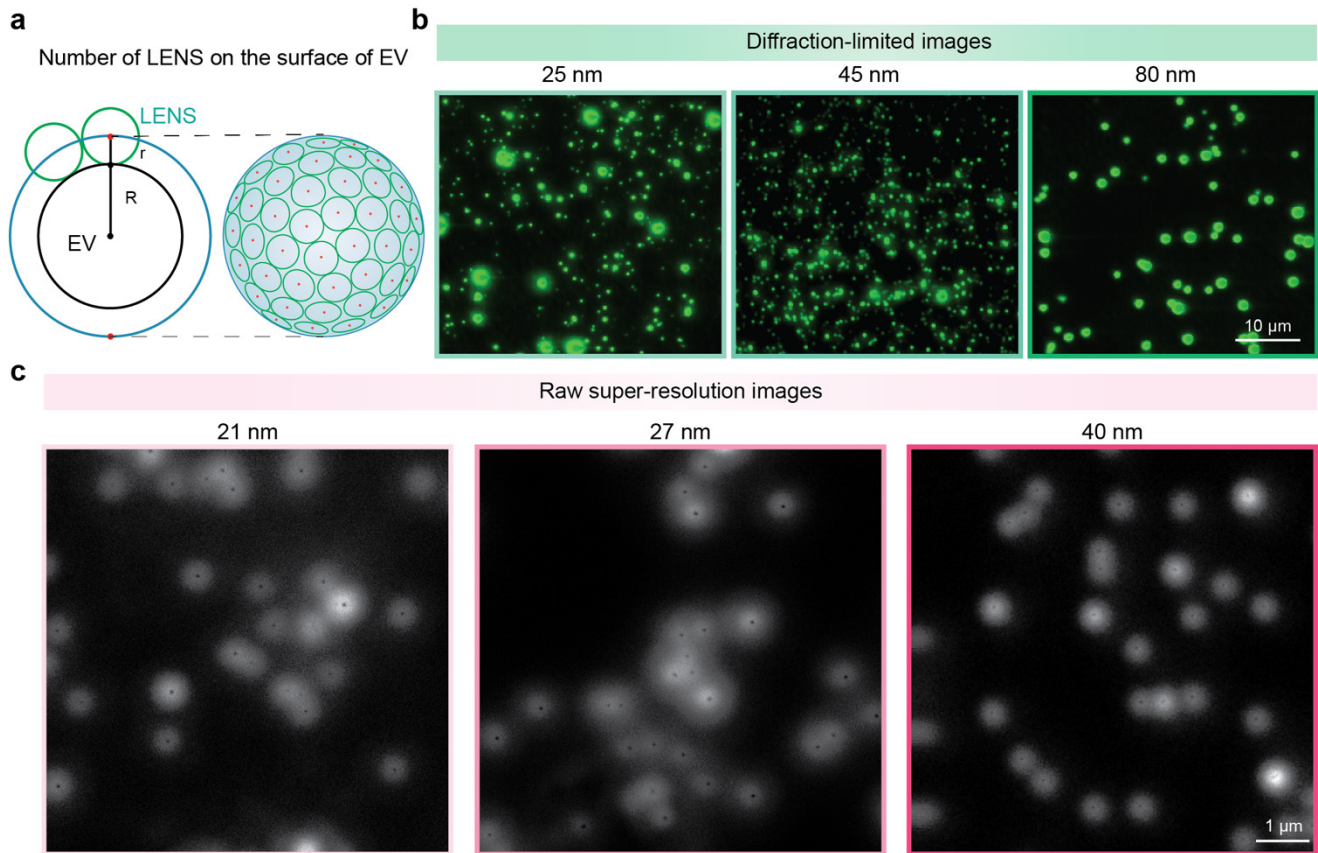


**Figure 3-13. Size related steric effects of LENS.** (a) Illustration of the theoretical number of LENS on the surface of EV. (b) Diffraction-limited images of CD9 EpCAM double positive EVs labelled by 25 nm, 45 nm, and 80nm  $\text{Er}^{3+}$ -doped LENS. (c) The raw super-resolution images of  $\text{EpCAM}^+$  EVs labelled by 21 nm, 27 nm and 42 nm  $\text{Tm}^{3+}$ -doped LENS. Pixel dwell time: 6000  $\mu\text{s}$  (21 nm), 5000  $\mu\text{s}$  (27 nm), 5000  $\mu\text{s}$  (42 nm); Excitation power: 250 mW.

Assuming the area of large sphere (Radium,  $R + r$ ) is surrounded by small sphere (Radium,  $r$ ),

$$\text{Area of Large sphere} = 4\pi(R + r)^2 \quad (3-2)$$

$$\text{Area of packing disk} = \pi r^2 \quad (3-3)$$

In three-dimensional space, there are three packing types for identical spheres: cubic lattice, face-centred cubic lattice, and hexagonal lattice. *Carl Friedrich Gauss* proved in 1831 that hexagonal packing is the densest possible amongst all possible lattice packings using the following equation<sup>207</sup>,

$$\text{Density} = \frac{\pi}{3\sqrt{2}} = 74\% \quad (3-4)$$

Whilst the best possible packing density is about 74%, the maximum number of small spheres on large sphere is calculated as,

$$N_{max} = \frac{4\pi(R+r)^2}{\pi r^2} \times 74\% \quad (3-5)$$

In view of the proposed hypothesis above, smaller size of LENS is better for efficient labelling with less steric hindrance. However, larger size of LENS is better for optical detection. To confirm the hypothesis is working with sub-100 nm LENS, we synthesised LENS with size range from 20 nm to 80 nm (**Fig. 3-14**). We then imaged sEVs labelled by 80 nm, 42 nm and 25 nm Er<sup>3+</sup>-doped using diffraction-limited imaging. We observed the expected increase in binding site quantity (**Fig. 3-13b**). Furthermore, to reach the smallest size of LENS for super-resolution imaging, we synthesised the Tm<sup>3+</sup>-doped LENS with size of 21 nm, 27 nm and 42 nm. 21 nm Tm<sup>3+</sup>-doped LENS is the minimum size that allow us to distinguish localization clouds within super-resolution imaging (**Fig. 3-13c**).

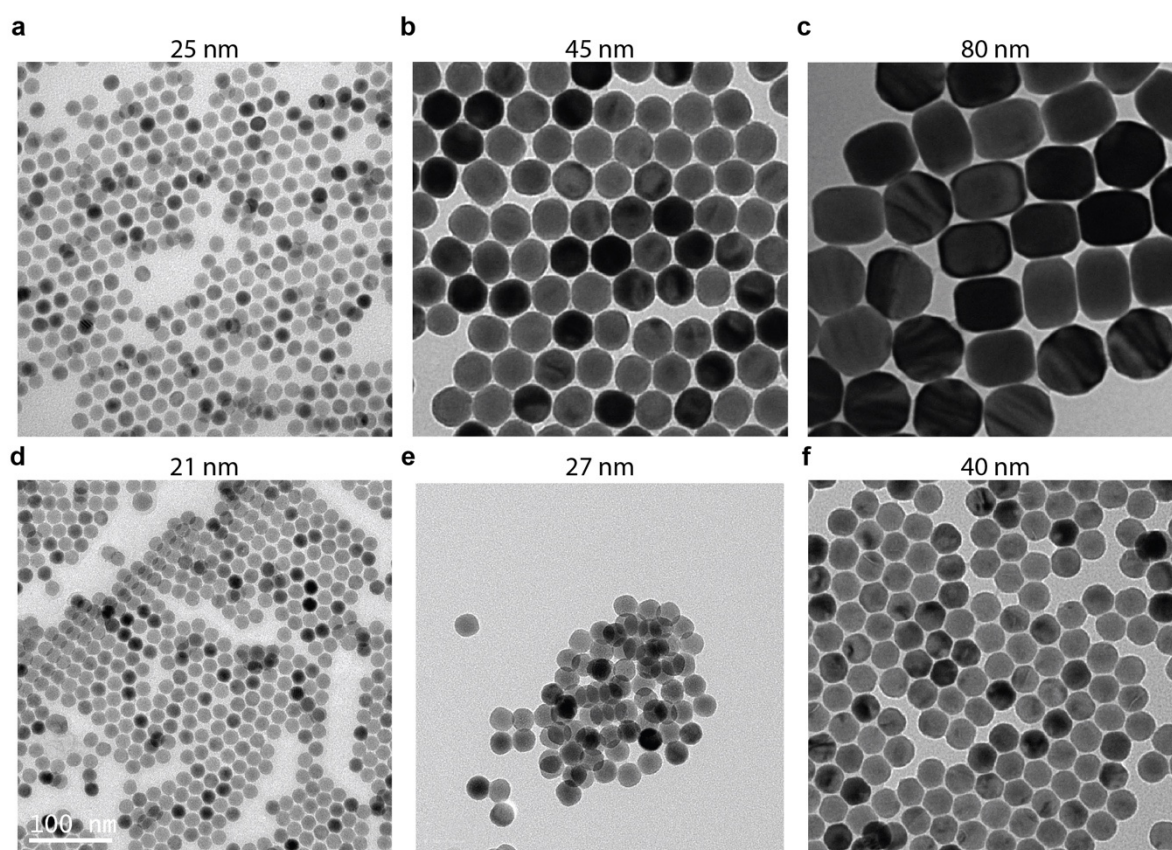


**Figure 3-14. TEM images and size the synthesized UCNPs.** (a,b,c) NaYF<sub>4</sub>:20%Yb<sup>3+</sup>,2%Er<sup>3+</sup>. (d,e,f) NaYF<sub>4</sub>:40%Yb<sup>3+</sup>,4%Tm<sup>3+</sup>.

The average size of sEVs is 144 nm, minimum size of LENS is 21 nm, the maximum number of LENS labelled on the sEVs (captured on the glass bottom) are 91 theoretically (half the  $N_{max}$ ). But in real sample labelling, target accessibility, labelling density, distance between the fluorophore and the target (or



linkage error) are influence factors, which makes the loading efficiency and specifies low. It's still a long way to go for LENS in super-resolution.

### 3.4 Conclusion and discussion

We introduced a STED-like super-resolution imaging to break through the light diffraction limit and achieve single  $\text{Ep}^{\text{CAM}^+}$ EVs imaging. Concerning the perspectives of resolution, illumination, probes, acquisition time, post-acquisition processing, it has incomparable advantages over other super-resolution techniques in single EV imaging. Compared with STED technique based on conventional dyes, UCNPs are background-free, stable and resistance to photo-bleaching and need lower excitation laser power. Compared with STORM, Our nanoscopy is fast, background-free, stable, high brightness. Compared with SIM and standard fluorescence microscopy, our nanoscopy is background-free and achieve higher resolution. Compared with TEM and CLEM, our nanoscopy is biocompatible and can be used for live tacking of EVs.

However, owing to brightness issues, the majority of currently developed UCNPs are relatively large (around 20-50 nm). It has been challenging to design and fabricate highly doped sub-10 nm UCNPs with emission output comparable with that of quantum dots and organic dyes. Compared with the small size of conventional quantum dots and organic dyes, multiplexing and definite quantification of markers on small single EVs is challenging.

Compared with our work in chapter 2 reporting single sEV enumeration<sup>203</sup>, the super-resolution approach presented here achieves a sub-50 nm imaging resolution for single sEV imaging. LENS increase in optical resolution comes at the expense of more exposures, longer acquisition times and/or higher energy loads, which conversely decreases temporal resolution and increases photobleaching and phototoxicity. Although the technique allowed us to have access to an order of magnitude smaller scale than conventional light microscopy, they cannot meet all of these requirements simultaneously. Compared with conventional probes such as organic dyes and quantum dots, UCNP-related super-resolution microscopy is still in the preliminary stage, and both opportunities and challenges exist. Therefore, their optimisation as well as emergence of new techniques will continue. The next ongoing revolution will be the application of LENS for three-dimensional (3D) super-resolution microscopy, which is able to provide 3D structural details of single EVs at sub-nanometre resolution. One particular labelling strategy worth mentioning is the nanobody technology to efficiently label targets with small probes. The tuning of multiple emission colours and lifetimes of LENS will allow for multiplexed super-resolution imaging of single sEVs.

## Statement of Contribution of Authors for Chapter 4

[4] Guan Huang, Laura Laura Rodriguez de la Fuente, David Gallego-Ortega, Yongtao Liu, Ying Zhu. Shihui Wen, Dayong Jin\*. Preclinical detection of circulating EVs (In preparation)

	G. H	L.F	D.G	Y.L	Y.Z	S.W	D.J.
Experiment Design	▪						▪
Sample preparation	▪	▪	▪				
Data collection	▪	▪		▪	▪	▪	
Analysis	▪		▪				▪
Manuscript	▪	▪	▪				▪

The concept of this paper was developed by my supervisor Dayong Jin. I designed the experiments and conducted the majority of experimental work, including modification of UCNPs, Characterization of UCNPs, EV isolation, LENS assay, data collection, data analysis, and manuscript writing.

---

## Chapter 4 Preclinical detection of circulating EVs

---

### Abstract

Tumour-derived EVs play important roles in tumour metastasis process. Due to the compositional heterogeneity of clinical biofluids, the direct and specific analysis of EVs in native biofluids remains technically challenging. Here, we adapt the LENS, TIRF imaging and Super-resolution imaging techniques to assess circulating EVs as a non-invasive tool for diagnosing breast cancer in preclinical samples. We examine blood samples collected from non-metastatic breast cancer mice (67NR, n = 4), high-metastatic breast cancer mice (4T1.2, n = 3), low-metastatic breast mice (PyMT/WT, n = 9) and high-metastatic breast mice (PyMT/Elf5, n = 10). Our results show that the LENS can be used to monitor the metastatic tumour progression in the above preclinical samples. Furthermore, we found that the number of LENS can digitalise the number of EpCAM biomarkers on single EVs so as to index the stage of metastatic tumour progression. Our validation studies suggest a viable approach for liquid biopsy for tumour diagnosis and prognosis.

### 4.1 Introduction

#### 4.1.1 Limitations in breast cancer clinical management

Breast cancer is one of the most common malignancies among women. Mammography often detects early-stage breast cancer before a mass becomes large enough to identify through physical examination<sup>208</sup>. However, this improvement is countered by false positives. Supplementary ultrasound and magnetic resonance imaging (MRI) may be combined with mammography to detected more breast cancer cases than solo mammography<sup>209,210</sup>. If the abnormality is suspected of being malignant, a tissue biopsy is performed and analysed to stage of the disease (pathology), assign a grade (histology), and analyse the molecular components (molecular analysis) to formulate a treatment plan.

The limitations of the analysis methods above are discussed. Firstly, clinicians traditionally examine metastases through computed tomography (CT) of the chest, bones, abdomen, and pelvis. However, imaging is not shown to provide any clear benefit for the early detection of metastases in asymptomatic patients and the physician's discretion. Secondly, for all malignant cases, tissue biopsies of the tumour are required. Biopsies coupled with image findings help clinicians stage the cancer and predict prognosis

for disease progression. Thirdly, molecular analysis provides physicians with important information for deciding personalized treatment pathways for each breast cancer patient. Though molecular profiling is a promising new classification technique for breast cancer management, it is still not thoroughly recommended in clinical guidelines and is considered secondary to the traditional pathology testing of receptor status for determining treatment and prognosis. Fourthly, after receiving the pathological report, a physician will use the information to create a treatment plan for each patient. However, the extent of breast removal is guided by the prognosis of the disease, the predicted response to therapies, and the stage at which the breast cancer is diagnosed. The fact that no widely available diagnostic tool is sensitive enough to detect minimal residual disease (MRD) at a very low cancer burden, which can cause relapse if not treated. Finally, monitoring is vital to gauge both treatment response and detect cancer recurrence. For all but metastatic cases, monitoring is considered “surveillance” and is enacted after treatment. Though imaging remains the mainstay for assessing treatment response in metastatic breast cancer, it is still limited by the sampling frequency, tumour size detection and the experience of the pathologist. In summary, these limitations motivated researchers to look for other tests to monitor disease such as liquid biopsies.

#### **4.1.2 Role of EVs in tumour metastases**

EVs translocate from the primary tumour, circulate with the human bloodstream, and finally exit the circulation and invade into the microenvironment of the foreign tissue, forming metastases (**Fig. 4-1**). Immune and stromal cells in the microenvironment, such as the natural killer (NK) cells, tumour-associated macrophages (TAMs), and cancer-associated fibroblasts (CAFs), also support tumour growth, metastatic dissemination, and colonization of the CTCs at secondary sites. EVs, shed by not only the primary tumour cells but also the immune and stromal cells, can facilitate intercellular communication, and promote tumour metastasis.

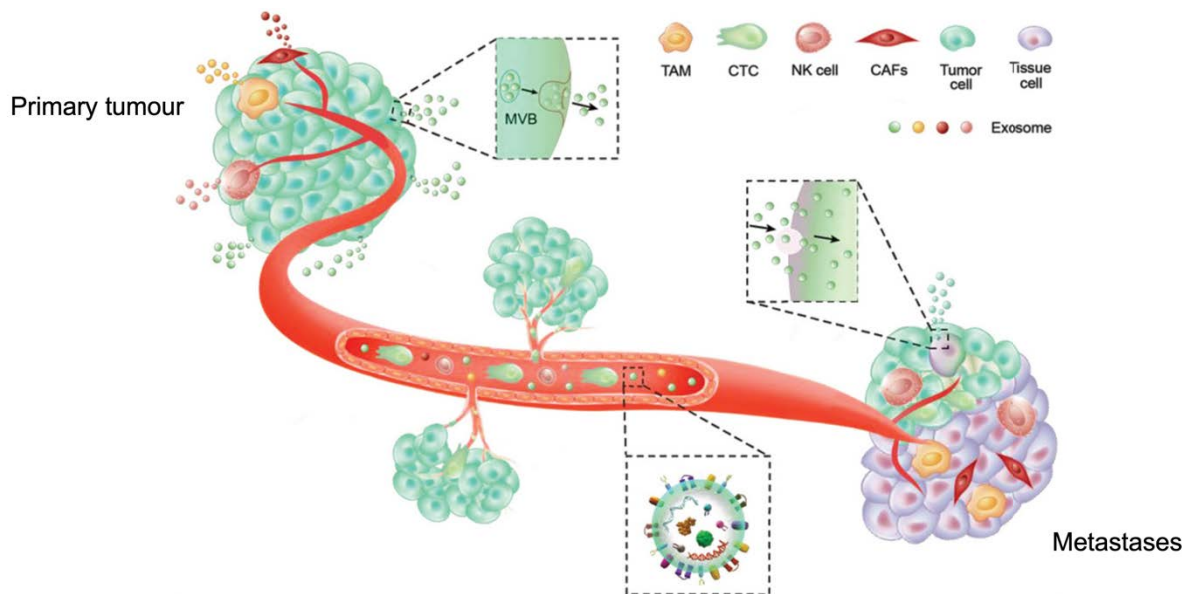


**Figure 4-1 | The roles of EVs in tumour metastasis.** Reprinted from reference<sup>211</sup>.

EVs are isolated for molecular analysis of proteins, nucleic acids, or lipids that can provide more concise information on the nature of a specific disease. EV membrane proteins can be targeted as a disease marker for breast cancer detection or molecular subtype identification. Heterogeneity also exists within different sites of a tumour or for example between primary cancer and metastases. An increasing number of studies have shed light on the heterogeneity of EVs, providing evidence for the existence of different subpopulations with unique RNA signatures, protein profiles and biological functions. These data suggest that the heterogeneity of the EVs might involve distinct or mixed biogenesis processes allowing for sorting of diverse cargos into different EV subpopulations.

#### **4.1.3 Role of EVs in indexing the stage of metastatic tumour progression**

The expression levels of surface proteins on circulating tumour-derived EVs has been of particular interest in providing valuable information about the physiological states of parental cells. This information can play a significant role in developing prognosis for potential metastasis and deciding the route for treatment. While performing these measurements there is an increasing need to know whether there is a significant change in EV marker expression levels, either overexpression or suppressed expression in individual EVs. This change during the early stages of treatment indicates how this information could be used as an indicator for disease detection and monitoring. Therefore, to understand the expression change of markers in EVs, we need to have a way to understand the starting sample population and consider that when measuring biomarker readout, as absolute readout could blind us and fail to understand the underlying process and its effects in a diseased condition.

#### 4.1.4 Murine preclinical cancer modelling

The clinical limitations including the diversity of human genetic background and the difficulty in tumour and tissue procurement, mouse mammary tumor models have been created in attempt to reproduce the morphological and mechanistic characteristics of human breast cancer. Murine cancer models designed to capture the complexities of human cancers currently offer the most advanced preclinical opportunity for navigating diverse mechanisms that provide a rationale for therapeutic development. A variety of approaches to mouse cancer modelling are illustrated in **Figure 4-2**, and each has strengths and weaknesses<sup>212</sup>. Here we address the Cell-line xenograft model (CLX), patient-derived xenograft model (PDX), syngeneic model and genetically engineered mouse model (GEMM).

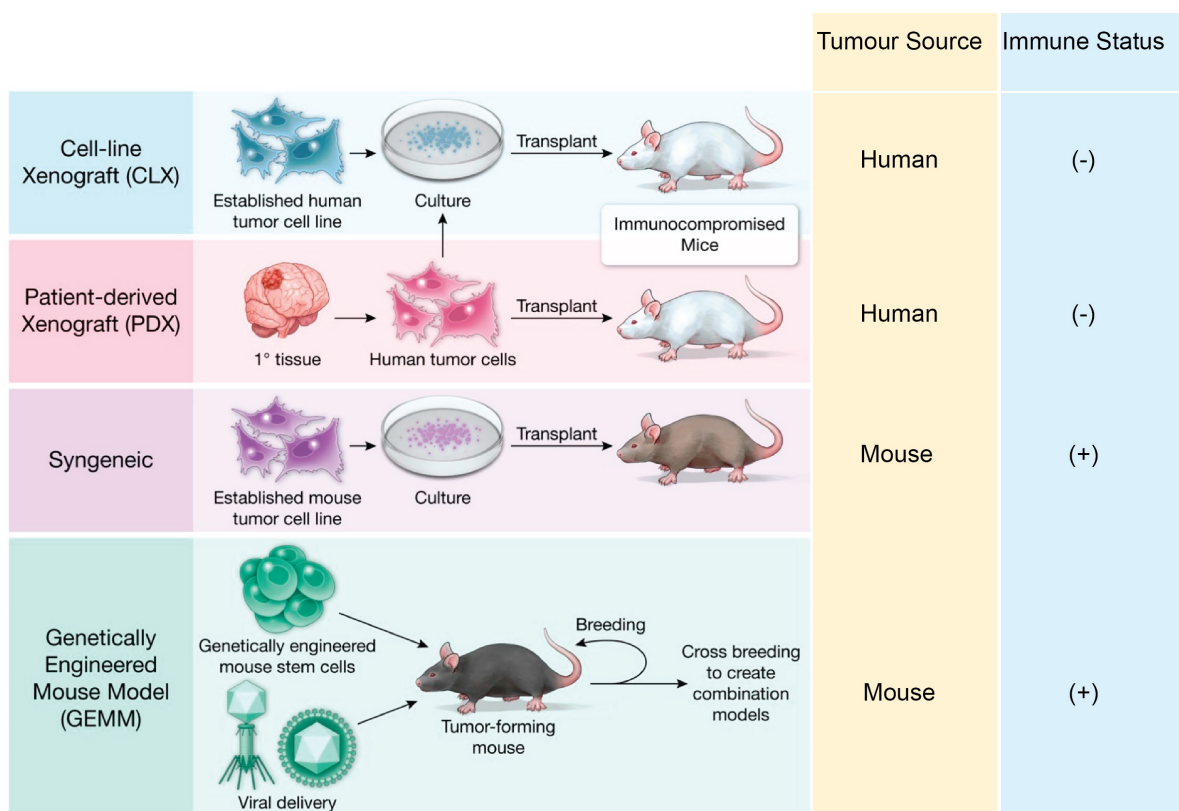


**Figure 4-2 | Murine preclinical cancer modelling.**

##### 4.1.4.1 Xenograft models

Historically, in cell-line xenograft models (CLX), cells are implanted into the desired location in the mouse. CLXs are a quick and reproducible strategy. However, they often result in well-circumscribed tumours that lack the characteristic infiltrative pattern. Further, the selective pressures of cell culture reduce the sub-clonal heterogeneity of CLXs and their ability to recapitulate the parent tumour.

In contrast to CLX models, patient-derived xenografts models (PDX) involve direct xenotransplantation of human biopsy tissue. Importantly, PDX models are exposed minimally, if at all, to in vitro culture,

which avoids adaptation to non-physiological conditions and preserves features of the tumour of origin. PDX models are better suited to recapitulate the stromal and interactions and invasiveness of parent tumours than their CLX counterparts.

Although xenograft is of value for the assessment of intrinsic events within the tumour cells, they lack the orthologous extracellular matrix, the species-matched stromal-tumour interactions and a functional immune system. Syngeneic models and transgenic overcome these limitations.

#### 4.1.4.2 Syngeneic Models

Unlike xenograft models, syngeneic models utilize tumour cells isolated from spontaneous mammary tumours in mice<sup>213–216</sup>. Syngeneic nature of the models allows the study of the interaction between the tumour growth and immune microenvironment, and the possibility of testing immunotherapies for cancer treatment<sup>217</sup>. Like other models that are based on cell line propagation, the syngeneic mouse model is subject to genetic drift with long term propagation. The tumour cells can be inoculated into the mammary gland as an allograft (**Fig. 4-3**) with genetic and immunological compatibility and the resulting tumours often progress extensively beyond localised growth within a timeframe of weeks rather than months<sup>218</sup>.

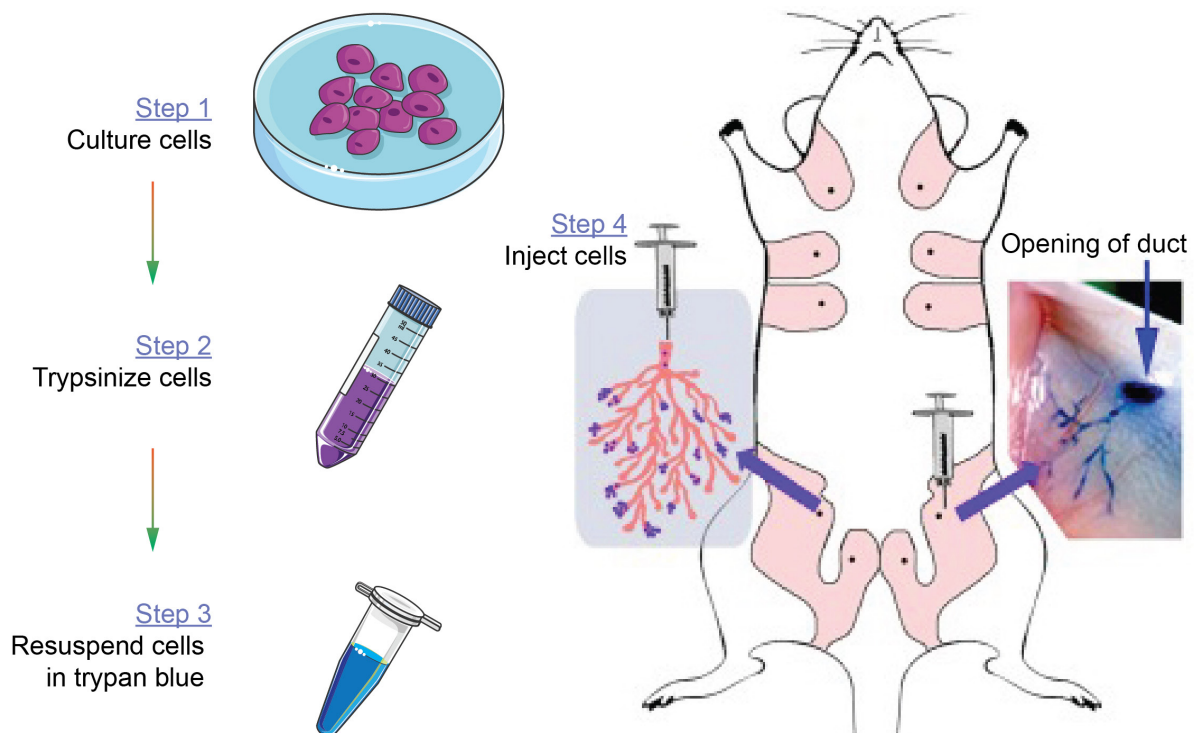


**Figure 4-3 | Schematic representation of mouse mammary intraductal injection.**

One pair of the syngeneic models we used in this study is the non-metastatic 67NR and high-metastatic 4T1.2 tumour models from 4T1 BALB/c model. Both 67NR and 4T1.2 allograft models were inoculated into the mammary gland as an allograft with genetic and immunological compatibility (BALB/c

background)<sup>219</sup>, developing mammary carcinomas within 2 weeks of cancer cell implantation. The 4T1 model has been the principal transplantable mouse model used to study both tumour- and host-derived factors involved in spontaneous metastasis<sup>216,220,221</sup>. Sublines of 4T1 cells, 4T1.2, which exhibit various degrees of metastatic dissemination, have been employed recently to generate distinct gene expression signatures for each stage of tumour progression, namely primary tumour formation, lymph node colonization, metastatic outgrowth in the lymph node, and distant organ metastasis.

The 4T1 tumour has several characteristics that make it a suitable experimental animal model for human mammary cancer. First, 4T1 cells, which originally derived from a spontaneous mouse mammary tumour of a BALB/C mouse, is highly tumorigenic, invasive and grow rapidly when injected into the fat pad of a syngeneic animal and metastasize to lymph nodes, blood, lungs, liver, bone, and brain<sup>222</sup>. Also, the progressive spread of 4T1 metastases to the draining lymph nodes and other organs is very similar to that of human mammary cancer. The most important one, the 4T1 model is the only system that has the capacity to metastasize to all organs affected in breast cancer in humans when introduced orthotopically. For this reason, and because of the ease of use and reproducibility that can be achieved, these imageable models provide ideal systems for determining anti-metastatic effects of cancer drugs and therapeutic regimens and is well suited for investigating the molecular, cellular and pathologic basis for metastasis to specific organs and tissues.

#### **4.1.4.3 GEMM**

Of all murine cancer models, GEMMs provide the most complete representation of cancer development and are frequently used to investigate the role of tumour-associated genes and their role in cancer progression and metastasis. GEMMs involve manipulation of the mouse genome to induce tumour formation. Immune-competent mice can cause autochthonous tumours to form in mouse tissue, which is a key advantage over xenograft models. GEMMs affords precise control over the molecular events leading to tumour formation, maintenance, and susceptibility to treatment. Furthermore, GEMMs allow for the ability to activate relevant oncogenes at specific time points in tissue development, and they permit testing of potential therapeutic agents at various stages of tumorigenesis. These properties offer distinct advantages over PDX models, which are nearly universally derived from advanced human tumours.

However, the timeframe for tumour development is often months, and metastasis is generally limited to a modest number of lung nodules<sup>218</sup>. Species differences must be carefully considered in experimental



designs and interpretations. Extensive experience and infrastructure are required to ensure the use of optimally accurate models and to achieve sufficiently populated well-controlled preclinical studies. Yet, GEEM cancer models provide the natural complex dynamic processes that contribute to overall disease properties, and in particular, constitute a source of the inter- and intra-tumoral heterogeneity that challenges successful therapeutic development.

Polyoma middle T antigen (PyMT) transgenic mice are one of the GEMMs for breast cancer research. MMTV-PyMT transgenic mice which the expression of the oncogene is driven by the Mouse Mammary Tumour Virus promoter) develop metastasis in lung and lymph nodes, mainly after their first pregnancy, while other transgenic mice have to be combined to generate double-transgenic mice that efficiently develop malignant cancers. In PyMT mice, four distinctly identifiable stages of tumour progression (hyperplasia, adenoma/mammary intra-epithelial neoplasia, and early and late carcinoma) occur in a single primary tumour focus and this malignant transition is followed by a high frequency of distant metastasis (Fig. 4-4). These stages are comparable to human breast diseases classified as benign or in situ proliferative lesions to invasive carcinomas. In addition to the morphological similarities with human breast cancer, the expression of biomarkers in PyMT-induced tumours is also consistent with those associated with poor outcome in humans.

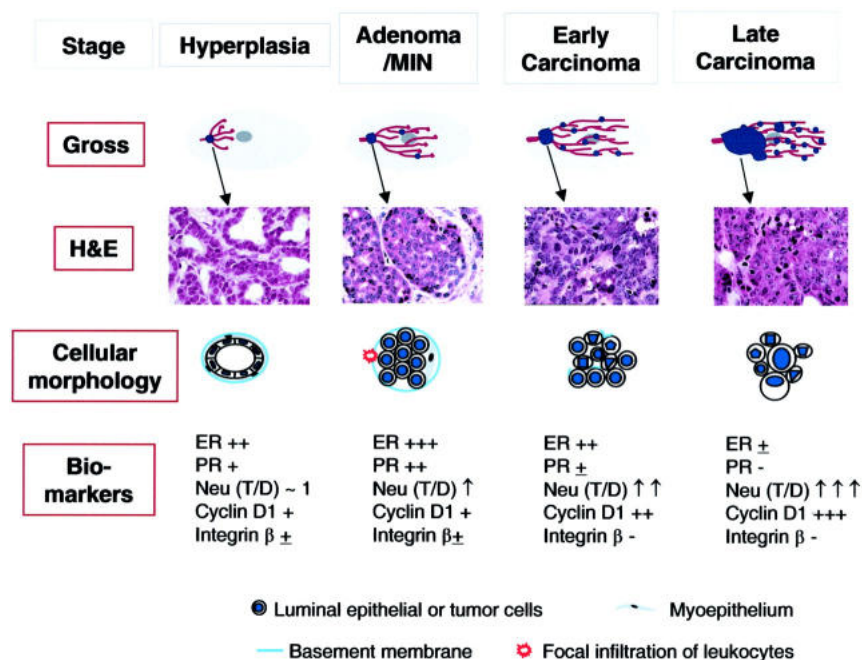


**Figure 4-4 | Summary of tumour progression and biomarker expression in PyMT mouse model of breast cancer.** Top: Gross, displays the overall development of lesions in mammary glands of PyMT mice. Tumour lesions are indicated by blue dots. The H&E panel displays the corresponding histology

of primary lesions at different stages of tumour progression. The cellular morphology panel schematically illustrates changes in the cytology of the cells as well as the integrity of the basement membrane and the presence or absence of myoepithelial and focal inflammation. Moreover, the changes in biomarkers during tumour progression is summarized in the panel of biomarkers. T/D, the ratio of Neu expression between lesions and normal ducts in age-matched mammary glands. Reprinted from reference<sup>223</sup>.

In the mouse mammary tumour virus-Polyoma Middle T (MMTV-PyMT) model of luminal breast cancer, induction of Elf5 levels increased leukocyte infiltration, angiogenesis, and blood vessel permeability in primary tumours and greatly increased the size and number of lung metastasis. The transcription factor Elf5 drives the spread of tumour cells to the lungs. Elf5 can reduce tumour cell proliferation and induce Epithelial Properties. Elf5 can produce haemorrhage, leukocyte infiltration, and angiogenesis in MMTV-PyMT Primary Tumours (**Fig. 4-5a, b**). Forced Elf5 Expression can induce metastatic ability of PyMT Mammary Tumours (**Fig. 4-5c**).

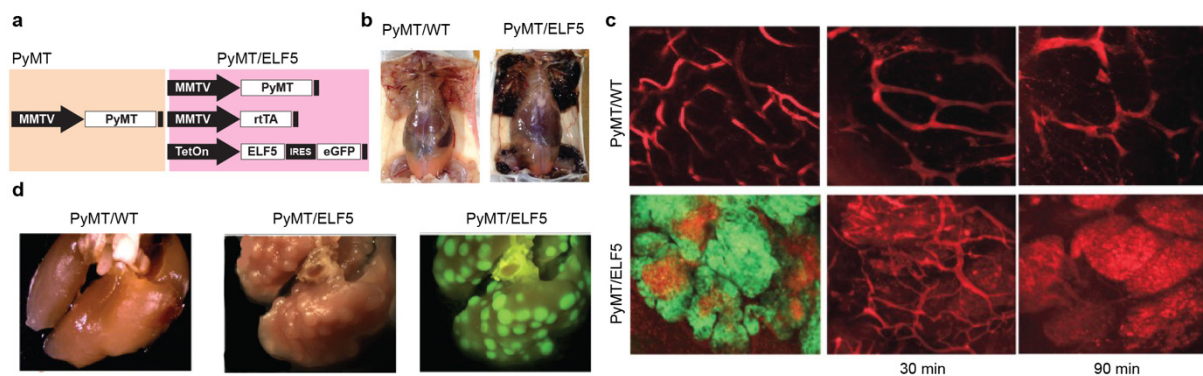


**Figure 4-5 | ELF5 Drives Lung Metastasis in Luminal Breast Cancer.** (a) The appearance of PyMT-driven tumours in WT mice or those experiencing long-term (8 wk) forced expression of Elf5. (b) Intravital real-time microscopy of blood tracer quantum dots (red) injected into the vasculature of mice of the indicated genotypes. LHS panels, quantum dots visualized together with EGFP (green) marking Elf5 expression. RHS panels, imaging of quantum dots (red) in the tumours 30, 60, and 90 min after injection. (c) The appearance of lungs from a control PyMT animal following long term (8 wk) DOX treatment. The appearance of lungs following long term ELF5 expression. Visualization of EGFP of the lungs in Panel E. Reprinted from reference<sup>224</sup>.

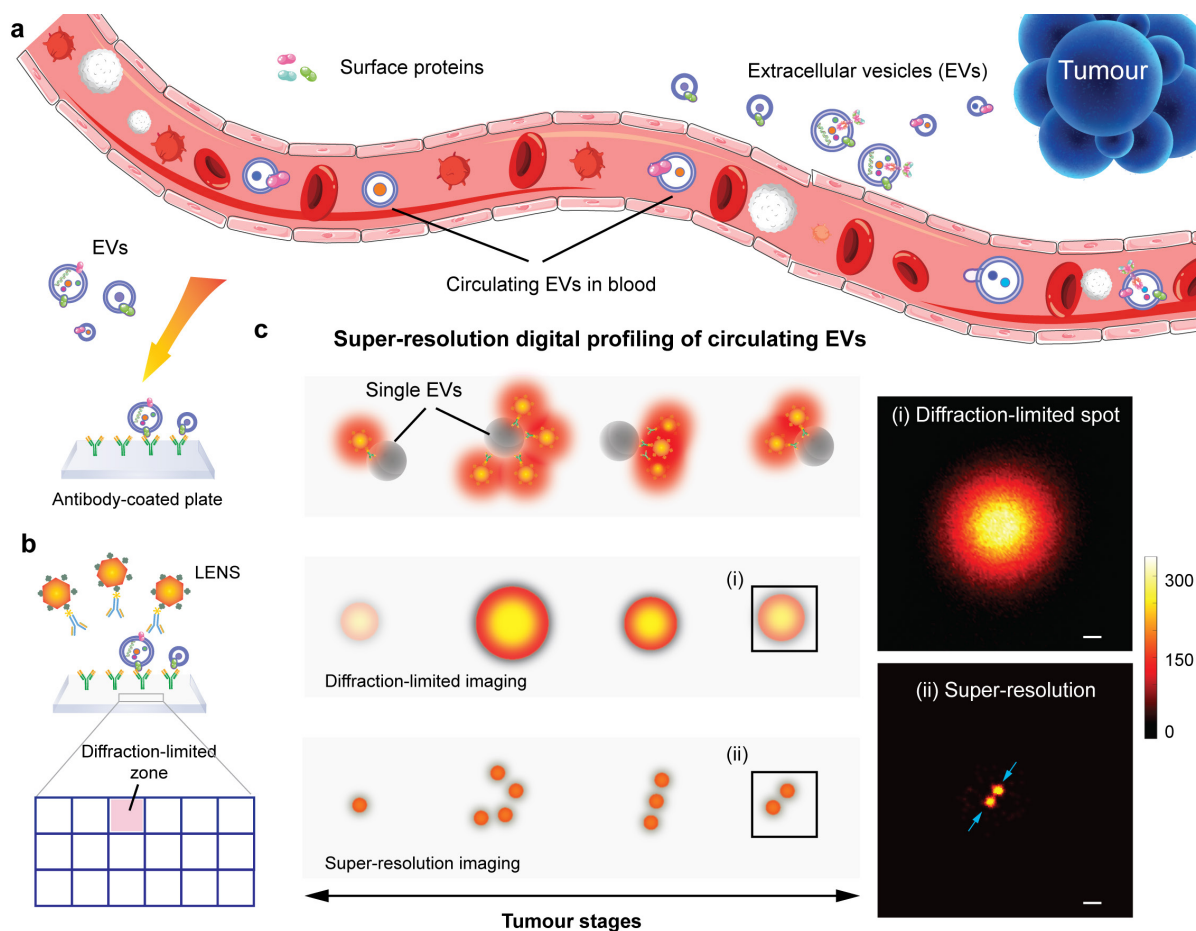


**Figure 4-6 | Lanthanide-doped EV-targeting Nanoscopic Signal-amplifiers (LENS) for the super-resolution digital profiling of surface biomarkers on tumour-derived circulating EVs.** (a) circulating EVs carrying heterogeneous distributions of biomarkers are released from the tumour's site, and can be captured on an antibody-coated plate. (b) Single circulating EVs labelled by LENS can be detected in a diffraction-limited zone by microscopic imaging. (c) LENS-EV conjugates detected as bright spots with different intensities can be super-resolved in super-resolution nanoscopy. Scale bar: 100 nm.

In this chapter, we made one step further to utilize the single EV enumerate platform (chapter 2) and single EV super-resolution imaging platform (chapter 3) to digitalize the amount of EpCAM biomarkers on a large population of EVs released from two types of breast cancer mouse models (**Fig. 4-6**). Firstly, tumour-derived sEVs were isolated by size exclusive chromatography method. Then sEVs were captured by EV-specific CD81, CD63 and CD9 antibodies and subsequently detected by the functionalized LENSs conjugated with anti-mouse EpCAM antibody. The presence of single sEVs can be directly counted according to the number of bright spots. Furthermore, we utilized the steric hindrance effect of LENS and find that the number of LENS can digitalize the amount of EpCAM biomarkers on a large population of EVs, so that to index the stage of metastatic tumour progression. With the ultra-sensitivity, photo

stability, super resolution and high throughput achieved simultaneously, our finding has been thoroughly examined by two types of breast cancer mouse models towards clinical translations.

## 4.2 Methods

**4.2.1 Experimental Animal Models.** A total of 26 mice were enrolled in this project. Mice were maintained following the Australian code of practice for the care and use of animals for scientific purposes observed by the Garvan Institute of Medical Research/St. Vincent's Hospital Animal Ethics Committee (AEC), AEC#14/27. The blood processing and diagnosis experiments were conducted under National Statement on Ethical Conduct in Human Research (2007), #UTS HREC REF NO. ETH20-5218. The mouse mammary tumour virus-Polyoma Middle T (MMTV-PyMT) model of luminal breast cancer<sup>225</sup> and the MMTV-PyMT doxycycline-inducible ELF5 expression mice<sup>226</sup> were used as genetically engineered mouse models (GEMM) of tumour-spontaneous development. Induction of the expression of the transcription factor ELF5 in MMTV-PyMT mice at 6 weeks old increases the level of lung metastasis<sup>226</sup>. When tumours mass reached  $\geq 10\%$  (approximately 13-14 weeks old), mice were euthanized with CO<sub>2</sub> for blood and lungs collection.

For the mouse intraductal (MIND) model, wild-type female Balb/c mice, 7-9 weeks old, were purchased from the Australian BioResources (MossVale, Australia) and inoculated with the highly metastatic cell line 4T1.2 and with the non-metastatic 67NR cell line. Briefly,  $5 \times 10^4$  viable cells for the 4T1.2 model and  $2 \times 10^4$  viable cells for the 67NR were injected directly into the 4<sup>th</sup> mammary gland ducts in a 4  $\mu$ L volume with PBS and 0.4% trypan blue at 1:5 dilution. Lungs and blood from tumour-bearing mice were collect at 14 and 24-26 days (2 and 4 weeks timepoints, respectively). The basal-like 4T1.2 cell line (highly metastatic) and the luminal-like 67NR (non-metastatic), both derived from the spontaneous mammary tumour within Balb/c/C3H mouse model<sup>216</sup>, were maintained in MEM (alpha modification) medium containing 5% FBS. Both cell lines were culture in monolayer at 37 °C in 5% CO<sub>2</sub> medium for no more than 4 weeks to minimize the genetic drift. Cells were used for intraductal injection between 3-5 passages. All cell lines were tested negative for mycoplasma.

**4.2.2 Intraductal mammary carcinoma implantation.** Mammary intraductal surgeries were performed on anesthetized mice with 2.5-4% Isoflurane at 1L/minute oxygen rate and eye ointment was applied to avoid dryness. Briefly, the region of the inguinal nipples was carefully shaved and swabbed with an ethanol wipe. Two curved tip forceps were used to hold the teat of the inguinal gland in vertical position before cutting it with a 3 mm cutting edge Vannas Spring Scissors. Trypan blue at 0.4% was added, after

removing superficially the teat, to visualize the hole for injecting the breast cancer cells directly into the mammary ducts of the 4th mammary gland of the mice with a Hamilton syringe with a 30-gauge blunted needle. Pedal reflex was checked at the beginning and during the whole procedure. Recovery was carried out in a cage “half on/half off” over a warm pad after administration of systemically (5mg/kg Ketoprofen) and locally (5ml/kg Bupivacaine) analgesia. Mice were monitored until total recovery and, then placed in their corresponding cages. Mouse weight, tumour growth and body condition were checked weekly until blood and lungs collection.

**4.2.3 Blood and lungs collection.** Blood was collected via cardiac puncture from CO<sub>2</sub> euthanized mice at 2 and 4 weeks from intraductal injection and placed in a Microtainer tube with EDTA additive. Blood was mixed with the EDTA by gently inverting the tube for at least 10 times to avoid clotting. Lungs were collected and fixed in 10% buffered formalin for 24 h and, then kept in 70% ethanol until paraffin embedding. Using a Leica RM2235 microtome (Leica Biosystems, Wetzlar, Germany), paraffin embedded blocks were cut into 4 µm sections and incubated on a Superfrost plus slide for 2 hours in a 60°C oven for maximum adhesion. Standard Hematoxylin and Eosin (H&E) staining was performed on a Leica Autostainer XL using Haematoxylin (ThermoFisher Scientific, Waltham, USA) and Eosin (Sigma-Aldrich, St. Louis, USA). Images were taken with a Leica Microscope MZ12 with the 1X lens for quantification with Andy’s Algorithm<sup>227</sup>, and 0.5X lens for whole lungs pictures. Histological sections from 13-14 week-old PyMT/WT and PyMT/ELF5 mice include 6 biological replicates, and for the timepoints 2 and 4 weeks of the 67NR/4T1.2 models include at least 3 biological replicates.

**4.2.4 Plasma isolation from fresh blood.** Peripheral blood was drawn into K<sub>2</sub>EDTA tubes (BD bioscience, San Jose, USA). The blood was processed within 2 hours of blood collection. Plasma was extracted after the first centrifugation of the blood at 3,000 rpm for 15 min at 4 °C. The plasma was immediately transferred into a clean tube without disturbing the buffy coat and followed by serial pre-purification steps at 4 °C as follows: Plasma was spun at 2,000 × g for 20 min and the supernatant was centrifuged at 10,000 × g for 20 min to remove cells and debris. The supernatant was then filtered through 0.22 µm pore Ultrafree centrifugal filter (Merck KGaA, Darmstadt, Germany) at 12,000 × g for 2 min. Aliquots of the purified plasma samples were stored at -80 °C and freeze-thawing was limited within two cycles for each sample.

**4.2.5 EVs isolation from Plasma.** Size exclusion chromatography, qEV35 (IZON Science, Christchurch, NZ), was used to isolate EVs from plasma with a target particle size 35nm – 350nm. EVs from 250 mL pre-purified plasma were isolated according to user manuals. Briefly, 250 mL pre-purified plasma were

loaded onto the SEC column, the 7-9 fraction (a total of 1.5 mL) was collected. A post-enrichment step to obtain a higher stock EV concentration was performed using Amicon® Ultra-4 10 KDa unit (Merck KGaA, Darmstadt, Germany). The concentrated EV samples were stored at -80 °C. EV samples are used within two freeze-thawing cycles for the following analysis. (certain volume of plasma for further LENS assay)

**4.2.6 Nanoparticle tracking analysis.** Same as Method 2.2.4.

**4.2.7 UCNP synthesis, surface modification and characterisation.** Same as Method 2.2.7, 2.2.10, 3.2.3 and 2.2.11.

**4.2.8 LENS procedure.** Same as Methods 2.2.4 except the antibodies. Antibodies: anti-mouse CD9 Monoclonal Antibody (clone: MZ3, Australian Biosearch), anti-mouse CD63 Monoclonal Antibody (clone: NVG-2, Australian Biosearch), anti-mouse CD81 antibody (clone: Eat-2, Australian Biosearch, 104902), biotinylated anti-mouse CD326 antibody (clone: G8.8, EpCAM, Australian Biosearch).

**4.2.9 TIRF setup and imaging.** Same as Method 2.2.12.

**4.2.10 Super-resolution setup.** Same as Method 3.2.8.

**4.2.11 Image and data processing.** Same as Method 2.2.14.

## **4.3 Results**

To evaluate the preclinical utility of LENS, we conducted a feasibility study using blood samples from two pairs of breast cancer mice (isogenic non-metastasis 67NR and high-metastasis 4T1.2 breast cancer models; transgenic PyMT/WT and PyMT/Elf5 breast cancer model). We aim to address the following questions: (i) if LENS could be directly applied to preclinical specimens for multiplexed measurements, (ii) the accuracy of LENS in distinguishing EV targets, and (iii) if the LENS signatures could differentiate additional preclinical characteristics (e.g., prognosis). We obtained cancer blood samples (n = 34; 26 for 67NR and 4T1.2, 8 for PyMT/WT and PyMT/Elf5) and performed LENS analysis directly on these samples.

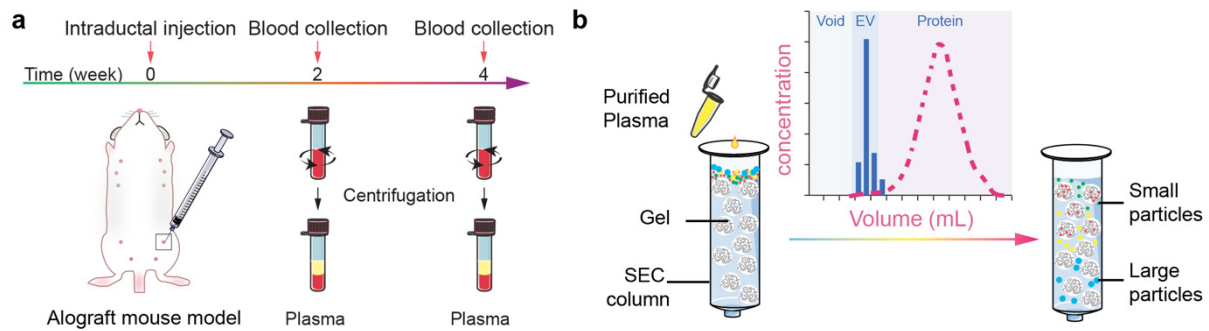


**Figure 4-7 | Schematic representation and description of the main steps involved in the SEC isolation of EVs from plasma.**

### 4.3.1 Preclinical prognosis of Syngeneic Models

To monitor the cancer metastasis and their longitudinal development, we conducted single-blind experiments (the information of the blood was kept unknown before we obtained the final results) to profile circulating EVs from breast cancer mice with different degrees of metastatic dissemination. We firstly used a pair of isogenic mouse models of triple-negative breast cancer (isogenic non-metastasis 67NR and high-metastasis 4T1.2 cancer models).

We collected blood and isolated EVs from 67NR and 4T1.2 mice by using well-established size exclusion chromatography (Fig. 4-7). The modal size distribution and concentration of EVs were determined by NTA (Fig. 4-8). The Particle modal sizes are  $109.2 \pm 3.6$  nm (67NR – 2 weeks),  $123.2 \pm 3.6$  nm (67NR – 4 weeks),  $103.6 \pm 2.7$  nm (4T1.2 - 2 weeks),  $107.8 \pm 3.3$  nm (4T1.2 - 4 weeks). An equal amount of EV samples was used for the following detection.

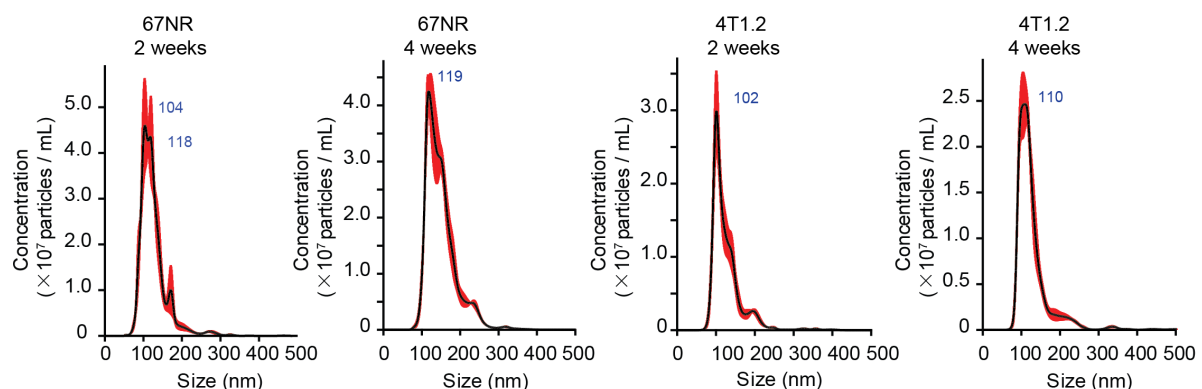


**Figure 4-8 | Size distribution and concentration of circulating EVs for different models – characterized by nanoparticle tracking analysis.**

### 4.3.1.2 LENS for circulating EV detection

Circulating EVs were captured by the cocktail mixture of three capture markers, e.g. CD9, CD81, and CD63 absorbed on the plate, and EpCAM expression of the EVs was quantified using digital imaging of LENS under TIRF (**Fig. 4-9a**). From TIRF imaging, the number of LENS-EV conjugate is correlated with metastatic dissemination, with a significant increase from 4T1.2 mouse compared with 67NR model at all time points (**Fig. 4-9b**).

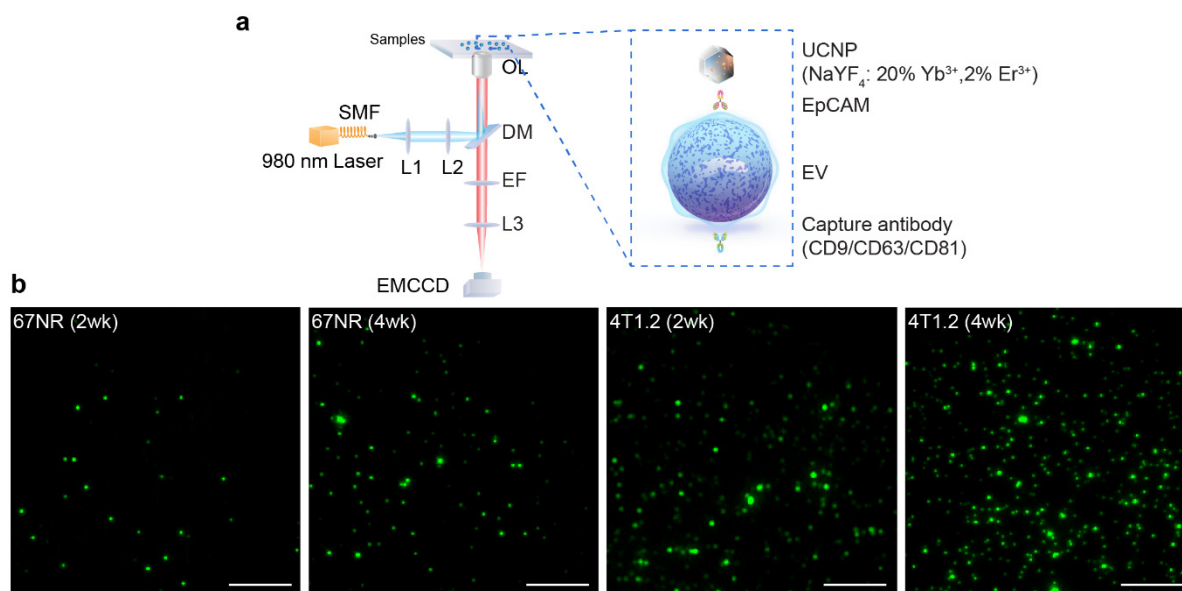


**Figure 4-9 | EpCAM levels in 4T1.2 and in 67NR EVs.** (a) Schematic illustration of circulating EV imaging labeled by LENS by TIRF imaging. (b) TIRF images of  $\text{EpCAM}^+$  circulating EVs on 67NR/4T1.2 mouse models identified by LENS. Exposure time: 500 ms. Scale bar: 10  $\mu\text{m}$ .

Statistical analyses of the LENS assay data in **Figure 4-10** were performed to quantitatively evaluate the diagnostic metrics of these EV capture markers. Analyses with receiver operating characteristic (ROC) curves revealed superior diagnosis accuracy for EV profiling. We compared the performance of mix and individual markers through receiver operating characteristic (ROC) curve analysis. The areas under the curve (AUCs) for  $\text{CD9}^+\text{EpCAM}^+$ ,  $\text{CD63}^+\text{EpCAM}^+$ ,  $\text{CD81}^+\text{EpCAM}^+$  and  $\text{CD9/CD63/CD81}^+\text{EpCAM}^+$  of EVs between non-metastatic 67NR and high-metastatic 4T1.2 are determined to be 1.00. The probing of EpCAM has been documented for metastatic breast cancer diagnosis with high accuracy. The areas under the curve (AUCs) for  $\text{CD9}^+\text{EpCAM}^+$ ,  $\text{CD63}^+\text{EpCAM}^+$ ,  $\text{CD81}^+\text{EpCAM}^+$  and  $\text{CD9/CD63/CD81}^+\text{EpCAM}^+$  of EVs between 2-week 4T1.2 and 4-week 4T1.2 are determined to be 0.786, 0.845, 0.714 and 0.804, respectively.  $\text{CD81}^+\text{EpCAM}^+$  and  $\text{CD9}^+\text{EpCAM}^+$  showed slightly less diagnostic power than  $\text{CD63}^+\text{EpCAM}^+$ .

We attribute this LENS performance to the following possibilities. Blood contain target protein markers in different organizational states. Recent studies have shown that these proteins are released through



different mechanisms and play different roles in disease progression, suggesting the potential utility of EVs as a more reflective indicator of disease aggressiveness and poor prognosis. Specifically, while free-floating membrane proteins are generally released during cell death, EVs are secreted during active tumor growth and carry multiple cargoes to promote metastasis.

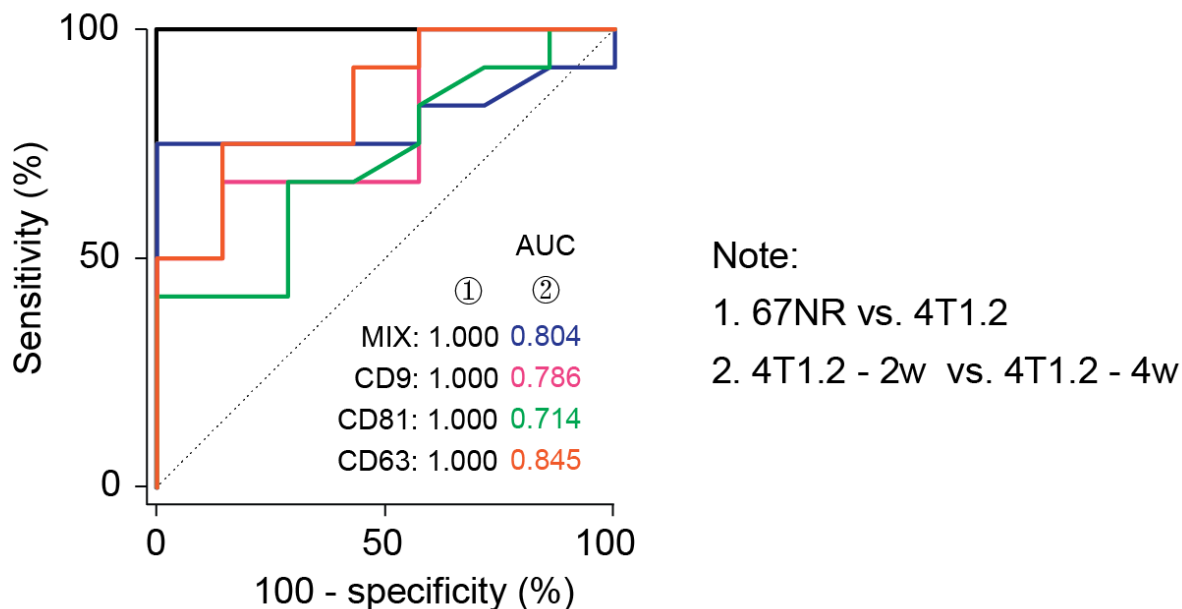


**Figure 4-10 | Receiver operating characteristic (ROC) curves of the LENS regression models on samples of between 67NR and 4T1.2 (①), between 4T1.2-2w and 4T1.2-4w (②).** ROC curves were constructed using individual markers or a combination of the capture markers (mix).

We assessed the LENS assay of three EV capture markers and their mix for detecting the 67NR - 2 week, 67NR - 4 week, 4T1.2 - 2 week and 4T1.2 - 4 week using one-way analysis of variance (ANOVA) with post-hoc Tukey's test (**Fig. 4-11**). The comparison tests between the groups revealed that CD9, CD63, CD81 could significantly differentiate the early-stage (2 week) breast cancer from the advanced (4 week). Moreover, the average number of  $^{EpCAM+}$ EVs at 4 weeks after inoculation was found to be 96% more than that of the 2-week 4T1.2 model ( $P < 0.0001$ ). The results suggest the increased EpCAM level on EVs along tumour metastasis progression. The EpCAM level of EVs in the plasma from 2 week and 4 week 4T1.2 mice as compared to that in 67NR tumour bearing mice. The EpCAM level of EVs increased significantly in mice bearing 4T1 cells compared to that in 67NR cells. The methodology used in this study for analysis of EpCAM expression yielded highly significant data characterizing the 4T1.2 metastatic phenotype.

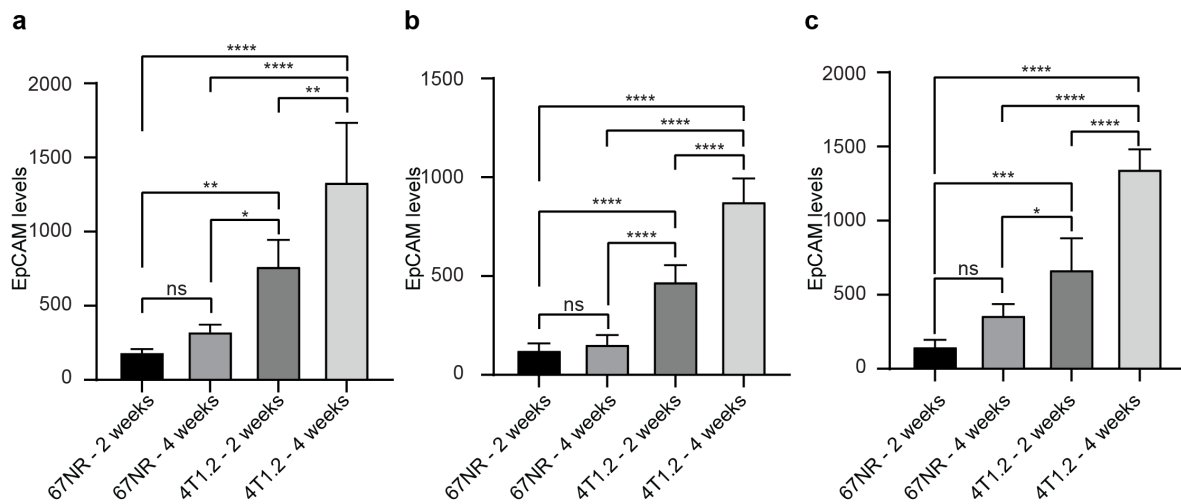


**Figure 4-11 | EpCAM expression profile among EV subpopulations from 67NR/4T1.2 mouse models measured by LENS.** (a), CD9 capture; (b), CD81 capture; (c), CD63 capture. One-way ANOVA with Tukey's multiple comparisons test. \* $P < 0.05$ , \*\* $P < 0.01$ , \*\*\* $P < 0.001$ , \*\*\*\* $P < 0.0001$ , ns: not significant.

To assess the feasibility of our technology for multiplexed EV profiling to identify disease fingerprints, we performed a non-supervised hierarchical clustering analysis of the measured levels of three capture markers and their mixture. The resultant heat map showed that the groups were classified into distinct three clusters by this three-marker and their combination (**Fig. 4-12**), suggesting the potential of EV profiling for breast cancer diagnosis and stratification. However, the clinical promise of these biomarkers needs rigorous validation with much larger cohorts.

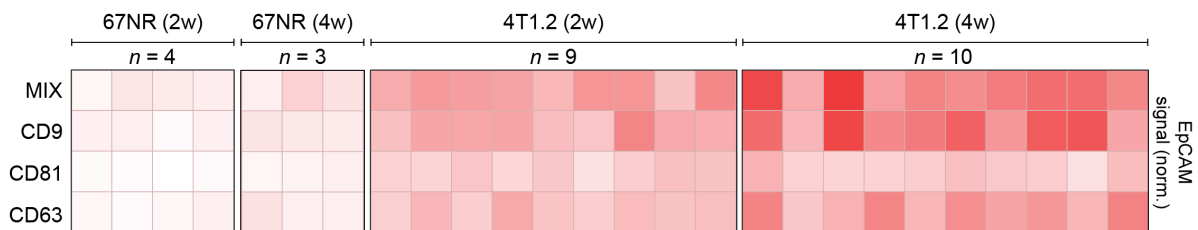


**Figure 4-12 | A heat map constructed by non-supervised hierarchical clustering of the levels of EpCAM recognized the non-metastatic and high-metastatic.** Heat map constructed by unsupervised hierarchical clustering of the EpCAM levels of different EV subtypes (CD9, CD81, CD 63 and CD9/CD81/CD63) in 67NR/4T1.2 models. The group of CD9/81/63 represents that when a cocktail of these antibodies was used simultaneously for EV capture.

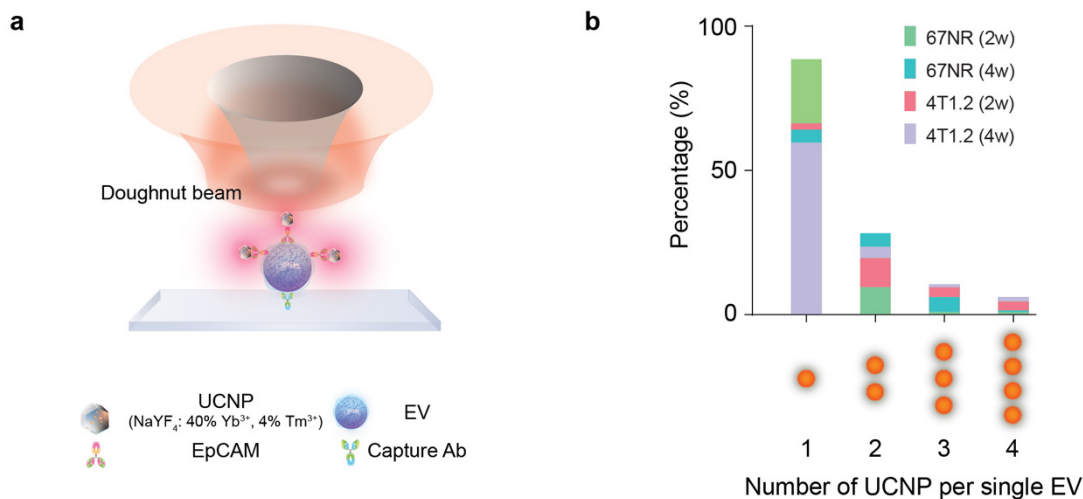


**Figure 4-13 | Single tumour-derived EV imaging by super-resolution microscope. (a) Super-resolution imaging of LENS on single EVs. (a)** Scanning a doughnut excitation beam to resolve LENS clusters on single EVs. **(b)** Percentage of single EVs carrying specific numbers of LENS (such as 1, 2, 3, and 4) measured by super-resolution imaging.

We further evaluated the frequency of EVs conjugated with the specific number of LENS, and found that these two dimensions are sufficient to distinguish 67NR and 4T1.2 models at different cancer metastasis stages. We observed that single EVs carrying an increasing number of LENS with tumour metastasis (**Fig. 4-13**). To rule out that this increase of the number of LENS in Week-4 4T1.2 model was due to the increased size of single EVs, we used NTA analysis to characterise the size of EVs. The result shows an opposite decrease with tumour metastasis progression (**Fig. 4-8**), and suggests that the increased LENS number on single EVs was unlikely due to the increased size of EVs, but more likely due to the increase of EpCAM biomarkers with the tumour progression.

To test whether circulating EVs reflect the molecular profiles of breast cancer tumour metastasis, we conducted immunofluorescence histological studies of the metastatic areas in lung. Study duration for the spontaneous development of metastases to lungs is 24 days. Lung metastatic burden was assessed 2 weeks and 4 weeks after primary tumour resection using immunohistochemical analyses. The results of histological examination of metastases in lung at selected times are shown in **Figure 4-14a**.

The extent of metastases in the lung is greater in 4T1 tumours than those derived from less metastatic 67NR (**Fig. 4-14b**). The 67NR and 4T1.2 (2-week) display little dissemination in the lung from the primary tumour. In 4T1.2 at 4-week, metastases were found within or in close proximity to afferent vessels and in most cases appeared infiltrative, large metastasis on the surface of the lung. This confirmed

that metastasis of 4T1 tumors is associated with extensive necrosis and inflammation within the primary tumor and hematopoiesis in several mouse organs including the spleen and liver.

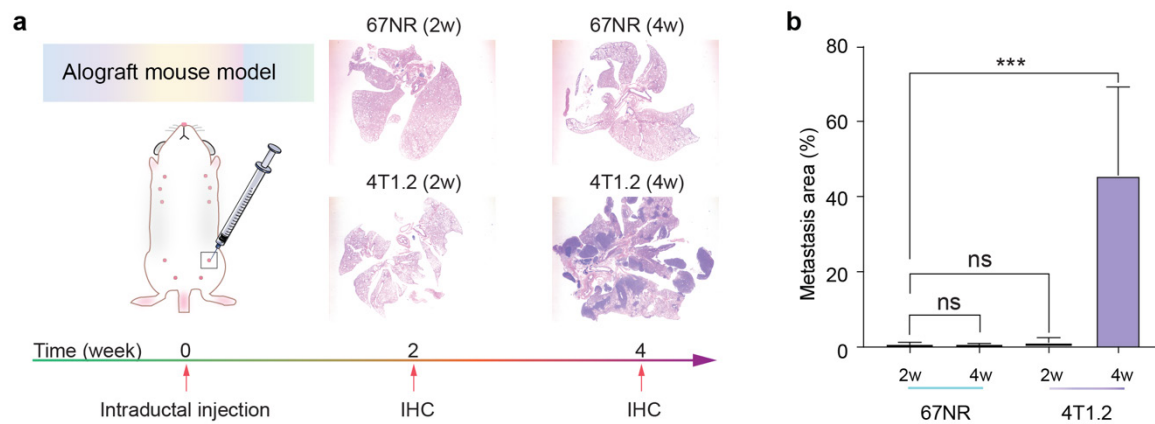


**Figure 4-14 | Metastasis to lungs at selective times.** (a) Immunohistochemistry (IHC) of tissue sections (lung metastasis) in the 67NR/4T1.2 mouse at Week 2 and Week 4 after intraductal. (b) Comparison of the percentage of metastases area for the 67NR/4T1.2 models. The metastases area is calculated based on Andy's Algorithms. n = 6 biological replicates.

The histological results suggest a correlation between the marker profile of circulating EVs and tumour metastases in lungs (**Fig. 4-12, Fig. 4-13b, Fig. 4-14b**), supporting potential applications of circulating EVs as a non-invasive surrogate biopsy for tumours. Moreover, digital profiling of LENS revealed a significantly higher EpCAM expression in EVs derived from 4T1.2 model after 2 weeks than 67NR. In contrast, immunohistochemistry (IHC) failed in detecting early-stage metastasis in week-2 4T1.2 model.

### 4.3.2 Preclinical prognosis of GEMMs

Generation of an ideal tumour microenvironment that mimics a human tumour is challenging, and there are bottlenecking limits to it at multiple levels. Mouse models with genetic alterations closely mimic the human tumour microenvironment and allow for studying the effect of one gene or a group of genes and their role in cancer progression and metastasis.

To differentiate the levels of tumour metastasis, we used a low-metastatic luminal breast cancer<sup>223</sup> MMTV-PyMT (PyMT) mouse mammary tumour model. An ELF5 variant can enhance metastatic dissemination to the lungs in about 80% of the animals. In Elf5 model, forced expression of Elf5 produced tumours that were detected earlier, but which took longer to then reach the ethical endpoint (10% tumour burden).

EVs were isolated from plasma samples from 14-week-old PyMT/WT and PyMT/ELF5 mice. We collected blood and isolated EVs from PyMT/WT and PyMT/Elf5 mice by using well-established size exclusion chromatography (Fig. 4-7). The modal size distribution and concentration of EVs were determined by NTA (Fig. 4-15). The Particle modal sizes are  $149.5 \pm 11.6$  nm (PyMT/WT) and  $146.3 \pm 3.3$  nm (PyMT/Elf5). An equal amount of EV samples was used for following detection.

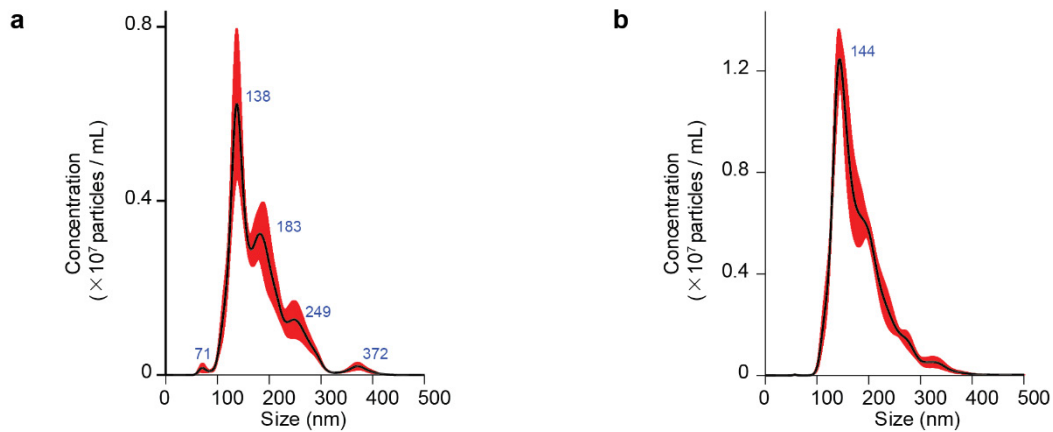


**Figure 4-15 | Size distribution and concentration of circulating EVs characterized by nanoparticle tracking analysis. (a) PyMT/WT. (b) PyMT/Elf5.**

Circulating EVs were captured by the sum of three capture marker CD9, CD81, and CD63 with EpCAM expression quantified using digital imaging of LENS. Circulating EVs were captured by the cocktail mixture of three capture marker CD9, CD81, and CD63 absorbed on the plate, and EpCAM expression of the EVs was quantified using digital imaging of LENS under TIRF (Fig. 4-16a). From TIRF imaging, the number of LENS-EV conjugate is correlated with metastatic dissemination, with a significant increase from Elf5 mice compared with in WT mice (Fig. 4-16b).

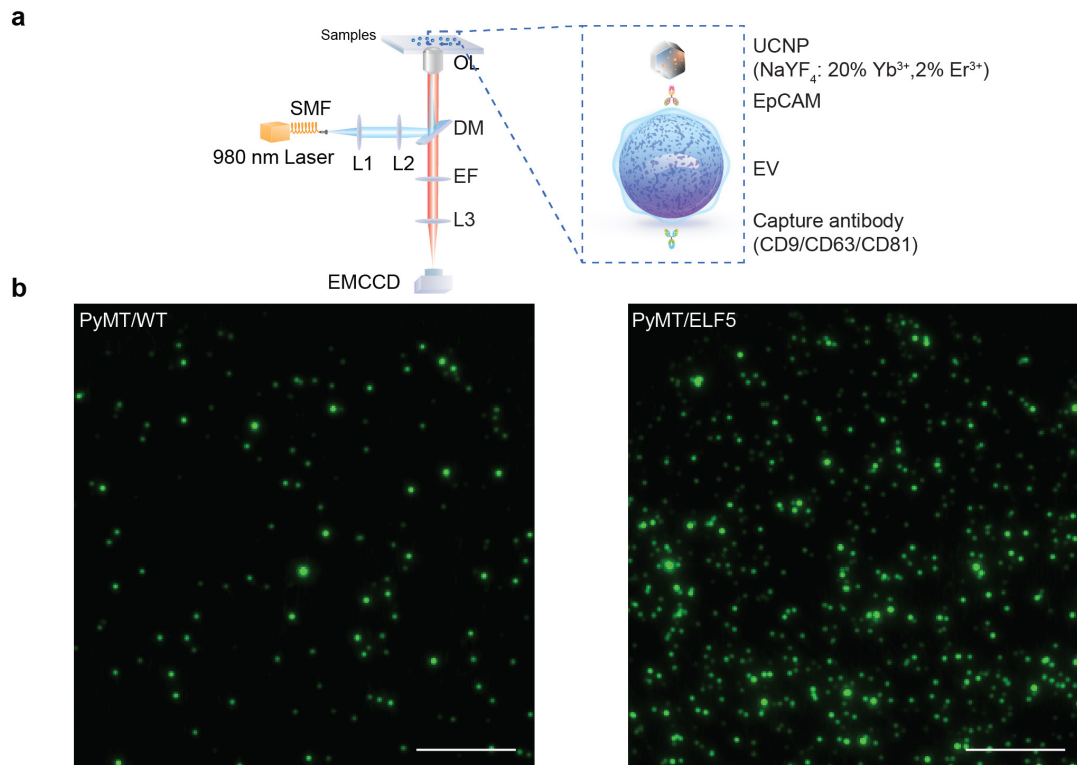


**Figure 4-16 | EpCAM level in Elf5 and in WT EVs.** (a) Schematic illustration of circulating EV imaging labeled by LENS by TIRF imaging. (b) TIRF images of  $\text{EpCAM}^+$  circulating EVs on WT/Elf5 mouse models identified by LENS. Exposure time: 500 ms. Scale bar: 10  $\mu\text{m}$ .

Statistical analyses of the LENS assay data in **Figure 4-17** were performed to quantitatively evaluate the diagnostic metrics of these EV capture markers. Analyses with ROC curves revealed superior diagnosis accuracy for EV profiling. We compared the performance of mix and individual markers through ROC curve analysis. The areas under the curve (AUCs) for  $\text{CD9}^+\text{EpCAM}^+$ ,  $\text{CD63}^+\text{EpCAM}^+$ ,  $\text{CD81}^+\text{EpCAM}^+$  and  $\text{CD9/CD63/CD81}^+\text{EpCAM}^+$  of EVs between low-metastatic WT and high-metastatic Elf are determined to be 1.00, 0.917, 0.833, and 1.00, respectively.  $\text{CD81}^+\text{EpCAM}^+$  and  $\text{CD63}^+\text{EpCAM}^+$  showed slightly less diagnostic power than  $\text{CD9}^+\text{EpCAM}^+$  and  $\text{CD9/CD63/CD81}^+\text{EpCAM}^+$ .

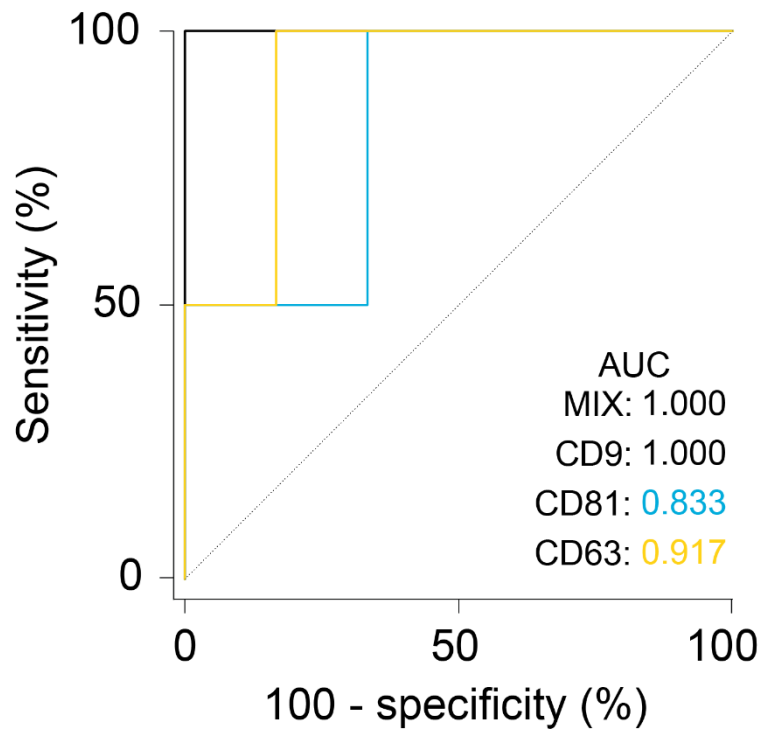


**Figure 4-17 | Receiver operating characteristic (ROC) curves of the LENS regression models on samples of between WT and Elf5.** ROC curves were constructed using individual markers or a combination of the capture markers (mix).

We assessed the LENS assay of three EV capture markers and their mix for detecting the WT and Elf5 using one-way ANOVA with post-hoc Tukey's test. The comparison tests between the groups revealed that CD9, CD63, CD81 could significantly differentiate the low-metastatic breast cancer from the high-metastatic breast cancer. The results suggest Induction of Elf5 greatly increased the amount of EpCAM present in EVs. **Figure 4-18** shows that multiparameter profiling by interrogating each capture marker can differentiate low-metastasis and high-metastasis mice. EpCAM expression level on  $CD9^+$ EVs was found to be able to significantly differentiate the PyMT/ELF5 from PyMT/WT, while those of  $CD63^+$  and  $CD81^+$  could not. Taken together, our validation studies indicate that LENS can reflect EpCAM expression levels of the EVs correlated with the development of cancer, differentiate low-metastasis and high-metastasis tumours, and can observe heterogeneity among ELF5 variation groups. The number of  $EpCAM^+$ EVs was associated with metastatic burden, suggested by the increased EpCAM signal in EVs isolated from the PyMT/ELF5 model compared with the PyMT/WT.

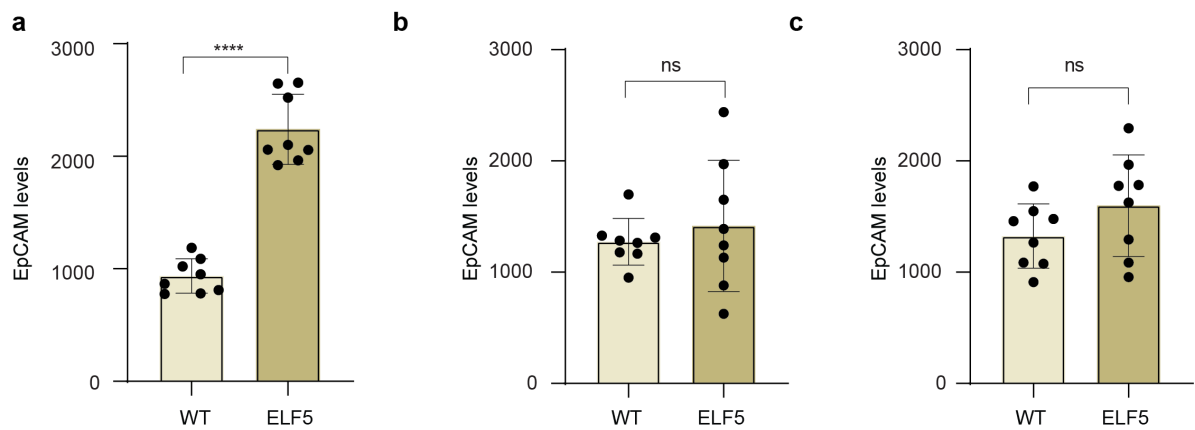


**Figure 4-18 | EpCAM expression profile among EV subpopulations from 67NR/4T1.2 mouse models measured by LENS. (a), CD9 capture; (b), CD81 capture; (c), CD63 capture. One-way ANOVA with Tukey’s multiple comparisons test. \* $P < 0.05$ , \*\* $P < 0.01$ , \*\*\* $P < 0.001$ , \*\*\*\* $P < 0.0001$ , ns: not significant.**

To assess the feasibility of our technology for multiplexed EV profiling to identify disease fingerprints, we performed non-supervised hierarchical clustering analysis of the measured levels of three capture markers and their mixture. The resultant heat map showed that the groups were classified into distinct two clusters by this three-marker and their combination (**Fig. 4-19**), suggesting the potential of EV profiling for GEMM breast cancer diagnosis and stratification. However, clinical promise of these biomarkers needs rigorous validation with much larger cohorts.

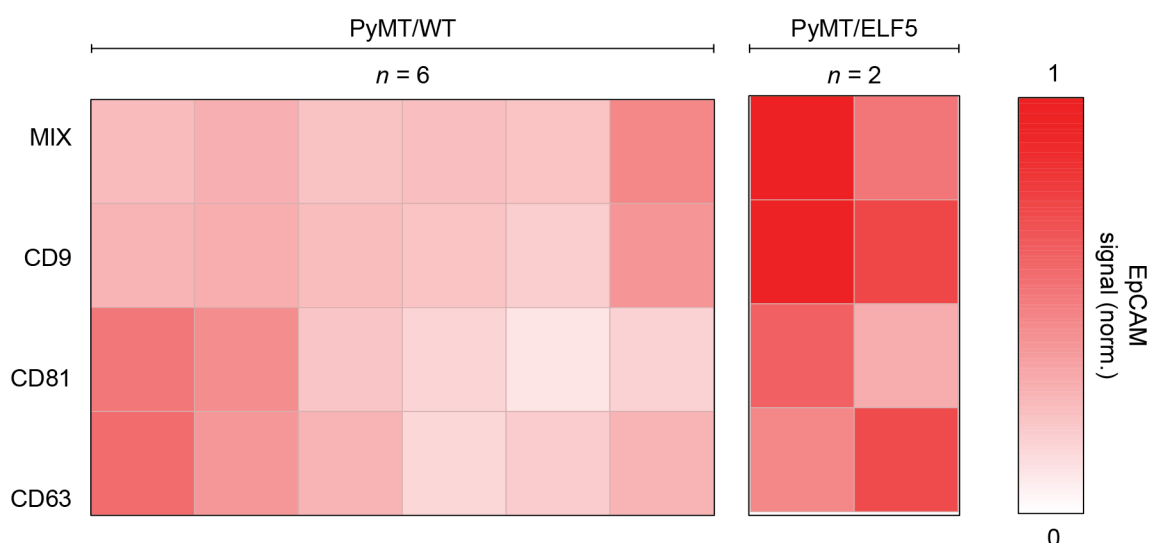


**Figure 4-19 | A heat map constructed by non-supervised hierarchical clustering of the levels of EpCAM recognized the non-metastatic PyMT/WT and high-metastatic PyMT/Elf5. Heat map**



constructed by unsupervised hierarchical clustering of the EpCAM levels of different EV subtypes (CD9, CD81, CD 63 and CD9/CD81/CD63) in WT/Elf5 models. The group of CD9/81/63 represents that when a cocktail of these antibodies was used simultaneously for EV capture.

We further evaluate the frequency of EVs conjugated with the specific number of LENS (**Fig. 4-20a**). We observed that single EVs carrying an increasing number of LENS with Elf drives. And we found that these two dimensions are sufficient to distinguish WT and Elf5 models (**Fig. 4-20b**).

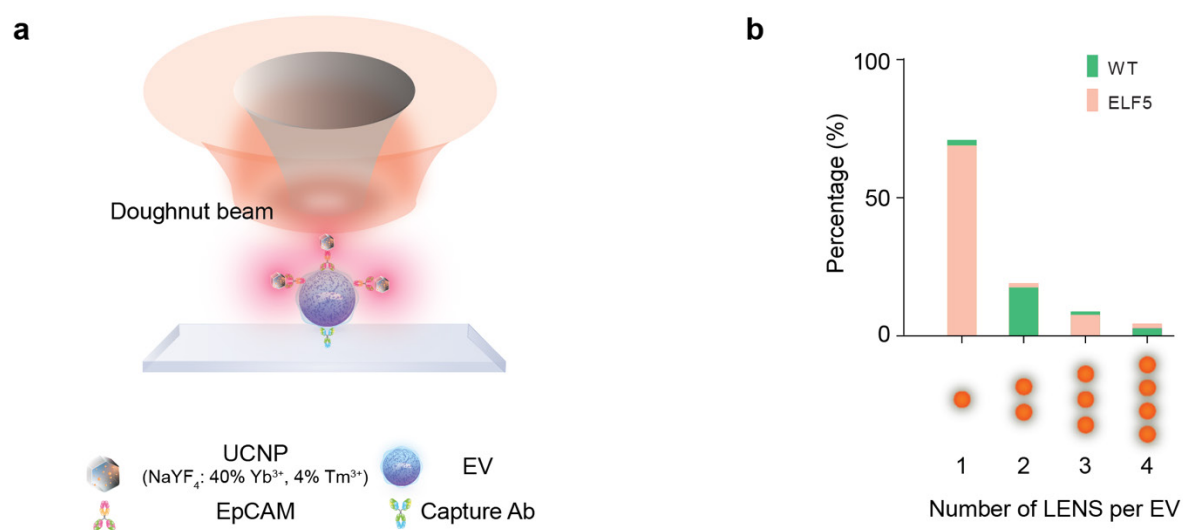


**Figure 4-20 | Single tumour-derived EV imaging by super-resolution microscope.** (a) Scanning a doughnut excitation beam to resolve LENS clusters on single EVs. (b) Percentage of single EVs carrying specific numbers of LENS (such as 1, 2, 3, and 4) measured by super-resolution imaging.

To test whether circulating EVs reflect the molecular profiles of breast cancer tumour metastasis, we conducted immunofluorescence histological studies of the metastatic areas in lung. The metastasis formation was observed for the PyMT model and its ELF5 variant by the week of 14 with different degrees (**Fig. 4-21a**)<sup>228</sup>. Tumours carrying the ELF5 transgene (PyMT/ELF5) present a much higher metastatic burden in the lungs than PyMT/WT mice, which was verified by IHC analysis (**Fig. 4-21b**). Now visible as large and numerous metastases within the lungs by H&E histology. And a heterogeneous pattern of expression was observed. Whereas, the WT display little dissemination in lung from the primary tumour.

The LENS result shows high similarity with tissue IHC result (**Fig. 4-19, Fig. 4-20, Fig 4-21**).

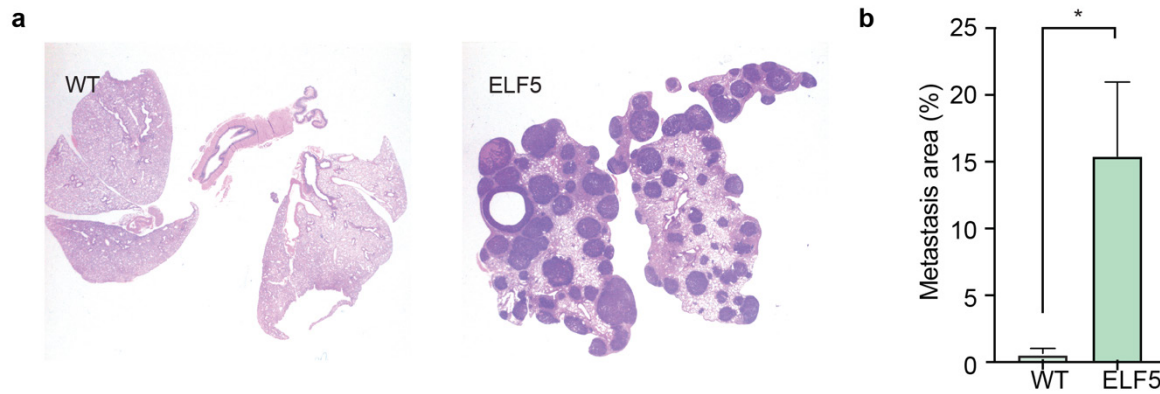


**Figure 4-21 | H&E histology of lungs from mice receiving 14-week induction of Elf5.** (a) Immunohistochemistry (IHC) of tissue sections (lung metastasis) in the 67NR/4T1.2 mouse at Week 2 and Week 4 after intraductal. (b) Comparison of the percentage of metastases area for the 67NR/4T1.2 models. The metastases area is calculated based on Andy's Algorithms<sup>35</sup>. n = 6 biological replicates. (c) Quantification of metastases area in the lungs of the mice with the indicated genotypes after long-term DOX exposure

The histological results suggest a correlation between the marker profile of circulating EVs and tumour metastases in lungs, supporting potential applications of circulating EVs as a non-invasive surrogate biopsy for GEMM tumours. Moreover, these results also suggest that LENS were sensitive enough to pick up the heterogeneous nature of the metastatic burden in the PyMT/ELF5 model.

#### 4.4 Conclusion and discussion

Compared with tissue biopsy (limitation for serial sampling and difficulty to access certain organs, such as brain and lung), EV-based liquid biopsy allows the real-time monitoring of cancer progression during the liquid phase of the metastatic cascade through the detection of different circulating analytes. These circulating analytes have specific biological functions and provide complementary information that can be continuously evaluated during cancer progression. Here, we combined use of the intensity of LENS on each EV and the population analysis of EVs according to the number of LENS further renders the diagnostic power to the non-invasive evaluations of blood samples. With the high sensitivity in detecting different EV subtypes, such as CD9+, CD81+ and CD63+, we demonstrate that LENS can differentiate the levels of cancer metastasis between transgenic PyMT/WT and PyMT/ELF5 models, and longitudinal dissemination of tumour in the isogenic 67NR/4T1.2 mouse models. LENS provides earlier information to inform cancer metastasis than IHC data. In particular, the difference in the EpCAM expression level

for the PyMT/ELF5 models suggests the level of EpCAM expression on EVs as a quantitative indicator to evaluate the heterogeneity of cancer progression.

Overall, our proof-of-concept preclinical analyses validate the ability of our technology for the highly sensitive and specific analysis of tumour-derived circulating EVs. Specially, heterogeneity exists within sites of a tumour between primary cancer and metastases. Tissue biopsy has limitations in capturing spatial and temporal tumour heterogeneity as its information is limited to a single location and time point besides being an invasive method. Our EV-based method could be further revolutionized to enable comprehensive, serial and non-invasive molecular profiling of any tumour-derived material shedded into the blood or other bodily fluids and thereby allows longitudinal monitoring of cancer progression. Therefore, our method is particularly compelling for the development of non-invasive tools for preclinical screening and the early-stage diagnosis of cancer.

---

## Chapter 5 Conclusion and Perspectives

---

The abilities of isolation, detection, and quantification of circulating EVs offer a new paradigm of ‘liquid biopsy’ for non-invasive cancer diagnosis. However, the counts of tumour-associated EVs in biofluids can be very rare during the early stage of disease development. The studies of single EV’s characteristics offer the extremely valuable information to indicate the tumour heterogeneity, rare tumour subtypes, phenotypic changes occurring during therapy, and tumoral changes. Currently available and clinically viable diagnostics approaches are all based on “bulk measurements”, which requires a typical population of  $10^5 - 10^6$  EVs per biomarker to determine the protein composition (e.g., Western, ELISA) or at least  $10^2 - 10^3$  EVs using the advanced methods, e.g.  $\mu$ NMR, nPLEX<sup>131,132</sup>. This presents the bottlenecks to reveal the heterogeneity information of different populations of single EVs, which requires ultra-sensitivity to analyse the low abundance biomarkers on single EVs.

### 5.1 Conclusion

The focus of this thesis is on advancing our abilities in detection, quantification and profiling of single EVs to reveal the disease-associated EV subtypes in the complex biofluid background. In the sequential logic of the three result chapters, I applied UCNPs to quantify the number of sEVs secreted from cancer cell line, adopted super resolution microscope to analyze the number of UCNPs on single sEVs, and finally integrate the power of enumerating single EVs and profiling their surface markers on single EVs to monitor the cancer metastasis and their longitudinal development in mouse models.

The strategy for immunoassay of single sEVs is based on a set of Lanthanide-doped EV-targeting Nanoscopic Signal-amplifiers (LENS). Taking advantage of the up-converting property of LENS and the off-plane background-eliminating property of Total Internal Reflection Fluorescence (TIRF) imaging technique, LENS assay recorded a limit of detection  $1.8 \times 10^6$  EVs mL<sup>-1</sup>, which was two orders of magnitude lower than the standard ELISA. The platform is suitable for evaluating the heterogeneous expression of cancer-derived EV subtypes and can be easily adapted to advance the conventional ELISA approach for future biomarker discoveries and disease diagnosis.

To image single UCNPs on single EpCAM<sup>+</sup>EVs beyond the diffraction limit of light, a super-resolution imaging approach based on a single donut beam scanning has been applied in this project. This approach pushes the resolution to resolve the cluster of several LENS on single EVs, so that the number, the

distribution and the intensity levels from the LENS cluster on single EVs can be used as a new metrics for profile the difference between single EVs.

Based on the above studies, the suit of enabling technologies has been further investigated to assess circulating EVs as non-invasive tool for the diagnosis of preclinical breast cancer samples, including non-metastatic breast cancer mice (67NR, n = 4), high-metastatic breast cancer mice (4T1.2, n = 3), low-metastatic breast mice (PyMT/WT, n = 9) and high-metastatic breast mice (PyMT/Elf5, n = 10). The new scope of single EV profiling suggests the new potentials in monitoring the metastatic tumour progression of preclinical samples.

Once the library of LENS caring a diverse range of colours and lifetime barcodes can be specifically labelled with a range of antibodies and biomarker-specific molecules, our method can be used to detect multiple EV protein markers. The potential capability of multiplexing detection of different EVs subpopulations will be crucial for investigating the heterogeneous nature of sEVs from cancer patients. Microfluidic device or microarray can be further integrated to increase the throughput.

LENS technology is attractive for clinical translation for the following aspects:

- (i) The femtomolar detection limit achieved by the approach suggests its potential for biomarker discovery and early-stage disease diagnosis.
- (ii) The platform could be adapted to measure multiple cancer biomarkers (e.g., HER2, CEA, OPN, PD-L1) of diverse cancer types (e.g., lung cancer, colorectal cancer, prostate cancer) by modifying accordingly the surface of the LENS-nanoprobes.
- (iii) With its ability to recognize cancer biomarkers in native clinical samples, the imaging-based technology could be expanded to measure other molecules and investigate their incorporation and/or association with diverse vesicles.
- (iv) The use of an advanced and relatively complex super-resolution technique allows us to reveal the heterogenous expression of surface markers on single EVs. Owing to the uniformity of LENS, their intensities in the diffraction-limited spot can be used to directly index their number on single EVs. This could bypass the use of the complex equipment by directly using more affordable wide-field-microscopic imaging.

## **5.2 Technical limitations**

Although the technique allowed us to have access to an order of magnitude smaller scale than conventional light microscopy, they cannot meet all of these requirements simultaneously. The majority

of currently developed UCNPs are relatively large (around 20-50 nm) and the trade-off in fabricating sub-10 nm UCNPs lies in the weak emissions. Compared with conventional probes such as organic dyes and quantum dots, UCNP-related super-resolution microscopy is still in the preliminary stage, and both opportunities and challenges exist. Nevertheless, sEVs were isolated using a commercial precipitant, which is difficult to avoid coprecipitate contamination of non-EV components like protein complexes and lipoproteins<sup>190,191</sup>. In addition, we recommend the use of size-exclusion chromatography for plasma EV isolation<sup>192</sup>.

### **5.3 Clinical translation limitations**

Despite promising progress made in nanotechnology-based diagnostic approaches, only a few examples have been advanced to clinical trials. The clinical translation of nanotechnology-based diagnostic approaches is an expensive and time-consuming process, which is usually far more complex in comparison to conventional diagnostic technology. A few major challenges need to be addressed for the clinical translation of the technologies.

(1) Reliability. To be applied in the clinic, it is essential to obtain reliable and quantitative detection results. Many factors can affect NP-based detection signals, including nonspecific binding, aggregation after long-term storage and unfit detection conditions. Fluctuations in the signals can also be attributed to complicated body fluid compositions and the batch-to-batch variations of NP. From a clinical validation perspective, assay reliability and reproducibility need to be extensively investigated in large clinical sample pools.

(2) Large-scale production of NP. Most of current NP are synthesized under highly optimized laboratory conditions; however, it could be still difficult to produce the NP in batches. The detection results could vary with the shape, size, composition, charge, and surface coating of nanoprobe. To minimize batch-to-batch changes, one may automate and simplify the synthesis and nanoprobe functionalization procedures, e.g. using automated synthesis machines.

(3) Easy-to-handle and cost-efficient NP-based devices. To bring the technology to most people in need, an ideal detection devices/hardware should be small and portable and without special training for use. This will facilitate the widespread use of the technology, especially for point of care settings or resource-limited conditions.

(4) Nanotoxicity induced by their systemic administration. This challenge arises from the applications of NP in vivo. Studies have shown that the properties of nanoparticles (such as shape, size, charge, surface

chemistry, targeting ligands, and composition) may influence their toxicity<sup>229</sup>. In this respect, one should consider the biodistribution, biodegradability, and pharmacokinetic properties of nanoparticles.

(5) Validation technique. Compared to conventional methods, the nanotechnology lacks clear regulatory guidelines specific for nanotechnology-based diagnostic approaches and lack of actionable information provided from quantification alone. Therefore, the use of nanotechnology demands an assessment of subgroup properties that requires with nano-dimensions, sensitive, easy to use, and non-expensive in order to allow direct signal observation, manipulation, analysis, and result validation.

#### **5.4 Perspectives**

More broadly, further technical advances through incorporating the latest developments of single molecular probes, advanced molecular recognition mechanisms, imaging and analytical tools will enable the quantitative and high throughput measurements of the rare and complex molecular signatures of single EVs. These studies will not only facilitate comprehensive vesicle characterization but also provide new insights into compositional changes of secreted factors during disease progression. In the following, we outline a few directions that could fuel new opportunities for the EVs research field (**Fig. 5-1**):

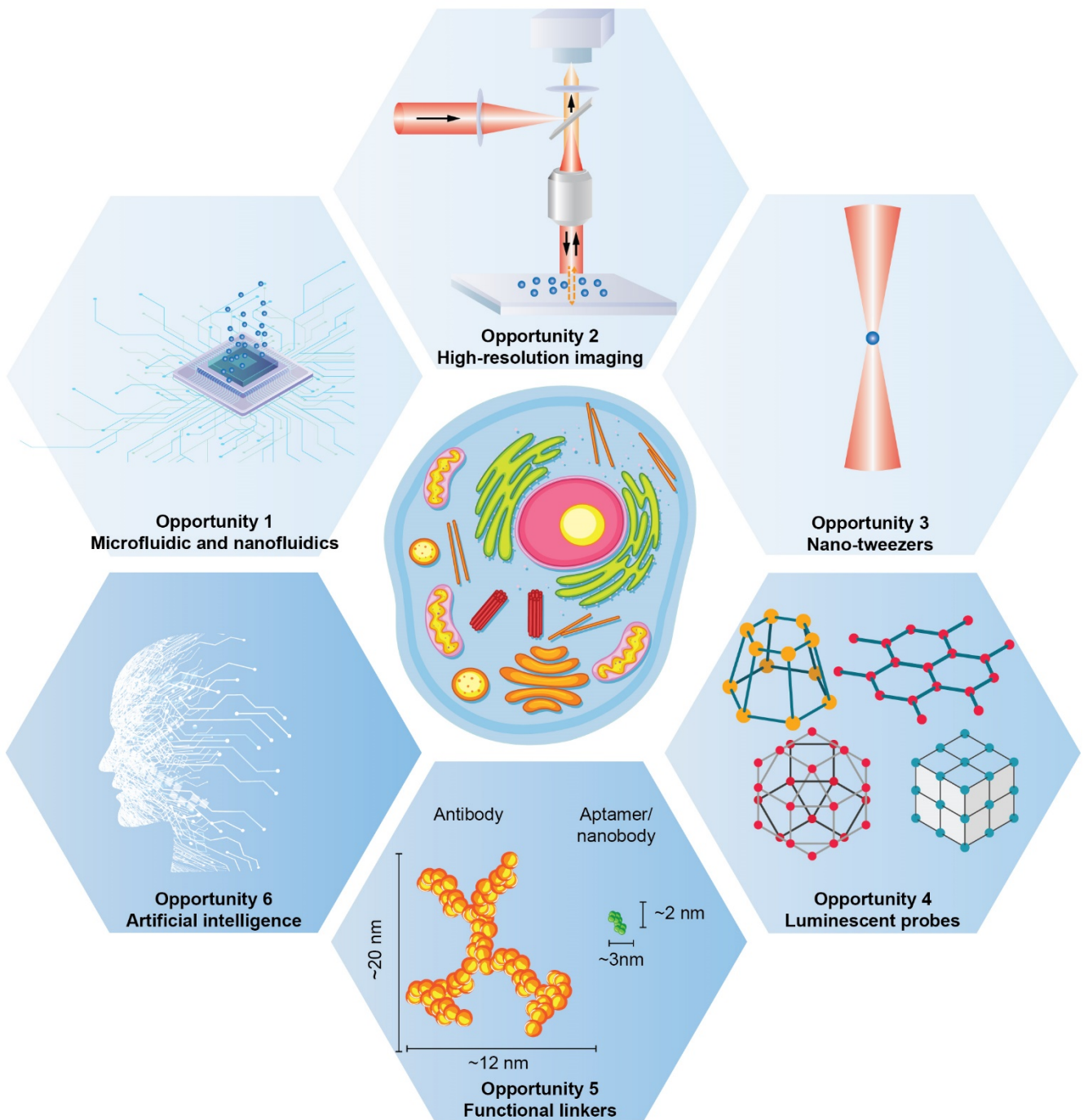


**Figure 5-1 | Overview of key opportunities in developing new capacities for EV heterogeneity research. Reproduced from reference<sup>18</sup>.**

**Three-dimensional super resolution microscope** to specifically recognize unique epitopes of one single EV are suggested to be involved in EV heterogeneity study. How many epitopes expressed in one single EV, in which site do they expressed the specific antigen, relationships between epitopes and parental cells are far from known. Three-dimensional super-resolution microscopy would fill the gap to provide the 3D information of epitopes in single EV.



**Optical tweezing** could trap and precisely manipulate small particles and is expected to play an increasingly important role to deliver molecules to cells in a highly controlled manner<sup>230,231</sup>. Recently, optical manipulation was used to directly image EV-cell interactions and to determine in a quantitative manner the contribution of surface co-receptors and extracellular protein modulators to the contacts<sup>232</sup>. Optical tweezing is emerging as a promising technique in revealing the spatiotemporal properties of single EVs, including the abundance of biomarkers expressed on the EV surface, or the dynamics of EV uptake and release, which are not reliable with traditional methods.

**New library of functional linkers.** Current approaches to isolate EVs including ultracentrifugation, polymer-based precipitation and filtration, could lead to high heterogeneity, contamination and EV damage. This has hampered the downstream analysis of EV heterogeneity with high fidelity. Effective strategies are crucially needed to bypass the expensive or bulky experiments. Designing functional linkers that are capable of highly efficient capture of EVs and subsequent release would be highly desirable. For example, a functional lipid nanoprobe composed of a labelling probe and a capture probe has been synthesized for the labelling of the lipid bilayer of EVs<sup>233</sup>. With optimized labelling efficiency, the probes embodied by biotin-tagged 1,2-distearoyl-sn-glycero-3-phosphoethanolamine-poly (ethylene glycol) can shorten the EV isolation procedures from hours to 15 min. A type of responsive materials such as allylated psoralen functionalized polyacrylamide gel are used to capture and release target nucleic acids spanning a wide range of lengths upon UV irradiation within 1 min<sup>234</sup>. Such responsive linkers should be possible for their use in the surface modification of microfluidic devices, micro- and nanocarriers for EV isolation. Only a few responsive linkers are currently available, but a range of responsive linkers should be possible through the rational synthetic design of functional groups for targeting EV surface markers and those responding to external stimuli, such as light, temperature and PH.

**Aptamers (~15 kDa) and nanobodies (~13 kDa)** are smaller than conventional antibodies (~150 kDa). They could break the limitations of heterogeneity analysis associated with steric hindrance, self-aggregation of labelling agents. In conventional immunostainings, the primary/secondary antibody complex can have a linear length of ~20 nm, complicating their penetration into tissue and reducing the number of epitopes detected. Aptamers are short single-stranded nucleic acid sequences capable of binding to target molecules in a way similar to antibodies<sup>235,236</sup>. Main advantages of aptamers in advanced microscopy lie in monomeric binding, small size, short generation time, low batch-to-batch variability, low/no immunogenicity, high modifiability and high target potential<sup>237–239</sup>. Nanobodies are recombinant,

antigen-specific, single-domain, variable fragments of camelid heavy chain-only antibodies<sup>240,241</sup>. The innate supremacy of nanobodies as a renewable source of affinity reagents, together with minimal size, great stability, reversible refolding and ability to specifically recognize unique epitopes with sub-nanomolar affinity<sup>242</sup>. We anticipate that aptamers and nanobodies would play an increasingly important role in labeling biomolecules in advanced microscope for EV heterogeneity research.

**Artificial intelligence** is emerging as a promising technique in helping process big data and classify complicated data based on patterns submerged inside to overcome the complexity and heterogeneity. It can easily detect signature of disease of large data and predict specific disease states<sup>243–245</sup>. Artificial intelligence including machine learning or deep learning provides an unprecedented opportunity to extract information from complex or big datasets in chromatography, mass spectrometry, nuclear magnetic resonance, and spectroscopy previously<sup>246</sup>. In addressing the complexity in heterogeneity, artificial intelligence is expected to offer a powerful tool in big data processing to decode the complexity of cell multi-omics and EV compositional profiling.

**Microfluidic platforms** enable the analysis and detection of cancer biomarkers<sup>247</sup>. Circulating tumor cells can be separated on-chip from whole blood using several microfluidic techniques. Cell-free DNA can be detected by microfluidic digital PCR or electrochemical biosensors. Exosomes can be captured and analyzed using immunoaffinity approaches. Multiple protein biomarkers can be quantitated by digital or analog immunoassays.

**Profiling EVs at single-cell level** is crucial to reveal EV heterogeneity as the heterogeneity of EVs may come from their parental cells. Statistical analysis over a number of single cells would provide more information that is often hidden in large cell populations<sup>248,249</sup>. The reconfigurability of a microfluidic device would provide unmatched advantages for the dynamic monitoring of secreted analytes released from single cells. This has been recently proven by trapping antibody-modified sensing microbeads with single cells inside picoliter-microcompartments<sup>251</sup> (**Fig. 5-2**). Furthermore, it is possible to create arrays of single cells for time-lapse studies of exosome secretion and cell behaviours<sup>252</sup>. Not limiting to analyzing secretions from localized single cells, innovations in microfluidic chips should address the translocation of single cells for downstream analysis<sup>254</sup>. The phenotypes between parental and progeny cells derived from single cells can be tracked. A collection of holistic EV secretion can be further analyzed by other in-depth sequencing technique such as digital PCR. Besides the information of surface proteins, correlation of single cell omics with the compositional profiling of EVs would establish crucial

database for understanding EV biogenesis, cell communications and disease progression. However, this would require addressing critical challenges to separate individual cells and establish one-to-one correlation with their secreted EVs.

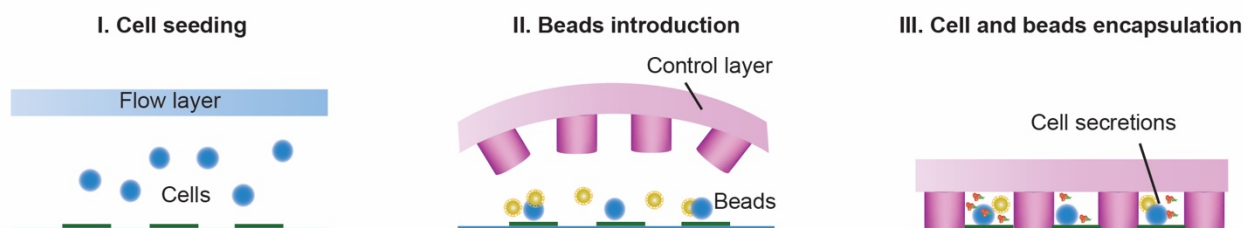


**Figure 5-2** | Microcompartment arrays for isolating single cells and monitoring release of exosomes over time using sensing beads<sup>251</sup>. (I) Cells are captured on the micropatterned floor (CD4 Ab, collagen). (II) Microbeads are flowed into the device and become entrapped inside the compartments. (III) Fluorescence increases overtime after exosomes bounded on the bead surface. Reprinted from reference<sup>18</sup>.

In summary, with the above capabilities, we would be more likely to expand a few key understandings of EVs, including: (1) how EV heterogeneity contributes to cell heterogeneity; (2) what factors contribute to EV heterogeneity and if they can be controlled for therapeutics, e.g. drug delivery; (3) how EV heterogeneity patterns inform disease status and may ultimately contribute to clinical diagnostics. This would require technology developers and end-users (biologists and clinicians) to work more closely to address common biological questions. By filling the significant gap between physicists, engineers, biologists and clinicians, more in-depth and precise investigations on the underlying complexity of EV heterogeneity would accelerate the advancement of EV-based early diagnostics and personalized therapeutic.

## Reference

1. Keller, L. & Pantel, K. Unravelling tumour heterogeneity by single-cell profiling of circulating tumour cells. *Nat. Rev. Cancer* **19**, 553–567 (2019).
2. Underwood, J. J. *et al.* Liquid Biopsy for Cancer: Review and Implications for the Radiologist. *Radiology* **294**, 5–17 (2019).
3. Zhou, E. *et al.* Circulating extracellular vesicles are effective biomarkers for predicting response to cancer therapy. *EBioMedicine* **67**, 103365 (2021).

4. Harris, L. *et al.* American Society of Clinical Oncology 2007 Update of Recommendations for the Use of Tumor Markers in Breast Cancer. *J. Clin. Oncol.* **25**, 5287–5312 (2007).
5. Jackson, J. M., Witek, M. A., Kamande, J. W. & Soper, S. A. Materials and microfluidics: enabling the efficient isolation and analysis of circulating tumour cells. *Chem. Soc. Rev.* **46**, 4245–4280 (2017).
6. Smerage, J. B. *et al.* Circulating Tumor Cells and Response to Chemotherapy in Metastatic Breast Cancer: SWOG S0500. *J. Clin. Oncol.* **32**, 3483–3489 (2014).
7. Yuana, Y. *et al.* Cryo-electron microscopy of extracellular vesicles in fresh plasma. *J. Extracell. Vesicles* **2**, 21494 (2013).
8. Arraud, N. *et al.* Extracellular vesicles from blood plasma: determination of their morphology, size, phenotype and concentration. *J. Thromb. Haemost.* **12**, 614–627 (2014).
9. Poliakov, A., Spilman, M., Dokland, T., Amling, C. L. & Mobley, J. A. Structural heterogeneity and protein composition of exosome-like vesicles (prostasomes) in human semen. *Prostate* **69**, 159–167 (2009).
10. Höög, J. L. & Lötvall, J. Diversity of extracellular vesicles in human ejaculates revealed by cryo-electron microscopy. *J. Extracell. vesicles* **4**, 28680 (2015).
11. RONQUIST, G., BRODY, I., GOTTFRIES, A. & STEGMAYR, B. An Mg<sup>2+</sup> and Ca<sup>2+</sup>-Stimulated Adenosine Triphosphatase in Human Prostatic Fluid: Part I. *Andrologia* **10**, 261–272 (1978).
12. Pisitkun, T., Shen, R.-F. & Knepper, M. A. Identification and proteomic profiling of exosomes in human urine. *Proc. Natl. Acad. Sci. U. S. A.* **101**, 13368–13373 (2004).
13. Yuan, D. *et al.* Macrophage exosomes as natural nanocarriers for protein delivery to inflamed brain. *Biomaterials* **142**, 1–12 (2017).
14. Zhou, Y. *et al.* Exosomes Transfer Among Different Species Cells and Mediating miRNAs Delivery. *J. Cell. Biochem.* **118**, 4267–4274 (2017).
15. Lässer, C. *et al.* Human saliva, plasma and breast milk exosomes contain RNA: uptake by macrophages. *J. Transl. Med.* **9**, 9 (2011).
16. Admyre, C. *et al.* Exosomes with Immune Modulatory Features Are Present in Human Breast

Milk. *J. Immunol.* **179**, 1969 LP – 1978 (2007).

17. Zonneveld, M. I. *et al.* Recovery of extracellular vesicles from human breast milk is influenced by sample collection and vesicle isolation procedures. *J. Extracell. vesicles* **3**, 10.3402/jev.v3.24215 (2014).
18. Huang, G., Lin, G., Zhu, Y., Duan, W. & Jin, D. Emerging technologies for profiling extracellular vesicle heterogeneity. *Lab Chip* **20**, 2423–2437 (2020).
19. Hessvik, N. P. & Llorente, A. Current knowledge on exosome biogenesis and release. *Cell. Mol. Life Sci.* **75**, 193–208 (2018).
20. Beach, A., Zhang, H.-G., Ratajczak, M. Z. & Kakar, S. S. Exosomes: an overview of biogenesis, composition and role in ovarian cancer. *Journal of ovarian research* vol. 7 14 (2014).
21. Barile, L. & Vassalli, G. Exosomes: Therapy delivery tools and biomarkers of diseases. *Pharmacol. Ther.* **174**, 63–78 (2017).
22. Kim, H. K., Song, K. S., Chung, J.-H., Lee, K. R. & Lee, S.-N. Platelet microparticles induce angiogenesis in vitro. *Br. J. Haematol.* **124**, 376–384 (2004).
23. Sarkar, A., Mitra, S., Mehta, S., Raices, R. & Wewers, M. D. Monocyte derived microvesicles deliver a cell death message via encapsulated caspase-1. *PloS one* vol. 4 e7140 (2009).
24. Liu, M.-L., Williams, K. J. & Werth, V. P. Microvesicles in Autoimmune Diseases. *Adv. Clin. Chem.* **77**, 125–175 (2016).
25. Zaldivia, M. T. K., McFadyen, J. D., Lim, B., Wang, X. & Peter, K. Platelet-Derived Microvesicles in Cardiovascular Diseases. *Frontiers in cardiovascular medicine* vol. 4 74 (2017).
26. Müller, I. *et al.* Intravascular tissue factor initiates coagulation via circulating microvesicles and platelets. *FASEB J.* **17**, 476–478 (2003).
27. Meehan, B., Rak, J. & Di Vizio, D. Oncosomes - large and small: what are they, where they came from? *Journal of extracellular vesicles* vol. 5 33109 (2016).
28. Caruso, S. & Poon, I. K. H. Apoptotic Cell-Derived Extracellular Vesicles: More Than Just Debris. *Frontiers in immunology* vol. 9 1486 (2018).
29. Möller, A. & Lobb, R. J. The evolving translational potential of small extracellular vesicles in

- cancer. *Nat. Rev. Cancer* **20**, 697–709 (2020).
30. Meehan, K. & Vella, L. J. The contribution of tumour-derived exosomes to the hallmarks of cancer. *Crit. Rev. Clin. Lab. Sci.* **53**, 121–131 (2016).
  31. Hanahan, D. & Weinberg, R. A. Hallmarks of Cancer: The Next Generation. *Cell* **144**, 646–674 (2011).
  32. Keller, S., Ridinger, J., Rupp, A.-K., Janssen, J. W. G. & Altevogt, P. Body fluid derived exosomes as a novel template for clinical diagnostics. *J. Transl. Med.* **9**, 86 (2011).
  33. Vasconcelos, M. H., Caires, H. R., Ābols, A., Xavier, C. P. R. & Linē, A. Extracellular vesicles as a novel source of biomarkers in liquid biopsies for monitoring cancer progression and drug resistance. *Drug Resist. Updat.* **47**, 100647 (2019).
  34. Rupert, D. L. M., Claudio, V., Lässer, C. & Bally, M. Methods for the physical characterization and quantification of extracellular vesicles in biological samples. *Biochim. Biophys. Acta - Gen. Subj.* **1861**, 3164–3179 (2017).
  35. Zhou, B. *et al.* Application of exosomes as liquid biopsy in clinical diagnosis. *Signal Transduct. Target. Ther.* **5**, 144 (2020).
  36. Mittal, S., Gupta, P., Chaluvally-Raghavan, P. & Pradeep, S. Emerging Role of Extracellular Vesicles in Immune Regulation and Cancer Progression. *Cancers* vol. 12 (2020).
  37. Bettegowda, C. *et al.* Detection of circulating tumor DNA in early- and late-stage human malignancies. *Sci. Transl. Med.* **6**, 224ra24 (2014).
  38. Zhang, J., Quadri, S., Wolfgang, C. L. & Zheng, L. New Development of Biomarkers for Gastrointestinal Cancers: From Neoplastic Cells to Tumor Microenvironment. *Biomedicines* **6**, 87 (2018).
  39. De Rubis, G., Rajeev Krishnan, S. & Bebawy, M. Liquid Biopsies in Cancer Diagnosis, Monitoring, and Prognosis. *Trends Pharmacol. Sci.* **40**, 172–186 (2019).
  40. Théry, C., Witwer, K. W. & Aikawa, E. a. Minimal information for studies of extracellular vesicles 2018 (MISEV2018): a position statement of the International Society for Extracellular Vesicles and update of the MISEV2014 guidelines. *J. Extracell. vesicles* **7**, 1535750 (2018).
  41. Kowal, J. *et al.* Proteomic comparison defines novel markers to characterize heterogeneous

- populations of extracellular vesicle subtypes. *Proc. Natl. Acad. Sci. U. S. A.* **113**, E968-77 (2016).
42. Willms, E. *et al.* Cells release subpopulations of exosomes with distinct molecular and biological properties. *Sci. Rep.* **6**, 22519 (2016).
  43. Ferguson, S. W. & Nguyen, J. Exosomes as therapeutics: The implications of molecular composition and exosomal heterogeneity. *J. Control. Release* **228**, 179–190 (2016).
  44. Willms, E., Cabañas, C., Mäger, I., Wood, M. J. A. & Vader, P. Extracellular Vesicle Heterogeneity: Subpopulations, Isolation Techniques, and Diverse Functions in Cancer Progression. *Front. Immunol.* **9**, 738 (2018).
  45. Lee, S.-S. *et al.* A novel population of extracellular vesicles smaller than exosomes promotes cell proliferation. *Cell Commun. Signal.* **17**, 95 (2019).
  46. Gyuris, A. *et al.* Physical and Molecular Landscapes of Mouse Glioma Extracellular Vesicles Define Heterogeneity. *Cell Rep.* **27**, 3972-3987.e6 (2019).
  47. Feingold, K. R. & Grunfeld, C. *Introduction to Lipids and Lipoproteins*. (MDText.com, Inc., South Dartmouth (MA), 2000).
  48. Margolis, L. & Sadovsky, Y. The biology of extracellular vesicles: The known unknowns. *PLOS Biol.* **17**, 1–12 (2019).
  49. Tkach, M., Kowal, J. & Théry, C. Why the need and how to approach the functional diversity of extracellular vesicles. *Philos. Trans. R. Soc. Lond. B. Biol. Sci.* **373**, (2018).
  50. Coleman, B. M., Hanssen, E., Lawson, V. A. & Hill, A. F. Prion-infected cells regulate the release of exosomes with distinct ultrastructural features. *FASEB J.* **26**, 4160–4173 (2012).
  51. Bosch, S. *et al.* Trehalose prevents aggregation of exosomes and cryodamage. *Sci. Rep.* **6**, 36162 (2016).
  52. van Niel, G. *et al.* Apolipoprotein E Regulates Amyloid Formation within Endosomes of Pigment Cells. *Cell Rep.* **13**, 43–51 (2015).
  53. Zabeo, D. *et al.* Exosomes purified from a single cell type have diverse morphology. *J. Extracell. Vesicles* **6**, 1329476 (2017).
  54. Zeev-Ben-Mordehai, T., Vasishtan, D., Siebert, C. A. & Grünewald, K. The full-length cell-cell

- fusogen EFF-1 is monomeric and upright on the membrane. *Nature communications* vol. 5 3912 (2014).
55. Rontogianni, S. *et al.* Proteomic profiling of extracellular vesicles allows for human breast cancer subtyping. *Commun. Biol.* **2**, 325 (2019).
  56. Smolarz, M., Pietrowska, M., Matysiak, N., Mielańczyk, Ł. & Widłak, P. Proteome Profiling of Exosomes Purified from a Small Amount of Human Serum: The Problem of Co-Purified Serum Components. *Proteomes* **7**, (2019).
  57. Jiao, Y.-J. *et al.* Characterization and proteomic profiling of pancreatic cancer-derived serum exosomes. *J. Cell. Biochem.* **120**, 988–999 (2019).
  58. Skotland, T., Hessvik, N. P., Sandvig, K. & Llorente, A. Exosomal lipid composition and the role of ether lipids and phosphoinositides in exosome biology. *J. Lipid Res.* **60**, 9–18 (2019).
  59. Brzozowski, J. S. *et al.* Lipidomic profiling of extracellular vesicles derived from prostate and prostate cancer cell lines. *Lipids Health Dis.* **17**, 211 (2018).
  60. Haraszti, R. A. *et al.* High-resolution proteomic and lipidomic analysis of exosomes and microvesicles from different cell sources. *J. Extracell. vesicles* **5**, 32570 (2016).
  61. Jeppesen, D. K. *et al.* Reassessment of Exosome Composition. *Cell* **177**, 428–445.e18 (2019).
  62. Squadrito, M. L. *et al.* Endogenous RNAs modulate microRNA sorting to exosomes and transfer to acceptor cells. *Cell Rep.* **8**, 1432–1446 (2014).
  63. Shurtleff, M. J., Temoche-Diaz, M. M., Karfilis, K. V, Ri, S. & Schekman, R. Y-box protein 1 is required to sort microRNAs into exosomes in cells and in a cell-free reaction. *Elife* **5**, (2016).
  64. Cha, D. J. *et al.* KRAS-dependent sorting of miRNA to exosomes. *Elife* **4**, e07197 (2015).
  65. Théry, C., Amigorena, S., Raposo, G. & Clayton, A. Isolation and Characterization of Exosomes from Cell Culture Supernatants and Biological Fluids. *Curr. Protoc. Cell Biol.* **30**, 3.22.1-3.22.29 (2006).
  66. Théry, C., Witwer, K. W., Aikawa, E. & Alcaraz, E. a. Minimal information for studies of extracellular vesicles 2018 (MISEV2018): a position statement of the International Society for Extracellular Vesicles and update of the MISEV2014 guidelines. *Journal of Extracellular Vesicles* vol. 7 1535750 (2018).



67. Keerthikumar, S. *et al.* Proteogenomic analysis reveals exosomes are more oncogenic than ectosomes. *Oncotarget* **6**, 15375–15396 (2015).
68. Koliha, N. *et al.* A novel multiplex bead-based platform highlights the diversity of extracellular vesicles. *J. Extracell. Vesicles* **5**, 29975 (2016).
69. Zhang, H. *et al.* Identification of distinct nanoparticles and subsets of extracellular vesicles by asymmetric flow field-flow fractionation. *Nat. Cell Biol.* **20**, 332–343 (2018).
70. Shen, W. *et al.* A Single Extracellular Vesicle (EV) Flow Cytometry Approach to Reveal EV Heterogeneity. *Angew. Chem. Int. Ed. Engl.* **57**, 15675–15680 (2018).
71. Stoner, S. A. *et al.* High sensitivity flow cytometry of membrane vesicles. *Cytometry. A* **89**, 196–206 (2016).
72. Tian, Y. *et al.* Protein Profiling and Sizing of Extracellular Vesicles from Colorectal Cancer Patients via Flow Cytometry. *ACS Nano* **12**, 671–680 (2018).
73. Görgens, A. *et al.* Optimisation of imaging flow cytometry for the analysis of single extracellular vesicles by using fluorescence-tagged vesicles as biological reference material. *J. Extracell. vesicles* **8**, 1587567 (2019).
74. Pérez-González, R. *et al.* A Method for Isolation of Extracellular Vesicles and Characterization of Exosomes from Brain Extracellular Space. *Methods Mol. Biol.* **1545**, 139–151 (2017).
75. Street, J. M., Koritzinsky, E. H., Glispie, D. M. & Yuen, P. S. T. Urine Exosome Isolation and Characterization. *Methods Mol. Biol.* **1641**, 413–423 (2017).
76. Benedikter, B. J. *et al.* Ultrafiltration combined with size exclusion chromatography efficiently isolates extracellular vesicles from cell culture media for compositional and functional studies. *Sci. Rep.* **7**, 15297 (2017).
77. Xu, R., Greening, D. W., Rai, A., Ji, H. & Simpson, R. J. Highly-purified exosomes and shed microvesicles isolated from the human colon cancer cell line LIM1863 by sequential centrifugal ultrafiltration are biochemically and functionally distinct. *Methods* **87**, 11–25 (2015).
78. Karimi, N. *et al.* Detailed analysis of the plasma extracellular vesicle proteome after separation from lipoproteins. *Cell. Mol. Life Sci.* **75**, 2873–2886 (2018).
79. Whitesides, G. M. The origins and the future of microfluidics. *Nature* **442**, 368–373 (2006).

80. Gholizadeh, S. *et al.* Microfluidic approaches for isolation, detection, and characterization of extracellular vesicles: Current status and future directions. *Biosens. Bioelectron.* **91**, 588–605 (2017).
81. Contreras-Naranjo, J. C., Wu, H.-J. & Ugaz, V. M. Microfluidics for exosome isolation and analysis: enabling liquid biopsy for personalized medicine. *Lab Chip* **17**, 3558–3577 (2017).
82. Liu, C. *et al.* Single-Exosome-Counting Immunoassays for Cancer Diagnostics. *Nano Lett.* **18**, 4226–4232 (2018).
83. Cizmar, P. & Yuana, Y. Detection and Characterization of Extracellular Vesicles by Transmission and Cryo-Transmission Electron Microscopy BT - Extracellular Vesicles: Methods and Protocols. in (eds. Kuo, W. P. & Jia, S.) 221–232 (Springer New York, 2017). doi:10.1007/978-1-4939-7253-1\_18.
84. Bachurski, D. *et al.* Extracellular vesicle measurements with nanoparticle tracking analysis – An accuracy and repeatability comparison between NanoSight NS300 and ZetaView. *J. Extracell. Vesicles* **8**, 1596016 (2019).
85. Dragovic, R. A. *et al.* Isolation of syncytiotrophoblast microvesicles and exosomes and their characterisation by multicolour flow cytometry and fluorescence Nanoparticle Tracking Analysis. *Methods* **87**, 64–74 (2015).
86. Tatischeff, I., Larquet, E., Falcón-Pérez, J. M., Turpin, P.-Y. & Kruglik, S. G. Fast characterisation of cell-derived extracellular vesicles by nanoparticles tracking analysis, cryo-electron microscopy, and Raman tweezers microspectroscopy. *J. Extracell. vesicles* **1**, 10.3402/jev.v1i0.19179 (2012).
87. Collard, L., Sinjab, F. & Notingher, I. Raman Spectroscopy Study of Curvature-Mediated Lipid Packing and Sorting in Single Lipid Vesicles. *Biophys. J.* **117**, 1589–1598 (2019).
88. Zhang, W. *et al.* Enabling Sensitive Phenotypic Profiling of Cancer-Derived Small Extracellular Vesicles Using Surface-Enhanced Raman Spectroscopy Nanotags. *ACS Sensors* **5**, 764–771 (2020).
89. Trueb, J., Avci, O., Sevenler, D., Connor, J. H. & Ünlü, M. S. Robust Visualization and Discrimination of Nanoparticles by Interferometric Imaging. *IEEE J. Sel. Top. Quantum Electron.* **23**, 6900610 (2017).

90. Daaboul, G. G. *et al.* Enhanced light microscopy visualization of virus particles from Zika virus to filamentous ebolaviruses. *PLoS One* **12**, e0179728 (2017).
91. Sebaihi, N., De Boeck, B., Yuana, Y., Nieuwland, R. & Pétry, J. Dimensional characterization of extracellular vesicles using atomic force microscopy. *Meas. Sci. Technol.* **28**, 34006 (2017).
92. He, D. *et al.* Total internal reflection-based single-vesicle in situ quantitative and stoichiometric analysis of tumor-derived exosomal microRNAs for diagnosis and treatment monitoring. *Theranostics* **9**, 4494–4507 (2019).
93. Cerdán, L. *et al.* FRET-assisted laser emission in colloidal suspensions of dye-doped latex nanoparticles. *Nat. Photonics* **6**, 621–626 (2012).
94. Nizamudeen, Z. *et al.* Rapid and accurate analysis of stem cell-derived extracellular vesicles with super resolution microscopy and live imaging. *Biochim. Biophys. acta. Mol. cell Res.* **1865**, 1891–1900 (2018).
95. Chen, W. W. *et al.* BEAMing and Droplet Digital PCR Analysis of Mutant IDH1 mRNA in Glioma Patient Serum and Cerebrospinal Fluid Extracellular Vesicles. *Mol. Ther. Nucleic Acids* **2**, e109–e109 (2013).
96. Notarangelo, M. *et al.* Ultrasensitive detection of cancer biomarkers by nickel-based isolation of polydisperse extracellular vesicles from blood. *EBioMedicine* **43**, 114–126 (2019).
97. Ko, J. *et al.* Single Extracellular Vesicle Protein Analysis Using Immuno-Droplet Digital Polymerase Chain Reaction Amplification. *Adv. Biosyst.* **n/a**, 1900307 (2020).
98. Lee, K. *et al.* Multiplexed Profiling of Single Extracellular Vesicles. *ACS Nano* **12**, 494–503 (2018).
99. Zhang, P. *et al.* Ultrasensitive detection of circulating exosomes with a 3D-nanopatterned microfluidic chip. *Nat. Biomed. Eng.* **3**, 438–451 (2019).
100. Liu, C. *et al.*  $\lambda$ -DNA- and Aptamer-Mediated Sorting and Analysis of Extracellular Vesicles. *J. Am. Chem. Soc.* **141**, 3817–3821 (2019).
101. Liu, C. *et al.* Low-cost thermophoretic profiling of extracellular-vesicle surface proteins for the early detection and classification of cancers. *Nat. Biomed. Eng.* **3**, 183–193 (2019).
102. Wu, X. *et al.* Exosome-templated nanoplasmonics for multiparametric molecular profiling. *Sci.*

*Adv.* **6**, eaba2556–eaba2556 (2020).

103. Tian, Q. *et al.* Nanoparticle Counting by Microscopic Digital Detection: Selective Quantitative Analysis of Exosomes via Surface-Anchored Nucleic Acid Amplification. *Anal. Chem.* **90**, 6556–6562 (2018).
104. Zong, S. *et al.* Single molecule localization imaging of exosomes using blinking silicon quantum dots. *Nanotechnology* **29**, 65705 (2018).
105. Polanco, J. C., Li, C., Durisic, N., Sullivan, R. & Götz, J. Exosomes taken up by neurons hijack the endosomal pathway to spread to interconnected neurons. *Acta Neuropathol. Commun.* **6**, 10 (2018).
106. Wolfbeis, O. S. An overview of nanoparticles commonly used in fluorescent bioimaging. *Chem. Soc. Rev.* **44**, 4743–4768 (2015).
107. Dadfar, S. M. *et al.* Iron oxide nanoparticles: Diagnostic, therapeutic and theranostic applications. *Adv. Drug Deliv. Rev.* **138**, 302–325 (2019).
108. Yokose, T. *et al.* O-Glycan-Altered Extracellular Vesicles: A Specific Serum Marker Elevated in Pancreatic Cancer. *Cancers* vol. 12 (2020).
109. Lee, J.-H. *et al.* Nondestructive Characterization of Stem Cell Neurogenesis by a Magneto-Plasmonic Nanomaterial-Based Exosomal miRNA Detection. *ACS Nano* **13**, 8793–8803 (2019).
110. Zhu, Y. *et al.* Graphene and Graphene Oxide: Synthesis, Properties, and Applications. *Adv. Mater.* **22**, 3906–3924 (2010).
111. Song, Y. *et al.* Recent advances in electrochemical biosensors based on graphene two-dimensional nanomaterials. *Biosens. Bioelectron.* **76**, 195–212 (2016).
112. Yu, Y. *et al.* Electrical and Label-Free Quantification of Exosomes with a Reduced Graphene Oxide Field Effect Transistor Biosensor. *Anal. Chem.* **91**, 10679–10686 (2019).
113. Zhang, P., He, M. & Zeng, Y. Ultrasensitive microfluidic analysis of circulating exosomes using a nanostructured graphene oxide/polydopamine coating. *Lab Chip* **16**, 3033–3042 (2016).
114. Inci, F. *et al.* Multitarget, quantitative nanoplasmonic electrical field-enhanced resonating device (NE&lt;sup&gt;2&lt;/sup&gt;RD) for diagnostics. *Proc. Natl. Acad. Sci.* **112**, E4354 LP-E4363 (2015).

115. Resch-Genger, U., Grabolle, M., Cavaliere-Jaricot, S., Nitschke, R. & Nann, T. Quantum dots versus organic dyes as fluorescent labels. *Nat. Methods* **5**, 763–775 (2008).
116. Rodrigues, M., Richards, N., Ning, B., Lyon, C. J. & Hu, T. Y. Rapid Lipid-Based Approach for Normalization of Quantum-Dot-Detected Biomarker Expression on Extracellular Vesicles in Complex Biological Samples. *Nano Lett.* **19**, 7623–7631 (2019).
117. Jiang, Y. *et al.* High-Throughput Counting and Superresolution Mapping of Tetraspanins on Exosomes Using a Single-Molecule Sensitive Flow Technique and Transistor-like Semiconducting Polymer Dots. *Angew. Chemie Int. Ed.* **60**, 13470–13475 (2021).
118. Tayebi, M., Tavakkoli Yaraki, M., Yang, H. Y. & Ai, Y. A MoS<sub>2</sub>–MWCNT based fluorometric nanosensor for exosome detection and quantification. *Nanoscale Adv.* **1**, 2866–2872 (2019).
119. Wang, Y. *et al.* An aptasensor based on upconversion nanoparticles as LRET donors for the detection of exosomes. *Sensors Actuators B Chem.* **298**, 126900 (2019).
120. Yang, D., Tayebi, M., Huang, Y., Yang, H. Y. & Ai, Y. A Microfluidic DNA Sensor Based on Three-Dimensional (3D) Hierarchical MoS<sub>2</sub>/Carbon Nanotube Nanocomposites. *Sensors (Basel)*. **16**, 1911 (2016).
121. Zhou, B., Shi, B., Jin, D. & Liu, X. Controlling upconversion nanocrystals for emerging applications. *Nat. Nanotechnol.* **10**, 924–936 (2015).
122. Jin, D. *et al.* Nanoparticles for super-resolution microscopy and single-molecule tracking. *Nat. Methods* **15**, 415–423 (2018).
123. Liu, Q., Feng, W., Yang, T., Yi, T. & Li, F. Upconversion luminescence imaging of cells and small animals. *Nat. Protoc.* **8**, 2033–2044 (2013).
124. Heer, S., Kömpe, K., Güdel, H. U. & Haase, M. Highly efficient multicolour upconversion emission in transparent colloids of lanthanide-doped NaYF<sub>4</sub> nanocrystals. *Adv. Mater.* **16**, 2102–2105 (2004).
125. Sharma, R. K. & Ghosh, P. Lanthanide-Doped Luminescent Nanophosphors via Ionic Liquids . *Frontiers in Chemistry* vol. 9 (2021).
126. Duan, C., Liang, L., Li, L., Zhang, R. & Xu, Z. P. Recent progress in upconversion luminescence nanomaterials for biomedical applications. *J. Mater. Chem. B* **6**, 192–209 (2018).

127. Liu, Y. *et al.* A Cyanine-Modified Nanosystem for in Vivo Upconversion Luminescence Bioimaging of Methylmercury. *J. Am. Chem. Soc.* **135**, 9869–9876 (2013).
128. Xu, S. *et al.* A novel upconversion fluorescence resonance energy transfer biosensor (FRET) for sensitive detection of lead ions in human serum. *Nanoscale* **6**, 12573–12579 (2014).
129. Gao, R., Hao, C., Xu, L., Xu, C. & Kuang, H. Spiny Nanorod and Upconversion Nanoparticle Satellite Assemblies for Ultrasensitive Detection of Messenger RNA in Living Cells. *Anal. Chem.* **90**, 5414–5421 (2018).
130. Wang, Y., Shen, P., Li, C., Wang, Y. & Liu, Z. Upconversion Fluorescence Resonance Energy Transfer Based Biosensor for Ultrasensitive Detection of Matrix Metalloproteinase-2 in Blood. *Anal. Chem.* **84**, 1466–1473 (2012).
131. Deng, R., Xie, X., Vendrell, M., Chang, Y.-T. & Liu, X. Intracellular Glutathione Detection Using MnO<sub>2</sub>-Nanosheet-Modified Upconversion Nanoparticles. *J. Am. Chem. Soc.* **133**, 20168–20171 (2011).
132. Hao, C. *et al.* Chiral Core–Shell Upconversion Nanoparticle@MOF Nanoassemblies for Quantification and Bioimaging of Reactive Oxygen Species in Vivo. *J. Am. Chem. Soc.* **141**, 19373–19378 (2019).
133. Wang, P. *et al.* In vivo therapeutic response monitoring by a self-reporting upconverting covalent organic framework nanoplatfrom. *Chem. Sci.* **11**, 1299–1306 (2020).
134. Ju, Q., Uddayasankar, U. & Krull, U. Paper-Based DNA Detection Using Lanthanide-Doped LiYF<sub>4</sub> Upconversion Nanocrystals As Bioprobe. *Small* **10**, 3912–3917 (2014).
135. He, M., Li, Z., Ge, Y. & Liu, Z. Portable Upconversion Nanoparticles-Based Paper Device for Field Testing of Drug Abuse. *Anal. Chem.* **88**, 1530–1534 (2016).
136. Wang, F., Li, W., Wang, J., Ren, J. & Qu, X. Detection of telomerase on upconversion nanoparticle modified cellulose paper. *Chem. Commun.* **51**, 11630–11633 (2015).
137. Wang, C. *et al.* Simultaneous isolation and detection of circulating tumor cells with a microfluidic silicon-nanowire-array integrated with magnetic upconversion nanoprobe. *Biomaterials* **54**, 55–62 (2015).
138. Kale, V. *et al.* Spectrally and Spatially Multiplexed Serological Array-in-Well Assay Utilizing

- Two-Color Upconversion Luminescence Imaging. *Anal. Chem.* **88**, 4470–4477 (2016).
139. Kumar, B. *et al.* Recent trends in the developments of analytical probes based on lanthanide-doped upconversion nanoparticles. *TrAC Trends Anal. Chem.* **139**, 116256 (2021).
  140. Huang, B., Bates, M. & Zhuang, X. Super-resolution fluorescence microscopy. *Annu. Rev. Biochem.* **78**, 993–1016 (2009).
  141. Schermelleh, L., Heintzmann, R. & Leonhardt, H. A guide to super-resolution fluorescence microscopy. *J. Cell Biol.* **190**, 165—175 (2010).
  142. Oxford Nanoimaging. *Technical note: Nanoimager & extracellular vesicles*. [oni.bio/tracking-extracellular-vesicles](https://oni.bio/tracking-extracellular-vesicles) (2019).
  143. Wu, D. *et al.* Profiling surface proteins on individual exosomes using a proximity barcoding assay. *Nat. Commun.* **10**, 3854 (2019).
  144. Sano, T., Smith, C. L. & Cantor, C. R. Immuno-PCR: very sensitive antigen detection by means of specific antibody-DNA conjugates. *Science* **258**, 120—122 (1992).
  145. Fredriksson, S. *et al.* Protein detection using proximity-dependent DNA ligation assays. *Nat. Biotechnol.* **20**, 473—477 (2002).
  146. Söderberg, O. *et al.* Direct observation of individual endogenous protein complexes in situ by proximity ligation. *Nat. Methods* **3**, 995—1000 (2006).
  147. Friedrich, R. *et al.* A nano flow cytometer for single lipid vesicle analysis. *Lab Chip* **17**, 830–841 (2017).
  148. Wu, S. & Butt, H.-J. Near-Infrared-Sensitive Materials Based on Upconverting Nanoparticles. *Adv. Mater.* **28**, 1208–1226 (2016).
  149. Liu, Y. *et al.* Amplified stimulated emission in upconversion nanoparticles for super-resolution nanoscopy. *Nature* **543**, 229–233 (2017).
  150. Huang, B. *et al.* One-scan fluorescence emission difference nanoscopy developed with excitation orthogonalized upconversion nanoparticles. *Nanoscale* **10**, 21025–21030 (2018).
  151. Hu, C. *et al.* MUTE-SIM: multiphoton up-conversion time-encoded structured illumination microscopy. *OSA Contin.* **3**, 594–608 (2020).

152. Liu, B., Wang, F., Chen, C., Dong, F. & McGloin, D. Self-evolving ghost imaging. *Optica* **8**, 1340–1349 (2021).
153. Zhang, X. *et al.* Exosomes in cancer: small particle, big player. *J. Hematol. Oncol.* **8**, 83 (2015).
154. Milane, L., Singh, A., Mattheolabakis, G., Suresh, M. & Amiji, M. M. Exosome mediated communication within the tumor microenvironment. *J. Control. Release* **219**, 278–294 (2015).
155. Sun, Z. *et al.* Emerging role of exosome-derived long non-coding RNAs in tumor microenvironment. *Mol. Cancer* **17**, 82 (2018).
156. Fujita, Y., Yoshioka, Y. & Ochiya, T. Extracellular vesicle transfer of cancer pathogenic components. *Cancer Sci.* **107**, 385–390 (2016).
157. Kalluri, R. The biology and function of exosomes in cancer. *J. Clin. Invest.* **126**, 1208–1215 (2016).
158. Maia, J., Caja, S., Strano Moraes, M. C., Couto, N. & Costa-Silva, B. Exosome-Based Cell-Cell Communication in the Tumor Microenvironment. *Front. Cell Dev. Biol.* **6**, 18 (2018).
159. Costa-Silva, B. *et al.* Pancreatic cancer exosomes initiate pre-metastatic niche formation in the liver. *Nat. Cell Biol.* **17**, 816–826 (2015).
160. Rupp, A.-K. *et al.* Loss of EpCAM expression in breast cancer derived serum exosomes: Role of proteolytic cleavage. *Gynecol. Oncol.* **122**, 437–446 (2011).
161. Moon, P.-G. *et al.* Identification of Developmental Endothelial Locus-1 on Circulating Extracellular Vesicles as a Novel Biomarker for Early Breast Cancer Detection. *Clin. Cancer Res.* **22**, 1757–1766 (2016).
162. Moon, P.-G. *et al.* Fibronectin on circulating extracellular vesicles as a liquid biopsy to detect breast cancer. *Oncotarget* **7**, 40189–40199 (2016).
163. Khan, S. *et al.* Early diagnostic value of survivin and its alternative splice variants in breast cancer. *BMC Cancer* **14**, 176 (2014).
164. Hannafon, B. N. *et al.* Plasma exosome microRNAs are indicative of breast cancer. *Breast Cancer Res.* **18**, 90 (2016).
165. Liu, C. *et al.* Serum exosomal miR-4772-3p is a predictor of tumor recurrence in stage II and III colon cancer. *Oncotarget* **7**, 76250–76260 (2016).



166. Khan, S. *et al.* Plasma-derived exosomal survivin, a plausible biomarker for early detection of prostate cancer. *PLoS One* **7**, e46737 (2012).
167. Nilsson, J. *et al.* Prostate cancer-derived urine exosomes: a novel approach to biomarkers for prostate cancer. *Br. J. Cancer* **100**, 1603—1607 (2009).
168. Melo, S. A. *et al.* Glypican-1 identifies cancer exosomes and detects early pancreatic cancer. *Nature* **523**, 177—182 (2015).
169. Szajnik, M. *et al.* Exosomes in Plasma of Patients with Ovarian Carcinoma: Potential Biomarkers of Tumor Progression and Response to Therapy. *Gynecol. Obstet. (Sunnyvale, Calif.) Suppl* **4**, 3 (2013).
170. Zhao, Z., Yang, Y., Zeng, Y. & He, M. A microfluidic ExoSearch chip for multiplexed exosome detection towards blood-based ovarian cancer diagnosis. *Lab Chip* **16**, 489—496 (2016).
171. Yoshioka, Y. *et al.* Ultra-sensitive liquid biopsy of circulating extracellular vesicles using ExoScreen. *Nat. Commun.* **5**, 3591 (2014).
172. Shao, H. *et al.* Protein typing of circulating microvesicles allows real-time monitoring of glioblastoma therapy. *Nat. Med.* **18**, 1835—1840 (2012).
173. Chang, L. *et al.* Liquid biopsy in ovarian cancer: recent advances in circulating extracellular vesicle detection for early diagnosis and monitoring progression. *Theranostics* **9**, 4130–4140 (2019).
174. Huang, X. *et al.* Characterization of human plasma-derived exosomal RNAs by deep sequencing. *BMC Genomics* **14**, 319 (2013).
175. Gao, Y. *et al.* Small Extracellular Vesicles: A Novel Avenue for Cancer Management . *Frontiers in Oncology* vol. 11 (2021).
176. Avci, O., Ünlü, N. L., Özkumur, A. Y. & Ünlü, M. S. Interferometric Reflectance Imaging Sensor (IRIS)—A Platform Technology for Multiplexed Diagnostics and Digital Detection. *Sensors* vol. 15 (2015).
177. Mathieu, M., Martin-Jaular, L., Lavieue, G. & Théry, C. Specificities of secretion and uptake of exosomes and other extracellular vesicles for cell-to-cell communication. *Nat. Cell Biol.* **21**, 9–17 (2019).

178. Wen, S. *et al.* Advances in highly doped upconversion nanoparticles. *Nat. Commun.* **9**, 2415 (2018).
179. Wang, F. *et al.* Simultaneous phase and size control of upconversion nanocrystals through lanthanide doping. *Nature* **463**, 1061–1065 (2010).
180. Patriarca, C., Macchi, R. M., Marschner, A. K. & Mellstedt, H. Epithelial cell adhesion molecule expression (CD326) in cancer: A short review. *Cancer Treat. Rev.* **38**, 68–75 (2012).
181. Munz, M., Baeuerle, P. A. & Gires, O. The Emerging Role of EpCAM in Cancer and Stem Cell Signaling. *Cancer Res.* **69**, 5627 LP – 5629 (2009).
182. Miller, M. C., Doyle, G. V & Terstappen, L. W. M. M. Significance of Circulating Tumor Cells Detected by the CellSearch System in Patients with Metastatic Breast Colorectal and Prostate Cancer. *J. Oncol.* **2010**, 617421 (2010).
183. Vestad, B. *et al.* Size and concentration analyses of extracellular vesicles by nanoparticle tracking analysis: a variation study. *J. Extracell. vesicles* **6**, 1344087 (2017).
184. Gardiner, C., Ferreira, Y. J., Dragovic, R. A., Redman, C. W. G. & Sargent, I. L. Extracellular vesicle sizing and enumeration by nanoparticle tracking analysis. *J. Extracell. vesicles* **2**, 10.3402/jev.v2i0.19671 (2013).
185. Mackenzie, L. E. *et al.* The theoretical molecular weight of NaYF<sub>4</sub>:RE upconversion nanoparticles. *Sci. Rep.* **8**, 1106 (2018).
186. Martínez-Maqueda, D., Miralles, B. & Recio, I. HT29 Cell Line BT - The Impact of Food Bioactives on Health: in vitro and ex vivo models. in (eds. Verhoeckx, K. *et al.*) 113–124 (Springer International Publishing, 2015). doi:10.1007/978-3-319-16104-4\_11.
187. Maddahfar, M. *et al.* Stable and Highly Efficient Antibody–Nanoparticles Conjugation. *Bioconjug. Chem.* **32**, 1146–1155 (2021).
188. Guesdon, J. L., Ternynck, T. & Avrameas, S. The use of avidin-biotin interaction in immunoenzymatic techniques. *J. Histochem. Cytochem.* **27**, 1131–1139 (1979).
189. Basu, A. S. Digital Assays Part I: Partitioning Statistics and Digital PCR. *SLAS Technol.* **22**, 369–386 (2017).
190. Coumans, F. A. W. *et al.* Methodological Guidelines to Study Extracellular Vesicles. *Circ. Res.*

- 120**, 1632–1648 (2017).
191. Shao, H. *et al.* New Technologies for Analysis of Extracellular Vesicles. *Chem. Rev.* **118**, 1917–1950 (2018).
192. Pang, B. *et al.* Quality Assessment and Comparison of Plasma-Derived Extracellular Vesicles Separated by Three Commercial Kits for Prostate Cancer Diagnosis. *Int. J. Nanomedicine* **15**, 10241–10256 (2020).
193. Chuo, S. T.-Y., Chien, J. C.-Y. & Lai, C. P.-K. Imaging extracellular vesicles: current and emerging methods. *J. Biomed. Sci.* **25**, 91 (2018).
194. Han, C. *et al.* Single-vesicle imaging and co-localization analysis for tetraspanin profiling of individual extracellular vesicles. *J. Extracell. Vesicles* **10**, e12047 (2021).
195. Iyer, R. R. *et al.* Label-free metabolic and structural profiling of dynamic biological samples using multimodal optical microscopy with sensorless adaptive optics. *Sci. Rep.* **12**, 3438 (2022).
196. Burbidge, K. *et al.* Cargo and cell-specific differences in extracellular vesicle populations identified by multiplexed immunofluorescent analysis. *J. Extracell. Vesicles* **9**, 1789326 (2020).
197. Corso, G. *et al.* Systematic characterization of extracellular vesicle sorting domains and quantification at the single molecule - single vesicle level by fluorescence correlation spectroscopy and single particle imaging. *J. Extracell. vesicles* **8**, 1663043 (2019).
198. Bordanaba-Florit, G., Royo, F., Kruglik, S. G. & Falcón-Pérez, J. M. Using single-vesicle technologies to unravel the heterogeneity of extracellular vesicles. *Nat. Protoc.* **16**, 3163–3185 (2021).
199. Schermelleh, L. *et al.* Super-resolution microscopy demystified. *Nat. Cell Biol.* **21**, 72–84 (2019).
200. Verweij, F. J. *et al.* The power of imaging to understand extracellular vesicle biology in vivo. *Nat. Methods* **18**, 1013–1026 (2021).
201. Liu, Y. *et al.* Super-Resolution Mapping of Single Nanoparticles inside Tumor Spheroids. *Small* **16**, 1905572 (2020).
202. Chen, C. *et al.* Multi-photon near-infrared emission saturation nanoscopy using upconversion nanoparticles. *Nat. Commun.* **9**, 3290 (2018).

203. Huang, G. *et al.* Single Small Extracellular Vesicle (sEV) Quantification by Upconversion Nanoparticles. *Nano Lett.* **22**, 3761–3769 (2022).
204. Green, R. & Rogers, E. J. Transformation of chemically competent *E. coli*. *Methods Enzymol.* **529**, 329–336 (2013).
205. Amrollahi, P. *et al.* Ultra-Sensitive Automated Profiling of EpCAM Expression on Tumor-Derived Extracellular Vesicles. *Front. Genet.* **10**, (2019).
206. Thomson, J. J. XXIV. On the structure of the atom: an investigation of the stability and periods of oscillation of a number of corpuscles arranged at equal intervals around the circumference of a circle; with application of the results to the theory of atomic structure. *London, Edinburgh, Dublin Philos. Mag. J. Sci.* **7**, 237–265 (1904).
207. Sloane, N. The proof of the packing. *Nature* **425**, 126–127 (2003).
208. Gilbert, F. J. & Pinker-Domenig, K. Diagnosis and Staging of Breast Cancer: When and How to Use Mammography, Tomosynthesis, Ultrasound, Contrast-Enhanced Mammography, and Magnetic Resonance Imaging. in (eds. Hodler, J., Kubik-Huch, R. A. & von Schulthess, G. K.) 155–166 (2019). doi:10.1007/978-3-030-11149-6\_13.
209. Scheel, J. R., Lee, J. M., Sprague, B. L., Lee, C. I. & Lehman, C. D. Screening ultrasound as an adjunct to mammography in women with mammographically dense breasts. *Am. J. Obstet. Gynecol.* **212**, 9–17 (2015).
210. Tagliafico, A. S. *et al.* Adjunct Screening With Tomosynthesis or Ultrasound in Women With Mammography-Negative Dense Breasts: Interim Report of a Prospective Comparative Trial. *J. Clin. Oncol.* **34**, 1882–1888 (2016).
211. Li, W. *et al.* Emerging Nanotechnologies for Liquid Biopsy: The Detection of Circulating Tumor Cells and Extracellular Vesicles. *Adv. Mater.* **31**, 1805344 (2019).
212. Hicks, W. H. *et al.* Contemporary Mouse Models in Glioma Research. *Cells* vol. 10 (2021).
213. CASEY, A. E., LASTER, W. R. J. & ROSS, G. L. Sustained enhanced growth of carcinoma EO771 in C57 black mice. *Proc. Soc. Exp. Biol. Med. Soc. Exp. Biol. Med. (New York, N.Y.)* **77**, 358–362 (1951).
214. Lelekakis, M. *et al.* A novel orthotopic model of breast cancer metastasis to bone. *Clin. Exp.*

*Metastasis* **17**, 163–170 (1999).

215. Rockwell, S. & Kallman, R. F. Cellular radiosensitivity and tumor radiation response in the EMT6 tumor cell system. *Radiat. Res.* **53**, 281–294 (1973).
216. Aslakson, C. J. & Miller, F. R. Selective Events in the Metastatic Process Defined by Analysis of the Sequential Dissemination of Subpopulations of a Mouse Mammary Tumor. *Cancer Res.* **52**, 1399 LP – 1405 (1992).
217. Fantozzi, A. & Christofori, G. Mouse models of breast cancer metastasis. *Breast Cancer Res.* **8**, 212 (2006).
218. Varticovski, L. *et al.* Accelerated Preclinical Testing Using Transplanted Tumors from Genetically Engineered Mouse Breast Cancer Models. *Clin. Cancer Res.* **13**, 2168 LP – 2177 (2007).
219. Sflomos, G. *et al.* A Preclinical Model for ER $\alpha$ -Positive Breast Cancer Points to the Epithelial Microenvironment as Determinant of Luminal Phenotype and Hormone Response. *Cancer Cell* **29**, 407–422 (2016).
220. Johnstone, C. N. *et al.* Functional and molecular characterisation of EO771.LMB tumours, a new C57BL/6-mouse-derived model of spontaneously metastatic mammary cancer. *Dis. Model. Mech.* **8**, 237–251 (2015).
221. Eckhardt, B. L. *et al.* Genomic Analysis of a Spontaneous Model of Breast Cancer Metastasis to Bone Reveals a Role for the Extracellular Matrix &lt;a id=&quot;xref-fn-1-1&quot; class=&quot;xref-&quot; href=&quot;#fn-1&quot;&gt;&lt;sup&gt;1&lt;/sup&gt;&lt;/a&gt; 1 Department of De. *Mol. Cancer Res.* **3**, 1 LP – 13 (2005).
222. Tao, K., Fang, M., Alroy, J. & Sahagian, G. G. Imagable 4T1 model for the study of late stage breast cancer. *BMC Cancer* **8**, 228 (2008).
223. Lin, E. Y. *et al.* Progression to malignancy in the polyoma middle T oncoprotein mouse breast cancer model provides a reliable model for human diseases. *Am. J. Pathol.* **163**, 2113–2126 (2003).
224. Gallego-Ortega, D. *et al.* ELF5 Drives Lung Metastasis in Luminal Breast Cancer through Recruitment of Gr1<sup>+</sup> CD11b<sup>+</sup> Myeloid-Derived Suppressor Cells. *PLoS Biol.* **13**, e1002330–

e1002330 (2015).

225. Guy, C. T., Cardiff, R. D. & Muller, W. J. Induction of mammary tumors by expression of polyomavirus middle T oncogene: a transgenic mouse model for metastatic disease. *Mol. Cell Biol.* **12**, 954–961 (1992).
226. Gallego-Ortega, D. *et al.* ELF5 Drives Lung Metastasis in Luminal Breast Cancer through Recruitment of Gr1<sup>+</sup> CD11b<sup>+</sup> Myeloid-Derived Suppressor Cells. *PLOS Biol.* **13**, e1002330 (2016).
227. Law, A. M. K. *et al.* Andy's Algorithms: new automated digital image analysis pipelines for FIJI. *Sci. Rep.* **7**, 15717 (2017).
228. Valdés-Mora, F. *et al.* Single-cell transcriptomics reveals involution mimicry during the specification of the basal breast cancer subtype. *Cell Rep.* **35**, 108945 (2021).
229. Albanese, A., Tang, P. S. & Chan, W. C. W. The Effect of Nanoparticle Size, Shape, and Surface Chemistry on Biological Systems. *Annu. Rev. Biomed. Eng.* **14**, 1–16 (2012).
230. Ashkin, A., Dziedzic, J. M., Bjorkholm, J. E. & Chu, S. Observation of a single-beam gradient force optical trap for dielectric particles. *Opt. Lett.* **11**, 288–290 (1986).
231. Grier, D. G. A revolution in optical manipulation. *Nature* **424**, 810–816 (2003).
232. Prada, I. *et al.* A new approach to follow a single extracellular vesicle-cell interaction using optical tweezers. *Biotechniques* **60**, 35–41 (2016).
233. Wan, Y. *et al.* Rapid magnetic isolation of extracellular vesicles via lipid-based nanoprobe. *Nat. Biomed. Eng.* **1**, (2017).
234. Zhang, Y., Chan, P. P. Y. & Herr, A. E. Rapid Capture and Release of Nucleic Acids through a Reversible Photo-Cycloaddition Reaction in a Psoralen-Functionalized Hydrogel. *Angew. Chem. Int. Ed. Engl.* **57**, 2357–2361 (2018).
235. Ellington, A. D. & Szostak, J. W. In vitro selection of RNA molecules that bind specific ligands. *Nature* **346**, 818–822 (1990).
236. Tuerk, C. & Gold, L. Systematic evolution of ligands by exponential enrichment: RNA ligands to bacteriophage T4 DNA polymerase. *Science (80-. )*. **249**, 505–510 (1990).
237. Strauss, S. *et al.* Modified aptamers enable quantitative sub-10-nm cellular DNA-PAINT

- imaging. *Nat. Methods* **15**, 685–688 (2018).
238. Yan, Q. *et al.* Using an RNA aptamer probe for super-resolution imaging of native EGFR. *Nanoscale Adv.* **1**, 291–298 (2019).
239. Zhang, Y., Lai, B. S. & Juhas, M. Recent Advances in Aptamer Discovery and Applications. *Molecules* **24**, 941 (2019).
240. Ries, J., Kaplan, C., Platonova, E., Eghlidi, H. & Ewers, H. A simple, versatile method for GFP-based super-resolution microscopy via nanobodies. *Nat. Methods* **9**, 582–584 (2012).
241. Gulati, S. *et al.* Targeting G protein-coupled receptor signaling at the G protein level with a selective nanobody inhibitor. *Nat. Commun.* **9**, 1996 (2018).
242. Mikhaylova, M. *et al.* Resolving bundled microtubules using anti-tubulin nanobodies. *Nat. Commun.* **6**, 7933 (2015).
243. Shin, H. *et al.* Early-Stage Lung Cancer Diagnosis by Deep Learning-Based Spectroscopic Analysis of Circulating Exosomes. *ACS Nano* (2020) doi:10.1021/acsnano.9b09119.
244. Gómez-de-Mariscal, E. *et al.* Deep-Learning-Based Segmentation of Small Extracellular Vesicles in Transmission Electron Microscopy Images. *Sci. Rep.* **9**, 13211 (2019).
245. Ko, J. *et al.* Combining Machine Learning and Nanofluidic Technology To Diagnose Pancreatic Cancer Using Exosomes. *ACS Nano* **11**, 11182–11193 (2017).
246. Lussier, F., Thibault, V., Charron, B., Wallace, G. Q. & Masson, J.-F. Deep learning and artificial intelligence methods for Raman and surface-enhanced Raman scattering. *TrAC Trends Anal. Chem.* **124**, 115796 (2020).
247. Garcia-Cordero, J. L. & Maerkl, S. J. Microfluidic systems for cancer diagnostics. *Curr. Opin. Biotechnol.* **65**, 37–44 (2020).
248. Walling, M. A. & Shepard, J. R. E. Cellular heterogeneity and live cell arrays. *Chem. Soc. Rev.* **40**, 4049–4076 (2011).
249. Weaver, W. M. *et al.* Advances in high-throughput single-cell microtechnologies. *Curr. Opin. Biotechnol.* **25**, 114–123 (2014).
250. Wootton, R. C. R. & Demello, A. J. Microfluidics: Exploiting elephants in the room. *Nature* **464**, 839–840 (2010).

251. Son, K. J. *et al.* Microfluidic compartments with sensing microbeads for dynamic monitoring of cytokine and exosome release from single cells. *Analyst* **141**, 679–688 (2016).
252. Chiu, Y.-J., Cai, W., Shih, Y.-R. V, Lian, I. & Lo, Y.-H. A Single-Cell Assay for Time Lapse Studies of Exosome Secretion and Cell Behaviors. *Small* **12**, 3658–3666 (2016).
253. Ji, Y. *et al.* Multiplexed profiling of single-cell extracellular vesicles secretion. *Proc. Natl. Acad. Sci. U. S. A.* (2019) doi:10.1073/pnas.1814348116.
254. Cai, W. *et al.* A single-cell translocation and secretion assay (TransSeA). *Lab Chip* **18**, 3154–3162 (2018).